PACIFIC EARTHQUAKE ENGINEERING
RESEARCH CENTER

Inelastic Seismic Response of Extended Pile Shaft Supported Bridge Structures

T. C. Hutchinson
University of California, Irvine
and
R. W. Boulanger, Y. H. Chai, and I. M. Idriss
University of California, Davis

PEER 2002/14
DEC. 2002

Inelastic Seismic Response of Extended Pile Shaft Supported Bridge Structures

T. C. Hutchinson
Department of Civil and Environmental Engineering
University of California, Irvine

and

R. W. Boulanger, Y. H. Chai, and I. M. Idriss
Department of Civil and Environmental Engineering
University of California, Davis

PEER Report 2002/14
Pacific Earthquake Engineering Research Center
College of Engineering
University of California, Berkeley

December 2002

ABSTRACT

Bridge and viaduct structures are often supported on cast-in-drilled-hole (CIDH) extended reinforced concrete piles. In bridge structures supported on these foundation elements, the inelastic response of the superstructure during an earthquake is strongly related to the supporting soil conditions through their influence on substructure stiffness and ground motion characteristics. Although the implications of soil-structure interaction on the overall response of the structure are well recognized, a quantitative assessment of such effects on the inelastic performance of the structure, which requires analytical models capable of capturing the nonlinearity of the soil and pile under dynamic reversed cyclic loading conditions, has not previously been thoroughly carried out.

This report summarizes a study of the inelastic seismic response of bridge and viaduct structures supported on extended pile shafts. Specifically, the work presented includes three main sections. First, the transverse response of reinforced concrete pile shafts is studied by (1) finite element (FE) modeling of a series of full-scale soil-pile lateral loading tests using a beam-on-nonlinear-Winkler (BNWF) approach, (2) comparison of the FE and field test data against a simple kinematic model for relating global and local ductility demands, and (3) a parametric study using the kinematic model over a range of soil types and strengths to evaluate current design practice for allowable ductility levels in these types of structures. Second, dynamic FE analyses are used to assess the performance of extended pile shaft supported bridge structures under strong, long-duration and/or long-period ground motions. Third, the dynamic FE analysis results are compared with current nonlinear static analysis procedures (e.g., R-μ_Δ-T relations), and an alternative “mean spectral displacement” approach for estimating inelastic displacements from the elastic response spectrum of the surface motion is evaluated.

ACKNOWLEDGMENTS

The research described in this report is largely taken from the dissertation of T. C. Hutchinson. The dynamic analyses described in Chapter 3 were performed in close collaboration with Dr. Christina Curras. Curras (2000) is acknowledged for establishing the baseline site characterization, select ground motion processing, the initial site response analyses, and subsequent study of how variations in lateral soil resistance affect structural performance. Dr. Robert Taylor and Dr. Filip Filippou generously shared their computer codes and provided valuable interaction throughout the analytical portions of this study. Dr. Norm Abrahamson provided select ground motions from the 1999 Taiwan earthquake. Dr. Karl Romstad provided helpful suggestions during the dissertation writing. The assistance of the aforementioned parties is greatly appreciated.

This work was supported in part by the Pacific Earthquake Engineering Research Center through the Earthquake Engineering Research Centers Program of the National Science Foundation under Award number 9701568 .

T. C. Hutchinson was also supported on a fellowship provided by the Earthquake Engineering Research Institute (EERI) for the last year of this research. This financial support is gratefully acknowledged.

CONTENTS

LIST OF FIGURES

LIST OF TABLES

LIST OF SYMBOLS

The following symbols are used in this report:

a_{max} = maximum acceleration
A_e = elastic strain energy stored in the system
A_g = gross sectional area
A_h = hysteretic energy dissipated in a cycle of motion
C_Δ = ratio of displacements
C_μ = ratio of displacement-ductility factors
d_b = diameter of longitudinal reinforcement
d_{sp} = diameter of spiral reinforcement
D = diameter
DAR= displacement amplification ratio
D_r = relative density
D1 = closest distance to the rupture surface
D2 = epicentral distance
D_{50} = median grain size
E_{max}= initial tangent Young's modulus
E_s = modulus of elasticity of steel
EI_e = effective flexural rigidity
f'_c = compressive strength of unconfined concrete
f'_{cc} = compressive strength of confined concrete
f'_l = effective confining pressure provided by transverse steel
f_{su} = ultimate strength of reinforcement
f_y = yield strength of longitudinal reinforcement
f_{yh} = yield strength of transverse reinforcement
I_a = Arias intensity
I_{af} = Arias intensity at the end of ground motion
k_e, k^o_e = stiffness (with and without P-Δ effects)
k_h = constant modulus of lateral subgrade reaction
K_{EFB} = equivalent elastic fixed-base cantilever column stiffness
K_p = Rankine passive pressure coefficient
K_{sp} = lateral stiffness of the soil-pile system
L_a, L^*_a = above-ground height and normalized above-ground height
L_f, L^*_f = depth-to-fixity and normalized depth-to-fixity
L_m, L^*_m = depth-to-maximum moment and normalized depth-to-maximum moment
L_p = plastic hinge length
m_p = scaling factor for ultimate strength
m_s = scaling factor for stiffness
M_{max}, M^*_{max} = flexural strength and normalized flexural strength
M_{soil}= moment due to soil reactions
M_y = first-yield moment
N_p = lateral bearing capacity factor
OCR= overconsolidation ratio
p_s = lateral soil resistance

p_{ult} = ultimate lateral soil resistance
P = axial force
R = force-reduction factor
R_c = characteristic length for an elastic pile embedded in a cohesive soil
R_n = characteristic length for an elastic pile embedded in a cohesionless soil
S_a = spectral acceleration
S_d = spectral displacement
S_v = spectral velocity
s_u = undrained shear strength of clay
SMSR = secondary-moment-strength ratio
t_d = duration of strong ground motion
T, T_e, $T^o{}_e$= period and equivalent elastic period (with and without P-Δ effects)
T_c = characteristic period
T_{eFB} = fixed-base elastic period
T_{LP} = predominant pulse period (in the long-period range)
T_p = predominant (pulse) period
T_{sec} = secant period
v_s = shear wave velocity
V = lateral force
V_{EFB}= equivalent fixed-base cantilever column lateral strength
V_{max}= maximum lateral force
V_u, V_u^* = ultimate lateral strength and normalized ultimate lateral strength
V_y, $V^o{}_y$ = yield strength (with and without P-Δ effects)
z = depth below ground surface
α_a = ratio of yield accelerations
Δ = displacement
Δ_{max}, $\Delta^o{}_{max}$ = maximum displacement (with and without P-Δ effects)
Δ_{mean}= mean displacement estimate
Δ_{res} = residual displacement
Δ_y = equivalent elasto-plastic yield displacement
Δ'_y = first-yield displacement
ε_{cu} = ultimate compressive strain of confined concrete
ε_{max} = maximum strain
ε_{sh} = strain at onset of strain hardening
ε_{sp} = spalling strain
ε_{su} = strain at maximum stress
ε_y = yield strain
ε_{50} = strain corresponding to a stress of 50% of the ultimate stress in a laboratory stress-strain curve
ϕ' = friction angle
ϕ_{max} = maximum curvature
ϕ_p = plastic curvature
ϕ_u = ultimate curvature capacity
ϕ_y = equivalent elasto-plastic yield curvature
ϕ'_y = first-yield curvature
γ = total unit weight

γ' = effective unit weight
γ_e = elastic drift ratio
$\gamma_{inelastic}$ = inelastic drift ratio
γ_{max}, γ°_{max}= maximum drift ratio (with and without P-Δ effects)
γ_{res}, γ°_{res} = residual drift ratio (with and without P-Δ effects)
λ_p = normalized length of plastic hinge
μ_Δ, μ°_Δ = displacement-ductility factor (with and without P-Δ effects)
μ_ϕ = curvature ductility factor
$(\mu_\phi)_{cap}$ = curvature ductility capacity
n_h = coefficient of lateral subgrade modulus
ρ_l = longitudinal reinforcement ratio
ρ_s = transverse reinforcement ratio
θ = stability index
θ_p = plastic rotation
σ'_v = effective overburden pressure
ξ_a = coefficient for above-ground height
ξ_{eff} = effective damping ratio
ξ_{eq} = equivalent viscous damping ratio
ξ_f = coefficient for the depth-to-fixity
ξ_v = viscous damping ratio

1 Introduction

1.1 BACKGROUND

Bridge and viaduct structures are often supported on cast-in-drilled-hole (CIDH) extended reinforced concrete piles. These systems can have significant cost savings when compared to groups of smaller driven piles integrated with a pile cap. Typical applications include the single-column and multi-column bent (shown in Figures 1.1 and 1.2) where each supporting pile shaft is extended above the ground into a column having approximately the same diameter and reinforcement. Large diameter single-column bents are often provided with a construction joint at or near the ground surface that includes a slight step in the cross section as a result of the reduction in concrete cover for the above ground portion of the column. However, the flexural strength of the extended pile shaft is fairly uniform along its length, resulting in the possible yielding of the pile shaft below ground level, as shown in Figure 1.2.

Structures supported on extended pile shafts will inevitably have an increase in flexibility due to the compliance of the foundation, which includes the effects of translation and rotation at the ground level. In typical seismic design, the influence of pile foundations is sometimes neglected or greatly simplified because period lengthening for most design spectra generally results in a decrease in design structural forces. However, this may not necessarily be the case when considering near-fault ground motions, where long-period pulses might be present in the spectra, or when structural displacements govern design.

Although the implications of large lateral displacements on the overall response of these types of structures are well recognized, a quantitative assessment of soil-structure-interaction effects on their inelastic performance has not yet been thoroughly carried out. Such an evaluation requires analytical models capable of capturing the nonlinearity of the soil and pile under dynamic reversed cyclic loading conditions. Design issues include the effect of the soil-structure-interaction on the plastic hinge length in the pile shaft and on the relation between global and local ductility demands. Moreover, there is a need to evaluate the performance of these generally long-period structures under strong ground motions with long-duration and/or long-period characteristics, in accordance with current design motion scenarios in California. Near-fault motions, for example, may contain strong velocity pulses that can subject the structure to very large displacement and ductility demands. Residual deformations in extended pile shaft supported structures after an earthquake may also be an important concern, and may be increased by the presence of strong, uni-directional pulses in the ground motion.

1.2 ORGANIZATION OF THIS REPORT

Nonlinear static and dynamic numerical analyses were performed to evaluate the inelastic seismic response of bridge structures supported on extended pile shafts. A finite element (FE) model was first developed and evaluated against a series of full-scale cyclic lateral load tests on piles in sand (Chapter 2). Results from the FE modeling are compared to a simplified kinematic model and extended to include other parameter variations such as pile shaft above ground height and surrounding soil strength.

Chapter 3 extends the FE modeling to incorporate dynamic loading by applying the free-field soil-column response to the system. A baseline parametric study is developed including a range of structural details (above ground height, axial load, and pile diameter) and a suite of ground motions. Particular emphasis is given to global and local measures used in assessing the seismic performance of bridge and viaduct structures subjected to strong ground motions. Local inelastic demands imposed on the pile shafts are presented and compared to the kinematic model described in Chapter 2. A subset of ground motions and structures are analyzed and used to assess the applicability of current design approaches to minimize or avoid P-Δ sensitive behavior for this class of structures. Dynamic instability is illustrated for several cases where the structure is subjected to strong, long-duration and/or long-period (pulse-type) motions.

Chapter 4 compares the dynamic FE analysis results with currently used nonlinear static methods, such as substitute structure and R-μ_Δ-T approaches. An alternative "mean spectral displacement" approach is presented using site-specific ground surface elastic response spectra to estimate inelastic displacement demands. A general summary and significant conclusions of this research are provided in Chapter 5. Performance measures important to the evaluation of the seismic response of bridge structures supported on extended pile shafts are highlighted.

Figure 1.1 Example of a bridge structure supported on single-column extended pile shafts in the San Francisco Bay Area.

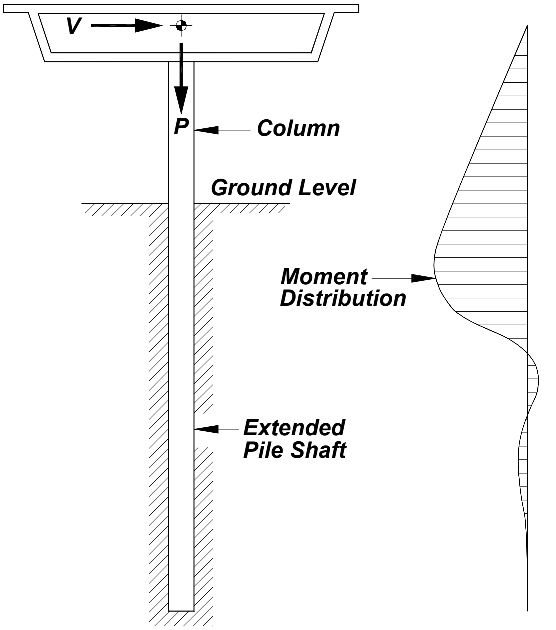

(a) Single-column Bent Supported on an Extended Pile Shaft

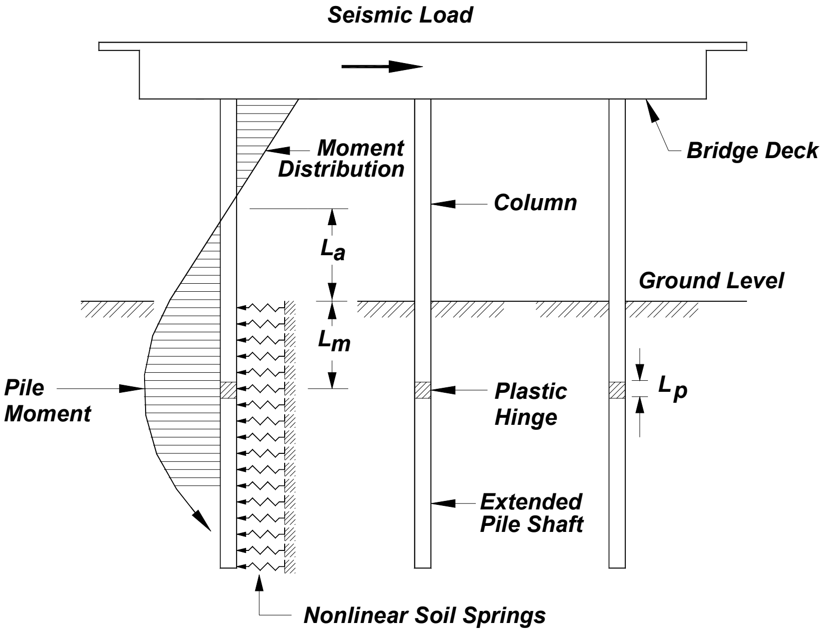

(b) Multi-column Bent Supported on Extended Pile Shafts

Figure 1.2 Plastic hinge formation in pile shafts due to inertial loading from the superstructure: (a) single-column bent and (b) multi-column bent (Chai and Hutchinson 1999).

2 Simulation of the Transverse Response of Reinforced Concrete Pile Shafts

2.1 INTRODUCTION

In this chapter, the relation between global and local seismic demands on reinforced concrete pile shafts is studied through finite element (FE) analyses and a simplified kinematic model. The FE approach used to model the soil-pile interaction was based on a beam-on-nonlinear-Winkler foundation (BNWF) framework, where the soil medium is modeled by a series of closely spaced nonlinear p-y soil elements. The pile shaft and column extensions are modeled by nonlinear flexibility-based fiber beam-column elements. The objective of the simulation was to establish a benchmark for further investigations of the inelastic response of bridge and viaduct systems under dynamic seismic loads (Chapter 3). In order to increase the confidence level of the approach, the finite element model was evaluated against a series of full-scale pile test results (Chai and Hutchinson 1999). The sensitivity of the FE model to the nonlinear soil reactions was studied by using two different p-y models for sand. Since the experimental results indicated that the lateral response of taller piles under high axial forces might be significantly influenced by geometric nonlinearities, the ability of the FE model to simulate the influence of P-Δ effects on the lateral response of taller piles is particularly important.

The simplified kinematic model is based on an equivalent cantilever approach whereby the flexibility of the surrounding soil is modeled by providing an extension of the column to an estimated depth-to-fixity and a concentrated plastic hinge is positioned between the ground surface and the equivalent cantilever base. The model is described in its entirety in Chai and Hutchinson (1999). In this Chapter, the kinematic relation between the global displacement ductility factor μ_Δ and local curvature ductility factor μ_ϕ is compared using these two analytical approaches.

2.2 ANALYTICAL MODELS USED FOR SOIL-PILE SYSTEMS

Various levels of sophistication are currently available for evaluating the lateral response of structures supported by embedded pile shafts. Analysis methods range from simplified two-step methods that uncouple the foundation and superstructure [e.g., Lam and Martin (1986)] to more complex 2D or 3D continuum-based methods [e.g., Randolph (1981) and Budhu and Davies (1987)]. The more rigorous approach, using 2D or 3D continuum analysis [e.g., Randolph (1981) and Budhu and Davies (1987)], tend to be much more computationally consuming and may not be justified in view of the uncertainty inherent in characterizing natural soil deposits and their disturbance during pile installations. Methods that are commonly used for modeling the seismic response of extended pile shaft supported structures are shown in Figure 2.1. Perhaps the simplest approach, which is suitable for the analysis of pile shafts under inertial loading from the superstructure, assumes that an equivalent fixed-base cantilever can replace the overall soil-pile system. In this case, the column above-ground portion remains and the pile shaft is extended and fixed at some elevation below ground. Such an approach provides added flexibility to the system in an attempt to account for the influence of the surrounding soil but in its simplest form does not capture the maximum bending moments in the piles or correctly model the formation of plastic hinging in the piles. The approach using nonlinear pile elements supported by nonlinear p-y soil springs offers a compromise between the simple equivalent fixed-base cantilever method and the continuum method without a significant sacrifice in the essential nonlinear features of the pile and soil. Although early developments of nonlinear p-y soil spring models are intended for monotonic loading or equivalent pushover loading [e.g., Matlock (1970) and Reese et al. (1975)], p-y models have been extended to include dynamic cyclic loading, gapping between the pile and soil, and energy loss due to the radiation damping in the soil for many years [e.g., Matlock et al. (1978), Novak and Sheta (1980), and Nogami et al. (1992)].

2.3 FINITE ELEMENT MODEL

The transverse response of bridge structures supported on extended pile shafts was studied using the FE model shown in Figure 2.2. The superstructure was assumed to be monolithically constructed with the extended pile shaft, which was assumed circular and prismatic. The above-ground height of the structure L_a is defined as the distance between the ground level and the center of mass of the superstructure. The bridge structure was loaded by a set of horizontal and vertical forces applied at the center of mass of the superstructure. The embedded length of the pile shaft was 13.5 times the pile shaft diameter for the load tests described in Section 2.4, and this same length-to-diameter ratio was used in the subsequent parametric studies. The pile tip was assumed to be translationally constrained in both the vertical and horizontal directions, but rotationally unconstrained. It is assumed that the extended pile shaft has been properly detailed for a ductile response with no possibility of brittle shear failure in the pile shaft, bond failure at the lap-slices, or compression buckling of the reinforcement.

Implementation of P-Δ effects in the finite element platform and the fiber beam-column elements used in this work are described in Taylor (1998) and Neuenhofer and Filippou (1998), respectively. The finite element platform used in this work (FEAP) allows for large deformation P-Δ effects to be incorporated in the analysis, while recent work by Neuenhofer and Filippou (1998) incorporate local P-δ effects into the element formulation. For the discussion of the FE results herein, the notation P-Δ effect implies both large deformation P-Δ and local P-δ effects are included.

2.3.1 Nonlinear Beam-Column Element

The general-purpose finite element analysis program FEAP (Taylor 1998) with element and material models suitable for reinforced concrete members was used in this study. In this case, the reinforced concrete pile shaft and above-ground extension were modeled using the nonlinear flexibility-based fiber beam-column element available in FEDEAS (Filippou 1999). The fiber beam-column element is based on an internal force interpolation (force formulation). Description of the element development is provided in Spacone et al. (1996). In this case, the element enables the cross section of the pile shaft to be discretized into an array of fibers representing the confined and unconfined concrete regions of the pile shaft and the longitudinal reinforcement. The longitudinal steel was assumed to be uniformly distributed around the pile shaft, with a steel fiber defined for each individual longitudinal bar. The nonlinear beam-column element used in this study assumes perfect bond between the concrete and reinforcement; i.e., no slip between the concrete and steel. The model also neglects the influence of shear, which is reasonable for members with medium to long span-to-depth ratios. As shown in Figure 2.2, the cover portion of the 406 mm diameter pile shaft was discretized into 36 concrete fibers, while the core portion of the pile shaft was discretized into 48 concrete fibers. Reasonable convergence was achieved with such a discretization, and further refinement of the cross section during preliminary analyses indicated little change in the results.

The force formulation of the beam-column element used in this study allows for the use of longer elements (when compared with displacement-based finite elements). However, for analyzing piles it is desirable to have the shortest possible spacing between the p-y elements to more closely represent the nonlinear soil pressure distribution. Therefore, a subset of reversed cyclic reinforced concrete column tests were modeled to assess the sensitivity and numerical stability of the force-formulated element using different element diameter-length aspect ratios (Hutchinson 2001). These analyses indicate that a minimum length to diameter element aspect ratio of 1D was required for numerical stability and convergence.

In this study, the portion of the pile shaft bounded by the transverse reinforcement is modeled with a confined concrete model, whereas the cover portion of the pile shaft is modeled with an unconfined concrete model, even though the presence of a soil medium around the pile shaft may provide a small amount of confinement to the cover concrete. The general model used to represent the uniaxial hysteretic response of the concrete (both confined and unconfined) is shown in Figure 2.3 (a) where the tensile strength of the concrete is ignored for both the confined and unconfined models. The equations governing the ascending and descending branch of the envelope of the response are given by the Kent-Park model (1971) with extensions by Scott et al. (1982). A rather rapid drop in stress characterizes the envelope curve for the unconfined concrete after the peak stress, whereas for the confined concrete model, the envelope curve is characterized by a more gradual post-peak stress-strain response due to the enhancement of the ultimate core stress and strain. For the unconfined cover concrete, a peak and ultimate strain of ε'_{co} = 0.002 and ε'_{cu} = 0.005 were used, respectively. For the confined concrete model, the enhanced compressive strength f'_{cc} is estimated using (Mander et al. 1988):

$$f'_{cc} = f'_c\left(2.254\sqrt{1+\frac{7.94f'_l}{f'_c}} - \frac{2f'_l}{f'_c} - 1.254\right) \qquad \text{(Eq 2.1)}$$

where f'_c = unconfined compressive strength of concrete, and f'_l = effective confining pressure provided by the transverse reinforcement. The ultimate compressive strain of the confined concrete ε_{cu}, assumed to be reached upon the fracture of the transverse reinforcement, is given by (Priestley et al. 1996):

$$\varepsilon_{cu} = \varepsilon_{sp} + 1.4 \frac{\rho_s f_{yh} \varepsilon_{su}}{f'_{cc}} \qquad \text{(Eq 2.2)}$$

where the spalling strain ε_{sp} is taken as 0.005 instead of 0.004 (Priestley et al. 1996), ρ_s = confining steel ratio, f_{yh} = yield strength of the transverse reinforcement and ε_{su} = strain at maximum stress of the transverse reinforcement.

The longitudinal reinforcement of the pile shaft is modeled using 7 steel fibers arrayed across the circular section. The hysteretic stress-strain relation of the reinforcement is shown in Figure 2.3(a), and is described by the Giuffre-Menegotto-Pinto model (Menegotto and Pinto 1973) with a modification to include isotropic strain hardening (Filippou et al. 1983). While some judgment is required for the selection of various parameters used in the steel model, the selection was partially guided by the actual stress-strain curves of the reinforcement used in the test piles. In this case, a strain-hardening ratio of $E_p/E_s = 0.009$ and a value of R = 15, a parameter for controlling the shape of the transition curve between the elastic and isotropic hardening branch, were used.

2.3.2 Nonlinear p-y Element

An important consideration in modeling the surrounding soil is the distribution of soil springs along the length of the pile. This may be partially guided by the anticipated deformed shape of the pile shaft under a lateral force but also (where applicable) by the layering of natural soil deposits. The soil surrounding the test piles was fairly homogeneous, and thus the soil springs were spaced at approximately one pile diameter on center in the upper region of the pile up to a depth of six pile diameters, and increased to 1.5 times the pile diameter for depths greater than six pile diameters, as shown in Figure 2.2.

The nonlinear behavior of the soil spring was based on the p-y element developed by Boulanger et al. (1999) and implemented in the finite element program FEAP. The element has the ability to simulate elastic and plastic deformations of the soil, opening and closing of the gap between the pile and soil, as well as the loss of energy by radiation damping during dynamic loading. The conceptual formulation of the nonlinear p-y element is shown in Figure 2.2, where the deformation of the p-y element is provided by (i) an elastic component representing the far-field deformation of the soil, (ii) a plastic component representing the yielding of the soil close to the pile, (iii) a closure component that simulates the opening and closing of the gap between the pile and soil, and (iv) a drag component that simulates the transfer of forces between the soil and sides of the pile. Note that the closure and drag components are connected in parallel, while the elastic and plastic components are connected in series. In this study, the residual drag was set to 30% of the ultimate lateral soil resistance based on recommendations by Wilson (1998). Although not applicable in this study, as only the quasi-static response of the pile shaft is simulated in this chapter, it is important to point out that the loss of energy due to radiation damping during dynamic loading is represented by a dashpot that is set in parallel with the elastic component of the p-y element.

The nonlinear p-y element has fairly flexible parameters to accommodate different soil conditions. In this study, two different monotonic p-y models were considered for the backbone curves of the sand. The hyperbolic tangent model, as recommended by the American Petroleum Institute (API 1987), was first used. However, the model was modified slightly for the lateral stiffness of deeper soils. API recommendations assume that the lateral stiffness increases linearly with depth, which tends to overestimate the lateral stiffness of deeper soils. In this study, recommendations by Boulanger et al. (1999) for modifying the lateral stiffness of deeper soils were followed. In this case, the initial lateral stiffness was assumed to increase proportionally with the square root of the depth for depths greater than three pile diameters. A sample of the hysteretic response obtained for sands used in this study under a reversed cyclic displacement history of linearly increasing amplitude is shown in Figure 2.3(a), while the API monotonic envelope is shown in Figure 2.3(b).

The monotonic p-y model proposed by Yan and Byrne (1992) was used as the second model for sands. The model differs substantially from the API monotonic hyperbolic tangent model in that it is characterized by a small lateral stiffness but with a higher strength when compared to the API hyperbolic tangent model, as can be seen in Figure 2.3(b). The model is divided into an elastic region, followed by a nonlinear strain-hardening region after the elastic limit. For the elastic region, the lateral force provided by the soil spring is linear until:

$$\frac{y}{D} = \alpha^{\left(\frac{1}{1-\beta}\right)} \tag{Eq 2.3}$$

The nonlinear portion of the curve is described by:

$$p_s = E_{\max} D\alpha\left(\frac{y}{D}\right)^{\beta} \quad \text{(Eq 2.4)}$$

where p_s = lateral soil resistance per unit length, E_{max} = initial tangent Young's modulus, y/D = pile head deflection to diameter ratio (in %), β can be taken as 0.5, and α is expressed as:

$$\alpha = 5(D_r)^{-0.8} \quad \text{(Eq 2.5)}$$

where D_r is the relative density of the sand (in %). It should be noted that the p-y parameters were chosen to reproduce the API and Yan and Byrne models as closely as possible; hence the two curves for each model shown in Figure 2.3(b). Curve fitting to the Yan and Byrne model was performed up to a lateral displacement of 0.4 m, approximately equal to the limiting lateral displacement of the 6D above-ground pile shafts (D = 0.406 mm) from the pile testing program (described in the next section).

For modeling cohesive soils in the parametric study described later, the model proposed by Matlock (1970) for soft clay is used. Figure 2.3(b) shows the general shape of the Matlock p-y curve compared to a curve fit used in this study. The input parameters p_{ult} and y_{50} were based on Matlock's (1970) equations:

$$p_{ult} = s_u D N_p \quad \text{(Eq 2.6)}$$

$$N_p = \left(3 + \frac{\gamma' z}{s_u} + \frac{Jz}{D}\right) \le 9.0 \quad \text{(Eq 2.7)}$$

$$y_{50} = 2.5 D \varepsilon_{50} \quad \text{(Eq 2.8)}$$

where p_{ult} = ultimate lateral soil resistance, s_u = undrained shear strength of the clay, N_p = lateral bearing capacity factor, γ' = effective unit weight, z = depth below ground surface, and ε_{50} = strain corresponding to a stress of 50% of the ultimate stress in a laboratory stress-strain curve. ε_{50} was taken as 0.005, and J was taken as 0.5 according to Matlock's recommendations for soft clay.

2.4 COMPARISON WITH FULL-SCALE PILE TESTS

Load-deformation data from a series of full-scale pile tests (Chai and Hutchinson 1999) were used for evaluating the FE model. Full-scale reinforced concrete piles (406 mm diameter) with reinforcement details representative of the California Department of Transportation (Caltrans) current design criteria for 70-ton piles were tested in a large-scale soil container. The piles were tested with above-ground heights of 2D and 6D (where D = pile diameter) in loose and dense dry sand conditions. The embedment length of the pile was 13.5D, which was sufficiently deep for the piles to act as "long" piles, even under a loose sand condition. Figure 2.4(a) shows the details of the test piles and Figure 2.4(b) shows a photograph of a fully assembled system prior to testing.

The test piles were subjected to a combination of constant axial compression and reversed cyclic quasi-static lateral loading. Except for the first test pile, the average axial force applied to the pile was P = 445 kN, corresponding to a nominal axial force of $0.1f'_cA_g$. For the first test pile, the average axial force applied to the test pile was slightly higher, at P = 490 kN. Longitudinal reinforcement was provided by seven Grade A706 No. 22 bars, representing a longitudinal reinforcement ratio of $\rho_l = 2.1\%$. A continuous spiral of MW25 or MW45 smooth-wire at a 50 mm pitch provided the transverse reinforcement. For the first and second test pile, the MW25 spiral provided a confining steel ratio of $\rho_s = 0.57\%$. For the third and fourth test pile, the MW45 spiral provided a confining steel ratio $\rho_s = 1.06\%$. A normal weight ready-mix concrete was used throughout the test program. The uniaxial compressive strength of the concrete was nearly the same for the first two piles at approximately $f'_c = 41$ MPa, and slightly higher for the third and fourth test pile at $f'_c = 47$ MPa.

Locally available river sand was used as the cohesionless soil for the pile tests. The soil can be classified as clean, poorly graded sand (SP) with about 3% fines (% passing No. 200 sieve) and no gravel (0% retained on No. 4 sieve) in accordance with the Unified Soil Classification System (USCS). The in-place mechanical properties of the soil were characterized by cone penetrometer tests (CPT soundings) and shear wave velocity measurements. Measured tip resistances were corrected for the influence of overburden pressure and then used to estimate the friction angle and relative density of the in-place soil. Using the average normalized tip resistances in the upper 1 to 3 meters, the friction angles were estimated to be $\phi' = 44$ and 42 for the dense sand in tests 1 and 3, and $\phi' = 37$ and 38 for the loose sand in tests 2 and 4. Based on the tip resistances, the relative density D_r of the sand was estimated to be about 94% and 85% for dense sand and 53% and 59% for the loose sand.

2.4.1 Lateral Force-Displacement Response

Figure 2.5 shows select results from monotonic pushover analyses using the API and the Yan and Byrne nonlinear p-y models compared to the envelope of measured response. Two cases are shown using the API model: the first with the estimated soil properties given previously, the second with the resulting p-y curves increased by a multiplier (applied to initial stiffness and strength, m_s and m_p, respectively) of 1.25. Improved agreement with the load tests was obtained by scaling the API p-y curves by a factor or 1.25. This is a relatively small correction given the scatter in the relations used to estimate the sand properties and p-y curves. No such p-y multiplier was necessary when using the Yan and Byrne relations. The lateral force and lateral displacement are both at the point of lateral force application; i.e., at a height of 2D or 6D above the ground level. Note that the scales for the axis in these figures are different between the piles with different above-ground heights.

For the shorter pile embedded in dense sand, using the Yan and Byrne p-y model provided a softer initial stiffness in the soil model, thus better capturing the initial portion of the soil-pile system response. In addition, the peak strength calculated using the Yan and Byrne model was nearly the same as that measured. The strength at the larger displacements is greater using the Yan and Byrne relations than when using the API relations because it strain hardens to higher lateral resistances p_s at larger lateral displacements y, as shown in Figure 2.3(b). For the pile with an above-ground height of 6D in dense sand, the initial stiffnesses and strengths calculated using each of the nonlinear p-y models were nearly the same. For these taller pile shafts, the influence of the different nonlinear spring models in modeling the surrounding soil should have a lesser effect on the overall soil-pile response. The preliminary results concur with the observations during testing which indicated that the lateral strength of the soil-pile system was fairly insensitive to the density of the surrounding soil. It should be noted that initial analyses of the pile load tests showed that the lateral soil stiffness was slightly underestimated when using the properties estimated from the CPT tests for input into the API model.

Measured and calculated reversed cyclic response of the four tests piles, with above-ground heights of 2D and 6D, embedded in dense and loose sand conditions are shown in Figure 2.6 and 2.7. For these analyses, the API model was used as the backbone p-y curve. The simulation was performed under displacement-controlled loading with single cycles of reversed lateral loading applied to the same target displacements used during pile testing.

For the test piles with an above-ground height of 2D, the FE model calculated maximum strengths of 122 kN and 96 kN (averaged for the two directions of loading) for the piles in dense and loose sand, respectively. Calculated peak strengths were 2% and 20% lower than measured during the experimental program. As can be seen in Figure 2.6(a) and (b), the simulated initial elastic stiffness of the soil-pile systems agreed well with that measured during the testing program. In addition, the FE model was fairly successful in capturing the post-peak strength degradation of the system. For the pile in dense sand, the FE model calculated a lateral strength at a displacement ductility of $\mu_\Delta = 4.1$, 40% lower than the peak strength (averaged for the push and pull direction). For the test pile in loose sand, the FE model calculated a post-peak strength degradation that was about 54% of the peak strength at a displacement ductility of $\mu_\Delta = 4.0$. During the experimental program, average strength degradations of 44% and 25% were determined from the measured test data for the piles in dense and loose sand, respectively. The FE model also captured the unloading and reloading of the reversed cyclic response fairly well, including being able to capture the stiffening of the soil-pile system upon reloading due to the pile bearing against the soil after moving through a gap.

As shown in Figure 2.7(a) and (b), second-order effects notably dominated the response of the taller piles. In this case, the FE model showed very good agreement with the measured initial stiffness, peak strength and unloading and reloading portions of the reversed cyclic response. The peak strengths calculated by the FE model were 51 kN and 45 kN (averaged for the two directions of loading) for the piles in dense and loose sand, respectively. Calculated peak strengths were less than 3% lower than measured values. At the first cycle to a displacement ductility of $\mu_\Delta = 4.6$ and 3.3, the FE model calculated the soil-pile system strength as 37% and 22% of the peak strength for the dense and loose sand, respectively. Measured strengths at the final target displacement were 12% and 26% of the peak at the same displacement ductility levels.

2.4.2 Bending Moment and Lateral Displacement Profiles

Figure 2.8(a) and (b) show the bending moment distribution and lateral displacement profiles calculated using the FE model. The depths to maximum bending moment as observed from the measured strains in the longitudinal steel and the post-test inspection of damage are also shown. For the test piles with an above-ground height of 2D, the FE model captured the depth-to-maximum moment fairly well [Figure 2.8(a)]. The FE model calculated the depth-to-maximum moment at 3D and 4D below ground level for the piles in dense and loose sand, respectively. The maximum damage was observed at 2.69D and 3.3D below ground level, for the piles embedded in dense and loose sand, respectively. The hinging about the maximum damage location and the minimal lateral displacement of the pile below these elevations is also evident in the lateral displacement profiles calculated by the FE model.

For the test piles with an above-ground height of 6D, the bending moment distribution was more spread, as was also evident in the pile testing program. However, the FE model slightly overpredicted the depth-to-maximum moment. For the test pile in dense sand, the FE model calculated that the depth-to-maximum moment was between 3D and 4D below ground, compared to 1.25D below ground level determined in the pile testing program. Similarly for the test pile in loose sand, the calculated depth-to-maximum moment was 4D below ground level, whereas the measured depth was shallower, at 2.31D below ground level.

2.5 PARAMETRIC STUDY USING FE AND KINEMATIC MODELS

The above comparison of calculated and measured soil-pile system response provided confidence in the FE model to perform a parametric study and investigate the sensitivity of varying soil strengths and pile shaft above-ground heights. Results were compared with a simplified kinematic model based on a concentrated plastic hinge and equivalent depth-to-fixity approach. The relations between global displacement ductility μ_Δ and local curvature ductility μ_ϕ for a range of conditions were studied using the FE model and the simplified kinematic model. The FE model was used to perform incremental pushover analysis for a wide range of pile shaft above-ground heights and cohesive and cohesionless soil conditions. The API (1987) p-y relations were used for cohesionless soils and Matlock's (1970) soft clay relations were used for the cohesive soils. Dry sand ranging from loose to dense with friction angles of $\phi' = 30^\circ, 35^\circ, 40^\circ$, and 45° were considered. Cohesive soil ranging from soft to very stiff with undrained shear strengths ($\phi_u = 0$) of s_u = 25, 50, 100, and 200 kPa were also used. Pile shaft above-ground heights of L_a = 4D, 6D, and 8D were considered with structural details matching those of the taller piles tested in the experimental program, namely, a 406 mm diameter pile shaft with a longitudinal steel ratio $\rho_l = 2.1\%$, a confining steel ratio $\rho_s = 1.06\%$ and an applied axial load $P = 0.1f'_cA_g$.

The kinematic model used for comparison is predicated on an equivalent cantilever, or equivalent depth-to-fixity, approach to account for the additional flexibility of the column embedded in a soil medium. Global displacement ductility μ_Δ is compared to local curvature ductility μ_ϕ demand in the pile shaft by assuming a concentrated plastic hinge rotation at the depth-to-maximum bending moment. Monotonic strength envelopes were developed with and without the inclusion of P-Δ effects. A simplified first-order approximation was used to estimate the reduced peak strength and post-peak stiffness degradation due to P-Δ effects. The details of the kinematic model are presented elsewhere (Chai and Hutchinson 1999); however, the basic equations and assumptions are given here.

2.5.1 Equivalent Depth-to-Fixity for Cohesionless Soils

The equivalent depth-to-fixity was derived by equating the lateral stiffness of an equivalent cantilever to the lateral stiffness of the soil-pile system using solutions for a pile embedded in an elastic Winkler foundation. The lateral resistance of cohesionless soil in a Winkler foundation is provided by a linearly increasing modulus of horizontal subgrade reaction (e.g., see Poulos and Davis 1980). The rate of increase with depth is defined by the coefficient of lateral subgrade modulus n_h (units of force/length^3). For a long pile (with an embedded length longer than 4 times the characteristic length R_n given in Equation 2.10) embedded in a cohesionless soil with a lateral subgrade modulus n_h that increases linearly with depth, the resulting soil-pile stiffness is given as:

$$K_{sp} \equiv \frac{V}{\Delta} = \frac{EI_e}{R_n^3} \cdot \frac{1}{\left(2.4 + 3.2\xi_a + 1.74\xi_a^2 + \xi_a^3/3\right)} \qquad \text{(Eq 2.9)}$$

where EI_e = effective flexural rigidity of the pile section, ξ_a = coefficient for above-ground height = L_a/R_n, L_a = height above-ground to point of application of loading, and R_n = characteristic length for an elastic pile embedded in a cohesionless soil and is given as:

$$R_n = \sqrt[5]{\frac{EI_e}{n_h}} \qquad \text{(Eq 2.10)}$$

The equivalent depth-to-fixity L_f is defined in terms of the characteristic length:

$$L_f \equiv \xi_f R_n \qquad \text{(Eq 2.11)}$$

where ξ_f is a coefficient for the depth-to-fixity that can be determined by equating the lateral stiffness of the soil-pile system K_{sp} from Equation 2.9 to the lateral stiffness of an equivalent cantilever column:

$$\xi_f = \sqrt[3]{7.2 + 9.6\xi_a + 5.22\xi_a^2 + \xi_a^3} - \xi_a \qquad \text{(Eq 2.12)}$$

The ultimate lateral soil resistance against the pile was modeled as a linearly increasing passive pressure distribution, as shown in Figure 2.9, based on Broms (1964a); where σ'_v = effective overburden pressure = $\gamma' z$, and K_p = Rankine passive pressure coefficient = $[1+\sin(\phi')] / [1-\sin(\phi')]$. By summing moments about the section of maximum moment and using the condition of zero shear force at this location, two equilibrium equations are developed and solved simultaneously to give the normalized depth-to-maximum-moment as:

$$L_m^* = \frac{1}{2}\left[\frac{\left(L_a^*\right)^2}{p} - L_a^* + p\right] \qquad \text{(Eq 2.13)}$$

where $L^*_m = L_m/D$, L_m = depth-to-maximum-moment and

$$p = \sqrt[3]{\frac{12}{C}M^*_{\max} - \left(L_a^*\right)^3 + \sqrt{\frac{24}{C}M^*_{\max}\left(\frac{6}{C}M^*_{\max} - \left(L_a^*\right)^3\right)}} \qquad \text{(Eq 2.14)}$$

where L^*_a = normalized above-ground height = L_a/D, C = a constant that can reasonably be taken as 3, and $M^*_{\max}$ is the normalized flexural strength and is given by:

$$M^*_{\max} = \frac{M_{\max}}{K_p \gamma' D^4} \qquad \text{(Eq 2.15)}$$

where $M_{\max}$ = ultimate flexural strength of the pile section. Subsequently, the normalized ultimate lateral strength of the soil-pile system can be determined as a function of the depth-to-maximum-moment:

$$V_u^* = \frac{C}{2}\left(L_m^*\right)^2 \qquad \text{(Eq 2.16)}$$

where $V^*_u = V_u/K_p\gamma' D^3$, and V_u = ultimate lateral strength of the soil-pile system.

2.5.2 Equivalent Depth-to-Fixity for Cohesive Soils

The lateral resistance of cohesive soils in a Winkler foundation is provided by a constant modulus of lateral subgrade reaction k_h (units of force/length^2)(e.g., see Poulos and Davis 1980). For a long pile (with an embedded length longer than 3.5 times the characteristic length R_c given in Equation 2.18) embedded in a cohesive soil the resulting soil-pile stiffness was determined as:

$$K_{sp} \equiv \frac{V}{\Delta} = \frac{3k_h R_c}{\left(3\sqrt{2} + 6\xi_a + 3\sqrt{2}\xi_a^2 + \xi_a^3\right)} \qquad \text{(Eq 2.17)}$$

where ξ_a = coefficient for above-ground height = L_a/R_c, and R_c = characteristic length for an elastic pile embedded in a cohesive soil and is given as:

$$R_c = \sqrt[4]{\frac{EI_e}{k_h}} \qquad \text{(Eq 2.18)}$$

The equivalent depth-to-fixity L_f is defined in terms of the characteristic length:

$$L_f \equiv \xi_f R_c \qquad \text{(Eq 2.19)}$$

where ξ_f is a coefficient for the depth-to-fixity that can again be determined by equating the lateral stiffness of the soil-pile system K_{sp} from Equation 2.17 to the lateral stiffness of an equivalent cantilever column:

$$\xi_f = \sqrt[3]{4.24 + 6\xi_a + 4.24\xi_a^2 + \xi_a^3} - \xi_a \qquad \text{(Eq 2.20)}$$

The ultimate soil pressure against the pile was modeled using the Broms (1964b) approach with zero pressure between ground level and 1.5D below ground level and a constant pressure of $9s_u$ from 1.5D to the depth of maximum moment L_m (as shown in Figure 2.9). Using rotational equilibrium at the location of maximum moment and the condition of zero shear force at this location, two simultaneous equations are developed and solved to give the normalized depth-to-maximum-moment:

$$L_m^* = -L_a^* + \frac{1}{18}\sqrt{\left(27 + 18L_a^*\right)^2 + 72M_{\max}^*} \qquad \text{(Eq 2.21)}$$

where $M^*_{\max}$ is the normalized flexural strength of the pile and for cohesive soils is given as:

$$M^*_{\max} = \frac{M_{\max}}{s_u D^3} \qquad \text{(Eq 2.22)}$$

where $M_{\max}$ = ultimate flexural strength of the pile section. Similarly, the normalized ultimate lateral strength of the soil-pile system is:

$$V^*_u = \frac{1}{2}\left(18L^*_m - 27\right) \qquad \text{(Eq 2.23)}$$

where $V^*_u = V_u/s_uD^2$, and V_u = ultimate lateral strength of the soil-pile system.

It should be noted that the assumed ultimate soil pressure distribution for cohesive soils, which ignores the upper 1.5D of soil pressure, tends to overpredict the depth-to-maximum-moment for stiff or very stiff clays. Recent solutions for the depth-to-maximum moment and the ultimate flexural and lateral strength assuming a parabolic soil pressure distribution are available (Chai 2002).

2.5.3 Kinematic Relation between Global and Local Ductility

The kinematic model used to relate global displacement ductility μ_Δ to local curvature ductility demand μ_ϕ in the pile shaft is based on an assumed concentrated plastic hinge rotation at the depth-to-maximum bending moment. For a given displacement ductility factor μ_Δ, the kinematic relation is used to solve for the local curvature ductility demand μ_ϕ in the pile. For cohesive or cohesionless soils this relation is:

$$\mu_\phi = \left(\frac{\mu_\Delta - 1}{3\lambda_p}\right) \cdot \left[\frac{\left(L^*_a + L^*_f\right)^3}{\left(L^*_a + L^*_m\right)}\right] \cdot \left(\frac{V^*_u}{M^*_{\max}}\right) + 1 \qquad \text{(Eq 2.24)}$$

where μ_ϕ = local curvature ductility demand = $\phi/\phi_y \geq 1.0$, μ_Δ = global displacement ductility = Δ/Δ_y, L^*_a = normalized above-ground height = L_a/D, L^*_f = normalized depth-to-fixity = L_f/D, L^*_m = normalized depth-to-maximum-moment = L_m/D, λ_p = normalized length of the plastic hinge = L_p/D, V^*_u = normalized ultimate lateral strength of the soil-pile system, $M^*_{\max}$ = normalized maximum moment. Note that the above relations neglect P-Δ effects.

A first-order approximation was used to include large deformation (P-Δ) effects based on the geometry shown in Figure 2.9. Assuming that the ultimate moment has been attained at the concentrated plastic hinge and using rotational equilibrium about the plastic hinge, the lateral force accounting for the moment due to the soil reactions and the axial loading acting at the lateral displacement is:

$$V = \frac{\left(M_{\max} - P\Delta + M_{soil}\right)}{\left(L_a + L_m\right)} \tag{Eq 2.25}$$

where M_{soil} = the moment due to the soil reactions above the plastic hinge. The idealized soil reactions shown in Figure 2.9 give:

$$M_{soil} = \frac{\gamma' K_p D L_m^3}{2} \tag{Eq 2.26}$$

for cohesionless soil and:

$$M_{soil} = 4.5 s_u D \left(L_m - 1.5D\right)^2 \tag{Eq 2.27}$$

for cohesive soil.

2.5.4 Global Response Results

In performing the parametric study, a target displacement ductility of $\mu_\Delta = 3.0$ was used, based on ATC-32 (1996) recommendations for *Limited Ductility Structures*. The FE models were also pushed to a target displacement demand $\mu_\Delta = 3.0$, where Δ_y was based on the yield displacement determined using the equivalent depth-to-fixity approach.

The results of the lateral force-displacement response predicted using the FE model and the equivalent depth-to-fixity approach for the pile shafts with above-ground heights of L_a = 4D, 6D, and 8D are shown in Figures 2.10–2.12. Note that the x- and y-axis scales between these three figures are different. The simplified first-order approximation discussed earlier (Equations 2.25–2.27) was used with the depth-to-fixity approach to estimate the influence of P-Δ effects beyond yield. The FE model incorporates both large deformation (P-Δ) effects and local (P-δ) effects as noted earlier. Good numerical correlation was seen between the two models in terms of lateral force-displacement results. With the exception of the pile shaft embedded in the stiffest clay [part (d) of Figures 2.10–2.12], the two analytical approaches match fairly well in terms of peak strength and post-peak stiffnesses. In addition, the simplified first-order approximation to include P-Δ effects applied to the equivalent depth-to-fixity approach roughly captured the reduction in strength and post-peak strength when compared to the response envelopes calculated by the FE model. For the stiffest cohesive soil considered, the assumption of Broms's ultimate soil pressure distribution provides for added flexibility by neglecting the upper 1.5D of lateral soil resistance, therefore providing for a softer soil-pile response than may otherwise be accounted for. This is evident in the cases with and without P-Δ effects shown in part (d) of Figures 2.10–2.12. At a displacement ductility demand $\mu_\Delta = 3.0$, the greatest difference between the strengths predicted by the two models for the soft soil conditions was 10%. For the stiffer soils, the maximum difference in post-peak strength at the target displacement ductility of $\mu_\Delta = 3.0$, between the two analytical approaches, was 16%. This occurred in the pile shaft with an above-ground height of 4D embedded in a very stiff clay, with $s_u = 200$ kPa [Figure 2.10(d)].

Evident in the response results produced by the depth-to-fixity approach are the inability of the model to capture the initial tangent stiffness of the system prior to yield, as well as the subsequent drop in strength immediately post-peak, due to the spalling of unconfined cover concrete at the depth-of-maximum bending moment. In comparing to the FE model predictions in Figures 2.10–2.12, the initial difference in pre-yield behavior of the system may have a more predominant effect when evaluating pile shafts embedded in a softer soil medium. However, it may be desirable to accurately capture only the initial tangent stiffness if the foundation system is designed to remain essentially elastic. If inelastic deformations are anticipated, a reasonable estimation of the post-peak response may be more desirable.

The resulting soil-pile elastic stiffnesses K_{sp} as calculated using Equations 2.9 and 2.17 and using the FE model for the range of parameters considered are shown in Figure 2.13(a) and (b). In the case of the FE model, the soil-pile stiffness is a secant stiffness corresponding to a secant line through the first-yield point of the longitudinal reinforcement. The soil-pile stiffnesses K_{sp} in Figure 2.13(a) and (b) have been normalized by an equivalent elastic fixed-base cantilever column stiffness $K_{EFB} = 3EI_e/L_a^3$. Note that this stiffness ignores shear deformations, which is sufficient for the flexible systems under consideration. These select results depict fairly good numerical agreement between the two different analysis techniques, with the closest agreement seen for the softer soil conditions, e.g., $\phi' = 30^\circ$ and $s_u = 25$ kPa.

It should be noted that for the stiffnesses K_{sp} predicted by the kinematic model for the cohesionless soil case [Figure 2.13(a)], a reduction has been applied to the lateral subgrade modulus n_h. In using the equivalent depth-to-fixity approach, the lateral subgrade modulus was reduced to 30% of the value recommended by ATC-32 (1996) (Figure 2.14). Tabular values of

n_h generally apply to working load stiffnesses and are not justifiable for the deformation level anticipated during seismic loading. Comparisons of the equivalent depth-to-fixity approach against measured stiffnesses obtained during the pile load test program (Chai and Hutchinson 1999) indicate this to be a reasonable value. For the cohesive soil case, k_h was estimated using the relation provided in Prakash and Sharma (1990), where $k_h = 67s_u$. While it is recognized that some correction to the lateral subgrade reaction k_h may also be needed, limited guidance is available suggesting the magnitude of such a reduction consistent with anticipated seismic deformation levels. Therefore, no reduction was applied to k_h.

The predicted ultimate strengths V_u of the various soil-pile systems studied are shown in Figure 2.15(a) and (b) normalized by an equivalent fixed-base cantilever column strength $V_{EFB} = M_{max}/L_a$, where M_{max} is the maximum flexural capacity of the section. The correlation between the two analytical approaches in terms of ultimate strength is also fairly good for the range of pile shaft above-ground heights and soil strengths considered, with the exception of the pile shafts embedded in a very stiff clay (s_u = 200 kPa). In this case, the kinematic model (conservatively) underestimates the ultimate strength V_u of the soil-pile system by about 14%. This is primarily due to the Broms ultimate soil pressure used in the depth-to-fixity approach, whereby the upper 1.5D of lateral soil reactions are assumed negligible and taken as zero. This assumption prohibits the simplified model from approaching the strength of an equivalent fixed-base cantilever, even at an above-ground height of 10D, where the maximum strength ratio $V_u/V_{EFB} \approx 0.85$ or 15% less than an equivalent fixed-base cantilever column. The difference between the resulting ratios V_u/V_{EFB} using the two different analytical techniques is much less for the cohesionless soil case, with a maximum difference using the two approaches of ≈ 6% for the pile shaft with an above-ground height of 4D embedded in a very dense sand with $\phi' = 45^\circ$.

2.5.5 Local Response Results

The FE model and the kinematic relation given in Equation 2.24 were used to investigate the sensitivity of local curvature ductility demand μ_ϕ to variations in soil strength and pile shaft above-ground height. In using the kinematic model, the estimate of curvature ductility μ_ϕ for the shorter pile shafts was fairly sensitive to the assumed plastic hinge length λ_p. Therefore, several different plastic hinge length models were investigated (Figure 2.16). During the experimental program, the plastic hinge length was back-calculated from measured curvature data. The equivalent plastic hinge lengths were determined as 1.2D and 1.6D for pile shafts with above-ground heights of 2D and 6D, respectively. The experimentally determined equivalent plastic hinge length was seen to be fairly insensitive to the density of the surrounding soil. In the California Department of Transportation design specifications (Caltrans 1999), for non-cased Type I pile shafts, the plastic hinge length variation with above-ground height is given as: L_p = D+.06L_a. The relation proposed by Budek (1997) was also considered, whereby the plastic hinge length is given as a function of the soil subgrade reaction modulus:

$$L_p = 1.23\left(D - \frac{n_h D}{200}\right) + 0.06L_a \qquad \text{(Eq 2.28)}$$

where n_h is in MN/m^3 in Equation 2.28. Figure 2.15 shows each of these models normalized by pile shaft diameter, $\lambda_p = L_p/D$, varying with normalized above-ground height, $L_a^* = L_a/D$. Budek (1997) suggested a model that was a function of the lateral subgrade reaction of the soil, therefore, an upper and lower bound are shown. Note that at n_h = 40 MN/m^3 Budek's model converges to that used by Caltrans. The Budek and Caltrans models are shown only to continue to a normalized above-ground height of 10D; however, no limiting value of λ_p is suggested. Chai and Hutchinson (1999), without experimental basis, conservatively suggest that λ_p be limited to a maximum value of 1.6 for above-ground heights of $L_a \geq 6D$. Figure 2.17 shows the local curvature ductility demand μ_ϕ as a function of the normalized pile shaft above-ground height L_a^*, for a constant global displacement ductility demand $\mu_\Delta = 3.0$. Recall that the local curvature ductility demand μ_ϕ is defined as the maximum curvature ϕ_{max} divided by the elasto-plastic (EP) yield curvature ϕ_y. For the FE analyses, maximum curvature demand was determined as:

$$\phi_{\max} \equiv \frac{\phi_p + \phi_y}{\phi_y} = \frac{\phi_p}{\phi_y} + 1 \qquad \text{(Eq 2.29)}$$

where ϕ_p = plastic curvature and can be determined as:

$$\phi_p = \frac{\theta_p}{L_p} \qquad \text{(Eq 2.30)}$$

where θ_p = plastic rotation in the pile shaft and L_p = plastic hinge length. For the kinematic model, results are shown for plastic hinge lengths defined by (1) Chai and Hutchinson (1999) and (2) using the Caltrans (1999) plastic hinge length L_p assumptions. For the FE model, plastic curvatures showed a mesh sensitivity whereas plastic rotations did not, which is reasonable for the FE modeling procedures used in this study. Consequently, in using the FE model to calculate local demands, plastic rotations were converted to plastic curvatures based on the Chai and Hutchinson (1999) plastic hinge length assumption. Therefore, the lower (dashed) set of curves provides the most appropriate comparison of the FE results with the kinematic model results.

In general, the FE model predictions of local curvature demand fall within those of the kinematic model. For the cohesionless soil cases [Figure 2.17(a)], the FE model predicts local demands between –6% and 50% (greater) than the kinematic model approach. This may be due in part to the assumption of a simplified ultimate soil pressure distribution and perhaps (to a lesser extent) to the differences between the use of a subgrade modulus n_h (in the kinematic model) versus the p-y element parameters in the FE model. Note that the difference in the two different analytical approaches, for the cohesionless soil cases, are greatest for the shorter pile shafts (4D tall), where, for these cases, accurate modeling of the surrounding soil would be most important.

The cohesive soil predictions [Figure 2.17(b)] compare slightly better, with the FE model calculating local curvature ductility between –3% and 30% (greater) than the kinematic model. Note that the greatest differences between the two analytical methods for the cohesive soil conditions were for the stiff clay (s_u = 200 kPa) cases. In this case, where the surrounding soil is very stiff, the maximum moment will occur fairly shallow and thus the idealized Broms soil pressure distribution used in the kinematic model formulation (where the upper 1.5D of ultimate soil pressure is ignored) will increase the depth-to-maximum-moment. For a given displacement level, a deeper maximum-moment will provide for smaller plastic rotations when using the kinematic model. Assuming a constant plastic hinge length L_p, for a given above-ground height, curvature ductility demand μ_ϕ will also be smaller. However, some compensating effects can be anticipated, since the yield displacement will also increase due to the deeper location of the maximum moment.

For a target global displacement of $\mu_\Delta = 3.0$, the maximum curvature ductility demand ranged from $\mu_\phi = 7.6$–16.2 for all of the cases considered (and both plastic hinge length models). This suggests that the ATC-32 (1996) design displacement ductility of $\mu_\Delta = 3.0$ could require local demands about as high as $\mu_\phi = 16$. However, for extended pile shafts, it may be desirable to limit the amount of damage to the plastic hinge region below ground level by limiting the local curvature demand. The detailing requirements for the plastic hinge region of reinforced concrete pile shafts in California frequently follow that of reinforced concrete columns. For axial loads in the range of 0.05 to $0.1f'_cA_g$ and longitudinal reinforcement ratios in the range of 0.01 to 0.02, the confining steel ratio specified by ATC-32 (1996) ranges between 0.01 to 0.015, depending on the material strength. Such levels of confinement are expected to result in a fairly ductile section with a dependable curvature ductility capacity of about 13 (ATC-32 1996).

Based on these levels, i.e., for a dependable curvature ductility capacity of $\mu_\phi \approx 13$ and an imposed design displacement ductility $\mu_\Delta = 3.0$, guidelines provided by ATC-32 (1996) result in a constant ductility ratio of $\mu_\phi / \mu_\Delta = 4.33$. Figure 2.18 shows the ductility ratios μ_ϕ / μ_Δ determined for the range of above-ground heights considered in this study. In this case, the Chai and Hutchinson (1999) plastic hinge length assumption is used and only the upper and lower bounds of soil strengths (e.g., the stiffest and softest considered in this parametric study) are shown. The results shown in Figure 2.18 indicate that for extended pile shafts, this ratio will be relatively insensitive to the above-ground height and more sensitive to the surrounding soil strength. For cohesionless soils, a reasonable range of ductility ratios μ_ϕ / μ_Δ might be 3.0–3.6 for dense sands and 4.4–5.1 for loose sands. For cohesive soils, a reasonable range of ductility ratios μ_ϕ / μ_Δ is 2.5–3.0 for stiff clays and 3.7–4.2 for soft clays. If the design constraint intended to minimize local demands to $\mu_\phi \leq 13$, then the above ratios would imply that acceptable ranges of μ_Δ might be 2.5 to 4.3 for loose to dense sands, respectively, and 3.1 to 5.2 for soft to stiff clays, respectively, over the full range of above-ground heights considered.

The relation between global and local ductility for larger diameter extended pile shafts (D = 1.5 m and 3.0 m) is evaluated in Chapter 3 for a more complicated soil profile. The FE and kinematic model results for these larger diameter pile shafts showed slightly smaller ductility ratios (μ_ϕ/μ_Δ) than obtained for the smaller diameter (D = 0.406 mm) piles in comparable strength (but idealized) dense sand conditions. For example, the D = 1.5 and D = 3.0 m pile shafts had μ_ϕ/μ_Δ ratios of 1.7–2.4 at a global displacement ductility of $\mu_\Delta = 3.0$.

2.6 SUMMARY AND CONCLUSIONS

The global and local inelastic seismic response of structures supported on extended pile shaft systems was studied through finite element (FE) analyses and a simplified kinematic model. The FE analysis used a fiber-based beam-column element to represent the pile shaft supported on nonlinear p-y elements. The FE model was evaluated by analyzing the full-scale bridge piles tested with above-ground heights of 2D and 6D and embedded in dry dense and loose sand. In the numerical simulation, two different nonlinear p-y spring models were investigated and comparisons of their global force-deformation response emphasize the importance of carefully modeling the nonlinearity of the soil reactions acting against the pile shaft. Reasonable agreement between global and local response quantities was seen when comparing the FE analysis to measured results. The reversed cyclic behavior of the system was captured fairly well by the FE model, supporting its use in dynamic time history analysis. A parametric study was then performed using the FE model and a simplified kinematic model based on a concentrated plastic hinge and depth-to-fixity approach.

The parametric study included varying the surrounding soil strengths and the pile shaft above-ground heights. A first-order approximation was used to incorporate P-Δ effects into the depth-to-fixity approach. This small addition to the model proved to be a reasonable approximation in terms of global pile shaft response results. Fairly good numerical agreement between the two different analytical techniques was seen in terms of soil-pile system stiffnesses K_{sp}, ultimate strengths V_u, and local curvature ductility μ_ϕ demands. Differences in local demands between the two analytical approaches can be attributed in part to the difference between the use of a subgrade modulus (in the kinematic model) and the p-y model input parameters and the assumed ultimate soil pressure distributions used with the kinematic model. Additional understanding and subsequent refinements to the assumed lateral soil pressure distribution against the pile in the kinematic model may reduce the differences in these two techniques.

For a target global displacement of $\mu_\Delta = 3.0$, the maximum curvature ductility demand ranged from $\mu_\phi = 7.6–16.2$ for all of the cases considered with D = 0.406 mm. This suggests that the ATC-32 (1996) design restraints of $\mu_\Delta = 3.0$ could require local demands about as high as $\mu_\phi = 16$. However, for extended pile shafts, it may be desirable to limit the amount of damage to the plastic hinge region below ground level by limiting the local curvature demand.

Ductility ratios μ_ϕ/μ_Δ for the range of above-ground heights and pile diameter (D = 0.406 mm) considered in this study were found to be relatively insensitive to the above-ground height, and more sensitive to the surrounding soil strength. For cohesionless soils, a reasonable range of ductility ratios μ_ϕ/μ_Δ might be 3.0–3.6 for dense sands and 4.4–5.1 for loose sands. For cohesive soils, a reasonable range of ductility ratios μ_ϕ/μ_Δ is 2.5–3.0 for stiff clays and 3.7–4.2 for soft clays. If the design constraint intended to minimize local demands to $\mu_\phi \leq 13$, then the above ratios would imply that acceptable ranges of μ_Δ might be 2.5 to 4.3 for loose to dense sands, respectively, and 3.1 to 5.2 for soft to stiff clays, respectively, over the full range of above-ground heights considered. These displacement ductility levels are dependent upon the structural configuration considered in the parametric study (i.e., 406 mm diameter pile shaft, $\rho_l = 2.1\%$, $\rho_s = 1.06\%$, and $P = 0.1f'_cA_g$) and may vary for larger diameter pile shafts and different detailing configurations. Subsequent analyses for large diameter pile shafts (D = 1.5 and 3.0 m) as presented in Chapter 3, produced significantly smaller μ_ϕ/μ_Δ. The kinematic model provides a simple and reasonable method for quantifying these effects in design practice.

Since the detailing of the extended pile shaft generally follows that of reinforced concrete columns, it is reasonable to assume a dependable local capacity of $\mu_\phi = 13$. However, bridge structures supported on extended pile shafts are termed *Limited Ductility Structures* by ATC-32 (1996), and designed to lower levels of displacement ductility with the intent of minimizing the damage below ground level. This would imply that a local demand less than 13 is more desirable. Analyses described here show that an imposed design displacement ductility of $\mu_\Delta = 3.0$ on small diameter bridge piles (D = 0.4 m) will not limit damage necessarily, but rather may still produce local curvature ductility μ_ϕ near the dependable local capacity level.

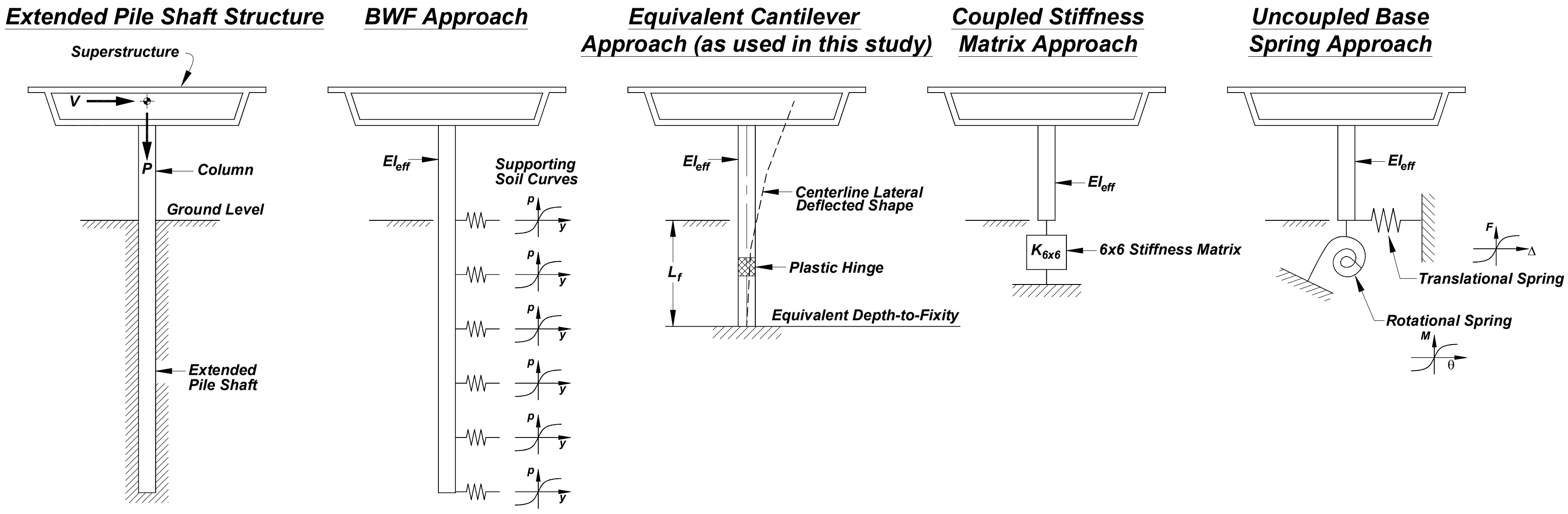

Figure 2.1 Various techniques for modeling the lateral response of bridge structures supported on extended pile shafts.

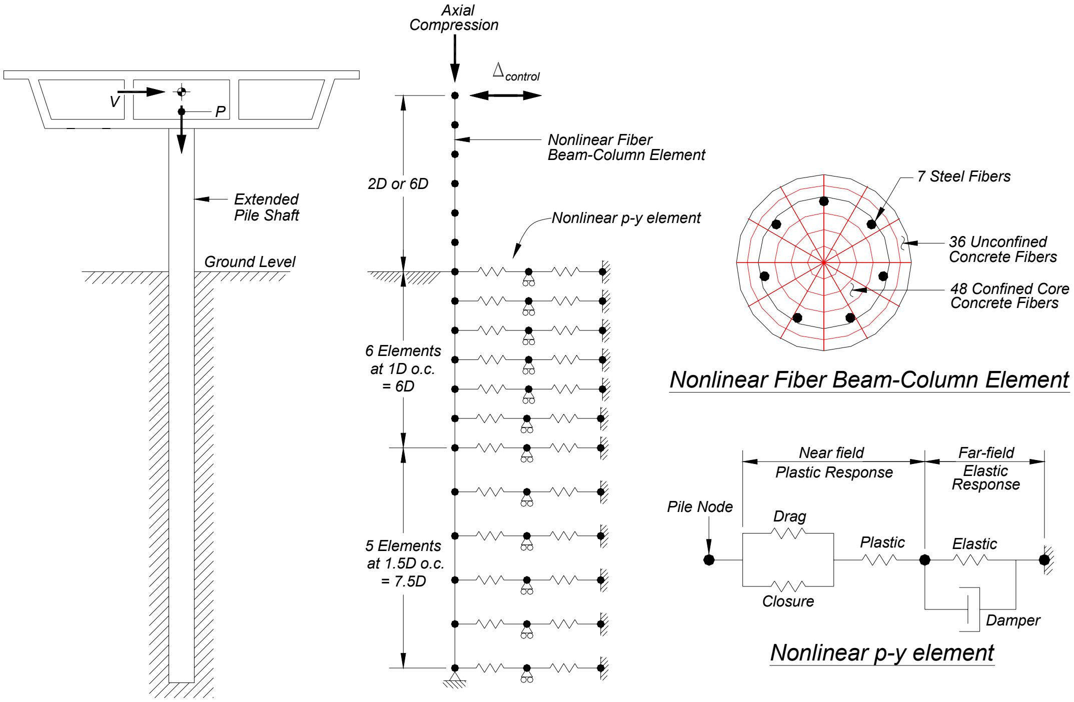

Figure 2.2 General schematic of the finite element (FE) model used for the BNWF analyses using the nonlinear fiber beam-column element and the nonlinear p-y element.

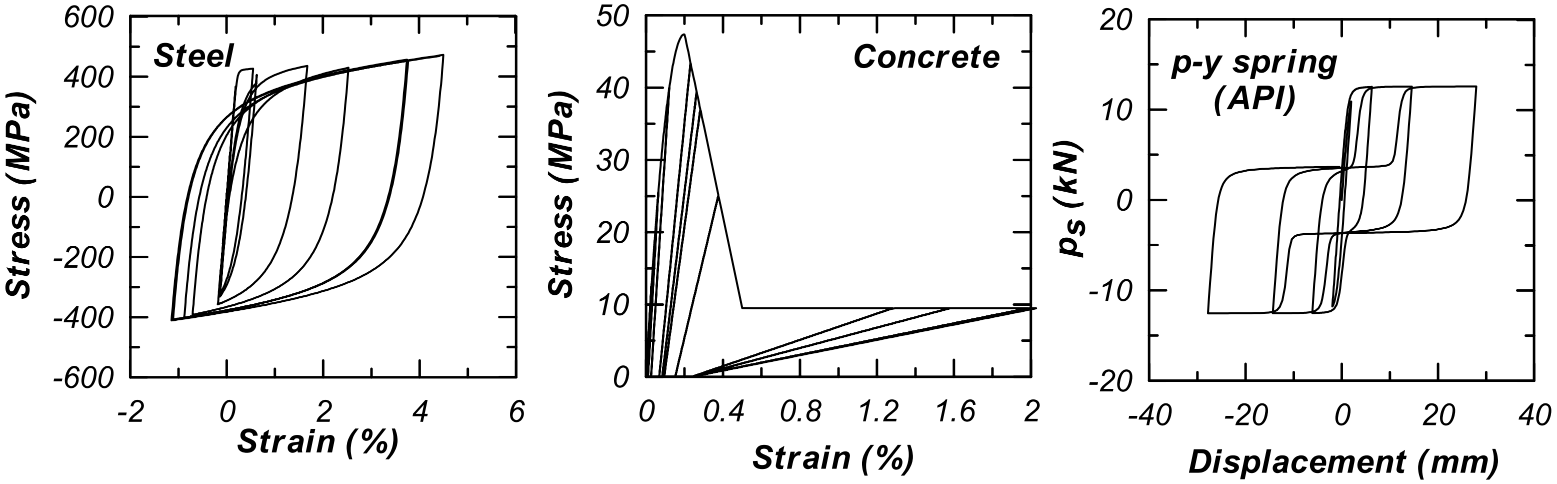

(a) Cyclic Models.

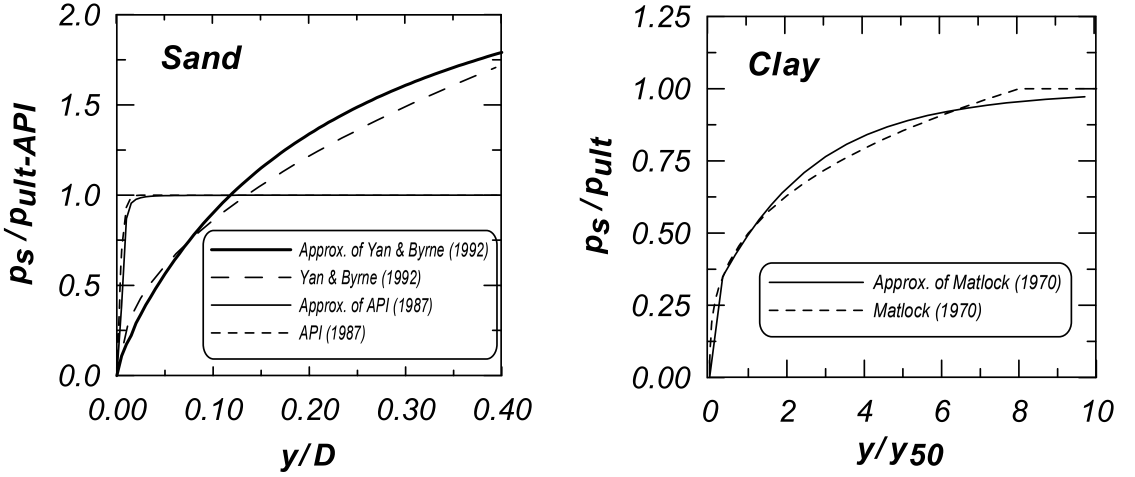

(b) Monotonic Models.

Figure 2.3 Material models used in this study: (a) cyclic models and (b) monotonic envelopes of sand and clay.

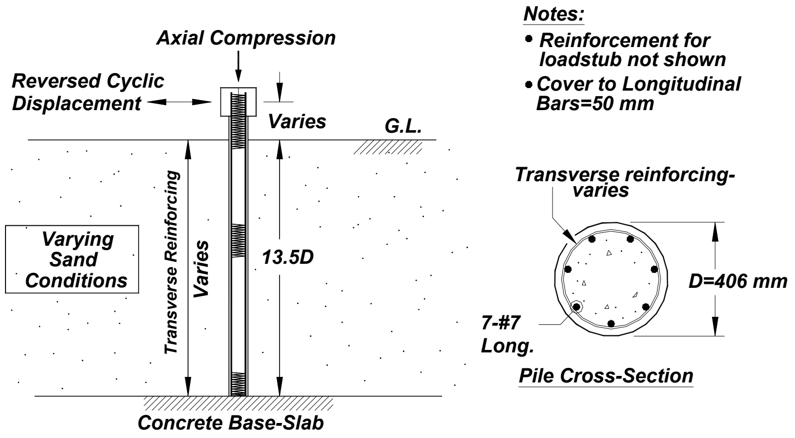

Test-Matrix:

Pile Test No.	Above-ground Height	Soil Condition	Compaction Effort	Transv. Reinf. Ratio
1	2D	Dense	3 Passes over 150mm Lift	0.57%
2	2D	Loose	1 Pass over 230mm Lift	0.57%
3	6D	Dense	3 Passes over 150mm Lift	1.06%
4	6D	Loose	1 Pass over 230mm Lift	1.06%

(a)

(b)

Figure 2.4 Soil-pile-interaction tests (Chai and Hutchinson 1999): (a) reinforcement details and test matrix and (b) photograph of fully assembled test — 6D above ground level.

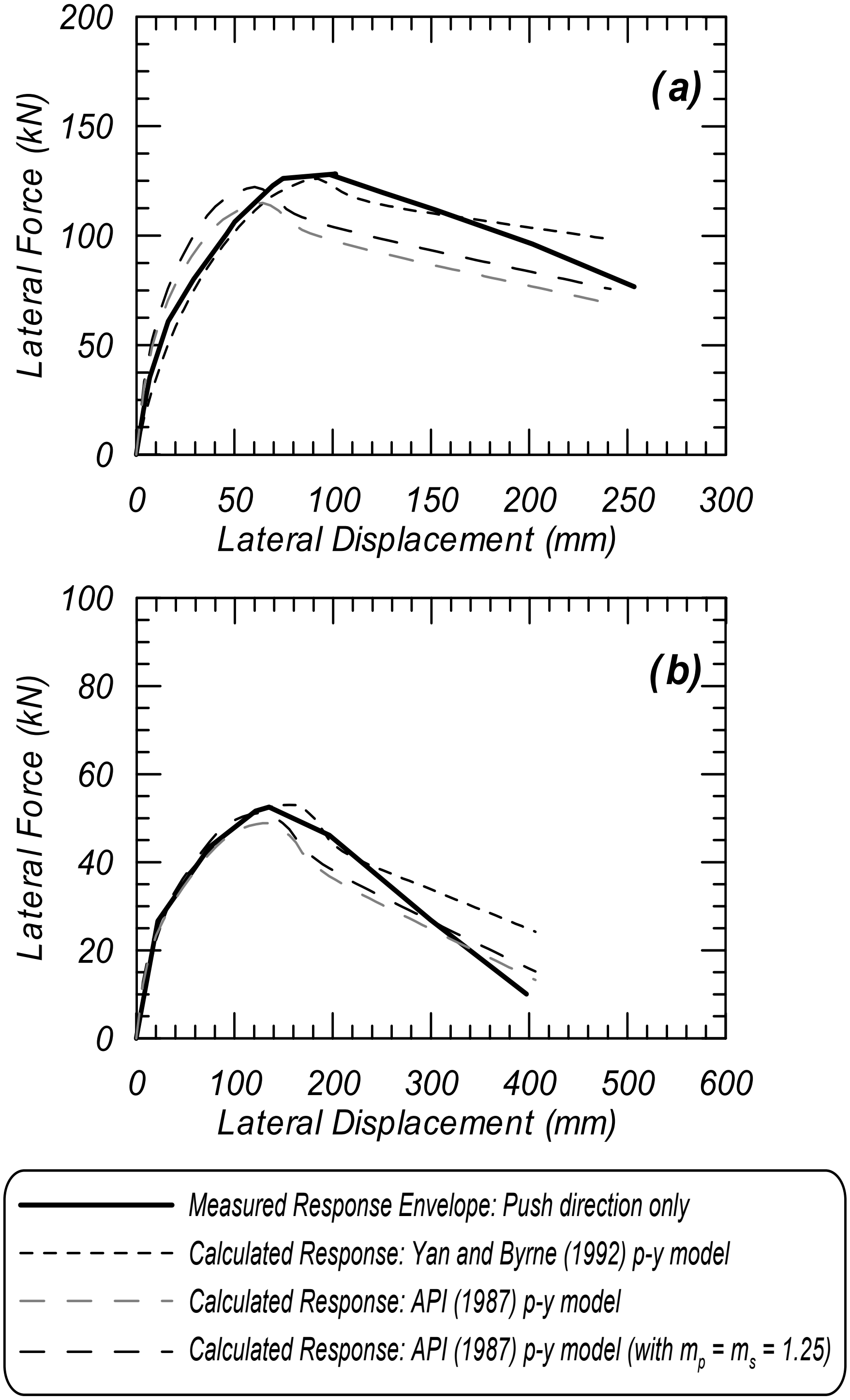

Figure 2.5 Measured and calculated lateral strength envelopes, using the two different p-y models: (a) 2D above ground level in dense sand and (b) 6D above ground level in dense sand.

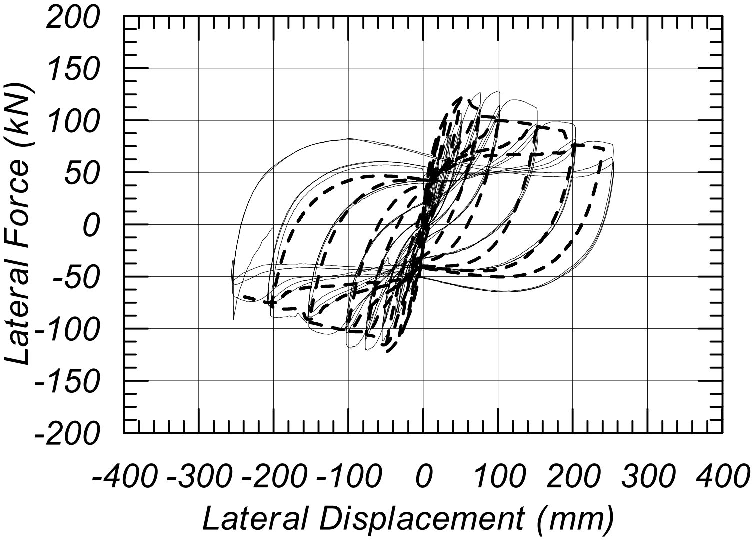

(a) 2D above ground in dense sand

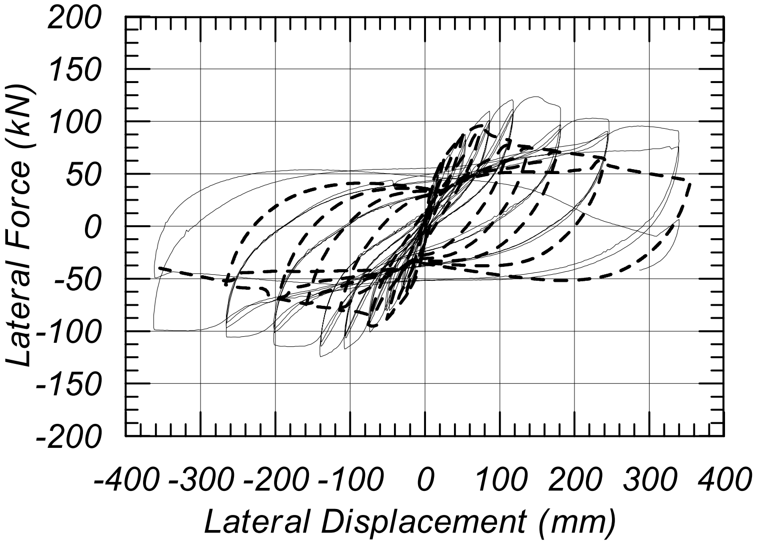

(b) 2D above ground in loose sand

——— Measured Response

- - - - - - - - - - Simulated with FE model - Quasi-static cyclic loading

Figure 2.6 Measured and calculated hysteretic response for full-scale test piles with an above-ground height of 2D: (a) in dense sand and (b) in loose sand.

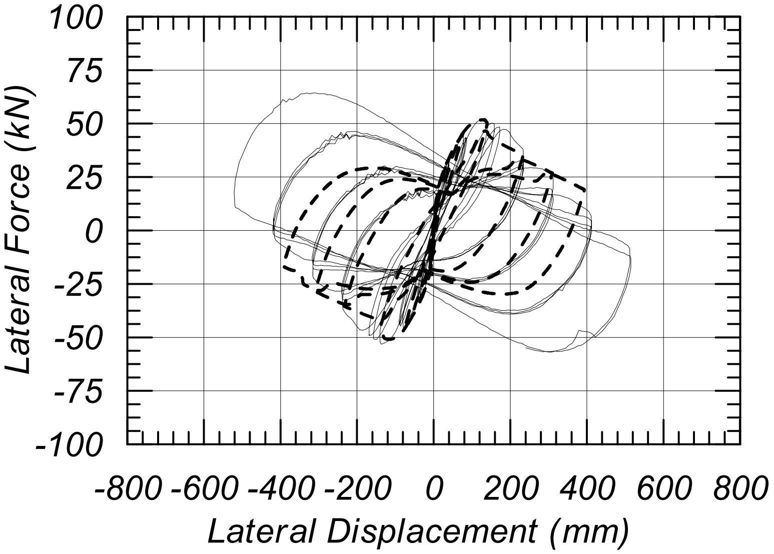

(a) 6D above-ground in dense sand

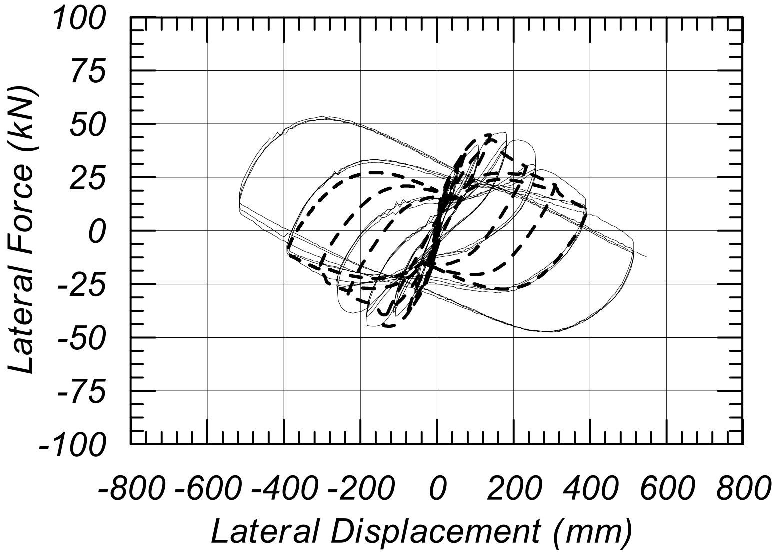

(b) 6D above-ground in loose sand

Figure 2.7 Measured and calculated hysteretic response for large-scale test piles with an above-ground height of 6D: (a) in dense sand and (b) in loose sand.

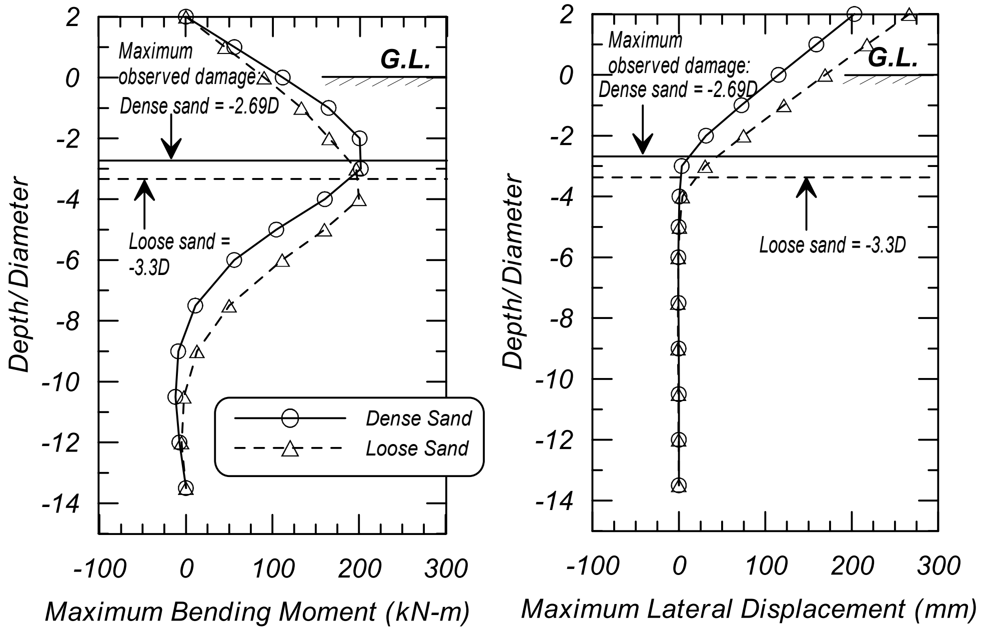

(a) Test piles with an above-ground height of 2D

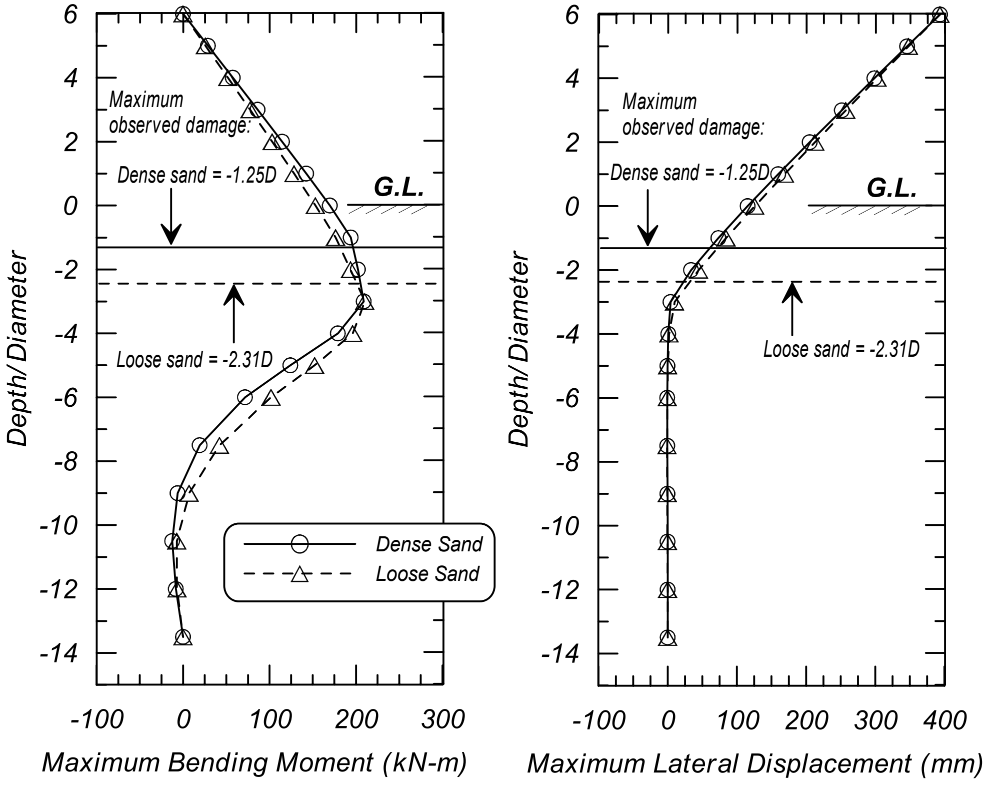

Figure 2.8 Maximum bending moment and lateral displacement profiles calculated with the FE model: (a) test piles with an above-ground height of 2D and (b) test piles with an above-ground height of 6D.

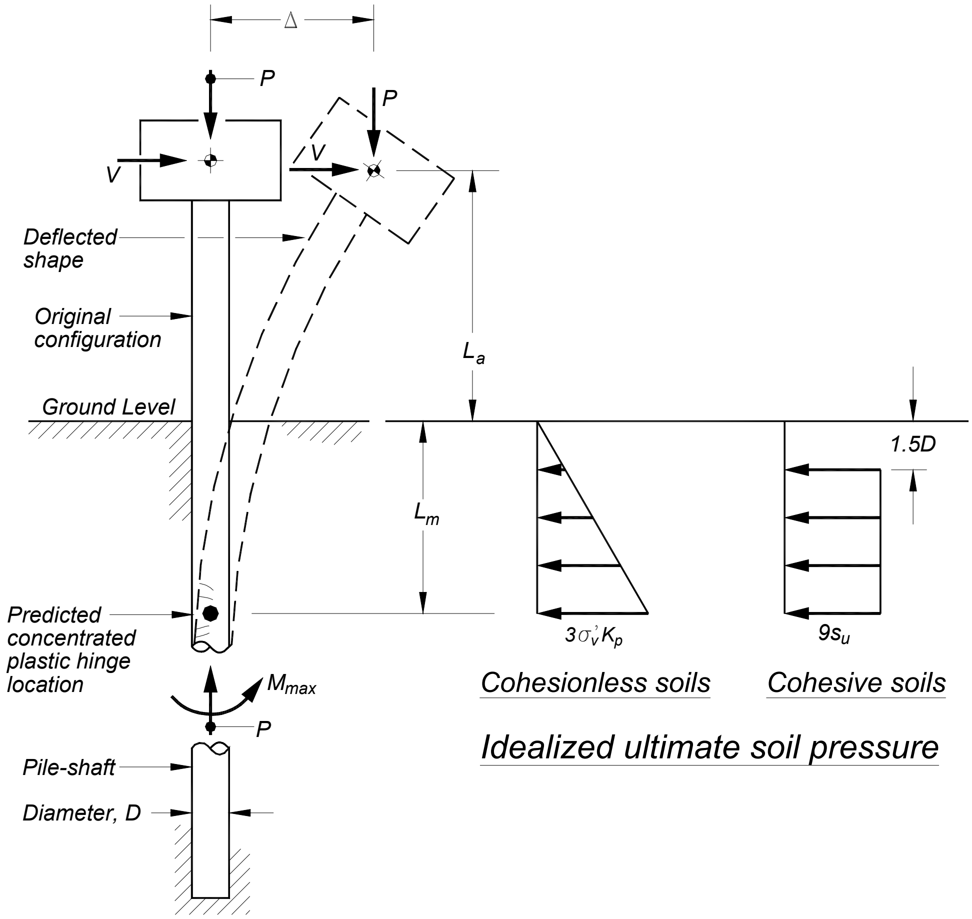

Figure 2.9 General kinematic relations for extended pile shafts.

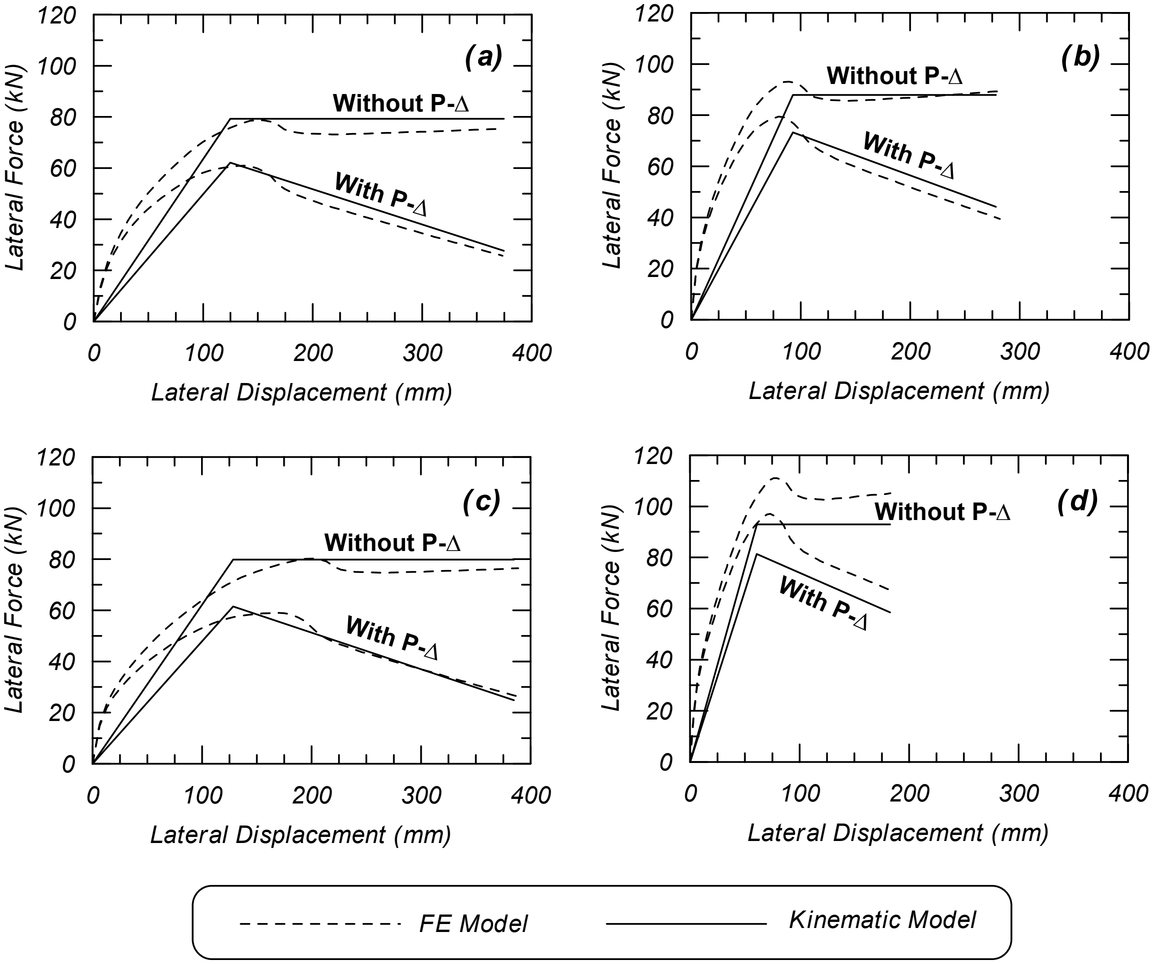

Figure 2.10 Lateral force-displacement response of soil-pile systems with an above-ground height of 4D as calculated by the FE model and the depth-to-fixity approach: (a) cohesionless soil with $\phi' = 30°$, (b) cohesionless soil with $\phi' = 45°$, (c) cohesive soil with $s_u = 25$ kPa, and (d) cohesive soil with $s_u = 200$ kPa.

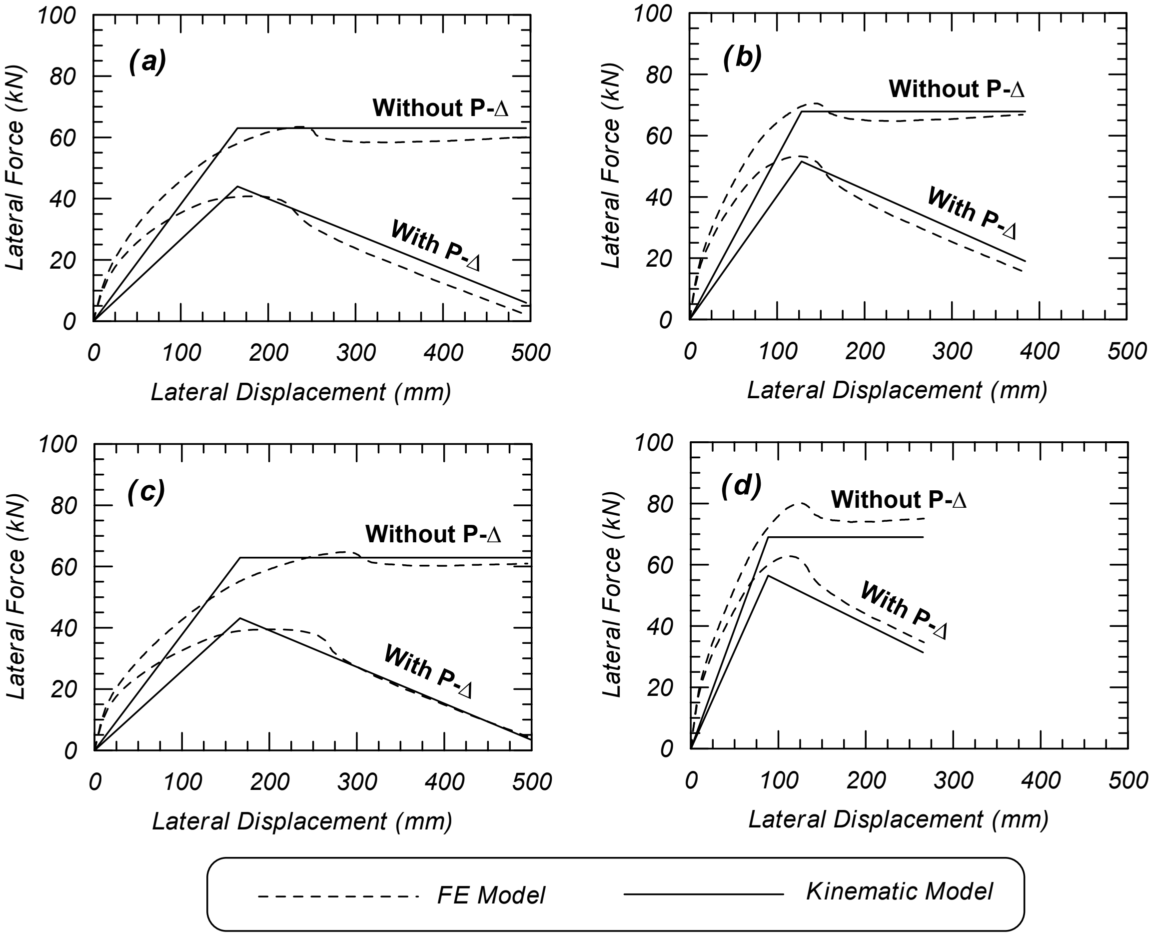

Figure 2.11 Lateral force-displacement response of soil-pile systems with an above-ground height of 6D as calculated by the FE model and the depth-to-fixity approach: (a) cohesionless soil with $\phi' = 30°$, (b) cohesionless soil with $\phi' = 45°$, (c) cohesive soil with $s_u = 25$ kPa, and (d) cohesive soil with $s_u = 200$ kPa.

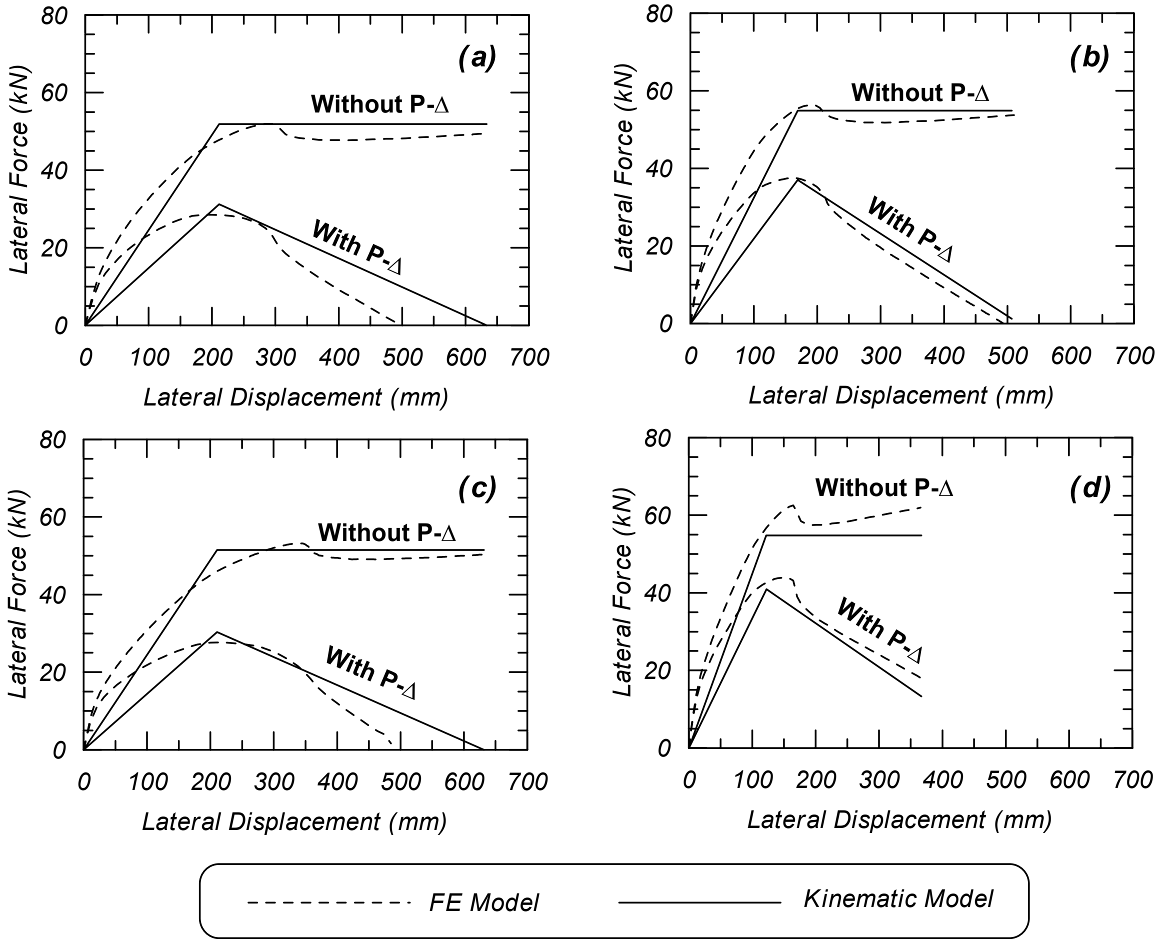

Figure 2.12 Lateral force-displacement response of soil-pile systems with an above-ground height of 8D as calculated by the FE model and the depth-to-fixity approach: (a) cohesionless soil with $\phi' = 30°$, (b) cohesionless soil with $\phi' = 45°$, (c) cohesive soil with $s_u = 25$ kPa, and (d) cohesive soil with $s_u = 200$ kPa.

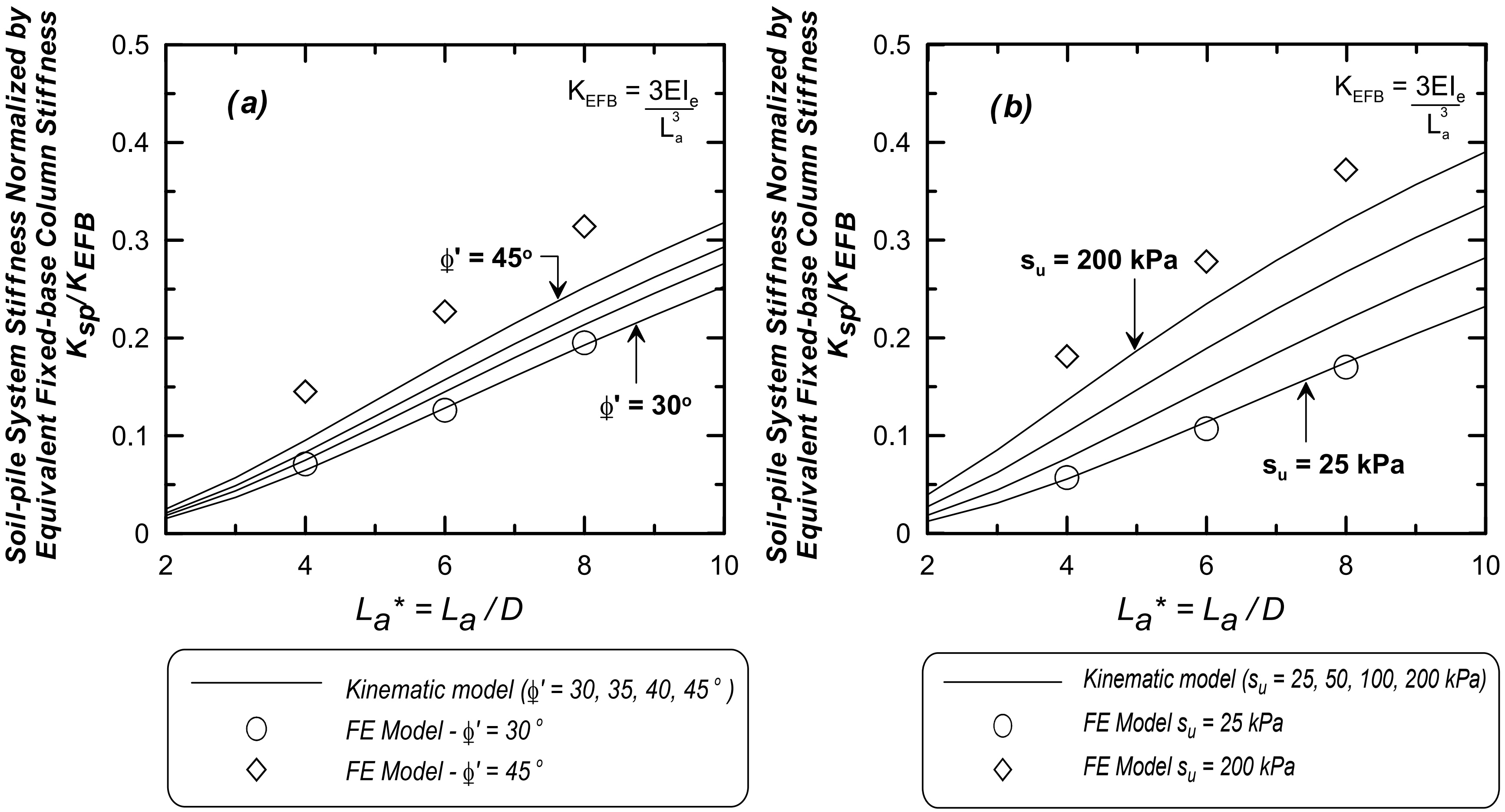

Figure 2.13 Soil-pile system stiffness normalized by equivalent fixed-base column stiffness as a function of the above-ground height: (a) cohesionless soil and (b) cohesive soil.

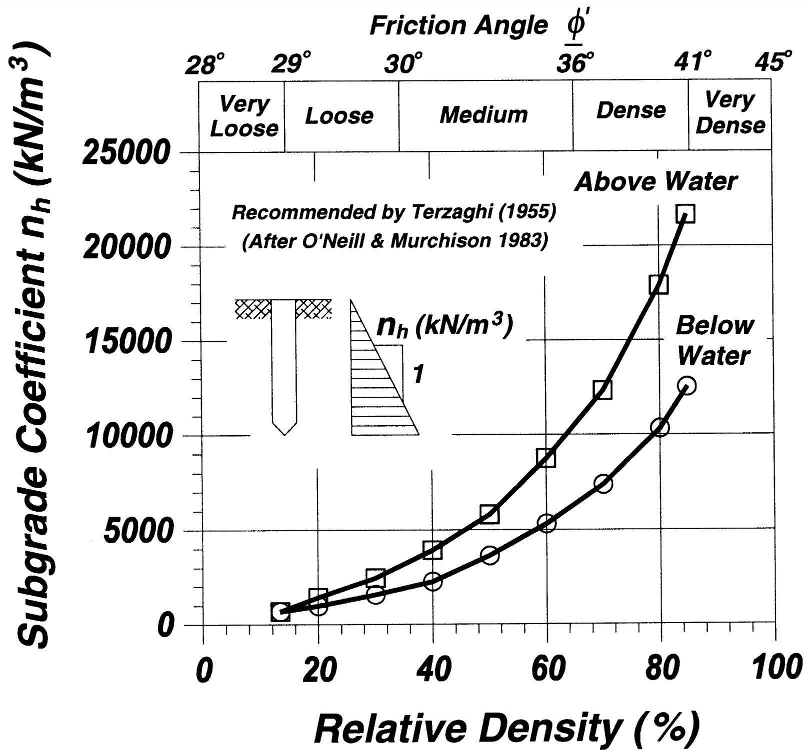

Figure 2.14 Recommended subgrade coefficient as a function of relative density and friction angle (after ATC-32 1996).

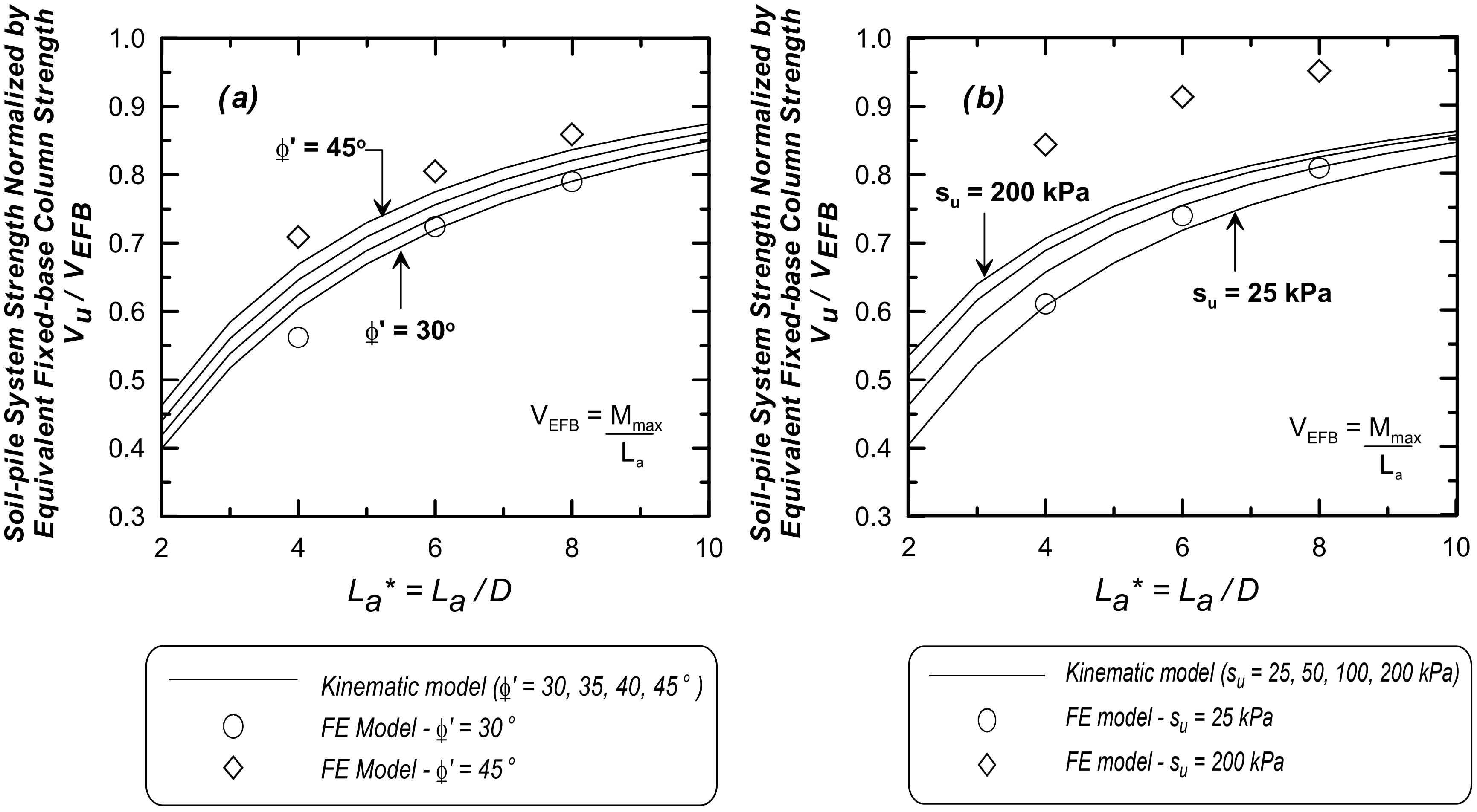

Figure 2.15 Soil-pile system strength normalized by equivalent fixed-base column strength as a function of the above-ground height: (a) cohesionless soil and (b) cohesive soil.

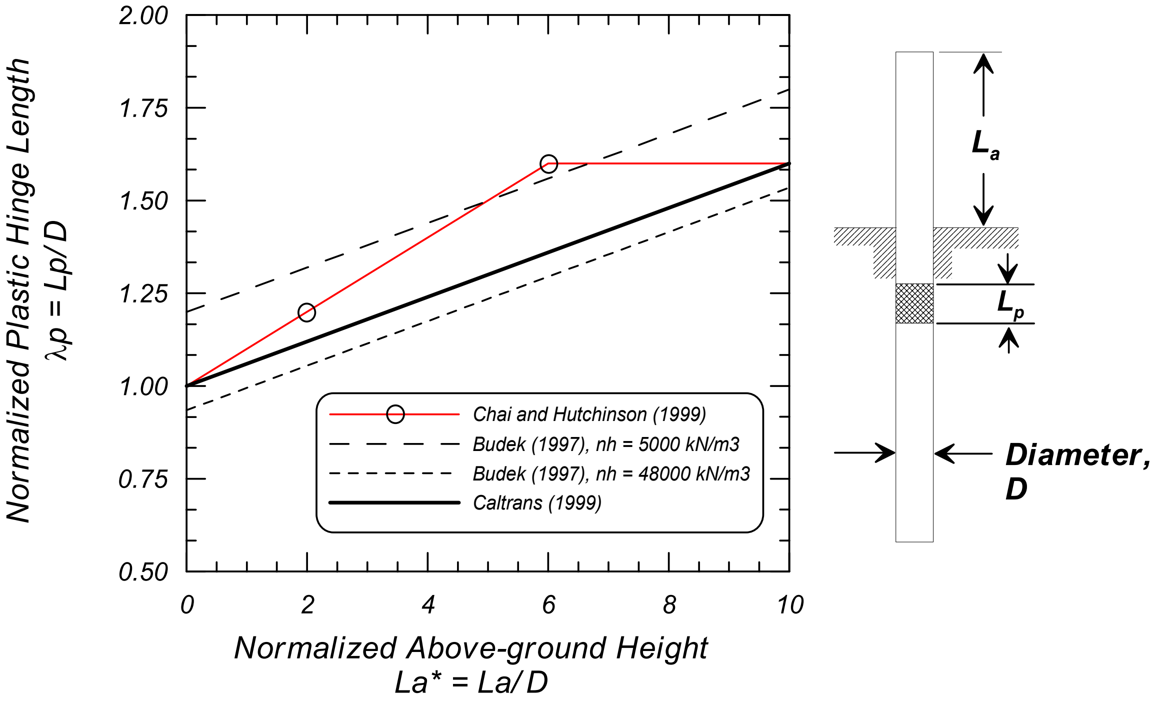

Figure 2.16 Various plastic hinge length models proposed for extended pile shafts.

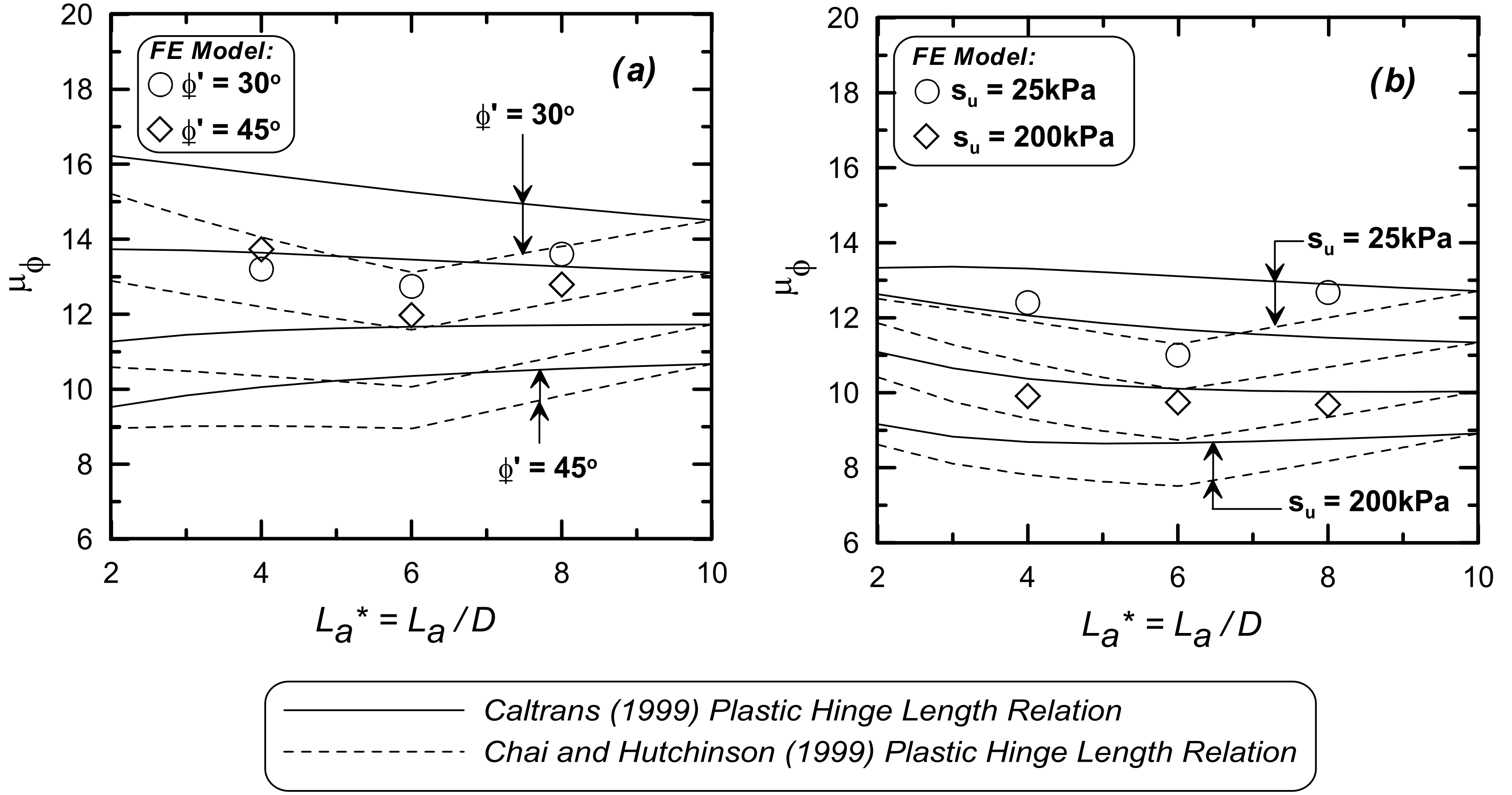

Figure 2.17 Local curvature ductility demand μ_ϕ as a function of pile shaft above-ground height (for a constant displacement ductility $\mu_\Delta = 3.0$): (a) cohesionless soil and (b) cohesive soil.

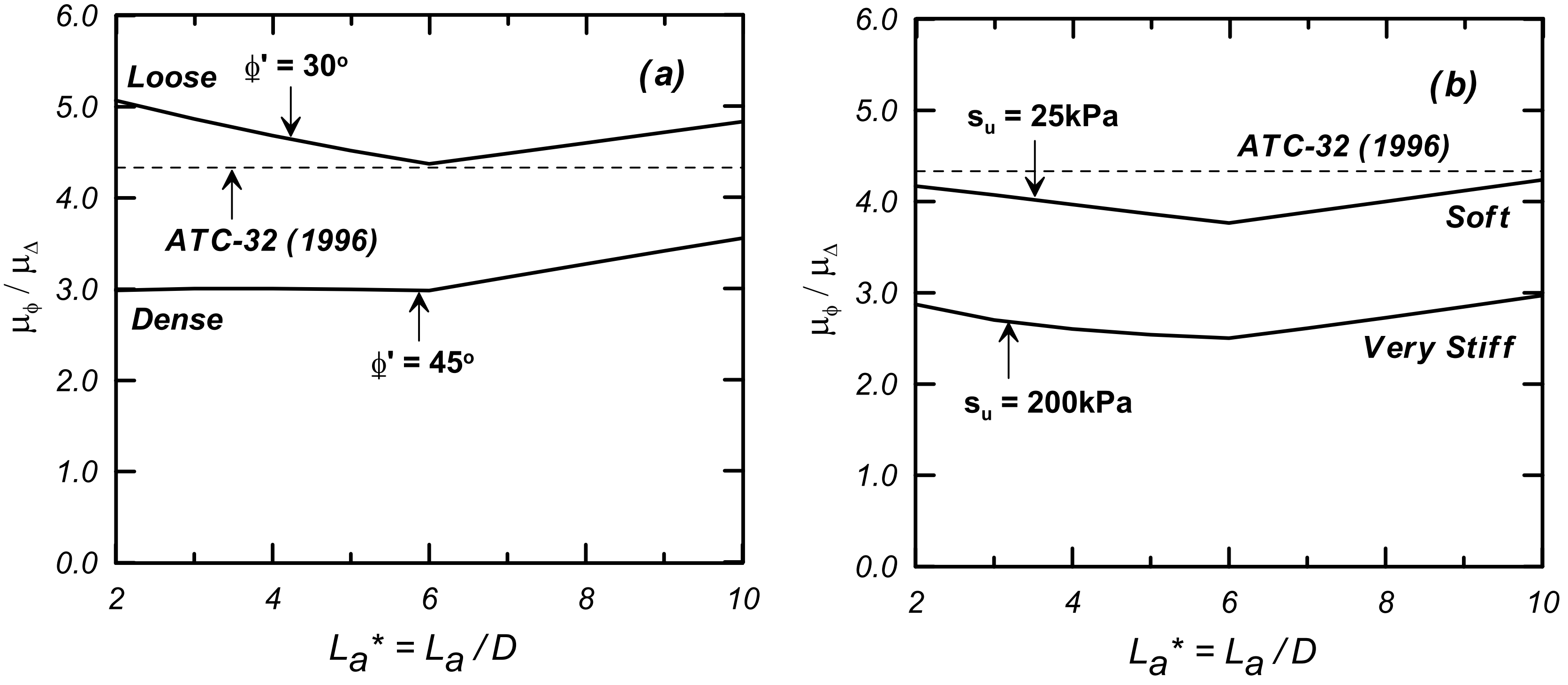

Figure 2.18 Ratio of local to global ductility for a range of above-ground heights and soil strengths: (a) cohesionless soils and (b) cohesive soils.

3 Performance during Strong, Long-Duration and/or Long-Period Ground Motions

3.1 INTRODUCTION

Near-fault ground motions with strong velocity pulses can subject bridge and viaduct structures to very large displacement and ductility demands. In bridge and viaduct structures supported on extended cast-in-drilled-hole (CIDH) pile shafts, plastic hinging in the pile shaft can develop below the ground surface. Residual deformations in these types of structures after an earthquake are an important concern, and may be increased by the presence of strong, uni-directional pulses in the ground motion. The magnitude of inelastic deformation demands in the structure will depend on the ground motion characteristics (including the amplitude, period, and shape of any large pulses), the lateral strength and period of the structure, and the hysteretic characteristics of the yielding elements (structural and soil). The seismic performance of these structures will be inherently coupled to the subsurface soil conditions through their influence on site response, foundation stiffness, and energy dissipation.

This chapter describes results from a series of nonlinear dynamic analyses used to evaluate the seismic performance of bridge and viaduct structures supported on extended, large-diameter, CIDH pile shafts. The study included consideration of ground motion characteristics, site response, lateral soil resistance, structural parameters (including geometric nonlinearity), and performance measures. The same nonlinear Winkler (BNWF) framework described in Chapter 2 will be used to model the soil-pile interaction coupled with the nonlinear fiber beam-column elements to model the reinforced concrete sections and the nonlinear p-y elements, also described in Chapter 2. The dynamic free-field soil profile response is determined from one-dimensional site response analyses of the soil profile.

This chapter presents (1) a description of the modeling method used, (2) details regarding the ground motions used in this study, (3) a description of the site and site response analyses, (4) details regarding the baseline structural configurations used, and (5) select dynamic response results. Particular emphasis will be given to the global and local measures used in assessing the seismic performance of bridge and viaduct structures subjected to strong ground motions. A subset of dynamic analyses were performed to evaluate the response of these structures to ground motions with (and without) large permanent displacement offsets in their record. Local inelastic demands imposed on the pile shafts are presented and compared to the kinematic model described in Chapter 2. Select results are also provided describing a subset of dynamic analyses used to evaluate the variation in system response due to a range of uncertainty in the surrounding soil parameters. The evaluation of P-Δ effects for this class of structures using a subset of the ground motions used in the overall dynamic analysis study is also described.

3.2 FINITE ELEMENT MODEL

A dynamic beam-on-nonlinear-Winkler (BNWF) analysis method, as shown in Figure 3.1, was used to model the soil-pile interaction. The model shown in Figure 3.1 is similar to that used in Chapter 2. In this case, the horizontal free-field soil motions obtained from one-dimensional site response calculations were input to the free-field ends of all p-y elements to represent dynamic earthquake loading. The structural system was modeled using the finite element analysis platform FEAP (Taylor 1998). The CIDH pile and extension are modeled using the same flexibility-based fiber beam-column element from the FEDEAS element library (Filippou 1999) described and used to simulate the full-scale pile test results (shown in Chapter 2). Dynamic masses of the beam-column elements are represented by multiplying the mass density by the sectional area and one-half of the element length and lumping the masses at the element end nodes. Force resultants in the element are obtained by integrating the fiber stresses over its cross section, assuming plane sections remain plane. A modified Kent-Park (1971) model was used to represent the concrete cyclic behavior, and a modified Menegotto-Pinto (1973) model was used to represent the reinforcing steel cyclic behavior. Spacone et al. (1996) describe the slight modifications made to these models. These constitutive laws follow those described in Chapter 2 and shown in Figure 2.3.

Pile nodes below ground are connected to horizontal p-y elements representing the lateral soil resistance. The nonlinear p-y elements, which account for gapping effects and radiation damping, are the same elements used in Chapter 2 (Boulanger et al. 1999), where radiation damping is now provided. Parameters for the p-y elements were based on common design procedures used in U.S. practice [e.g., API (1987) and Reese et al. (2000)].

Numerical convergence was obtained using a Hilber-Hughes-Taylor (Hilber et al. 1977) solution scheme, with coefficients to control numerical stability and accuracy of $\beta=0.5$, $\gamma=1$, and $\alpha=0.5$ (per Hilber et al. 1977 notation). Rayleigh damping was included in both the structural elements and p-y springs. Structural damping was set at 5% of the equivalent elastic yield period of the soil-pile systems (as determined from the nonlinear pushover analyses). Radiation damping in the far field of the soil column was modeled using a damper set in parallel with the elastic component of the p-y element (see Figure 3.1). Previous studies have shown that this avoids excessive damping forces in yielding elements [Wang et al. (1998) and Randolph (1991)].

3.3 FREE-FIELD SITE RESPONSE ANALYSES

3.3.1 Baseline Soil Profile

A baseline soil profile for this parameter study was modeled after the Gilroy 2 site in California (Figure 3.2). This site was considered to be a reasonable example of where extended large-diameter CIDH piles might be constructed to support a bridge structure. In addition, the relatively dense sands and stiff clays at the site limit the possibility of liquefaction occurring. In these analyses, it was assumed that liquefaction would not occur during dynamic loading.

The site consists of predominantly loamy soils but was classified more generally as a mix of dense sand and stiff clays (Curras 2000). Current ATC-32 (1996) [which are based on NEHRP (BSSC 1994)] provisions would classify this site as a type D, stiff soil site, based on the average properties of the upper 30 meters of the soil profile. The site was also characterized extensively by EPRI (1993), including shear wave velocity profiles and cyclic laboratory testing of field samples. Shear wave velocities at the site range from 200 to 500 m/s in the upper 30 m, as shown by the profile in Figure 3.3. Additional properties of the site relevant to the lateral soil response are listed in Table 3.1. The site also allowed for the calibration of the site response analyses using strong motion recordings from the 1989 Loma Prieta earthquake (Curras 2000).

The site response analyses used the equivalent-linear program SHAKE96 [Schnabel et al. (1972) and Idriss and Sun (1991)]. Normalized shear modulus (G/G_{max}) and damping relations for the site response analyses were based on the laboratory test data and are shown in Figure 3.4.

Idealization of the subsurface profile and selection of shear modulus and damping relations are described in Curras (2000).

3.3.2 Rock Outcrop Motions and Their Response

A range of earthquake motions with different frequency contents, intensities, durations and permanent displacements were used as rock outcrop motions in this study. Each motion was input as a rock outcrop at the base of the Gilroy 2 site and the peak rock outcrop acceleration (a_{max}) was scaled to produce several intensities. The range of intensities for each motion resulted in relatively moderate levels of maximum shear strains within the soil profile (less than 2% was calculated for the motions and intensities used herein). Six of these 12 motions, as listed in Table 3.2, were categorized as near-fault recordings and have a strong long-period pulse component. Records grouped as near-fault in this study also have the following characteristics: (1) recorded within 10 km of the rupture surface (based on the closest source-site distance), (2) peak acceleration of the recording was greater than 300 cm/s^2, (3) peak velocity of the recording was greater than 50 cm/s, and (4) the ratio of peak velocity to peak acceleration (v_{max}/a_{max}) is greater than 0.10 sec. The ratio of peak velocity to peak acceleration provides an indicator of the frequency content of the motion. It should be noted that the near-fault motions recorded during the Taiwan and Turkey earthquakes also have fairly large permanent displacements.

Two synthetic motions were chosen to study the influence of long-duration motions on the performance of these structures. Of the six "other motions" listed in Table 3.2, these two synthetic motions have a duration of t_d = 36 seconds. Although many definitions have been proposed for the duration of strong ground motion, in this study, the duration is taken as the difference in the time at which 5% and 95% of the final Arias intensity are reached (Trifunac and Brady 1975). The Arias intensity is defined as (Arias 1970):

$$I_a = \frac{\pi}{2g} \cdot \int_0^t [a(t)]^2 \, dt \tag{Eq 3.1}$$

Equation 3.1 represents the build-up of the Arias intensity. The Arias intensity at the end of the record can be determined by substituting the total time of the record t_f for t:

$$I_{af} = \frac{\pi}{2g} \cdot \int_0^{t_f} [a(t)]^2 \, dt \tag{Eq 3.2}$$

The normalized Arias intensity, shown in part (b) of Figures 3.5, 3.6, and 3.7, represents the build-up of the Arias intensity normalized by the total Arias intensity of the motion:

$$NormalizedAriasIntensity = \frac{I_a}{I_{af}} = \frac{\int_0^t [a(t)]^2\,dt}{\int_o^{t_f} [a(t)]^2\,dt} \qquad \text{(Eq 3.3)}$$

These plots were used to determine the duration of strong shaking t_d (based on the 5%–95% Trifunac and Brady definition). Note that the normalized Arias intensity is shown in percent.

Summaries of three of the twelve ground motions and their site response analyses will be discussed herein. The characteristics of the remainder of the motions used in this study and summaries of their site response analyses are provided in Appendix A. Summaries of the San Fernando Pacoima Dam, Northridge VA Hospital, and the Synthetic #2 (Bay Bridge) ground motion characteristics can be seen in Figures 3.5, 3.6, and 3.7, respectively. Note that the scale between each of these figures is different. Each of these motions has significantly different characteristics. The Pacoima Dam record was recorded very near to the fault rupture (3 km from the inferred slip surface, Page et al. 1972) and has a strong long-period component at T = 1.1 seconds (as seen in the acceleration response spectra). This long-duration pulse occurs early in the velocity time history [Figure 3.5(c)] at time t = 2.5 seconds. The Northridge VA Hospital record and the Synthetic #2 record predominantly contain energy in the high-frequency range (spectral accelerations greater than the zero period acceleration occur well within the 1 second period range). However, the Synthetic #2 ground motion has a much longer duration than the VA Hospital record (with t_d = 8 seconds). Note also that the Synthetic #2 motion has a relatively smooth spectrum when compared to either the VA Hospital or the Pacoima Dam acceleration spectra.

The site response analyses for each of these three motions scaled to the intensities listed in Table 3.2 are shown in Figures 3.8, 3.9, and 3.10. Elastic (5% damped) acceleration response spectra at the rock outcrop, at 9.0 m below ground surface (3D for the 3.0 m diameter pile shafts and 6D for the 1.5 m diameter pile shafts, see Section 3.4), and at the ground surface are shown for these three motions in Figures 3.11, 3.12, and 3.13. The acceleration response spectra are shown on semi-log scales when comparing the response at different depths to better articulate the range of frequency content contained in the original outcrop records.

The site response analyses of the Pacoima Dam record (Figure 3.8) show a strong amplification of the long-period component at T = 1.1 seconds, which is also evident in the surface acceleration time history by the long-duration acceleration pulse that occurs early in the time history. Note that this pulse is evident in each of the scaled outcrop intensities [parts (d) and (e) of Figure 3.8]. Figure 3.11 shows the predominant period of the motion shifting from T = 0.39 seconds (at the rock outcrop) to T = 1.1 seconds (at the ground surface). This figure also shows the gradual increase in magnitude of the long-period component as the motion propagates up to the ground surface. Similar period shifting occurs in the VA Hospital motion (Figure 3.12) where the predominant period shifts from T = 0.3 seconds (at the rock outcrop) to either T = 0.44 or T = 0.81 seconds (depending on the scaled intensity). Note that at the ground surface for the VA Hospital motion, there are several predominant periods (T = 0.4 and T = 0.90 seconds), each having approximately the same spectral acceleration value. The acceleration spectra of these three motions also show little difference in spectral acceleration content between the motions at 9.0 m and at the ground surface at periods greater than about 1.0 second.

The surface response in terms of spectral acceleration for the Synthetic #2 motion [Figure 3.10(a)] shows the gradual lengthening of the dominant period as the intensity increases, as would be expected due to the larger shear strains and corresponding decrease in secant shear modulus. This trend is not as evident with either the Pacoima Dam or the VA Hospital record where only two scaled intensities were used. Note also that the highest shear strains for all of these motions [part (c) of Figures 3.8, 3.9, and 3.10] are within the upper sand layer with the lower shear wave velocity (when compared to the remainder of the soil stratum, with approximately $v_s \leq 300$ m/s). For the depths of interest of lateral pile response (less than 6D = 9.0 m or 18.0 m for the 1.5 m and 3.0 m diameter pile shafts, respectively), the maximum accelerations do not vary significantly with depth [part (b)] and in general, for these motions the maximum shear strain is less than 1% [part (c)]. Similar trends were observed for the eight other motions used in this study (shown in Appendix C).

Elastic (5% damped) acceleration response spectra, normalized by peak ground acceleration, are shown in Figure 3.14 for each of the twelve motions listed in Table 3.2. Noticeable differences in spectral content for the near-fault motions are seen between periods of 2 and 5 seconds. Peaks in the elastic (5% damped) response spectra (acceleration and velocity) were used to define a dominant period in the long-period range (T_{LP}) that would most affect the response of this class of structures. The values of T_{LP} ranged from 1.1 to 3.2 seconds for these near-fault motions. Alternative definitions for the pulse period were studied and some of these are discussed in more detail in Chapter 4. For example, the characteristic period T_c was also evaluated for potentially defining the period of the pulse associated with the near-fault motions. The characteristics period is equivalent to the peak of the input energy spectrum, which is nearly equivalent to the transition between the constant velocity and constant acceleration regions of a Newmark-Hall tripartite plot (Newmark and Hall 1982). For the motions considered, the use of the characteristics period generally resulted in shorter periods (T_c ranged from 1.0 to 2.3 seconds). The structures considered in this study, however, generally have much longer elastic periods (as high as $T_e = 3.8$ seconds). The difficulty in using the characteristics period or other definitions to define a period associated with the pulse in the ground motion is that the frequency characteristics of the structural system under consideration are not accounted for in the selection. For this reason, the pulse period (T_{LP}) definition described above was adopted.

3.4 STRUCTURAL SYSTEMS USED IN THIS STUDY

3.4.1 Structural Details

Twelve different bridge structures supported on large-diameter extended CIDH pile shafts were modeled. It is assumed that the transverse response of the bridge structure may be characterized by the response of a single bent, as would be the case for a regular bridge with coherent ground shaking applied to all bents. The extended pile shafts have an above-ground cross section that is slightly smaller than their below-ground cross section (Figure 3.15) in accordance with standard construction detailing. These structures have above-ground heights L_a = 2D, 4D, and 6D, where D (below-ground pile diameter) was taken as both D = 1.5 m and D = 3.0 m. The embedded pile length was set at 14D for each case based on providing reasonable axial load-carrying capacities. The tip of the pile shafts relative to the baseline soil profile is shown in Figure 3.3. Two different axial loads were used in the study, $0.05 \cdot f'_c A_g$ and $0.1 \cdot f'_c A_g$, where f'_c = unconfined compressive strength of the concrete, and A_g = gross area of the pile shaft. The results for the $0.1 \cdot f'_c A_g$ analyses were focused on evaluating the sensitivity of these structures to P-Δ effects and are discussed in Section 3.9.

A concrete compressive strength of $f'_c = 27.6$ MPa was used for both the pile and the above-ground extension. Although concrete strengths may be different for the pile and the above-ground extension, and actual concrete compressive strengths may be greater than the assumed f'_c value, the resulting lateral stiffness and strength of the pile are not very sensitive to the value of f'_c. The longitudinal and transverse reinforcement ratios (see Table 3.3) were about 1%, with nominal yield strengths of $f_y = 414$ MPa. A longitudinal reinforcement ratio of 1% represented the lower end of the longitudinal reinforcement ratios used in practice, but the objective of this study was to investigate the severity of the inelastic demands in bridge structures with low lateral strengths when subjected to ground motions with long-period characteristics. For the level of axial load imposed on the pile extension, the amount of confining steel is compatible with current practice (ATC-32 1996).

Moment-curvature simulations of the above- and below-ground sections of each of the structures used in this study are shown in Figures 3.16 and 3.17, respectively. Table 3.4 summarizes the flexural properties of each section. The moment-curvature simulation was performed assuming the Mander model (Mander et al. 1988) to incorporate the additional sectional strength and ductility capacity due to the confining steel. Note that the flexural strength and deformation capacity of the below-ground sections of each pile shaft was slightly larger than that of the above-ground sections due to the reduction in cover and subsequent reduction in gross sectional area in the above-ground section (Figure 3.15). The range of flexural strength increase provided due to the stepped section at the ground surface was between 14% and 18%. The difference in curvature capacity between the above- and below-ground sections used in this study was fairly small, with a range of increase in ultimate curvature ductility capacity $(\mu_\phi)_{cap}$ between 0% and 9%. Note that this range will vary slightly depending on the assumed steel properties used in Mander's model when estimating the ultimate compressive strain of the core concrete.

3.4.2 Lateral Soil Resistance

Table 3.1 lists the baseline site parameters used to define the nonlinear p-y springs. These parameters were based on the available data (boring logs and test data) taken from the Gilroy 2 site. Parameters for the p-y elements were based on common design procedures used in U.S. practice [e.g., API (1987) and Reese et al. (2000)]. The p-y representation of sand layers was modeled using the hyperbolic tangent model provided in API (1987). The clay layers were modeled using the backbone curves described by Matlock (1970). Parameters for both of these models are described in Chapter 2.

3.4.3 Nonlinear Static Pushover Analyses

A nonlinear static pushover analysis of each of the bridge structures considered in this study was performed to assess the global capacity of these systems. The analyses were performed by applying an incremental lateral displacement to the center of gravity of the superstructure. During the pushover analyses, local element demands were monitored in terms of moment and rotation values at integration points along the length of each element. At any point at which a section first exceeded the first-yield moment, the point of first yield can be defined. The first yield moment is defined as the moment associated with the first longitudinal bar reaching the yield strain. Figures 3.18–3.20 show the pushover analyses results for the different structures considered in this study where P-Δ effects are both included and not included in the analyses. Also noted on each figure are the first-yield points. Note that the axis between the upper and lower portions of each figure are different as the 2D-tall structures are generally about twice as strong as the taller, more flexible (4D- or 6D-tall) structures.

Global capacity is generally idealized into an elasto-plastic (EP) response to quantify design parameters such as yield strength and displacement. Elasto-plastic (EP) idealizations of the pushover results in this study were obtained using the procedure shown in Figure 3.21. The equivalent elastic stiffness is defined as the secant stiffness through the first-yield point. This equivalent elastic stiffness defines the corresponding equivalent elastic period of the structure (T_e or T^o_e — note that in this work the superscript "o" has been adopted for the case where P-Δ effects are not included in the analyses). The EP yield point is defined by the intersection of the equivalent elastic and plastic secant lines as shown in Figure 3.21. The post-elastic portion of the EP idealization was defined by extending a secant line through $3\Delta'_y$ and $5\Delta'_y$, which is nominally within current design ductility for these types of structures (e.g., ATC-32 1996). The EP yield point identifies the EP yield displacement Δ_y and the EP lateral yield force V_y (or V^o_y). Note that P-Δ effects have a fairly small effect on the first yield displacement Δ_y and as such yield displacements are generally assumed to be approximately the same between the analyses with and without P-Δ effects. However, there may be a greater impact on the EP lateral yield strength of the system (for a given analysis with and without P-Δ effects), as evident in the pushover analyses results shown in Figures 3.18–3.20.

The results of the nonlinear pushover analyses of these structures are summarized in Table 3.5. For the 1.5 m diameter pile shafts, the range of lateral strengths was from 562 kN to nearly double this, with $V^o_y = 1160$ kN for the 2D-tall structures. Doubling the below-ground pile shaft diameter resulted in soil-pile systems with lateral strengths ranging from 2080 kN to 5550 kN, for the different heights and axial loads considered. The structures considered in this study also had fairly long equivalent elastic periods, with a range of $T^o_e = 0.92$ to 3.79 seconds. For comparison, assuming the supporting structure is fixed at the ground surface results in fixed-base elastic periods ranging from $T_{eFB} = 0.24$ to 2.45 seconds, or from 26% to 65% of the elastic periods of the extended pile shaft systems.

3.5 DYNAMIC ANALYSES RESULTS

3.5.1 Typical Results

The response quantities for a typical structure and motion — the 3.0 m diameter CIDH pile shaft with an above-ground height of 4D and an axial load of $0.05f_c'A_g$ — are shown in Figures 3.22–3.24. The same structure is shown subjected to three outcrop motions: the San Fernando, Pacoima Dam (Figure 3.22), Northridge VA Hospital (Figure 3.23), and the Synthetic #2 Bay Bridge motion (Figure 3.24), each scaled to a peak rock outcrop intensity of $a_{max} = 0.7g$. These analyses included P-Δ effects. The superstructure horizontal acceleration and displacement time histories are shown in parts (a) and (b), respectively, where the acceleration is absolute and the displacement is relative to the pile tip. The maximum displacement of these systems is very different, even though the rock outcrop intensities were scaled to the same magnitude. The structure subjected to the San Fernando motion had a maximum displacement of $\Delta_{max} = 540$ mm which, when divided by the elasto-plastic (EP) yield displacement of $\Delta_y = 274$ mm, gives a global displacement ductility demand of $\mu_\Delta = 2.0$. The same structure subjected to the Northridge, VA Hospital motion remained nearly elastic and experienced a maximum displacement of $\Delta_{max} = 307$ mm, which yields a global displacement ductility demand of $\mu_\Delta = 1.1$. The long-duration Synthetic #2 motion imposed the largest displacement on this structure (of these three motions) with $\Delta_{max} = 1451$ mm, resulting in a displacement ductility demand of $\mu_\Delta = 5.3$.

The residual deformation at the end of shaking is also very different between these three motions. The magnitude of residual displacement is important for the repairability of the structure following an earthquake and will be discussed in the following section. However, for the analyses cases compared here, both the Northridge VA Hospital and the San Fernando motion resulted in fairly small residual displacements remaining in this structure, with Δ_{res} = 10 mm and 6 mm, respectively. In contrast, analysis of the same structure subjected to the Synthetic #2 motion resulted in a much larger residual displacement of Δ_{res} = 230 mm.

3.5.2 Maximum and Residual Drift Ratios

For near-fault ground motions, the inelastic response of the bridge structures tends to be associated with a biased response in one direction resulting in a large permanent displacement and rotation. The biased lateral response of the structure is often worsened by the combined effect of high axial force, low lateral strength, and increased flexibility due to soil compliance, which collectively increase the importance of geometric nonlinearities or $P-\Delta$ effects. The recent Japanese experience from the 1995 Hanshin earthquake indicated that large residual deformations, particularly the residual rotation at the ground level, might render the structure unserviceable or even irreparable after the earthquake (MacRae and Kawashima 1997). Bridges supported on reinforced concrete columns with permanent drift ratios larger than 1.75% had to be demolished following this event. Subsequent to the 1995 Hanshin earthquake, and based on the study of MacRae and Kawashima (1997), the Japan Road Association (1996) design guidelines specified an allowable residual drift ratio of 1% for important bridge structures.

In the study described herein, the permanent or residual drift ratio γ_{res}, defined as the slope (from vertical) of the above-ground pile extension after the earthquake, is used to quantify the magnitude of the permanent deformation in the bridge structure. Residual drift ratios γ_{res} would reasonably be expected to correlate with the maximum drift ratio γ_{max}, which is defined as the slope of the above-ground pile extension at its peak displacement response. Figure 3.25 shows the residual drift ratio γ_{res} versus the maximum drift ratio γ_{max} in the structures supported on 3.0 m diameter pile shafts, with an axial load of $0.05 \cdot f_c' A_g$, and subjected to the motions listed in Table 3.2. These analyses included $P-\Delta$ effects. The residual drift ratio γ_{res} generally increases with the maximum drift ratio γ_{max}, and although there is considerable scatter in Figure 3.25, the increase appears to be exponential. Very large maximum drift ratios (greater than 10%) were calculated for some of the bridge structures as a result of their low lateral strength relative to the ground motion demands. The structures that remained elastic are not shown in Figure 3.25.

An allowable residual drift ratio of γ_{res} = 1%, as suggested by MacRae and Kawashima (1997), has also been plotted in Figure 3.25 for comparison. It is interesting to note that the larger residual drift ratios ($\gamma_{res} > 1\%$) in Figure 3.25 were associated with the near-fault and long-duration ground motions, indicating that these ground motions may be very damaging from a repairability perspective. The exponential fit to the data indicates that if maximum drift ratios are less than about 8%, residual drift ratios will generally be less than 1% (based on the mean trend in the data) and at most 1.75%. Note that yield drift ratios for these structures (based on the definitions used in this study for drift ratio) were γ_y = 1.2, 1.4, and 1.6% for the 2D, 4D, and 6D-tall structures. Therefore, a maximum drift ratio of γ_{max} = 8% would roughly correlate to a displacement ductility between μ_Δ = 5 to 6.7. A higher degree of confidence in keeping residual drift ratios less than 1% may be achieved by using the upper-bound relation between γ_{max} and γ_{res}, in which case, maximum drift ratios would be limited to less than about 6%. Several analyses indicated that the structure would collapse under the near-fault Taiwan and Turkey ground motions, but these results could not be plotted in Figure 3.25. Analyses cases that indicated collapse will be summarized and discussed in Section 3.9. It is also worth noting that, to the authors' knowledge, allowable residual drift ratio limits have not been prescribed in current bridge seismic design codes in the United States.

3.5.3 Ground Motion Duration

Figure 3.26 shows the maximum and residual drift ratios plotted against the duration of strong ground motion shaking (as defined in Section 3.3). The results shown are for the 3.0 m diameter pile shafts, where P-Δ effects are included in the analysis. Ground motions with near-fault characteristics are not included in Figure 3.26. Although the trend is not very strong, there is an increase in both maximum and residual drift ratios with increasing ground motion duration, and the largest maximum and residual drift ratios calculated were from the long-duration synthetic motions. It should be noted that the response results shown in Figure 3.26 consist of a range of scaled acceleration intensities. The duration of strong shaking was seen to have an impact on the sensitivity of the extended pile shaft system's response to dynamic P-Δ effects (such as excessive displacement demands and/or overturning). These results will be discussed in Section 3.9.

3.6 GROUND MOTIONS WITH LARGE PERMANENT DISPLACEMENT OFFSETS

Near-source effects can vary depending on the orientation of the seismic source with respect to the site under consideration. Seismologists characterize these source effects in terms of their orientation along the fault rupture. Abrahamson (1998) uses recordings from the 1992 Landers earthquake to describe the dependence of the resulting shaking at a site on the rupture direction (toward the site or away from it). This dependence on rupture direction is termed "directivity." If the rupture is propagating toward the site (forward directivity) the resulting waves arrive in succession causing a large pulse over a short period of time. In contrast, if the rupture is moving away from the site (backward directivity) the resulting shaking is of lower intensity over a much longer duration. Perhaps the first recognition of directivity effects was provided by Benioff (1955) in his comparison of recordings from the 1955 Kern County earthquake to the Doppler effect. Recordings near the fault rupture with large permanent displacements can also exhibit a large velocity pulse. Ground motions with these large permanent offsets have previously been described as having a "fling" in their recording (Bolt 1981).

Directivity effects can also result in orthogonal components of motion with very different characteristics. Near the end of the fault rupture, the motion on the horizontal component oriented perpendicular to the fault rupture plane (fault normal) is typically more severe than the horizontal component oriented parallel to the fault rupture plane (fault parallel) [Singh (1985) and Somerville et al. (1997)]. Abrahamson (1998) points out that near the epicenter the converse may be the case (i.e., the strike-parallel component has been seen to be larger than the strike-normal component). Using empirical analysis of near-fault recordings, seismologists have proposed modifications to existing attenuation relations to incorporate rupture directivity effects including the variation between fault-normal and fault-parallel components (e.g., Somerville et al. 1997).

To evaluate the performance of structures due to near-source loading, previous researchers have attempted to isolate the pulse that may occur in the motion using simplified triangular loading or smooth sinusoidal pulses representative of the characteristics of real recordings [e.g., Krawinkler and Alavi (1998), Mahin and Hachem (1998), and Makris and Chang (2000)]. Several perspectives have been taken to address the use of simplified pulses to mimic the long-period characteristics associated with near-fault recordings.

Krawinkler and Alavi (1998) studied the response of SDOF and MDOF single-bay frame structures subjected to both the original near-fault recording and its source effects idealized by equivalent pulses. Results indicate that if the ratio of the elastic period T_e to the period of the idealized pulse T_p was greater than 0.5 and less than 3.0 ($0.5<T_e/T_p<3.0$, where T_p = period of the idealized pulse) the representation using an equivalent pulse is sufficient to capture the displacement demands imposed on the system. Makris and Chang (2000) use smooth pulses to idealize select recordings from recent California earthquakes (Landers, Imperial Valley, and Northridge). In evaluating the inelastic response of SDOF oscillators subjected to the pulse equivalent and the real recordings, they found that the response of structures that were susceptible to the high-frequency content of the motion could not be reliably captured using the pulse idealization. Their work suggested that if the equivalent elastic period of the system is less than 2.0 sec ($T_e<2.0$ sec) the system's response might be substantially affected by any high-frequency content of the original source that could not be captured when using an idealized pulse.

This section will focus on assessing the response of a subset of the pile-supported structures used in this study to motions with acceleration pulses that result in unusually large velocity pulses. As described above, these pulses are typically the more severe case resulting from the earthquake rupture moving toward the site (forward directivity) or from large permanent displacement demands associated with the fault rupture process. In this study, two of the motions recorded during the 1999 Taiwan earthquake were separated into their permanent and (remaining) transient components of shaking (Abrahamson 2001). The motivation for removing the large permanent displacement in these recordings was to evaluate whether dynamic motions associated with large fault rupturing at the ground surface are damaging to structures. The implication, from the seismologists' perspective is whether or not these fling components need to be included in developing design ground motions.

The results of the numerical cases described will demonstrate the importance of the permanent displacement component of the motion to the site response and overall behavior of the structural systems considered. The permanent component, as separated from the original recording, could also be viewed as an idealized pulse that represents the strong long-period content of the original motion. As such, results from this study are compared to previous suggestions regarding the period range which may be applicable when using idealized pulses to capture inelastic response due to near-fault motions.

3.6.1 Permanent and Transient Components of Motion

The permanent displacement associated with the large fault rupture can be removed from the recording numerically by fitting a function to the permanent component of the displacement time history. This was done for the Taiwan 075E and Taiwan 068E recordings by Abrahamson (2001) and is shown in acceleration, velocity and displacement time history form in Figures 3.27–3.32. Some judgment is needed in selecting the function used to fit the permanent displacement offset. It should be noted that the concept used herein is relatively new from the seismological viewpoint, thus the mechanisms used to choose corners, fitting functions and other aspects, are continuously evolving as the strong motion database grows.

The acceleration time histories (Figures 3.27 and 3.30) show the long-period spike that, when integrated once results in a large, half-sine waveform in the velocity record, and when integrated again results in a quarter-sine waveform in the displacement record. The elastic 5% damped acceleration and displacement spectra of these motions are shown in Figure 3.33 and Figure 3.34 for the 068E and 075E original, permanent, and transient components of motion.

The time histories shown in Figures 3.27–3.32 show that the long-duration acceleration pulse has an associated period of T_p = 3.72 and 3.23 sec for the 068E and 075E records, respectively. The period T_p, in this case, is defined by the duration of the acceleration pulse shown in the permanent component of these motions [part (c) of Figures 3.27 and 3.30] although it is clear that the pulse is not symmetrical and thus contains shorter- and longer-period components. The time histories also show that the resulting permanent ground displacement in these records was 5.1 and 1.6 meters for the 068E and 075E records, respectively. The spectra show that the long-period content of the transient component of both motions is significantly less than both the permanent components and the original records. For example, Figure 3.34(b) shows the rapid drop in spectral displacement at about $T > 4$ seconds for the transient component of motion, whereas for T less than approximately 2.8 seconds, both the transient and original record show higher spectral displacements than the long-period permanent component of the motion.

3.6.2 Influence of Site Response

The site response was performed using the permanent and transient components of the original records with the baseline site soil profile site described in this Chapter. The same 1-D equivalent linear site response analysis procedure (SHAKE96) was used. The components of each motion were scaled to a peak rock outcrop acceleration of $a_{max} = 0.5g$. The resulting ground surface acceleration and displacement time histories for the 068E and 075E motions are shown in Figures 3.35–3.38. In each case, for the permanent component of motion, the ground surface acceleration time history has a slight elongation of the period of the pulse and the surface motion is no longer a simple pulse. The resulting motion more closely resembles two half pulses of very different periods. For example, in Figure 3.35(c), the first negative half pulse of acceleration has a duration of about 1 seconds, which implies a full cycle has an associated pulse period of $T_p = 2.0$ seconds. Reversal of loading in the positive acceleration region produces a half cycle occurring over about 2.5 seconds, resulting in a pulse period of $T_p = 5.0$ seconds. These examples illustrate the complexity of the pulse and the associated difficulty in defining pulse characteristics. Alternatively, the pulse period may have been defined as the time to complete one full revolution, regardless of the symmetry of the pulse, or using the ground surface spectra (acceleration, velocity, or displacement, each of which may give slightly different results).

3.6.3 Dynamic Analyses Results

To study the impact of the components of these records on the inelastic response of structural systems, a subset of the pile-supported bridge structures used in this study were subjected to the transient and permanent components of the 075E and 068E Taiwan motions. In this case, structures supported on 3.0 m diameter pile shafts with axial loads of $0.05f'_cA_g$ and above-ground heights of 2D, 4D, and 6D were used, with P-Δ effects included in the analysis. Dynamic analyses results for these cases were compared with results from the same structure subjected to the original motion.

Lateral force-displacement responses and displacement time histories at the superstructure for the systems subjected to the Taiwan 068E motion are shown in Figures 3.39–3.41. Also shown in these figures are the velocity time histories of the superstructure superimposed with the rock outcrop velocity time history. Note that the permanent component of the original motion results in a half waveform that is generally amplified at the superstructure and produces several cycles of loading reversals in all cases. As discussed previously, this resulting smooth waveform in the velocity trace of the permanent component of the motion is similar to waveforms used to isolate and study the response of near-fault motions with large pulses [e.g., Krawinkler and Alavi (1998); Mahin and Hachem (1998); and Makris and Chang (2000)].

The inertial responses of the structures subjected to the original motion are enveloped at the peak displacement and force with a dashed line. For comparison, these dashed lines are superimposed on the lower figures (parts b and c of each figure) to accentuate the differences in response when components of the original motion were separated. These structures (each with different above-ground heights), subjected to the different components of the 068E motion show very different inertial responses, and a clear trend identifying which component of motion provided for the greatest amount of damage might not be identified immediately. For example, Figure 3.39 shows the response of a 2D-tall structure, where maximum displacement ductility demand of $\mu_\Delta = 6.14$ was seen for the structure subjected to the original component of motion (part a). In contrast, smaller demands of $\mu_\Delta = 3.91$ and 3.86 were calculated when the structure was subjected to the permanent and transient components of motion, respectively. However, the permanent component of motion produced the largest residual drift ratio of these three cases with $\gamma_{res} = 1.35\%$. Residual drift ratios for the original and transient motions were slightly smaller with $\gamma_{res} = 0.68$ and 0.21%, respectively. Figure 3.41 illustrates a 6D-tall structure subjected to the original motion (part a), which indicated a substantial loss of lateral strength and subsequently ratcheted to collapse (zero lateral strength) during small higher-frequency shaking cycles following a large displacement excursion in the record. Even though the outcrop peak velocity was the same between the original and permanent motions, the same structure subjected to the permanent motion had smaller maximum displacement ductility demand of $\mu_\Delta = 8.26$. The peak displacement demand of the same structure subjected to the transient component of motion was much smaller at $\mu_\Delta = 3.19$. This indicates, for these cases, removing the permanent component of the motion produces highly unconservative results.

Comparing the spectral ordinates (displacement and acceleration, shown in Figure 3.42) at the equivalent elastic period of these different structures to the inelastic displacement demands calculated using the FE model was evaluated as a means to explain the large differences seen between parts (a), (b), and (c) in Figures 3.39–3.41. A similar evaluation was attempted later for the Taiwan 075E motion. In some cases, the FE results were reasonably consistent with those expected based on the structure's elastic period T_e and the ground surface response spectra, but in other cases it was not entirely consistent. The 4D-tall case perhaps provides the most consistent comparison of these, where, observing the ground surface spectral acceleration [Figure 3.42(a)] at the equivalent elastic period of this structure ($T_e = 1.89$ seconds), both the original and permanent motions are increasing in spectral acceleration demand as the structural period elongates immediately beyond T_e. Whereas the spectral accelerations of the transient component of motion rapidly descends at periods within 1–2 seconds greater than T_e. Observing the inertial response for this structure (Figure 3.40), the transient component had the smallest peak displacement demand, nearly 40% of what the original motion produced. Such a comparison was not as consistent for the 2D-tall structure where the transient and original motion had the highest (and very similar) spectral acceleration demands at the equivalent elastic period of the system. Figure 3.39 shows the inertial response of this structure, where the maximum inelastic displacement demands are approximately equal, even though the spectral acceleration of the permanent component of motion is about 60% of the other two motions at the equivalent elastic period of this structure.

Similar lateral force-displacement responses, displacement time histories, and velocity time histories for the structures subjected to the Taiwan 075E motion are shown in Figures 3.43–3.45. The inertial responses of the structures subjected to the original motion are also enveloped in these figures with a dashed line. The response for these three structural configurations subjected to the different components of the 075E motion show very dramatic differences.

Figure 3.43 illustrates an interesting case, where the response of a 2D-tall structure to the original motion showed the smallest peak and residual displacement demands, with a maximum displacement ductility demand of $\mu_\Delta = 3.27$. Global displacement demands of $\mu_\Delta = 4.89$ and 8.67 were calculated when the structure was subjected to the permanent and transient components of motion, respectively. The spectra of these motions (Figure 3.46) somewhat agree with these trends. At the onset of shaking, when the structure has an elastic period $T_e = 1.10$ sec, the acceleration spectrum shows that the both the transient and the permanent components of the motion have much larger demands at T_e. In addition, the transient component is increasing fairly rapidly when compared to the permanent component of the motion, which also shows higher demand than the original motion but has a fairly flat, wide band of high spectral content just beyond the elastic period of this structure. In this case, residual drift ratios for these three analyses remained fairly small at γ_{res} = 0.17, 0.38, and 0.80% for the original, permanent, and transient motions, respectively.

Figure 3.47 summarizes the global performance measures of interest in this study for the different components of the Taiwan 068E and 075E motions. This figure shows the maximum and residual drift ratios calculated from the modified motions (i.e., the permanent and transient components) as a function of the drift ratios calculated using the original motion. Points falling on the one-to-one line indicate no change in (maximum or residual) drift ratio. Recall that two of the taller structures (L_a = 6D) indicated collapse when subjected to the original motion. Maximum and residual drift ratios for these analyses were taken as the displacement of the structure at zero lateral strength.

The general trend in Figure 3.47 is for the modified motions to result in smaller drift ratio demands, with a few exceptions, however. In the case of maximum drift ratios, only two cases showed $\gamma_{max(Modified)} > \gamma_{max(Original)}$. Recall that these were the analyses shown in Figure 3.43, where the original motion (075E) had a rapid drop in spectral content immediately beyond the equivalent elastic period of the system (2D-tall structure with T_e = 1.10 sec). In general, there are large differences between the responses of each structure to the original, transient, and permanent components of motions. The differences are particularly large for the residual drift ratios, where the largest difference was $\gamma_{res(permanent)} - \gamma_{res(transient)}$ = 9.6% for the 4D-tall structure subjected to the 068E motions. Note also that for any particular structure the trend between the analyses of the structure to the 068E motion did not always agree with the trend observed for the 075E motion (e.g., the 2D-tall structural response shown in Figures 3.39 and 3.43).

The results of the study by Krawinkler and Alavi (1998) suggest that the inelastic response of a system subjected to near-fault motions can be captured using idealized pulses if the ratio of the system's elastic period T_e to the period of the idealized (input) pulse T_p is between 0.5 and 3.0 ($0.5<T_e/T_p<3.0$). Figure 3.48 shows this relation for the cases studied herein. This figure shows the difference in maximum drift ratio obtained for the original motion ($\gamma_{max,original}$) and the permanent component of the motion ($\gamma_{max,permanent}$). Recall that the permanent component of motion was essentially idealized as a long-duration pulse. In calculating the period of the pulse T_p of the ground surface motion, the period of the pulse with the largest associated acceleration demand was used (T_p = 2.0 and 2.4 seconds, as shown in Figures 3.35 and 3.37).

This definition roughly corresponds with the definition adopted in the study by Krawinkler and Alavi (1998). However, their study only considered symmetric pulses. Note that the magnitude of the secondary half cycle in the resulting ground motions used in this study was very near to the magnitude of the first half cycle, however the length of each secondary half cycle was longer. Regardless of the pulse period chosen, the analyses indicate a large variation in the change in maximum drift ratio between the different motions and structures considered, particularly for $T_e/T_p>0.5$, where differences in maximum drift ratio as high as 19% were seen. If the longer length of the two pulses had been used, the resulting T_e/T_p ratios would be smaller, thus shifting some of the data outside of the period range suggested by Krawinkler and Alavi (1998).

3.7 CURVATURE DUCTILITY DEMANDS μ_ϕ

Another important performance measure is the local curvature ductility demand μ_ϕ imposed on the structure by an earthquake, because damage to the pile (such as spalling of cover concrete, crack widths, potential for buckling or fracture of longitudinal reinforcement) is related to the local curvature ductility. This section presents the local inelastic demands imposed on these pile-supported structures. For bridge structures supported on extended pile shafts, the local ductility demand imposed on the pile shaft might govern the design of the system. Recall that the local ductility factor is defined as the maximum curvature ϕ_{max} divided by the elasto-plastic yield curvature ϕ_y, i.e.,

$$\mu_\phi \equiv \frac{\phi_{\max}}{\phi_y} = \frac{\phi_p + \phi_y}{\phi_y} \qquad \text{(Eq 3.4)}$$

where ϕ_y = elastic-plastic (EP) yield curvature (listed in Table 3.4), ϕ_{max} = maximum curvature along the length of the pile, and ϕ_p = plastic curvature, and can be estimated as:

$$\phi_p = \frac{\theta_p}{L_p} \qquad \text{(Eq 3.5)}$$

where θ_p = plastic rotation in the pile shaft, and L_p is determined using the relation proposed by Chai and Hutchinson (1999): L_p = 1.2D, 1.4D, and 1.6D for the 2D, 4D, and 6D-tall structures, respectively.

In this work, the relation between global displacement μ_Δ and local curvature μ_ϕ ductility demands as determined by the dynamic FE analyses was compared to the simplified kinematic model described in Chapter 2 [Chai and Hutchinson (1999)]. Figure 3.49 shows the relation between local curvature and global displacement ductility for the 3.0 m diameter pile shaft structures supporting an axial load of $0.05f'_cA_g$. These are shown separately for the 2D, 4D, and 6D-tall structures. Results are also shown for the kinematic model, where the upper 4D of surrounding soil predominantly contributes to the lateral behavior of the soil-pile system. The figure also shows the ultimate curvature ductility capacities of the above- and below-ground sections of the pile shaft, as determined from the moment-curvature simulations. Recall that the curvature ductility capacity $(\mu_\phi)_{cap}$ is defined as $(\mu_\phi)_{cap} = (\phi_u)_{cap} / \phi_y$, and is listed in Table 3.4 for the different structures considered. The design displacement ductility levels for these structures (recommended by ATC-32, 1996) are also shown for comparison. The kinematic model generally matches the FE results fairly well, with the largest scatter in the data seen in the analysis of the 2D-tall structures. These structures will be more sensitive to the choice of surrounding soil properties due to their relatively small above-ground height and deeper maximum moment. In this case, the subgrade modulus n_h used in the kinematic model calculations was taken directly from values recommended by ATC-32 (reproduced in Figure 2.14, Chapter 2). However, recall that the values recommended by ATC-32 are typically representative of working load levels, and when the kinematic model was compared to experimental results (Chai and Hutchinson 1999), indicated that reductions of up to 30% of the original value of n_h were required to match measured results. Figure 3.50 shows these same data where n_h is increased and decreased by a factor of 2 from the original recommended value. These upper and lower bounds could reasonably be considered representative of the scatter associated with predicting the in-situ lateral subgrade modulus and the nominal adjustment that might be required beyond working load levels. The resulting bounds on the kinematic model envelop 85% of the analyses cases shown. Figure 3.50 also reconfirms that the 2D-tall structures are more sensitive to the choice of lateral subgrade modulus as there is a larger spread in the upper and lower bounds of the kinematic model.

Similar results are shown in Figure 3.51 for the 1.5 m diameter pile shafts with an axial load level of $0.05f'_cA_g$. These structures were subjected to a subset of motions (Turkey, Yarimca Petkim motion; the Lucerne, Landers motion; and the Synthetic #2 motion) with the rock outcrop scaled to the intensities listed in Table 3.2. All of the FE analyses cases shown in Figure 3.51 fall within 15% of the kinematic model predictions. In this case, a reduction of the recommended lateral subgrade modulus values of 55% ($n_h = 0.55 * n_{h(\text{chart})}$) bounds all of the cases considered.

To minimize local demands in accord with ATC-32 recommendations ($\mu_\phi \leq 13$), the allowable global displacement ductility would range from $\mu_\Delta = 5.2$–6.1 for the 1.5 m diameter pile shafts and from $\mu_\Delta = 4.8$–5.5 for the 3.0 m diameter pile shafts. However, there is considerable range in these values. As previously noted in Chapter 2, the amount of tolerable displacement ductility, given a limiting local ductility, is fairly insensitive to the above-ground height of the extended pile shaft, but is more sensitive to the strength of the surrounding soil. For example, the kinematic model upper and lower bounds of the selected n_h shown in Figure 3.50(a) suggest a range of displacement ductility between $\mu_\Delta = 4.6$–7.8 when a reliable local curvature capacity of $\mu_\phi = 13$ is assumed. Alternatively, if a design displacement ductility of $\mu_\Delta = 3.0$ is considered, for these larger diameter pile shafts, local curvature demands were fairly small, ranging from $\mu_\phi = 5.1$–6.9 for the 1.5 m diameter pile shafts and from $\mu_\phi = 6.9$–7.2 for the 3.0 m diameter pile shafts. In using the kinematic model in this study, however, the upper 4D region of the site in this study was represented by a (very) dense sand condition with $n_h = 42700$ kN/m^3, resulting in relatively small values of curvature ductility demand. However, the local curvature ductility demand increases with decreasing stiffness of the soil. For example, upon reducing the value of $n_h = 20000$ kN/m^3 for a medium-dense sand condition, the local curvature ductility demand increases to $\mu_\phi = 7.1$–7.6 for the 3.0 m diameter pile shafts and $\mu_\Delta = 3.0$. These results show that the pile diameter is also an important factor in relating global to local ductility. For example, for the smaller (406 mm diameter pile shafts) studied in Chapter 2, considering the dense sand condition [Figure 2.17(b)], the local curvature ductility μ_ϕ corresponding to a global displacement of $\mu_\Delta = 3.0$ remains fairly constant at about $\mu_\phi = 9.0$ for $L_a = 2D$, 4D, and 6D.

3.8 SOIL PARAMETER VARIATION

The sensitivity of the dynamic response of these types of structures to the lateral soil resistance, or p-y parameters, was evaluated for a subset of structures and ground motions by Curras (Curras 2000; Curras et al. 2001). Select results of this sensitivity study are reproduced and summarized in this section for completeness in describing the results of this collaborative research project.

The parametric study considered the effects p-y parameter variations have on various performance measures for the structure, including peak superstructure displacement and local curvature ductility in the pile. Prior to describing the results of this parametric study, general sources of uncertainty in p-y parameters and a reasonable range of variation that might be encountered in practice are discussed. Sources of uncertainty in predicting the lateral loading response of piles include (after Curras et al. 2001):

- Limitations in our ability to accurately characterize the soil profile, including the extent and continuity of individual soil layers.
- Limitations in current methods for estimating soil parameters, which often include empirical relations, SPT or CPT correlations, or laboratory testing of samples.
- Effects of construction methods on the soil properties and lateral stresses around the pile (e.g., driving vs. vibration vs. pre-drilling vs. CIDH). Construction effects are poorly understood and are not incorporated into current design practice.
- Generalized p-y relations may not capture the wide range of soil and loading conditions, including layering, loading rate, load history, cyclic degradation, 2D loading, diameter effects, or other influences.
- Limitations in our modeling of the nonlinear behavior of reinforced concrete and other pile materials.

Curras (2000) evaluated the potential variability in p-y parameters for a variety of soil conditions by re-analyzing a set of full-scale load tests. Analyses were performed to determine a range of initial stiffness and ultimate strength scaling factors to reasonably match measured pile response. The resulting scaling factors represented the combined effects of all influencing factors including model inadequacy and soil variability. Scaling factors on p-y ultimate strength m_p and stiffness m_s of 2.0, either up or down ($m_p = m_s = 2.0$ and $m_p = m_s = ½$), were chosen as being representative of reasonable ranges of variability. The effects of p-y stiffness and capacity on static and dynamic response were evaluated for the structures supported on 1.5 m and 3.0 m diameter pile shafts (supporting $0.05f'_cA_g$ axial load) and a subset of the ground motions used herein. The subset of outcrop motions consisted of the Synthetic #2 and the Turkey, Yarimca Petkim motion each scaled to peak accelerations $a_{max} = 0.3$, 0.5, and 0.7g for a total of 6 motions.

Figure 3.52 shows the effect of p-y parameter variations on the lateral displacement time histories and the force-displacement histories of the 1.5 m diameter, 4D-tall structure subjected to the Synthetic #2 outcrop motion with a_{max} = 0.7g. The baseline soil parameter results are shown in parts (b) and (e) of Figure 3.52, with the stiffer, stronger system (m_p=m_s=2.0) results to the left [parts (a) and (d)] and the softer, weaker system (m_p=m_s=½) results to the right [parts (c) and (f)]. Dashed lines that envelop the baseline structure's peak response are shown on parts (a), (c), (d), and (f) for comparison purposes. For these cases, it can be seen that the stiffer system had lower peak and residual displacements and that the softer system had larger peak and residual displacements. The resulting global displacement ductility demands for these systems are μ_Δ = 4.1 for the baseline system, μ_Δ = 4.1 for the stiffer system (although the maximum displacement is lower than for the baseline system, the yield displacement is also lower), and μ_Δ = 5.5 for the softer system.

A summary of the changes in peak response quantities from the p-y parameter study is shown in Figure 3.53 for the 1.5 m diameter pile shafts. These figures show the peak response quantity found in the soil parameter study versus the peak response for the corresponding baseline soil system, such that points falling on the one-to-one line indicate no change in that response quantity. The maximum superstructure displacements in Figure 3.53(b) show that the overall trend is for the stiffer systems to have smaller displacements and the softer systems to have larger displacements, although for most cases the differences are small. Overall, about 80% of the μ_Δ results are within ±20% of their baseline value.

The results in Figure 3.53 illustrate some important observations. Assume that a structure was designed for the baseline soil conditions, but in reality the soil properties were closer to either the softer or stiffer p-y conditions. If the soil is softer, the maximum displacements would likely be larger than anticipated, but the global displacement ductility demand might be smaller. Conversely, if the soil is actually stiffer than expected, the displacements would likely be smaller, but the forces and global ductility demand might be larger. This suggests that for the structures and motions studied, a conservative design for the structural strength would assume stiffer soil conditions resulting in larger design values for global ductility and force demand. On the other hand, a conservative design to limit structural drift would assume softer soil conditions. These results illustrate the long-recognized point that neither softer nor stiffer p-y parameters can be assumed to be conservative for seismic design, in contrast to the common expectation, usually derived from static design experiences, that assumes softer soil conditions are conservative.

Curras et al. (2001) also studied the effect p-y parameter variation had on the local ductility demands for both the 1.5 m and 3.0 m diameter pile shafts with axial loads of $0.05 \cdot f_c' A_g$ (Figure 3.54). These results indicate that the soil variation generally had a smaller effect on the local ductility than it did on the other performance measures studied. For both pile shaft diameters, about one half of the cases were within 10% of their baseline value and about two thirds of the cases were within 15% of their baseline value (Figure 3.54). The percent effect of the p-y parameter variations on the local ductility was generally greater at low levels of local ductility demand.

To understand this result, it is first necessary to examine the relation between local and global ductility (μ_ϕ and μ_Δ, respectively). Softer, weaker p-y parameters ($m_p = m_s = ½$) resulted in larger local to global ductility demand ratios (μ_ϕ/μ_Δ) than for the baseline case, and stiffer, stronger p-y parameters ($m_p = m_s = 2$) resulted in smaller μ_ϕ/μ_Δ ratios. This trend is the same for both shaft diameters, although the 1.5 m diameter shaft had larger μ_ϕ/μ_Δ ratios than the 3.0 m diameter shaft. The predicted trend between soil conditions and μ_ϕ/μ_Δ ratios are consistent with experimental data.

Curras et al. (2001) summarized typical effects that p-y parameter variations had on the structure's response. When softer, weaker p-y parameters ($m_p = m_s = ½$) were assumed:

- Yield displacement Δ_y increased
- Equivalent elastic period T_e increased
- Maximum displacement demand Δ_{max} increased
- Global displacement ductility μ_Δ demand decreased
- The ratio of local to global ductility factors μ_ϕ/μ_Δ increased

As shown in Figure 3.54, these factors can combine to cause the local curvature ductility demand μ_ϕ to be relatively unaffected. However, it should be recognized that the relative insensitivity of curvature ductility demand is noted only when both the strength (m_p) and stiffness (m_s) soil parameters were varied by a factor of two. For soils with conditions varying from dense to loose, the parameter variation (for stiffness, for example) is larger than a factor of two perhaps in the range of m_s = 6–8. Thus, a change in soil density may be expected to result in more significant changes in curvature ductility demand, more than may be anticipated due to uncertainty in estimating soil parameters. Moreover, it should be noted that a thorough site characterization is essential to estimating inelastic demands imposed on these structures. The preceding analyses only considered the effect of p-y variability at sites with relatively thorough subsurface characterizations. In the absence of a thorough site investigation, the uncertainty in the p-y parameters could be an order of magnitude greater and their effect on inelastic demands becomes substantial. Furthermore, an inadequate site characterization leads to greater uncertainty in the site response, which directly impacts the imposed demands on the structural system.

3.9 P-Δ EFFECTS

For bridge structures supported on extended pile shafts, the extension of the supporting foundation below ground level increases the flexibility of the system and decreases its lateral strength, thus increasing its susceptibility to amplification of displacement demands and/or collapse due to the combined effects of gravity loading acting through large lateral displacements (P-Δ effects). P-Δ effects are dependent on the hysteretic model; thus, structures that tend to have strain-hardening characteristics, such as redundant steel frame buildings may be less susceptible. Bridge structures supported on extended pile shafts are typically constructed of reinforced concrete and inherently have softening type hysteretic characteristics. In addition, bridge structures are more susceptible to P-Δ effects than buildings due to the minimal redundancy and limited overstrength typically provided in the structural system. On the other hand, axial loads in bridges are generally smaller than buildings.

The sensitivity of these structures to second-order effects was evaluated by analyzing the 3.0 m diameter pile shafts with and without P-Δ effects incorporated in the time history analysis (Hutchinson 2001). An overview of the results of this study is given here. Two different axial loads were used to assess the sensitivity of the response to a reasonable range of anticipated axial loads, namely $0.05f'_cA_g$ and $0.10f'_cA_g$. Six of the 12 motions used in the overall study were used in these analyses; namely both the Taiwan and Synthetic motions, the Landers, Lucerne motion and the Chile, Valparaiso motion. The measures used to evaluate P-Δ sensitive behavior are discussed in the following section.

3.9.1 Measures Used to Evaluate P-Δ Sensitive Behavior

From a static perspective, P-Δ effects will slightly reduce the elastic stiffness of the system, but to a greater extent, result in a reduction in the post-yield stiffness. Figure 3.55 illustrates the possible static P-Δ influence on the global lateral force-displacement response. It should be noted that the relation between the systems response with P-Δ effects is often described by the first-order response and the stability index θ. The stability index θ is defined as:

$$\theta \equiv \frac{P \cdot \Delta_y}{V_y^o \cdot h} \qquad \text{(Eq 3.6)}$$

where Δ_y = lateral displacement at first yield, V°_y = lateral load (associated with the lateral displacement at first yield of the response without P-Δ effects), and h = height above the ground surface to the point of application of lateral load V. Although Equation 3.6 is generally applied to fixed-base columns, the stability index for the extended pile shaft system may be approximated by modeling the system as an equivalent cantilever. In determining the stability index θ, for bridge structures supported on extended pile shafts with inelastic response anticipated below ground level, the difficulty is in determining the height h. Two possible choices were considered for the selection of h in this work, the depth-to-fixity L_f and the depth-to-maximum-moment L_m. The depth-to-fixity L_f is associated with the elastic displaced shape of the extended pile shaft, whereas the depth-to-maximum-moment L_m is a function of the strength of the soil-pile system. In this case, the height h was taken as the height above ground level L_a plus the depth-to-fixity L_f below ground level. Use of the depth-to-maximum-moment L_m provides for slightly smaller values of h and hence results in slightly larger values of the stability indices θ. However, the scatter of the data described in the following discussions existed for either choice of height h used in the calculation of the stability indices. The depth-to-fixity L_f was determined using the equivalent fixed-base cantilever approach described in Chapter 2. The range of system configurations (e.g., above-ground heights and axial loads) provided for a range of stability indices between θ = 0.02 and 0.014.

Based on the analysis of multistory reinforced concrete frames, Paulay (1978) suggested that P-Δ effects could be ignored if the story stability index θ times the displacement ductility demand was small enough. Results indicated that if the following was satisfied P-Δ effects could be ignored:

$$\mu_\Delta^o \cdot \theta < 0.15 \qquad \text{(Eq 3.7)}$$

where μ°_{Δ} = displacement ductility (of the system without P-Δ effects) and θ = stability index (as defined in Equation 3.6 and shown in Figure 3.55). If the above relation is not satisfied and inter-story drift ratios are large, Paulay suggests that the strength of the system should be increased such that the energy under the monotonic force-displacement relation (with and without P-Δ effects) is the same. Others have suggested slight variations to the limiting value provided above [e.g., Mahin and Borescheck (1991) suggest $\mu^{o}_{\Delta}\theta < 0.20$]. The limit provided in the above relation is somewhat semi-empirical and may vary for the assumptions used in individual studies (different structural systems and ground motions).

Alternatively, using nonlinear static pushover analysis, current bridge design codes [e.g., Caltrans (1999) and ATC-32 (1996)] suggest avoiding P-Δ sensitive behavior by evaluating the ratio of the axial load times the lateral displacement demand to the section flexural capacity. In the work described herein, this has been termed secondary-moment-strength ratio (*SMSR):*

$$SMSR \equiv \frac{P \cdot \Delta}{M_p} \qquad \text{(Eq 3.8)}$$

where P = axial load, Δ = displacement demand (without P-Δ effects), and M_p = plastic moment capacity of the section where inelastic action is anticipated. Note that the secondary-moment-strength ratio is often presented in terms of a percentage. Suggested recommendations for maximum secondary-moment-strength ratios to avoid P-Δ sensitive behavior for bridge structures come from the analyses of the SDOF systems described above [Mahin and Borescheck (1991) and MacRae et al. (1993)]. Current recommendations in Caltrans (1999), for example, indicate that if *SMSR*≤20%, dynamic P-Δ effects may be negligible and no further consideration is necessary. ATC-32 (1996) allows for a slightly larger value of *SMSR* ≤25%. In addition, ATC-32 does emphasize the importance of including the added flexibility of structures supported on flexible foundations, as the soil-foundation interaction may amplify dynamic P-Δ effects. Since ATC-32 has not been fully adopted by Caltrans practice, current guidelines by Caltrans (1999) will be used for comparison in this work. Caltrans (1999) design guidelines suggest that if *SMSR*>20%, either the system strength must be increased such that excessive deformations due to P-Δ effects or dynamic instability is avoided, or dynamic P-Δ effects must be accounted for directly by using nonlinear time history analysis. In general, the design philosophy described above attempts to avoid any significant effects that dynamic P-Δ moments will have on the system's response by providing design overstrength and minimizing excessive lateral drifts. The secondary-moment-strength ratio and the stability index θ are related:

$$SMSR = \frac{\mu_\Delta^o \theta}{\left(1 + \mu_\Delta^o \theta\right)} \qquad \text{(Eq 3.9)}$$

This relation is shown in Figure 3.56. Guidelines suggested by Caltrans (1999) and ATC-32 (1996) requiring *SMSR*≤20 and 25%, respectively, result in $\mu^o_\Delta \theta \leq 0.25$ and 0.33, respectively. Recall that these are slightly larger than earlier suggestions by Paulay (1978). In designing a bridge structure, guidelines suggested by ATC-32 (1996) imply a stability index of $\theta \leq 0.33$ or that the idealized elastic stiffness considering P-Δ effects is a minimum of 67% of the elastic stiffness when P-Δ effects are not considered, i.e., $k_e \geq 0.67 * k^o_e$. Alternatively, Caltrans guidelines (*SMSR* ≤20%) provide for a stability index of $\theta \leq 0.25$, or that the ratio of elastic stiffnesses remain slightly larger at $k_e \geq 0.75 * k^o_e$. This would imply that the elongation in equivalent elastic period due to P-Δ effects is minimized to within 15% of the equivalent elastic period of the system without P-Δ effects, i.e., $T_e/T^o_e \leq 1.15$.

Figure 3.57(a) shows the difference in maximum displacement demand ($\Delta_{max} - \Delta^o_{max}$) for the 3.0 m diameter pile shafts versus the displacement ductility factor times the stability indices ($\mu^o_\Delta * \theta$) for these structures. Figure 3.57(b) shows the maximum displacement amplification ratio *DAR* versus $\mu^o_\Delta * \theta$ for the same set of structures. The displacement amplification ratio *DAR* is defined as:

$$DAR \equiv \frac{\Delta_{\max}}{\Delta^o_{\max}} \qquad \text{(Eq 3.10)}$$

where Δ_{max} = maximum displacement calculated from the FE analysis *with* P-Δ effects and Δ^o_{max} = maximum displacement calculated from the FE analysis *without* P-Δ effects. In Figure 3.57, μ^o_Δ is the displacement ductility calculated from the FE analysis without P-Δ effects. Recommendations by Paulay (1978) that $(\mu^o_\Delta)\theta < 0.15$ are shown for reference. For all of the data with $(\mu^o_\Delta)\theta \leq 0.15$, the mean displacement amplification ratio was *DAR* = 1.02, with an associated COV = 10%. For the data with $(\mu^o_\Delta)\theta > 0.15$, the data have a slightly higher mean displacement amplification ratio *DAR* = 1.12, and an associated COV = 12%. Figure 3.57(a) also shows that at the transition recommended by Paulay, the difference in maximum displacements with and without P-Δ effects ($\Delta_{max}-\Delta^o_{max}$) increases with increasing $(\mu^o_\Delta)\theta$. Similarly, the trend in the *DAR* [Figure 3.57(b)] is to increase slightly with increasing $(\mu^o_\Delta)\theta$. For all of the analyses considered, with $0.05f'_cA_g$, 79% of the data showed less than a 10% amplification of maximum displacements, i.e., *DAR* ≤ 1.10. For the $0.10f'_cA_g$ cases, 65% of the data resulted in a *DAR* ≤ 1.10.

These same data are compared to system secondary-moment-strength ratios in Figure 3.58. Guidelines suggested by Caltrans (1999) are shown for reference. Note that amplifications of peak displacement as high as 135% (*DAR* = 1.35) were seen in a few analyses for *SMSR* ≤ 20% (where P-Δ effects would not be considered in current bridge design guidelines). The *DAR* for *SMSR*>20% appear to be relatively insensitive to the increasing secondary-moment-strength ratio (up to about *SMSR*~30%). The highest amplification of displacements (with the exception of those systems that indicated collapse) was *DAR* = 1.43, for a 3.0 m diameter pile shaft, 6D tall with an axial load of $0.05f'_cA_g$ during the Lucerne transverse motion with $a_{max} = 0.7g$. Note, however, that the systems that indicated collapse are not shown on these figures as *SMSR*~100% for these structures. De-amplification in displacements, in some cases, can be attributed to a shift in the system's period away from the more dominant periods of the ground motion.

Differences in maximum and residual drift ratios for these analyses are shown in Figures 3.59 and 3.60. Figure 3.59 shows the change in maximum drift ratio for the analyses with and without P-Δ effects as a function of the displacement ductility μ°_Δ and the maximum drift ratio γ°_{max} (both without P-Δ effects). The design ductility level recommended for these structures ($\mu_\Delta = 3.0$, ATC-32 1996) is shown for reference. For the analyses with $\mu^\circ_\Delta<3.0$, differences in maximum drift ratio ($\gamma_{max} - \gamma^\circ_{max}$) as high as 3.3% were calculated (for one case); however, the mean difference in maximum drift ratios was fairly low at +0.26%. Second-degree polynomial fits are drawn through these data emphasizing the increase in drift ratio with displacement ductility level and maximum drift ratio level. As anticipated, the amount of increase is dependent on the axial load level. At a displacement ductility of $\mu_\Delta = 3.0$, the trend lines shown in Figure 3.59 suggest that the maximum drift ratio (with P-Δ effects) will be on average +0.5% greater than the analysis without P-Δ effects predicts.

Residual drift ratios for these same data are shown in Figure 3.60. The data in this figure show that for design ductility $\mu^\circ_\Delta>3.0$ or for a maximum drift ratio of $\gamma^\circ_{max}>8\%$, there is a large scatter in the change in residual drift ratio. Recall that if the maximum drift ratio was less than ~8%, the mean of the data indicated residual drift ratios would be less than 1%. The polynomial fit shown emphasizes the increase in the difference in residual drift ratio with increasing maximum drift ratio and displacement ductility. For the cases considered, 83% reported a positive increase in residual drift ratio when P-Δ effects are accounted for. Although the data in Figure 3.60 indicate that the differences in residual drift ratios for the $0.05f'_cA_g$ cases are slightly higher than the differences reported for the $0.10f'_cA_g$ cases, the trend lines shown do not include the cases that indicated collapse. For these analyses, more $0.10f'_cA_g$ cases indicated collapse; therefore the regression is performed on a different number of cases. Of the cases where P-Δ effects result in slightly lower residual drift ratios, the magnitude of difference was very small, less than 0.1%. This was not necessarily the case when considering changes to the maximum drift ratio where, of the cases considered, 85% showed increases in maximum drift ratio when P-Δ effects were included in the analysis.

3.9.2 Dynamic P-Δ Effects

It is instructive to observe the dynamic characteristics in terms of the lateral force displacement response of some of these structures. During dynamic motions, depending on the characteristics of the ground motions, P-Δ moments can be large enough to cause collapse resulting from progressive yielding in one direction, particularly for near-fault ground motions, where uni-directional loading may lead to a biased response. In this section, a number of pile-supported structures that indicated collapse during the analysis will be discussed. It is important to note that the structures that did indicate collapse were subjected to a ground motion with either a particularly long duration of shaking or with large pulse type characteristics indicative of a near-fault recording.

Previous researchers have recognized the influence strong motion duration can have on the stability of a system when P-Δ effects are considered [e.g., Mahin and Borescheck (1991), Mahin (1976), and Sun et al. (1973)]. This is primarily because long-duration earthquakes can cause ratcheting if the post-yield stiffness of the structure is negative enough. This ratcheting phenomenon is not new [Newmark and Rosenblueth (1971), MacRae (1994)] but was primarily tied to ground motions with long-duration characteristics. It was also found in this work that strong near-fault ground motions with large uni-directional pulses can provide for large displacement demands and when considering P-Δ effects in the analysis, provide a destabilizing component that makes these structures susceptible to collapse. This may be particular to long-period systems such as the flexible pile-supported structures studied in this work.

Figure 3.61 compares the dynamic response of a structure with and without P−Δ effects subjected to a near-fault recording from the Taiwan earthquake (Taiwan 075E motion with a_{max} = 0.5g). The structure had a pile diameter of 3.0 m, an above-ground height of 4D (L_a = 12 m), and an axial load of $0.05f'_cA_g$. The ground surface velocity time history is also shown with the peak in the record indicated. The structure with P−Δ effects experiences a single large displacement excursion to a displacement ductility of $\mu_\Delta = 9.6$ at t = 11 seconds with only limited yielding in the reverse direction and during subsequent shaking. The large displacement demand resulted in a large residual drift ratio of γ_{res} = 10.6%. In contrast, the same structure analyzed without P−Δ effects experiences a slightly lower displacement ductility demand of $\mu^\circ_\Delta = 7.6$ and a much smaller residual drift ratio of γ°_{res} = 1.2%. For this system *SMSR* = 34%. This and other examples illustrate that strong near-fault ground motions with large uni-directional pulses can impose large deformation demands resulting in dramatically different dynamic response when P-Δ effects are included in the analysis.

Figure 3.62 illustrates several extreme cases where including P-Δ effects in the analysis caused the structures to collapse. The analyses without P-Δ effects are also shown on these figures to illustrate the dramatic difference in global response had P-Δ effects been ignored. The structures shown in Figure 3.62 were supported on 3.0 m diameter pile shafts with an above-ground height of 6D (L_a = 18 m) and carrying an axial load of $0.05f'_cA_g$. The important characteristic from a dynamic response perspective, which is evident in the figure, is that if sufficient yielding occurs in one direction, subsequent softening of the system will tend to be in the same direction. Several of the analyses cases exhibited a ratcheting to collapse in one direction following a large displacement excursion. The response shown in Figure 3.62(a) for example, shows a large-velocity pulse that occurs at about t = 7 seconds, which caused substantial softening and subsequent strong shaking, and resulted in a biased response and ratcheting to collapse. The structure analyzed without P-Δ effects remained stable with a peak displacement ductility demand of $\mu^o_\Delta = 5.0$. Each of these examples indicates relatively stable behavior, had P-Δ effects not been accounted for.

Table 3.6 summarizes the structures that indicated collapse when P-Δ effects were included in the analysis. Also listed in the table are the force-reduction factors R, the displacement ductility demand μ°_{Δ}, the maximum drift ratio γ^{o}_{max}, and the calculated secondary-moment-strength ratios. Calculation of the force-reduction factor R is discussed later in Chapter 4 (Section 4.3). These quantities have been calculated for the structures without P-Δ effects included in the analysis. It should be noted that six of the cases that collapsed when supporting a 10% axial load were reanalyzed with an axial load of 5% and did not indicate collapse. It is important to note that the analysis that indicated collapse when P-Δ effects were included had secondary-moment-strength ratios greater than current Caltrans design limits (when P-Δ effects were not included in the analysis). In this case, if the deformation level without P-Δ effects had been predicted (e.g., from a site spectrum or a time history analysis), such guidelines would require either the system strength be increased, or a more rigorous dynamic analysis be performed to assess the possibility of collapse due to dynamic P-Δ effects. Three of the analyses cases listed in Table 3.6 were re-analyzed as part of the soil parameter study (Curras 2000). The shorter of these (4D-tall, 1.5 m diameter pile shaft subjected to the Yarimca Petkim motion) remained stable when the surrounding soil strength and stiffness were doubled. However, increasing the strength and stiffness of the surrounding soil by a factor of two did not inhibit the dynamic instability for the two taller structures (6D-tall; 1.5 m and 3.0 m diameter pile shafts with $0.05f'_cA_g$, also subjected to the Yarimca Petkim motion).

3.10 SUMMARY AND CONCLUSIONS

The performance of bridge structures supported on large-diameter extended CIDH pile shafts subjected to a suite of ground motions was evaluated using a series of nonlinear dynamic analyses. Earthquake motions with a range of frequency contents, intensities, durations and permanent displacements were used as rock outcrop motions. Performance measures used in evaluating the seismic response of these structures included maximum and residual drift ratios and both local and global ductility demands. The correlation between maximum and residual drift ratios from the dynamic analyses indicates that strong near-fault motions and motions with long durations of shaking may result in large permanent displacements in the structure, rendering it unusable or even unsafe. The exponential fit to the data indicates that if maximum drift ratios are less than about 8%, residual drift ratios will generally be less than 1% (based on the mean trend in the data) and at most 1.75%. A higher degree of confidence in keeping residual drift ratios less than 1% may be achieved by using the upper-bound relation between γ_{max} and γ_{res}, in which case, maximum drift ratios would be limited to less than about 6%. However, it is recommended that the ability of the FE model to specifically capture residual displacements has not been fully explored and thus warrants calibration against experimental data.

The effect of near-fault ground motions with large permanent offsets was studied for a subset of the CIDH pile-supported bridge structures used in this study by subjecting these structures to the original, permanent, and transient components of motion. Removing the permanent displacement component of the motion was often unconservative in terms of the peak and residual displacement demands imposed on the system. Removing the permanent displacement component changes the frequency content of the motion, and in some cases, greater demands can actually be imposed on the system if the shift in frequency causes the predominant period of the motion to be closer to the fundamental period of the structure. If residual deformations are of interest in the performance assessment of the system, results from these analyses indicate a large scatter in the residual drift ratios produced by the different components of motion. Consequently, it is important that the fling effect from permanent ground displacements (due to surface rupture) on ground motions and their elastic response spectra be included in the design process.

Subjecting these structures to the permanent displacement component of motion provided an opportunity to study the response of structures to smooth, idealized pulses in an attempt to isolate the contribution of the fling effects. The data were compared to suggestions provided by previous researchers on the range of validity of such an approximation. The results indicate that previous suggestions for the range of period ratio (T_e/T_p) where idealized pulses reasonably capture inelastic response were not applicable for the structures and motions considered in this study. However, the separated components of ground surface acceleration time histories used in this study were not symmetric and were better approximated as 2 one-sided pulses of greatly different pulse periods (e.g., T_p = 2.0 and 5.0 seconds). Therefore, it is difficult to uniquely define a single period T_p to describe the pulse, and hence a single T_e/T_p ratio did not provide a good measure for comparison.

The effect of variable lateral soil resistance on the dynamic response of these structures was also described. Scaling the p-y capacity m_p and stiffness m_s by factors of $m_p = m_s = 2.0$ and

$m_p = m_s = ½$ was studied for a subset of motions and structures. Stronger, stiffer p-y parameters generally resulted in a larger lateral yield force, smaller lateral yield displacement, smaller equivalent elastic period, smaller displacement demand, slightly larger global displacement ductility demand, and relatively similar local curvature ductility demand. Softening the p-y parameters generally had the opposite effects. These results should not be generalized to other classes of structures, however, because there are clearly situations where variations in the substructure stiffness can have a much more significant effect on system performance.

The relation between local and global ductility demands was also studied. Results from the dynamic analyses were compared to a simplified kinematic model. In general, the kinematic model reasonably bounded the dynamic FE analysis results. As might be anticipated, the shorter 2D-tall structures showed more scatter in the relation between global and local ductility. Invariably, these structures were also more sensitive to the selection of soil parameters and the piles sectional properties when using the kinematic model. Reasonable allowances for uncertainties in the lateral subgrade modulus values resulted in the kinematic model bounding the dynamic analyses results.

Limiting local demands in accord with ATC-32 recommendations ($\mu_\phi \leq 13$), results in global displacement ductility ranging between $\mu_\Delta = 5.2–6.1$ for the 1.5 m diameter pile shafts and from $\mu_\Delta = 4.8–5.5$ for the 3.0 m diameter pile shafts. Alternatively, if a design displacement ductility of $\mu_\Delta = 3.0$ is used, for these larger diameter pile shafts, local curvature demands were fairly small and ranged from $\mu_\phi = 5.1–6.9$ for the 1.5 m diameter pile shafts and from $\mu_\phi = 6.9–7.2$ for the 3.0 m diameter pile shafts. For the smaller (406 mm diameter pile shafts) studied in Chapter 2, considering the dense sand condition [Figure 2.17(b)], the local curvature ductility μ_ϕ corresponding to a global displacement of $\mu_\Delta = 3.0$ remains fairly constant at $\mu_\phi = 9.0$ for L_a = 2D, 4D, and 6D.

A subset of motions and pile-supported bridge structures used in the study were analyzed with and without P-Δ effects. Results from these analyses were compared with current design approaches used to minimize or avoid P-Δ sensitive behavior (such as large amplification of lateral displacements or substantial strength loss). Differences in peak inelastic displacements and displacement amplification ratios were compared to the system stability index times the displacement ductility factor $\mu^o_\Delta\theta$ and the secondary-moment-strength ratio. The stability index times the displacement ductility factor ($\mu^{o}{}_{\Delta}\theta$) did not provide a clear indication of dynamic instability or P-Δ sensitive behavior. Recommendations suggested by Paulay (1978), in which $\mu^{o}{}_{\Delta}\theta$ is limited to less than 0.15, appear to be acceptable for the cases considered herein. Several dynamic analyses cases subjected to long-duration or near-fault ground motions indicated collapse when P-Δ effects were included in the analysis, but all of these cases had $\mu^{o}{}_{\Delta}\theta$ or secondary-moment-strength ratio values outside the limits of current bridge design practice. The results indicate that the current practice of limiting secondary-moment-strength ratio (where $SMSR \equiv P\Delta/M_p$) to avoid detrimental P-Δ effects was found to be acceptable, although it is noted that the consequences of exceeding this criteria were not very significant in many cases.

Table 3.1 Soil properties for lateral loading behavior (courtesy of Curras 2000).

Depth (m)	Soil Type	γ (kN/m^3)	ϕ' (deg)	k (MN/ m^3)	s_u/σ'_{vo}	OCR	ε_{50}
0-7.5	Sand	19	38	42.7	-	-	-
7.5-10.5	Clay	19	-	-	$0.35 \cdot OCR^{0.8}$	3.0	0.005
10.5-22.5	Sand	19	42	61.0	-	-	-
22.5*-42	Clay	19	-	-	$0.35 \cdot OCR^{0.8}$	4.0	0.005

* Ground Water Table at 22.5m

Where:
γ = total unit weight of soil
ϕ' = effective friction angle
k = soil modulus
s_u = undrained shear strength of soil
σ'_{vo} = initial effective vertical stress
OCR = over-consolidation ratio
ε_{50} = strain corresponding to ½ the maximum principle stress difference on a triaxial test

Table 3.2 Rock outcrop motions used in this study.

Earthquake name and Location of recording	Year	M_w	Channel	D1[1] (km)	D2[2] (km)	a_{max} (g)	v_{max} (m/s)	v_{max}/a_{max} (s)	d_{max} (m)	t_d (s)	T_{LP} (s)	Scaled a_{max} in analyses (g)
(a) Near-fault motions												
San Fernando, Pacoima Dam[3]	1971	6.6	S16°E	2.8	8.5	0.67	0.956	0.15	0.507	7	1.1	0.5, 0.7
Landers, Lucerne	1992	7.3	Transverse	1.0	42.0	0.71	0.744	0.11	0.697	13	1.2	0.3, 0.5, 0.7, 0.9
Northridge, Sylmar	1994	6.7	0°	7.6	15.8	0.84	1.288	0.16	0.304	5	1.4	0.7, 0.9
Chi-Chi Taiwan, Station 068	1999	7.6	East-West	1.0	46.3	0.51	2.807	0.56	7.076	12	2.5	0.3, 0.5
Chi-Chi Taiwan, Station 075	1999	7.6	East-West	1.5	18.4	0.33	1.163	0.36	1.715	27	2.1	0.3, 0.5
Turkey, Yarimca Petkim	1999	7.1	Transverse	4.4	15.0	0.32	0.878	0.28	1.451	29[4]	3.2	0.3, 0.5, 0.7
(b) Other motions												
Synthetic #1 (Seed and Idriss)	1969	8.0	--	--	--	0.50	0.460	0.09	0.170	36	--	0.5, 0.7
Chile, Valparaiso (aftershock)	1985	6.3	160°	N/A	87.2	0.41	0.270	0.07	0.074	19	--	0.3, 0.5, 0.7
Loma Prieta, Gilroy #1	1989	7.0	0°	10.0	28.4	0.44	0.318	0.07	0.107	7	--	0.3, 0.5, 0.7
Loma Prieta, Santa Cruz	1989	7.0	0°	20.2	16.6	0.44	0.217	0.05	0.104	9	--	0.5, 0.7
Northridge, VA Hospital	1994	6.7	360°	8.9	7.3	0.94	0.754	0.08	0.358	8	--	0.7, 0.9
Synthetic #2 (Bay Bridge)	1999	7.5	--	--	--	0.52	0.841	0.16	0.456	36	--	0.3, 0.5, 0.7

[1] D1 = Closest distance to the rupture surface.

[2] D2 = Epicentral distance – provided by COSMOS Virtual Data Center http://db.cosmos-eq.org/

[3] Filtering by Page et al. (1972) and topographical modifications by Boore (1973).

[4] Duration was determined using the 5–95% cumulative Arias intensity from the first event added with the 5–95% cumulative Arias intensity from the second event that immediately followed the first.

N/A = Not Available

-- = Not Applicable

Table 3.3 Nominal reinforcement ratios used in baseline structures.

Diameter	Section Location	ρ_l	ρ_s
3.0 m	Below Ground	1.03%	1.04%
2.7 m	Above Ground	1.01%	1.04%
1.5 m	Below Ground	1.16%	1.12%
1.4 m	Above Ground	1.03%	1.12%

Where:

ρ_l = longitudinal reinforcement ratio

ρ_s = transverse reinforcement ratio

Table 3.4 Summary of moment curvature analyses for above- and below-ground level sections.

Diam (m)	Axial load (% $f'_c A_g$)	Section Location	M_y (kN-m)	M_{max} (kN-m)	ϕ'_y (x1e^{-3} rad/m)	ϕ_y (x1e^{-3} rad/m)	ϕ_u (x1e^{-3} rad/m)	$(\mu_\phi)_{cap}$	EI_e (MN-m^2)
1.5	5.0	Below-ground	4618	7697	2.25	3.76	86.6	23.0	2049
1.4	5.0	Above-ground	3806	6551	2.30	3.95	91.4	23.1	1658
3.0	5.0	Below-ground	33865	53181	1.14	1.79	43.9	24.5	29727
2.7	5.0	Above-ground	26540	45340	1.21	2.06	46.5	22.6	21999
3.0	10.0	Below-ground	41478	59098	1.23	1.75	37.2	21.2	33778
2.7	10.0	Above-ground	33539	51851	1.32	2.04	39.4	19.3	25455

Where:

M_y = first yield moment (moment at which first longitudinal bar yields)

M_{max} = maximum moment of the section

ϕ'_y = first yield curvature

ϕ_y = equivalent elasto-plastic (EP) yield curvature

ϕ_u = ultimate curvature

$(\mu_\phi)_{cap}$ = curvature ductility capacity $\equiv (\phi_u)_{cap} / \phi_y$

EI_e = effective flexural rigidity.

Table 3.5 Summary of nonlinear pushover analyses results *without* P-Δ effects (denoted with superscript “o”).

Diam. (m)	Height L_a Above ground Level	Axial Load (% of $f'_c A_g$)	Δ^o_y (mm)	V^o_y (kN)	T^o_e (sec)	T_{eFB} (sec)
1.5	2D	5.0	96	1160	0.92	0.24
	4D	5.0	171	777	1.51	0.67
	6D	5.0	260	562	2.18	1.23
3.0	2D	5.0	150	4836	1.12	0.36
	4D	5.0	274	3006	1.89	1.01
	6D	5.0	429	2080	2.84	1.86
3.0	2D	10.0	162	5550	1.51	0.47
	4D	10.0	300	3485	2.60	1.33
	6D	10.0	463	2521	3.79	2.45

Where:
Δ^o_y = elasto-plastic yield displacement
V^o_y = elasto-plastic yield strength
T^o_e = equivalent elastic period of soil-pile system
T_{eFB} = equivalent elastic period of same structure fixed at ground surface

Table 3.6 Summary of pile-supported structures that collapsed.

Above-ground height L_a	Earthquake and scaled rock outcrop acceleration	Total record (s)	Time of collapse (s)	Force Reduction Factor R	Displacement Ductility[2] μ^o_Δ	Max. Drift Ratio[2] γ^o_{max} (%)	*DAR*[1]	*SMSR*[2] (%)
(a) 3.0 m diam shafts, 5% axial load								
6D[3]	Yarimca Petkim, 0.7g	70	42	5.26	5.0	10.6	2.42	42
6D	Taiwan 068EW, 0.5g	40	23	4.92	6.3	14.0	1.93	52
6D	Taiwan 075EW, 0.5g	70	14	4.04	7.5	16.2	1.61	63
(b) 3.0 m diam shafts, 10% axial load								
2D	Taiwan 068EW, 0.5g	40	40	4.04	9.4	19.6	2.09	54
4D	Taiwan 068EW, 0.5g	40	20	7.57	8.3	14.2	1.36	88
6D	Taiwan 068EW, 0.5g	40	11	4.87	6.0	13.8	0.96	97
4D	Taiwan 075EW, 0.5g	70	11	5.07	10.5	20.7	1.14	92
6D	Taiwan 075EW, 0.3g	70	15	2.74	3.5	8.2	1.73	58
6D	Taiwan 075EW, 0.5g	70	11	5.75	7.8	18.3	0.76	100
6D	Lucerne Transverse, 0.9g	31.98	13	3.62	4.7	10.9	1.28	36
6D	Synthetic #2, 0.7g	60	14	3.03	3.7	8.6	1.62	59
(c) 1.5 m diam shafts, 5% axial load								
4D[4]	Yarimca Petkim, 0.7g	70	17	5.71	N/A	N/A	N/A	N/A
6D[3]	Yarimca Petkim, 0.7g	70	10	3.66	N/A	N/A	N/A	N/A

[1] In this case $DAR \equiv \Delta_p/\Delta^o_{max}$, where Δ_p = plastic displacement capacity of the system (at zero lateral strength).

[2] For the system without P-Δ effects that remained stable.

[3] These cases were also analyzed as part of the soil parameter study (Curras 2000). Although the strength and stiffness of the soil was scaled up and down by a factor of 2.0, these systems still collapsed.

[4] Also part of the soil parameter study (Curras 2000), increasing the strength and stiffness of the soil prevented this structure from collapsing.

N/A = Not Available

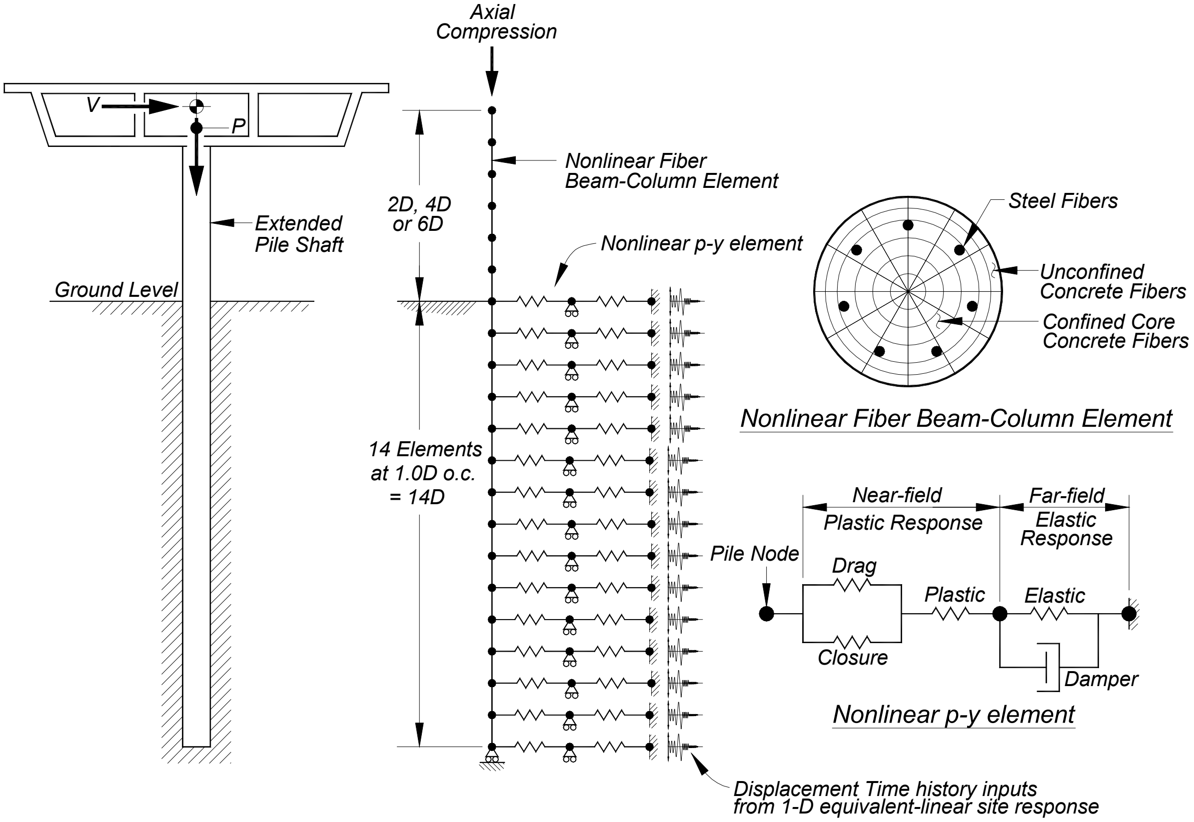

Figure 3.1 General schematic of the finite element model for the dynamic BNWF analyses using the nonlinear fiber beam-column element and the nonlinear p-y element.

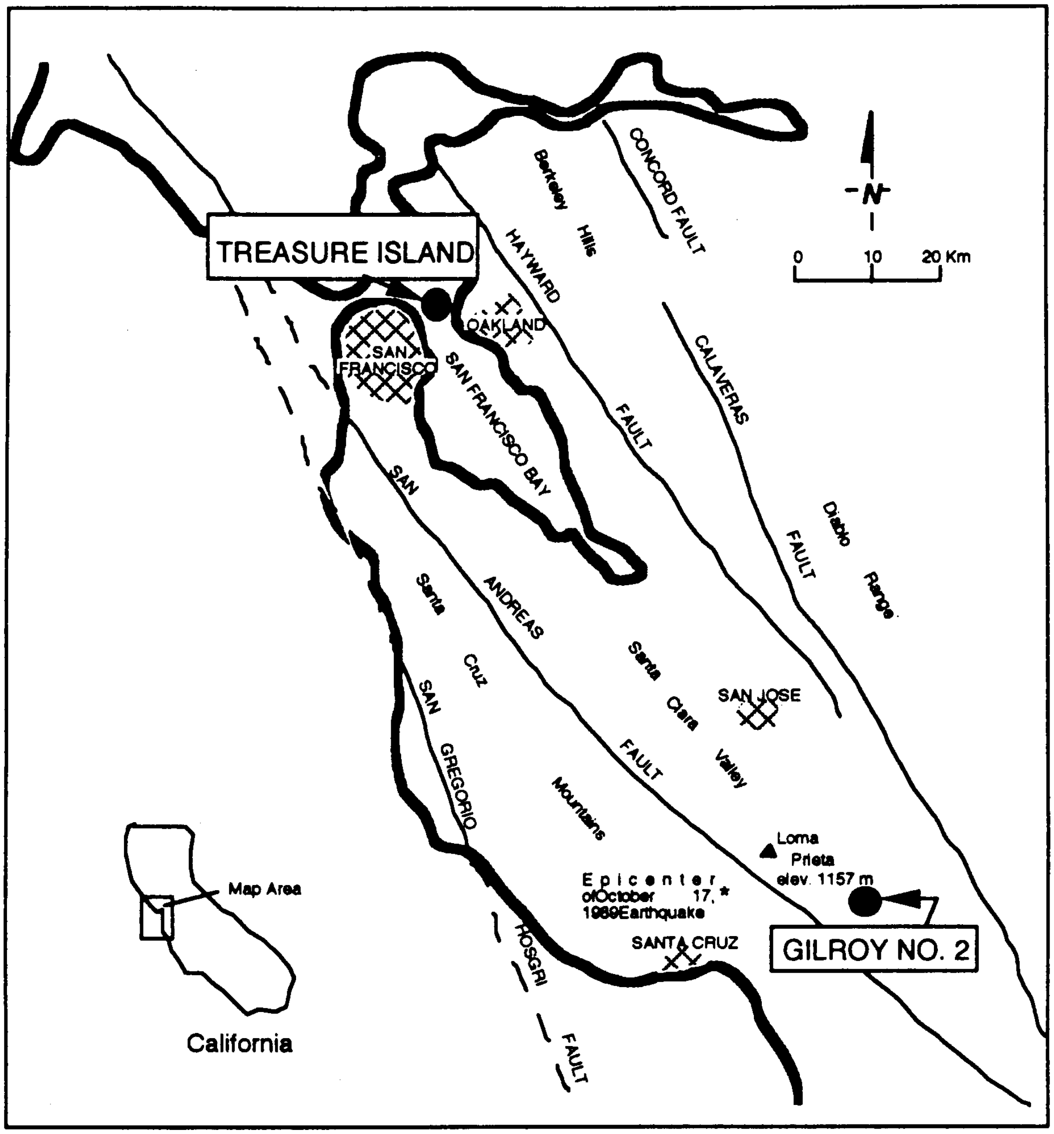

Figure 3.2 Map of the San Francisco Bay Area locating the Gilroy 2 site (EPRI 1993).

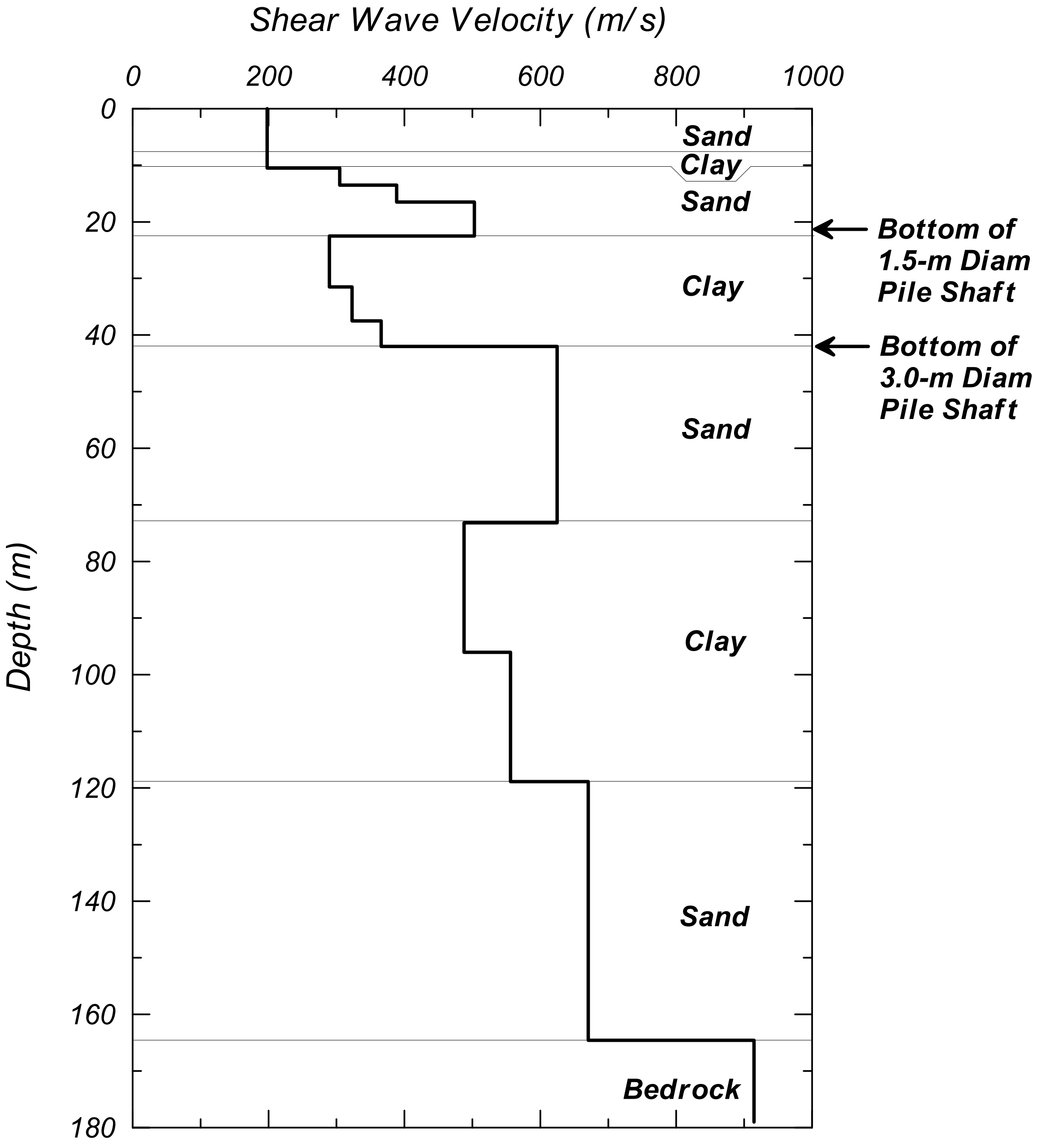

Figure 3.3 Shear wave velocity profile for baseline site (Courtesy of Curras 2000).

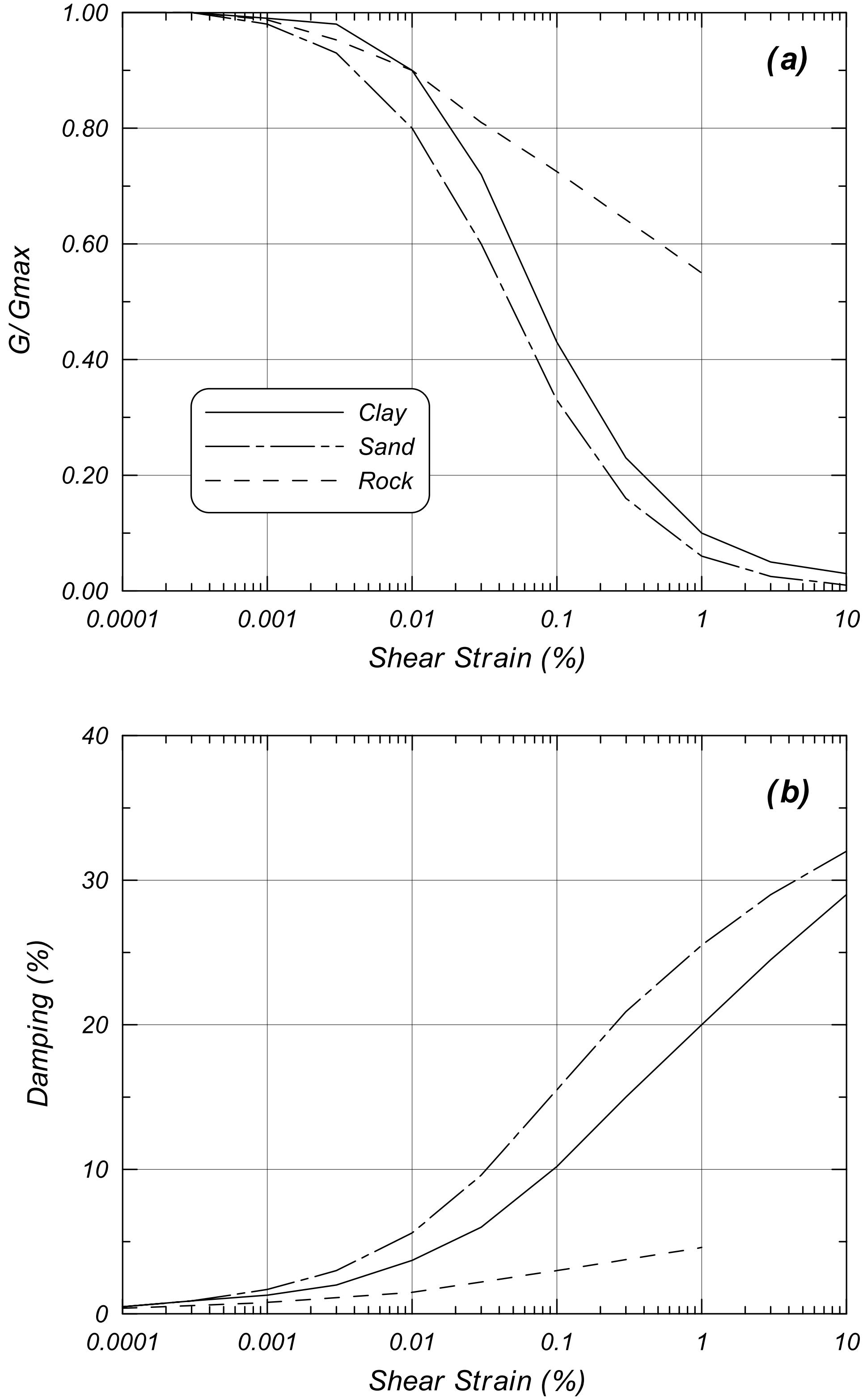

Figure 3.4 (a) Shear modulus and (b) damping curves used for the SHAKE analysis of the Gilroy 2 site (Courtesy of Curras 2000).

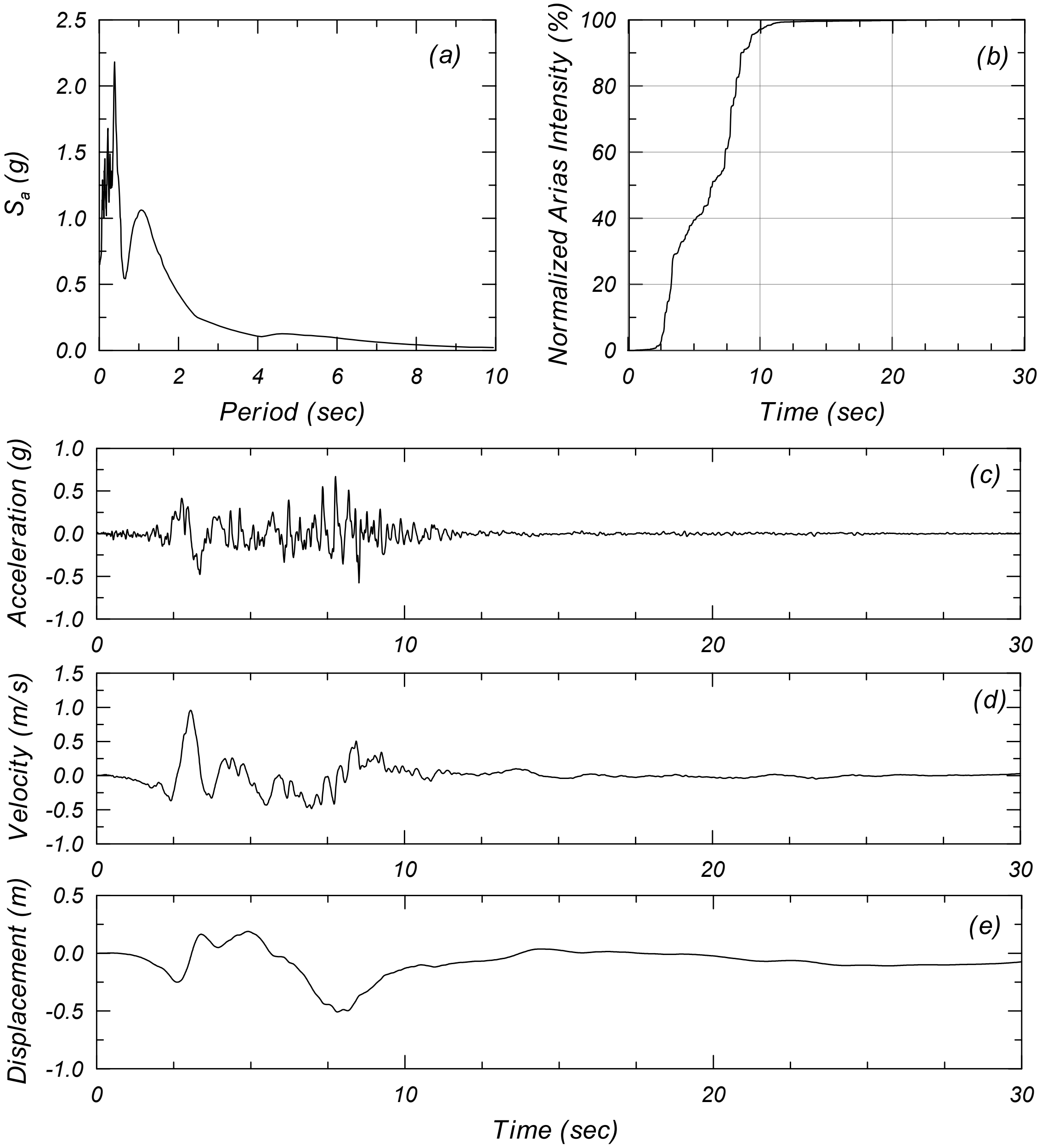

Figure 3.5 Summary of San Fernando, Pacoima Dam ground motion (motion used as rock outcrop): (a) elastic 5% damped response spectra, (b) normalized Arias intensity, (c) acceleration time history, (d) velocity time history, and (e) displacement time history.

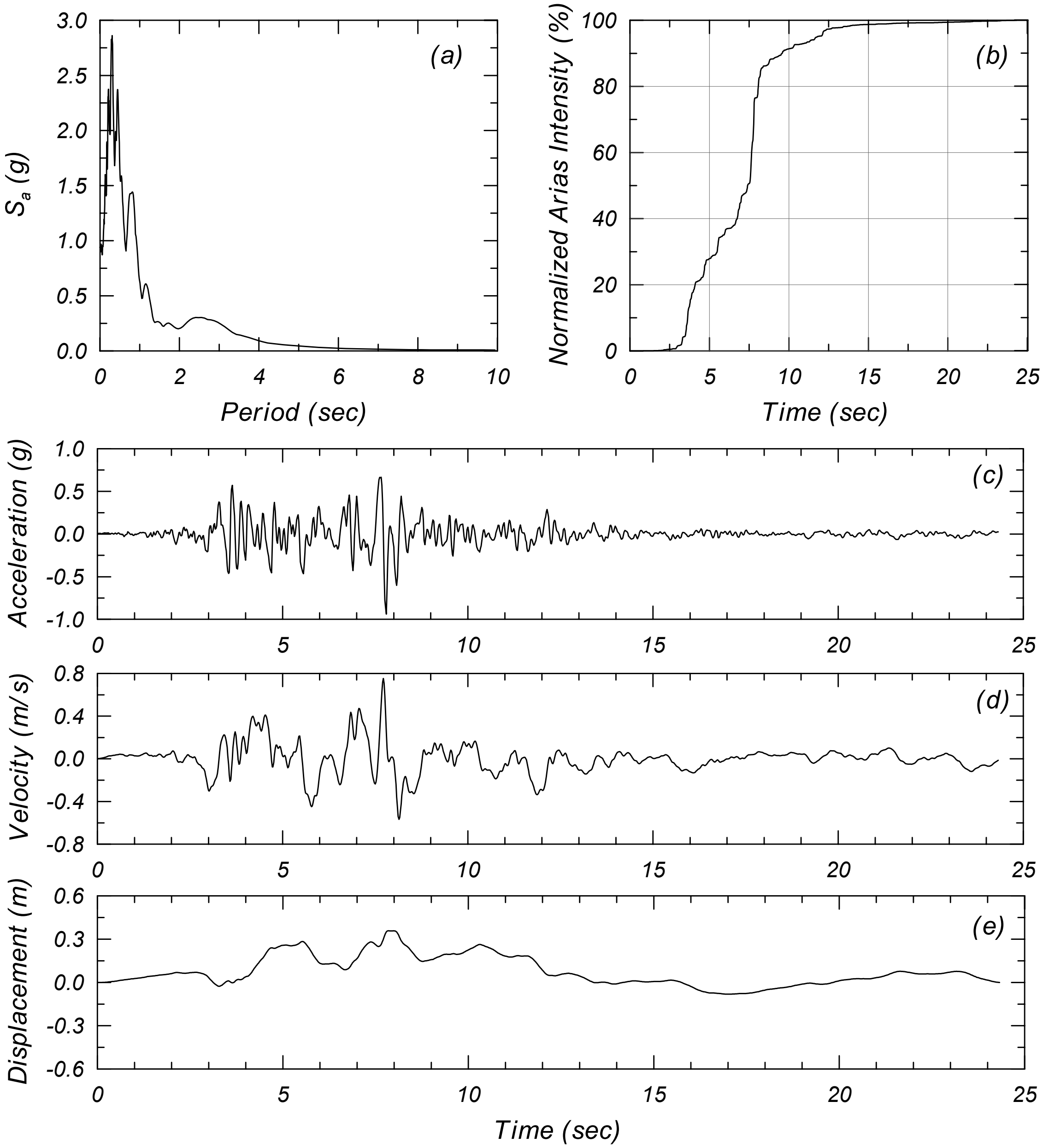

Figure 3.6 Summary of Northridge, VA Hospital ground motion (motion used as rock outcrop): (a) elastic 5% damped response spectra, (b) normalized Arias intensity, (c) acceleration time history, (d) velocity time history, and (e) displacement time history.

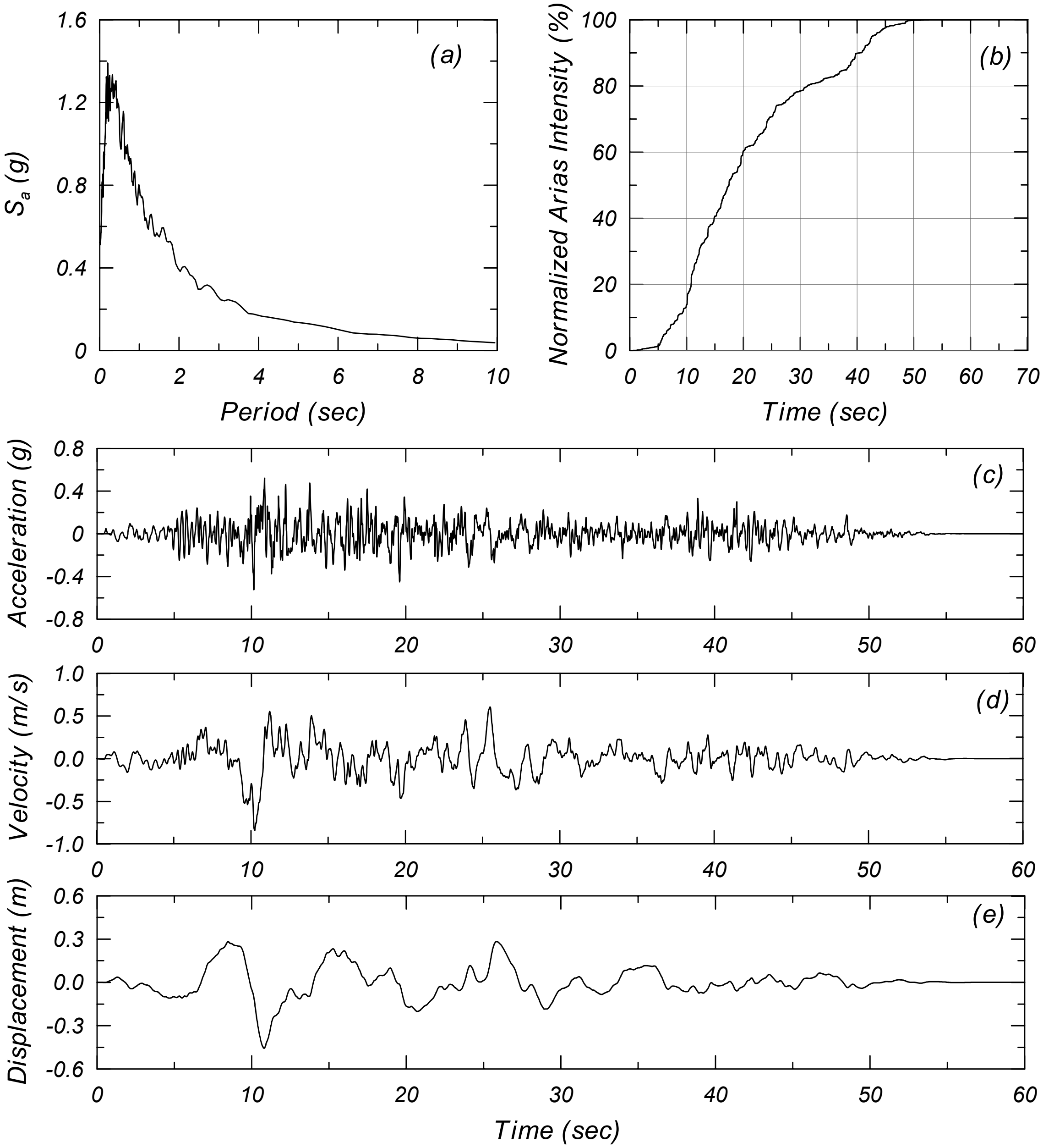

Figure 3.7 Summary of Synthetic #2 (Bay Bridge) ground motion (motion used as rock outcrop): (a) elastic 5% damped response spectra, (b) normalized Arias intensity, (c) acceleration time history, (d) velocity time history, and (e) displacement time history.

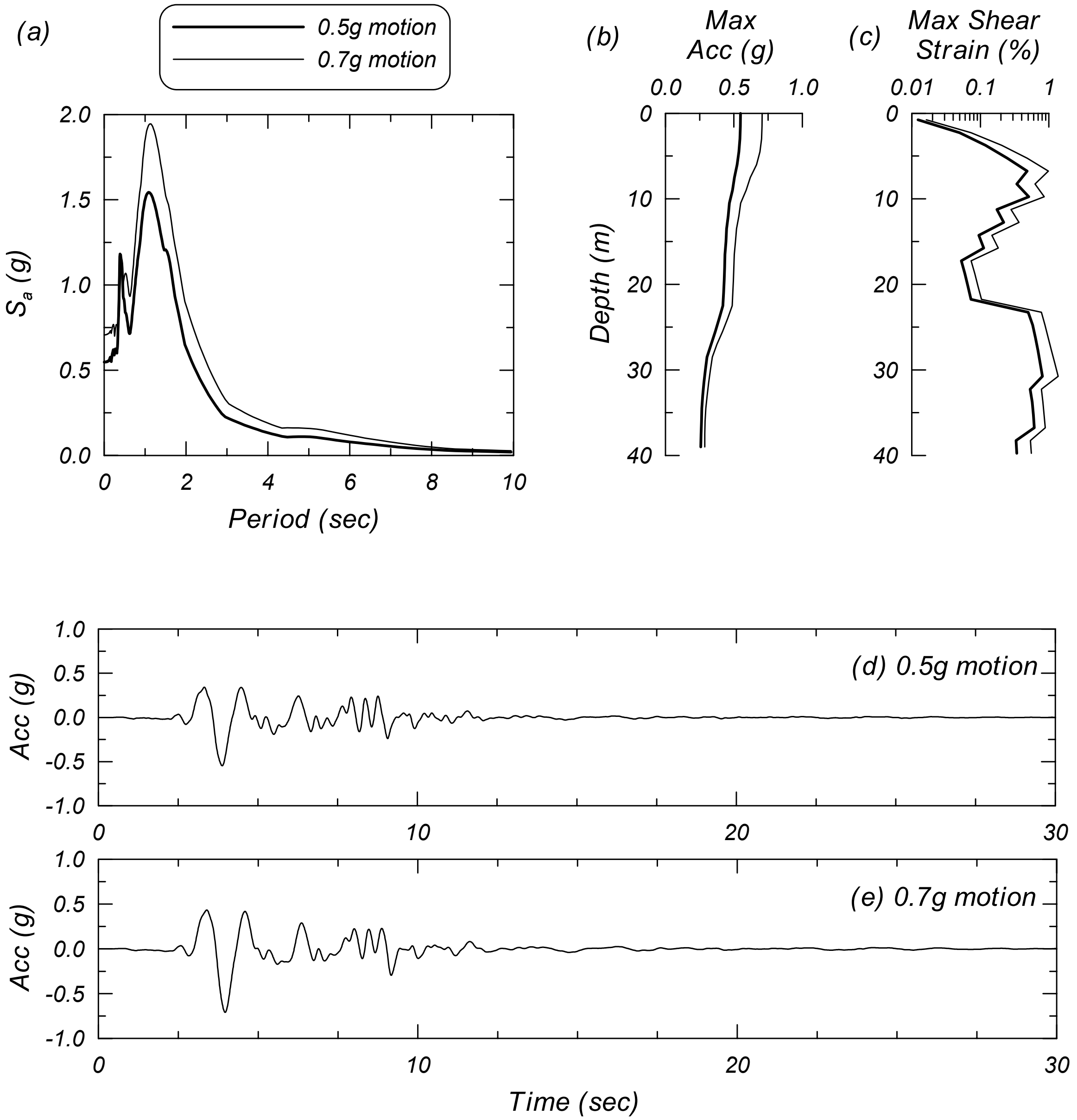

Figure 3.8 Site response for San Fernando, Pacoima Dam motion: (a) elastic acceleration response spectra (5% damping) at the ground surface, (b) maximum acceleration vs. depth, (c) maximum shear strain vs. depth, (d) surface acceleration history for 0.5g outcrop motion, and (e) surface acceleration history for 0.7g outcrop motion.

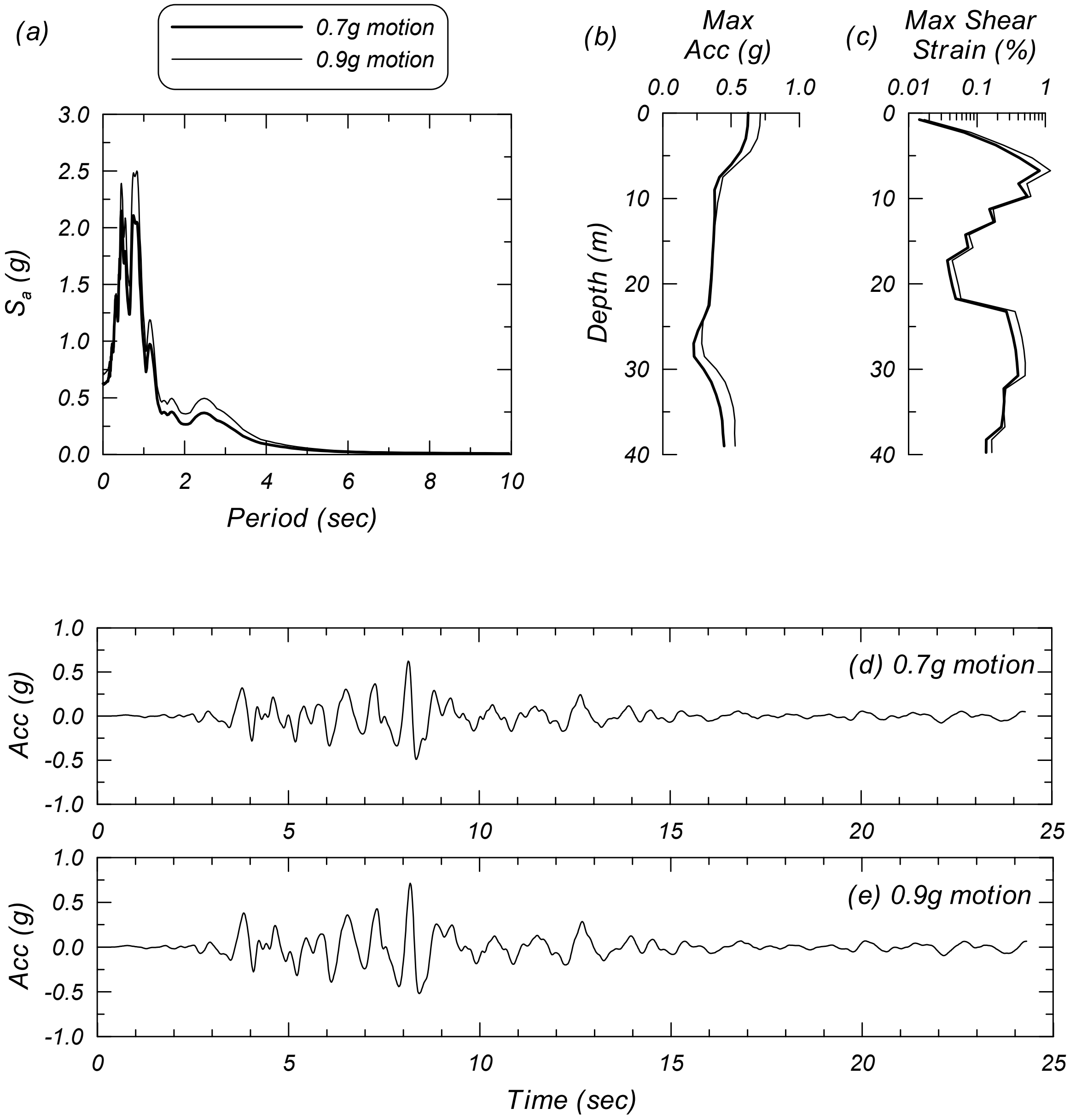

Figure 3.9 Site response for the Northridge, VA Hospital motion: (a) elastic acceleration response spectra (5% damping) at the ground surface, (b) maximum acceleration vs. depth, (c) maximum shear strain vs. depth, (d) surface acceleration history for 0.7g outcrop motion, and (e) surface acceleration history for 0.9g outcrop motion.

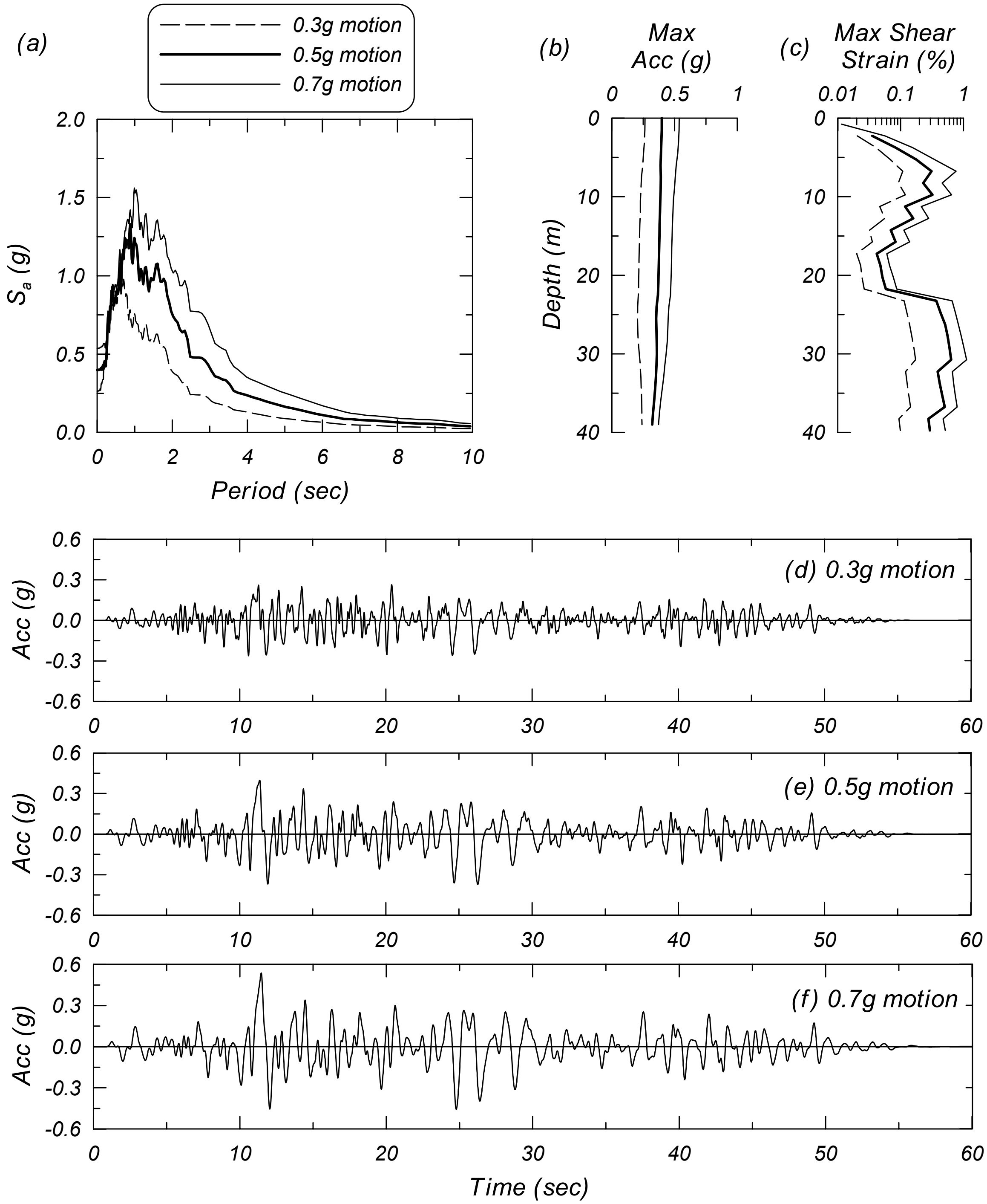

Figure 3.10 Site response for the Synthetic #2 (Bay Bridge) motion: (a) elastic acceleration response spectra (5% damping) at the ground surface, (b) maximum acceleration vs. depth, (c) maximum shear strain vs. depth, (d) surface acceleration history for 0.3g outcrop motion, (e) surface acceleration history for 0.5g outcrop motion, and (f) surface acceleration history for 0.7g outcrop motion.

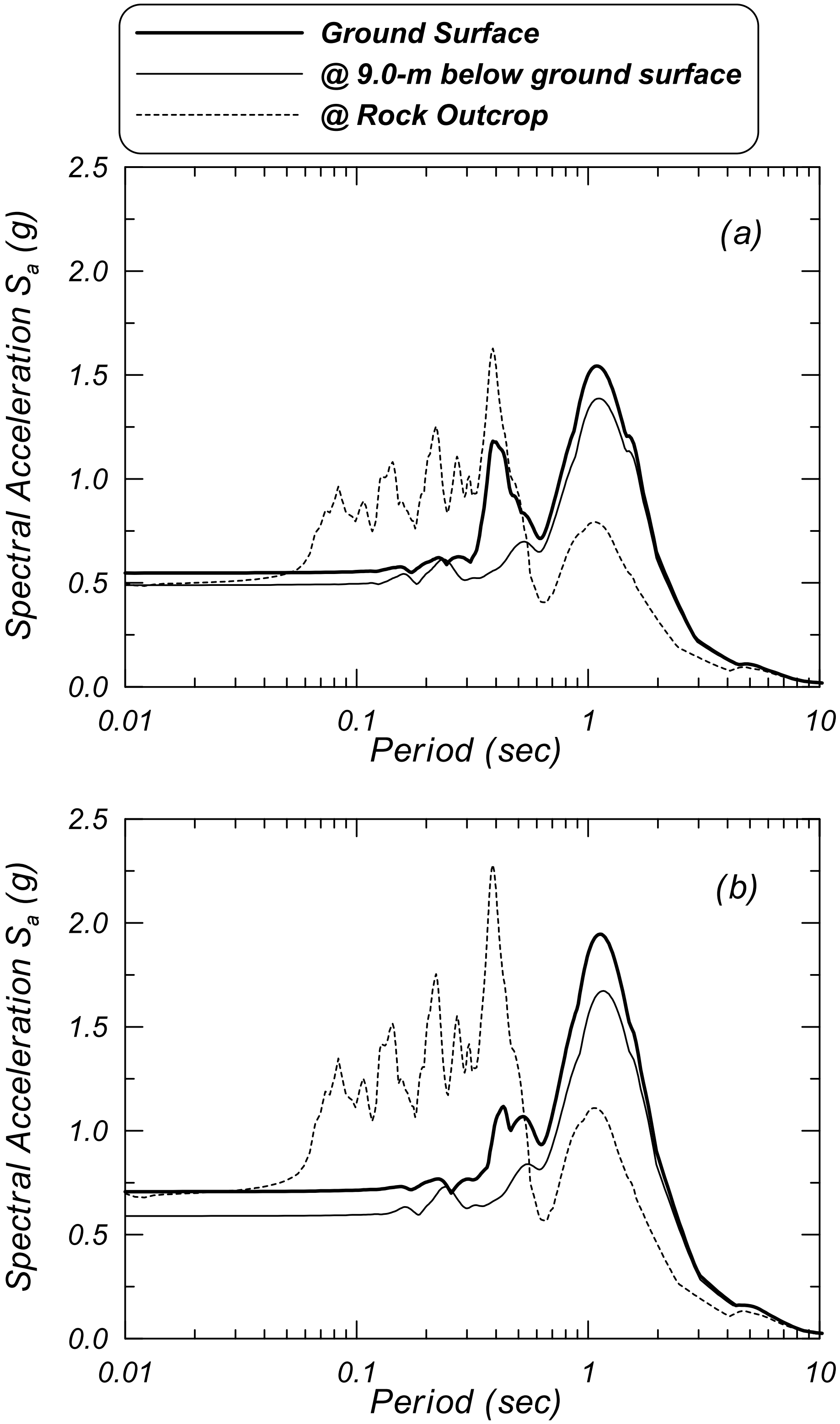

Figure 3.11 Variation in elastic (5% damped) acceleration response spectra for the San Fernando, Pacoima Dam motion, SHAKE analyses of the (a) 0.5g outcrop motion and (b) 0.7g outcrop motion.

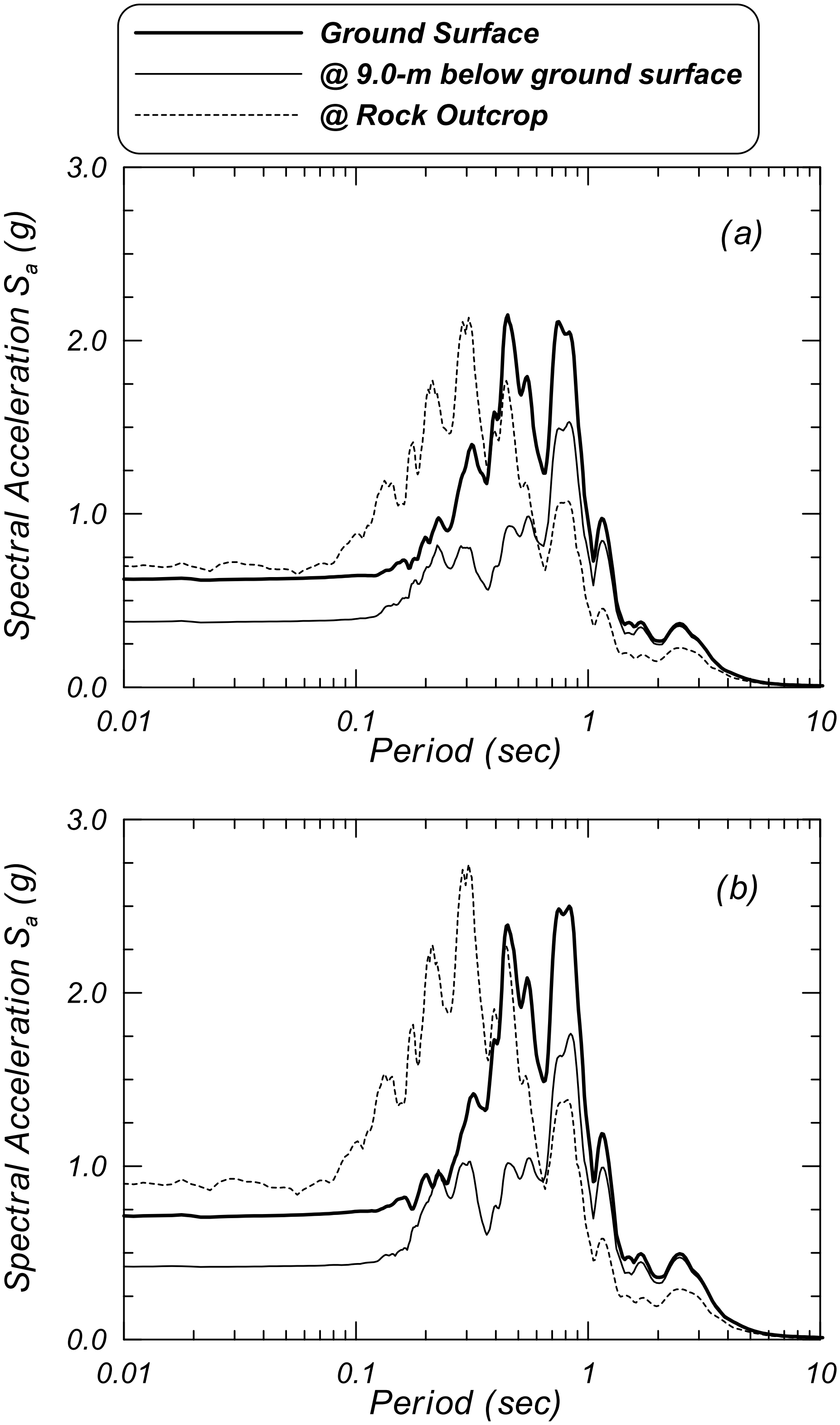

Figure 3.12 Variation in elastic (5% damped) acceleration response spectra for the Northridge, VA Hospital motion, SHAKE analyses of the (a) 0.7g outcrop motion and (b) 0.9g outcrop motion.

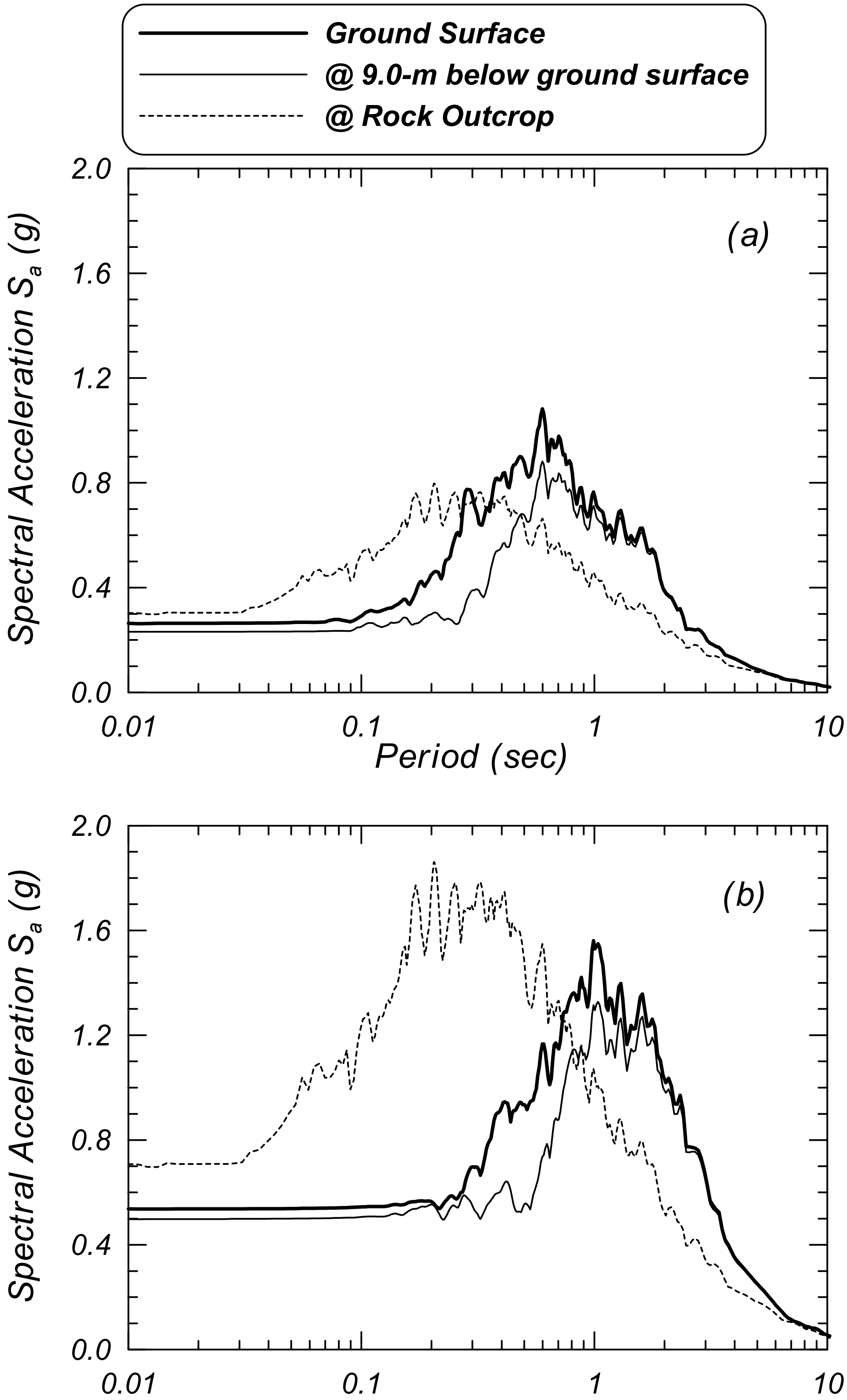

Figure 3.13 Variation in elastic (5% damped) acceleration response spectra for the Synthetic #2 (Bay Bridge) motion, SHAKE analyses of the (a) 0.3g outcrop motion and (b) 0.7g outcrop motion.

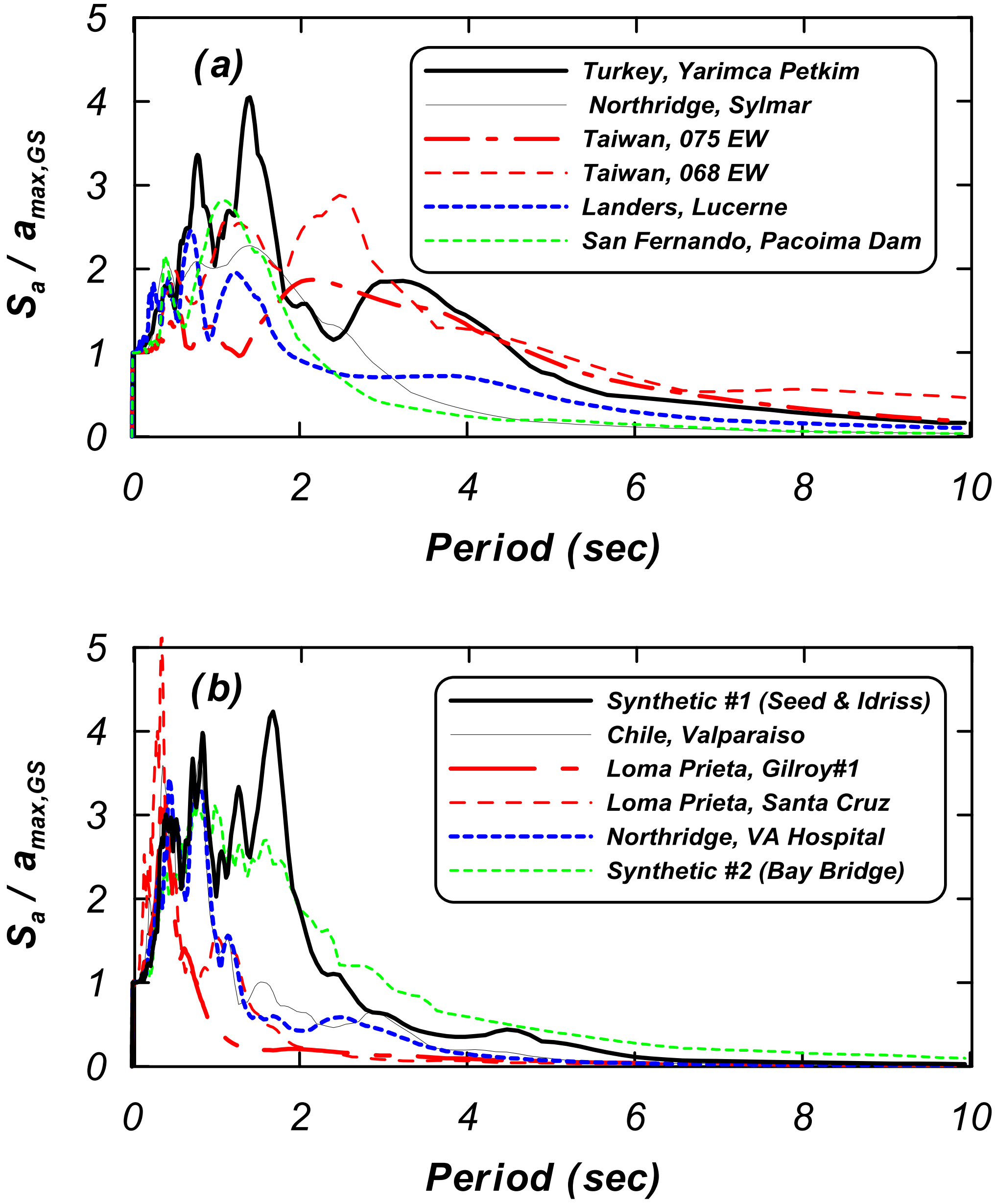

Figure 3.14 Elastic acceleration response spectra (5% damping) normalized by the peak ground surface acceleration for (a) near-fault motions and (b) other motions used in this study.

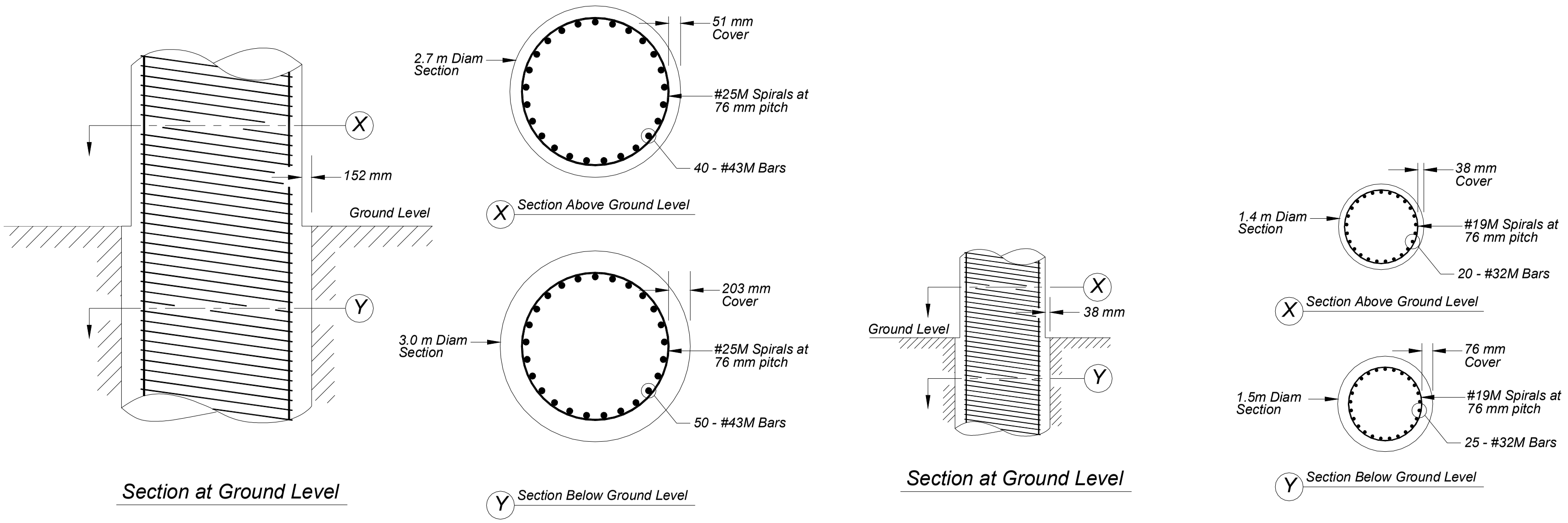

a) 3.0-meter Pile Shaft Section at Ground Level

b) 1.5-meter Pile Shaft Section at Ground Level

Figure 3.15 Details of the pile shaft and column extension for the (a) 3.0 meter diameter pile shaft and (b) 1.5 meter diameter pile shaft.

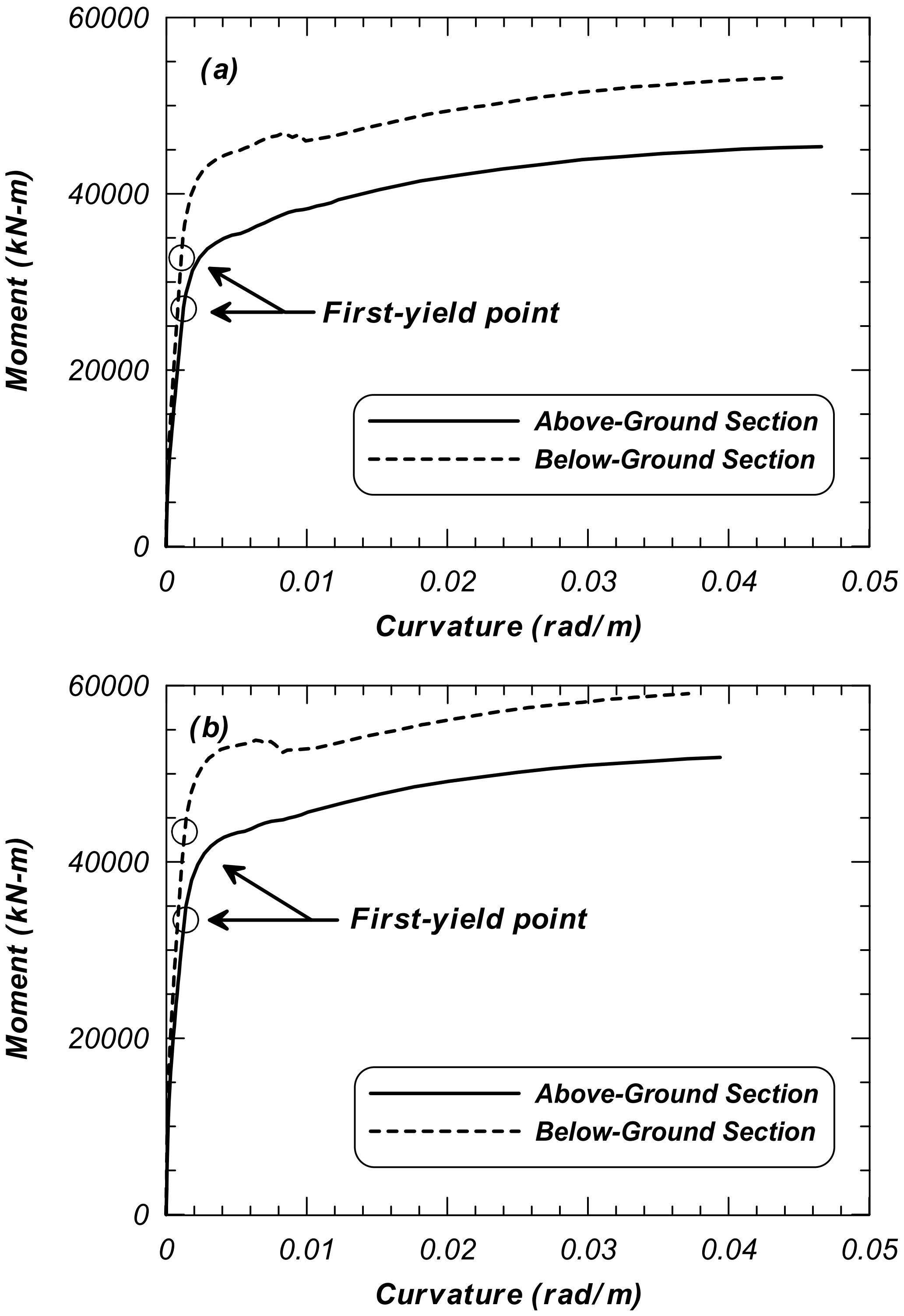

Figure 3.16 Moment-curvature simulations of the above- and below-ground sections of the 3.0 m diameter pile shaft with axial loads of (a) $0.05f'_cA_g$ and (b) $0.10f'_cA_g$.

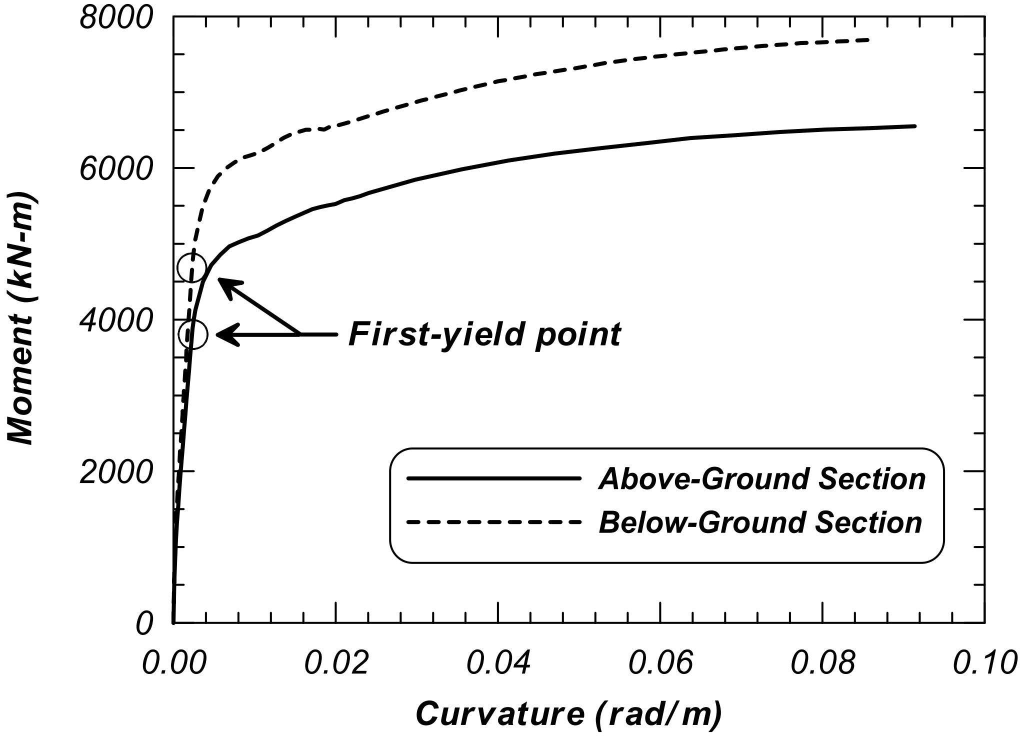

Figure 3.17 Moment-curvature simulations of the above- and below-ground sections of the 1.5 m diameter pile shaft with an axial load of $0.05f'_cA_g$.

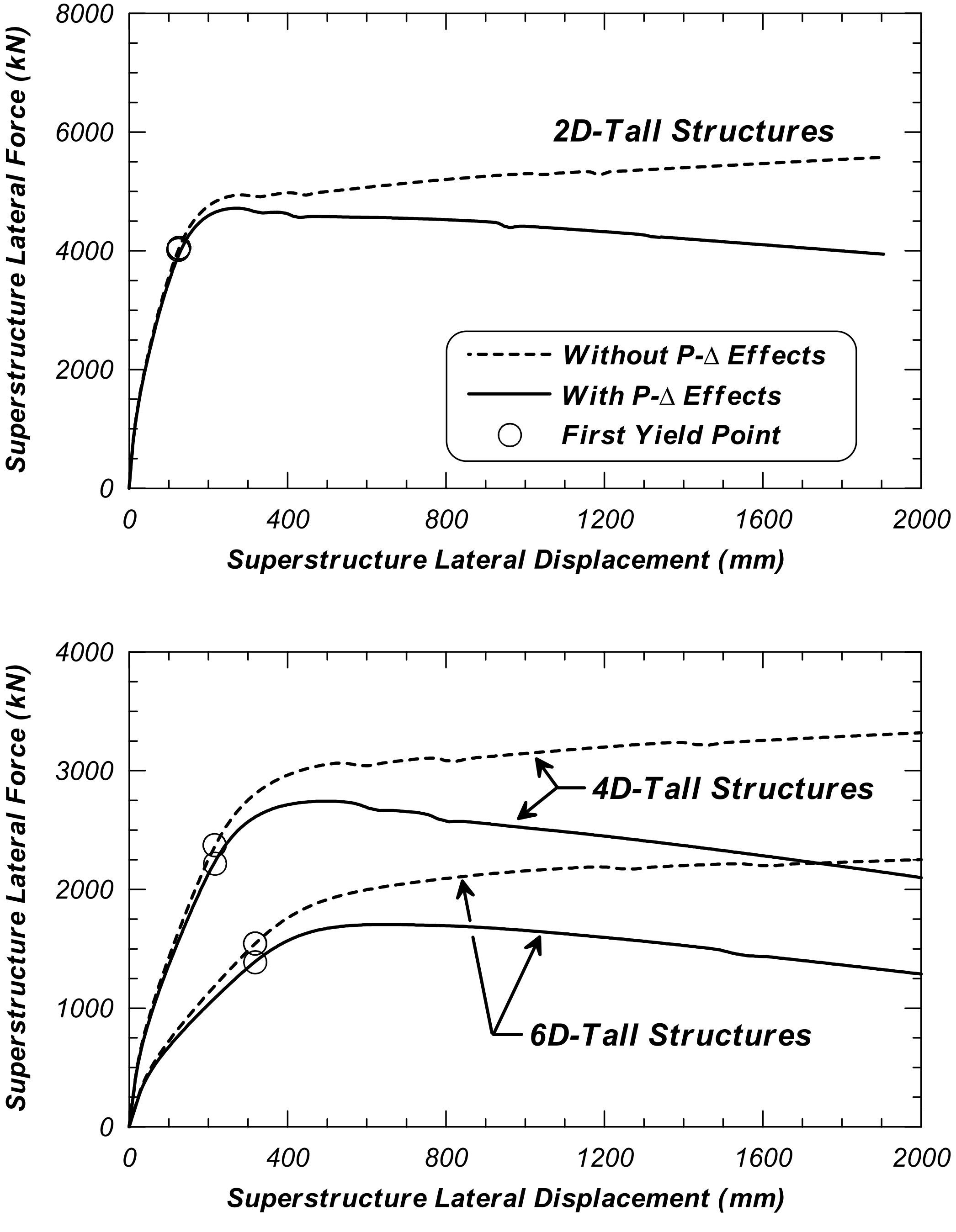

Figure 3.18 Nonlinear pushover analysis of the 3.0 m diameter pile shaft structure with an axial load of $0.05f'_cA_g$.

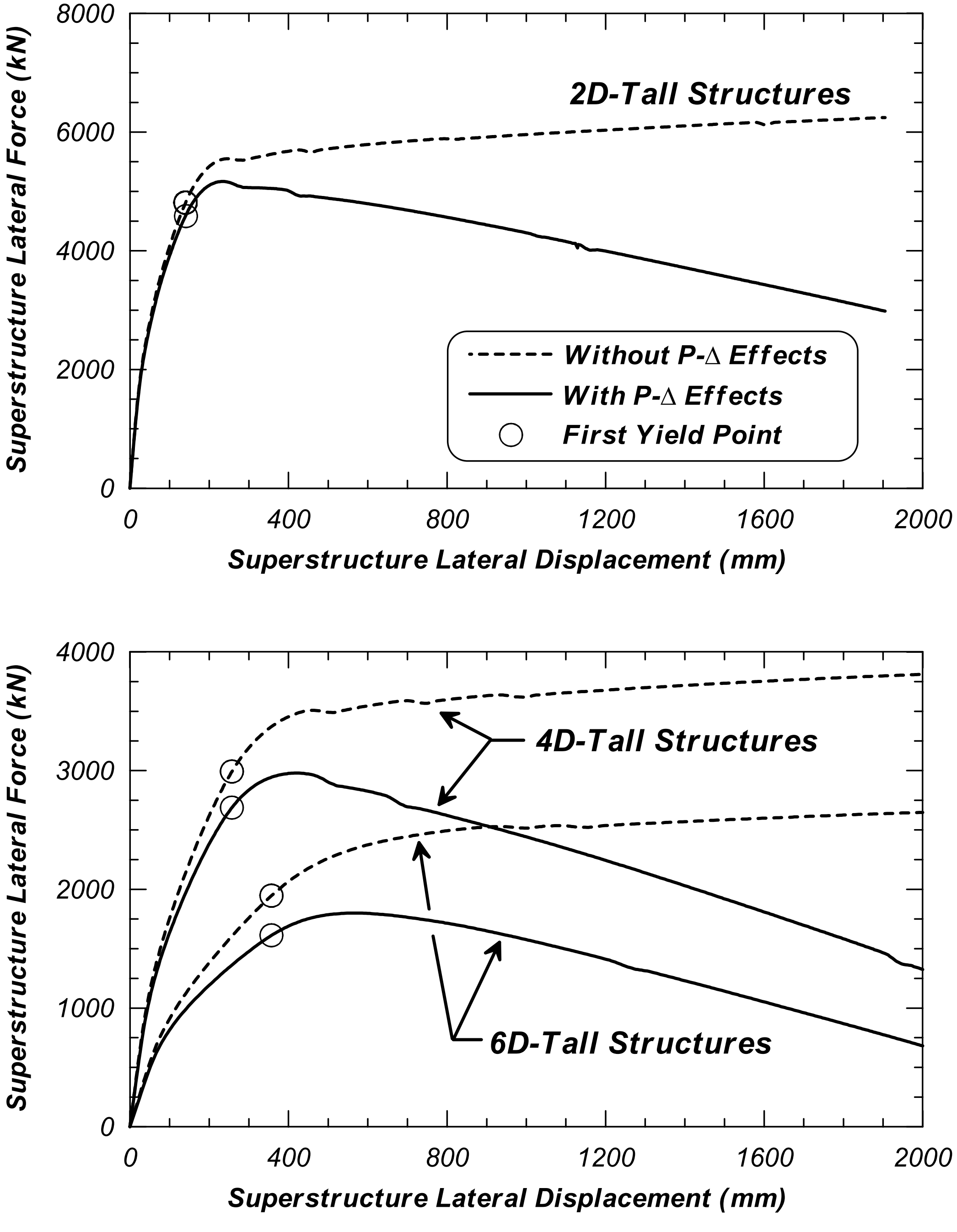

Figure 3.19 Nonlinear pushover analysis of the 3.0 m diameter pile shaft structure with an axial load of $0.10f'_cA_g$.

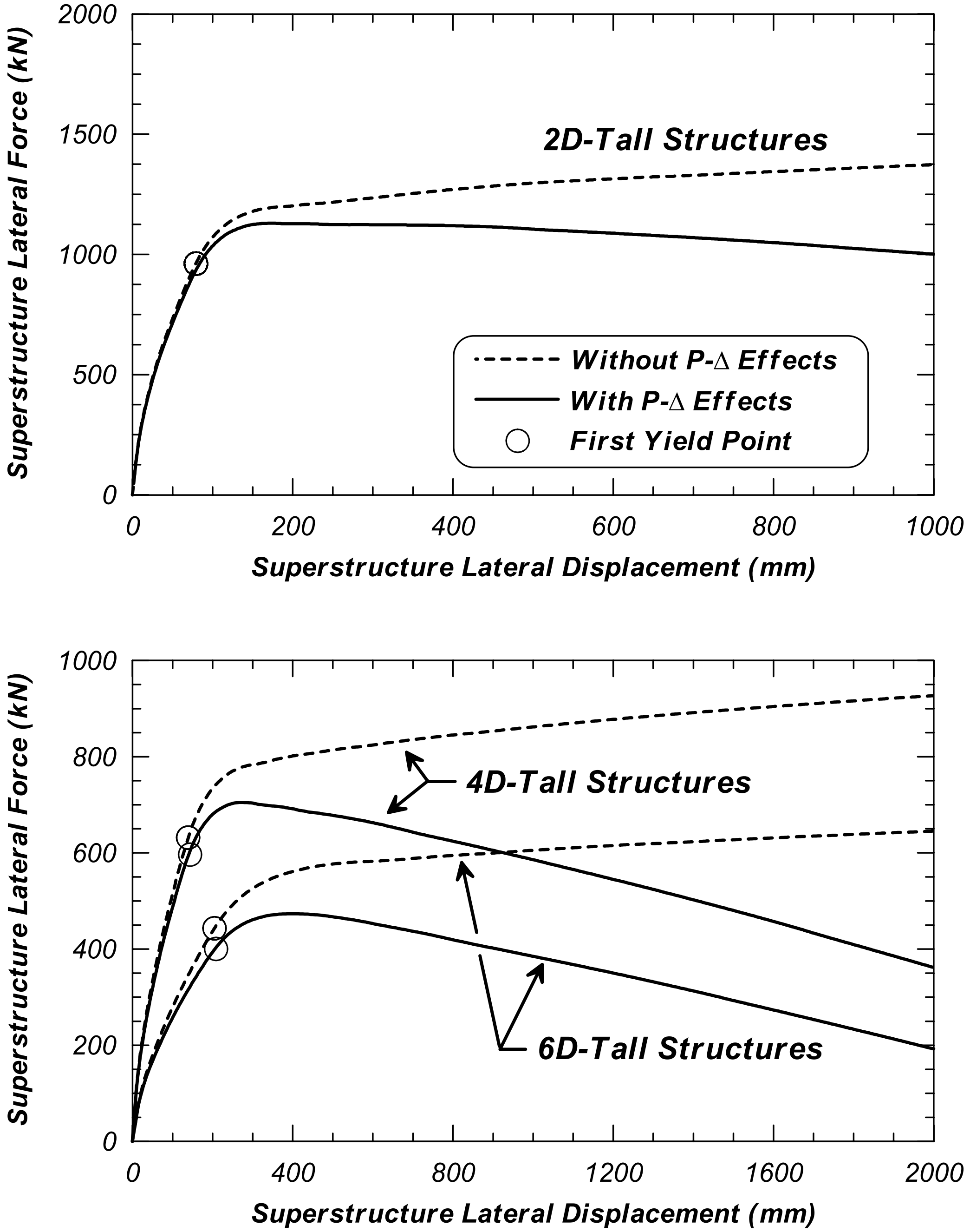

Figure 3.20 Nonlinear pushover analysis of the 1.5 m diameter pile shaft structure with an axial load of $0.05f'_cA_g$.

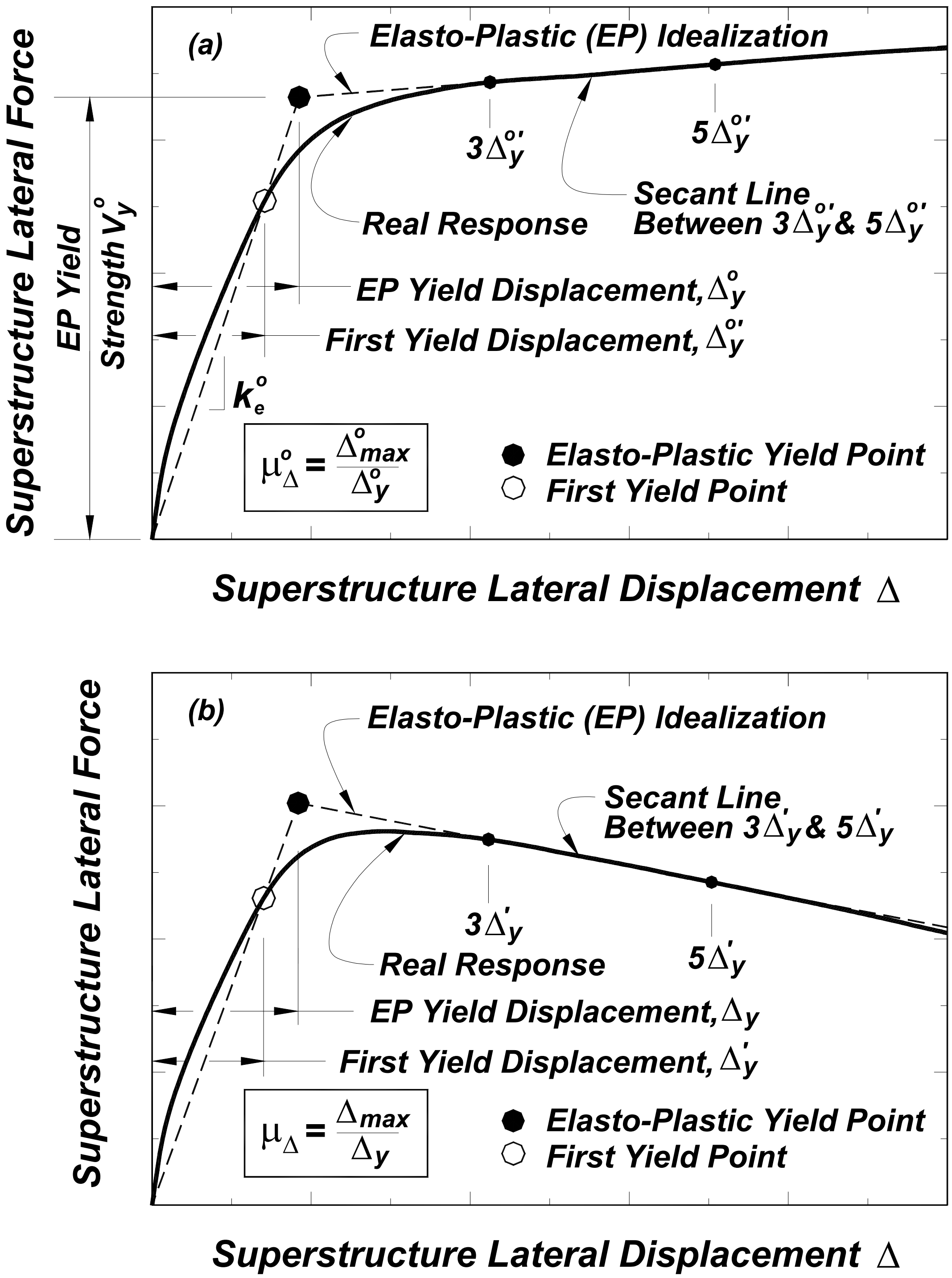

Figure 3.21 Nonlinear pushover analyses idealized into elasto-plastic (EP) response for soil-pile systems: (a) without P-Δ effects and (b) with P-Δ effects.

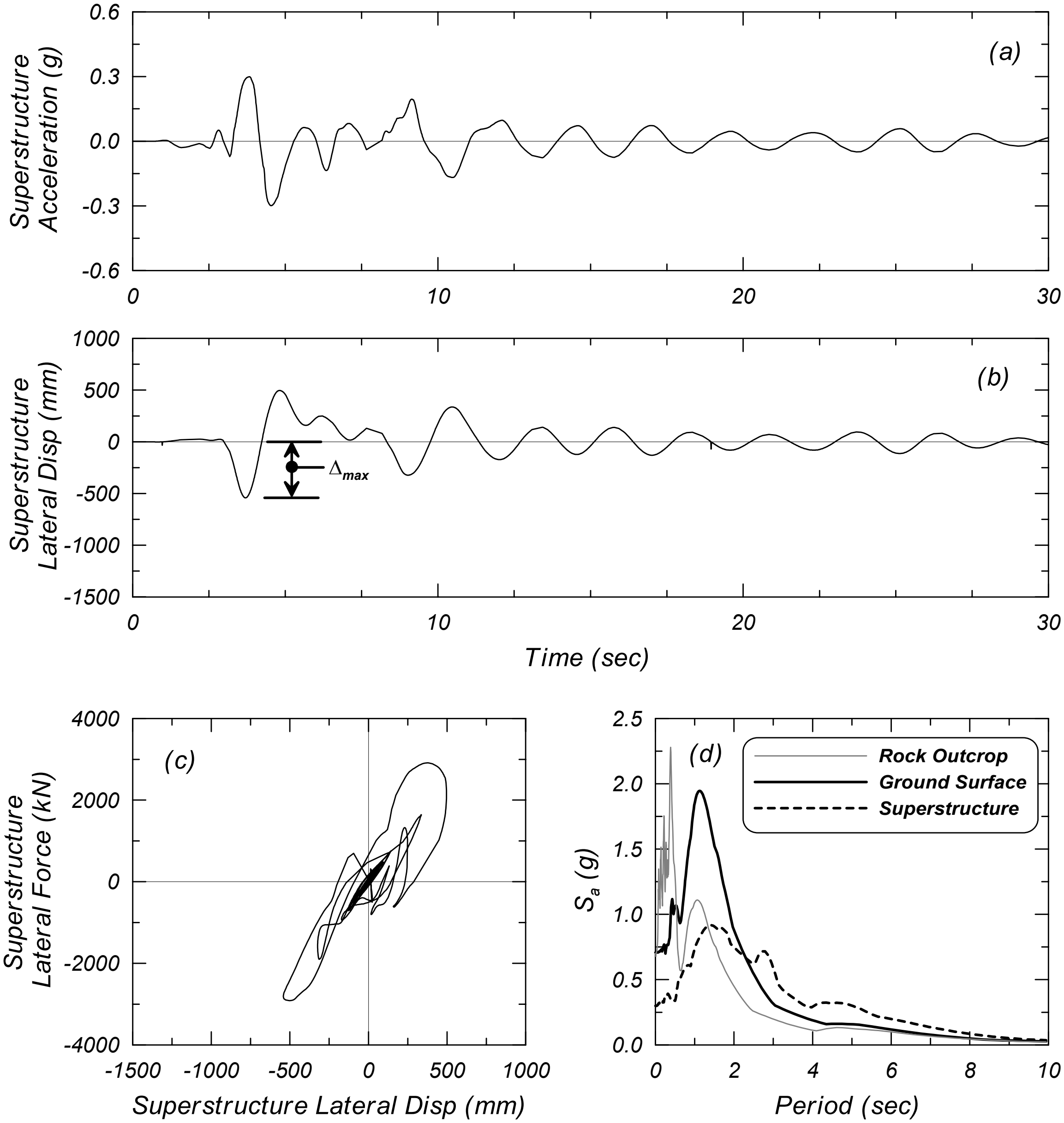

Figure 3.22 Dynamic response of a bridge structure supported on a 3.0 m diameter pile shaft with an above-ground height of 4D and $0.05f'cA_g$ axial load subjected to the San Fernando, Pacoima Dam outcrop motion with $a_{max} = 0.7g$: (a) superstructure acceleration, (b) superstructure lateral displacement, (c) superstructure lateral force-displacement, and (d) elastic 5% damped acceleration response spectra.

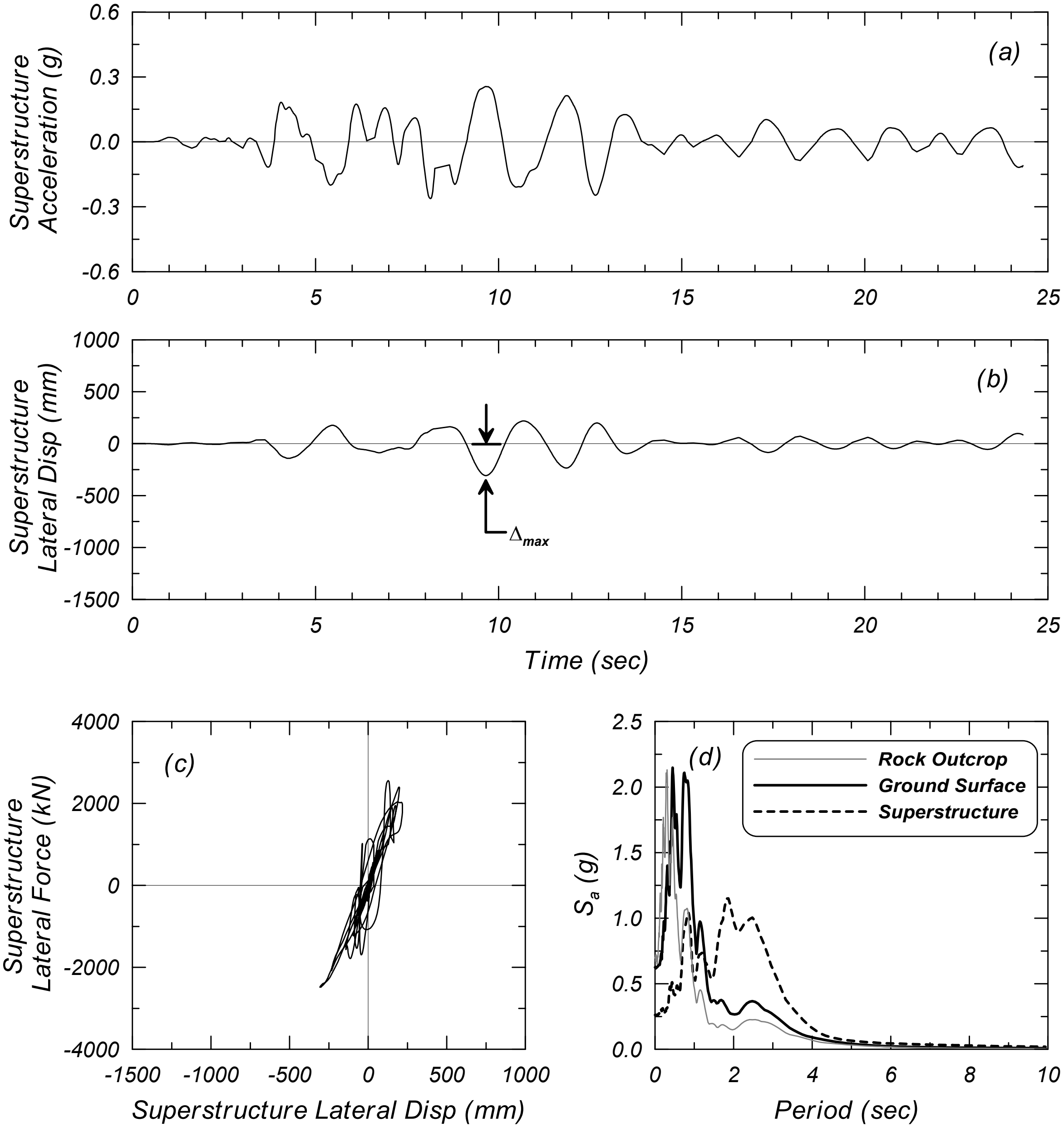

Figure 3.23 Dynamic response of a bridge structure supported on a 3.0 m diameter pile shaft with an above-ground height of 4D and $0.05f'cA_g$ axial load subjected to the Northridge, VA Hospital outcrop motion with $a_{max} = 0.7g$: (a) superstructure acceleration, (b) superstructure lateral displacement, (c) superstructure lateral force-displacement, and (d) elastic 5% damped acceleration response spectra.

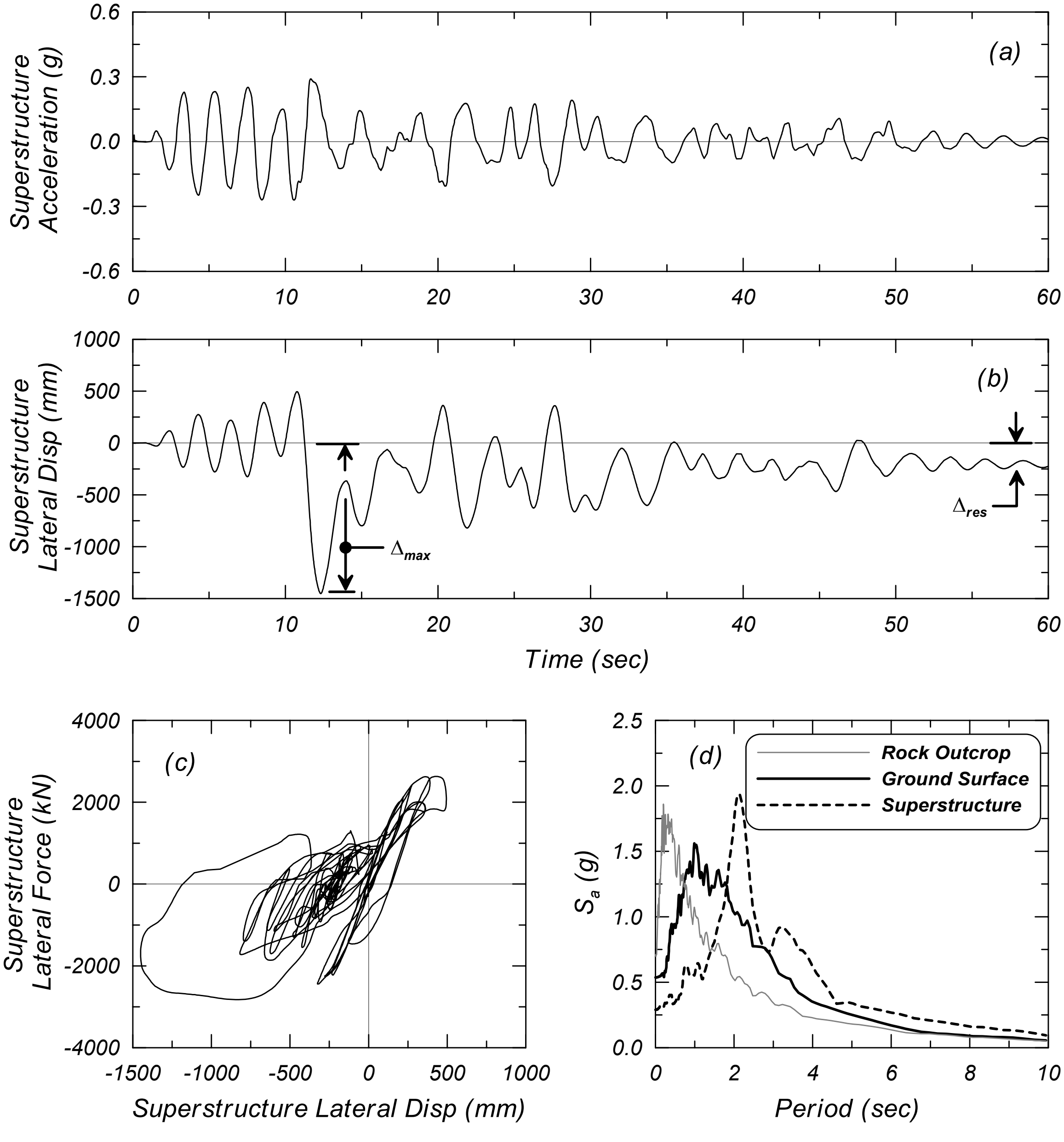

Figure 3.24 Dynamic response of a bridge structure supported on a 3.0 m diameter pile shaft with an above-ground height of 4D and $0.05f'_cA_g$ axial load subjected to the Synthetic #2 (Bay Bridge) outcrop motion with a_{max} = 0.7g: (a) superstructure acceleration, (b) superstructure lateral displacement, (c) superstructure lateral force-displacement, and (d) elastic 5% damped acceleration response spectra.

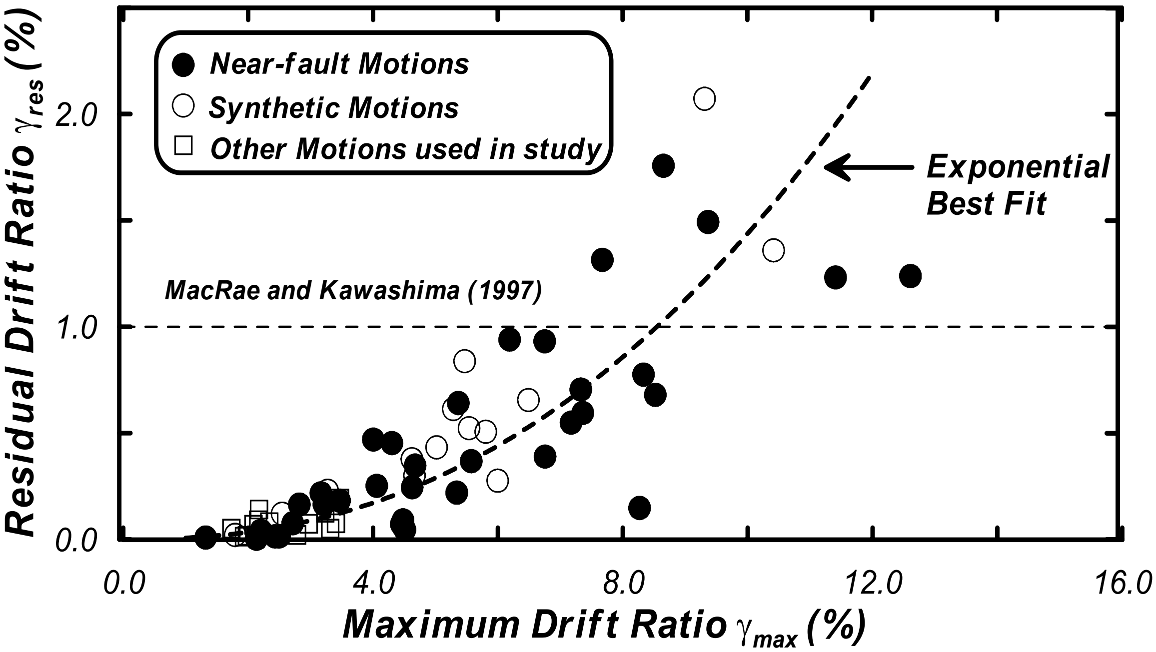

Figure 3.25 Residual drift ratio γ_{res} as a function of the maximum drift ratio γ_{max} in the superstructure (3.0 m diameter pile shafts with P-Δ effects).

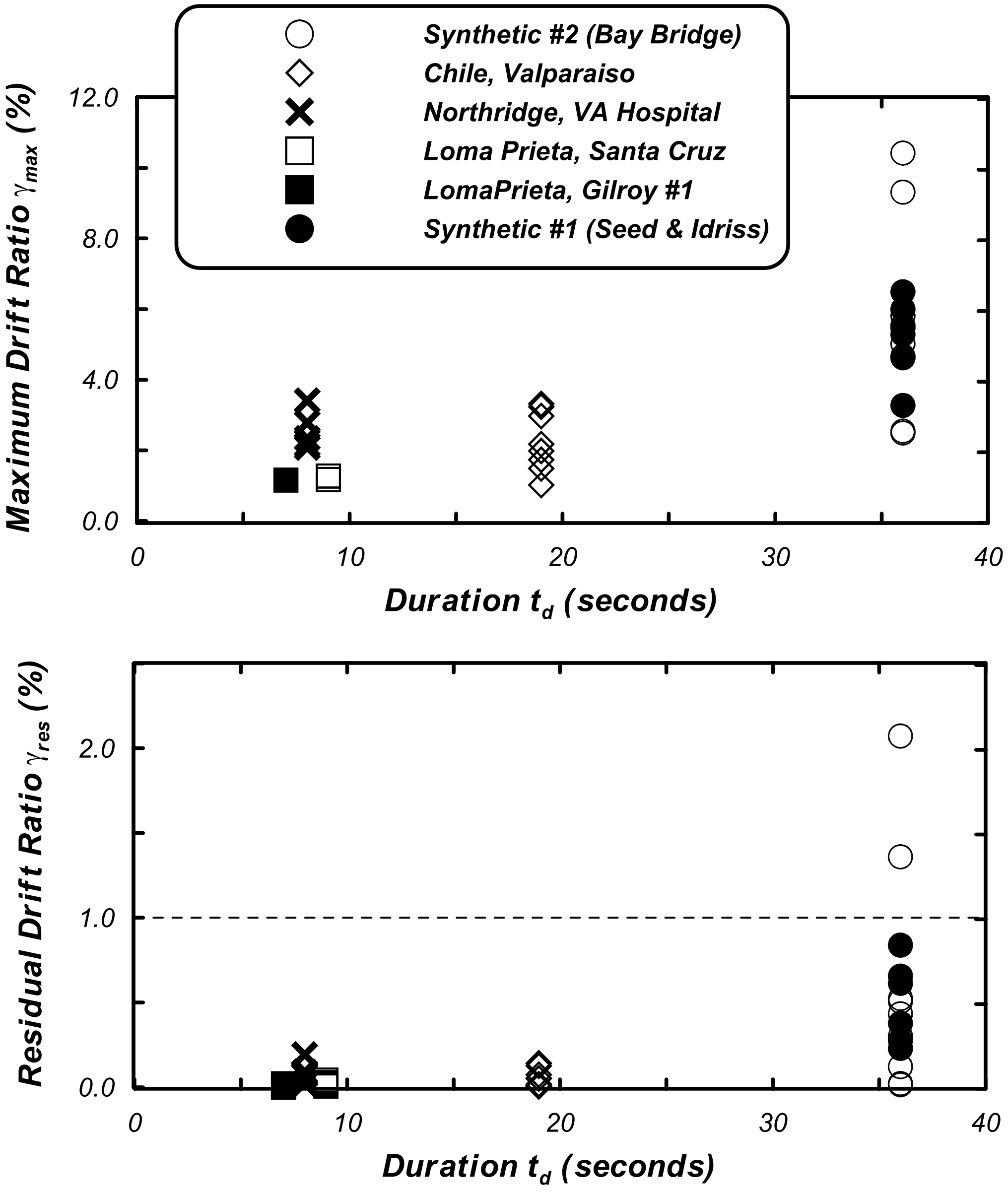

Figure 3.26 Maximum and residual drift ratios (γ_{max} and γ_{res}) as a function of ground motion duration t_d (3.0 m diameter pile shafts with P-Δ effects).

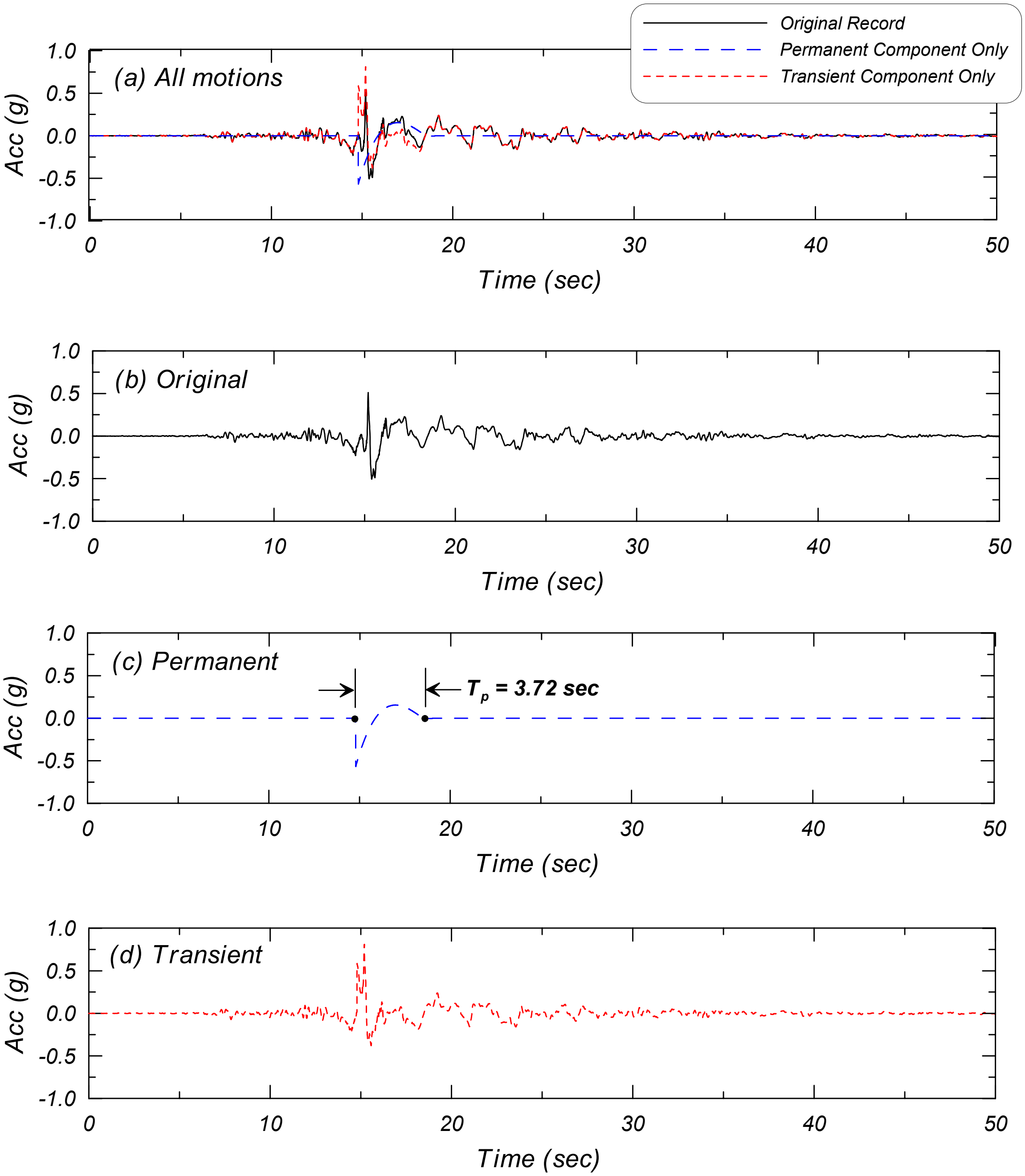

Figure 3.27 Summary of Taiwan 068E components acceleration time history: (a) overlay of original, transient, and permanent motions; (b) original motion; (c) permanent component only; and (d) transient component only.

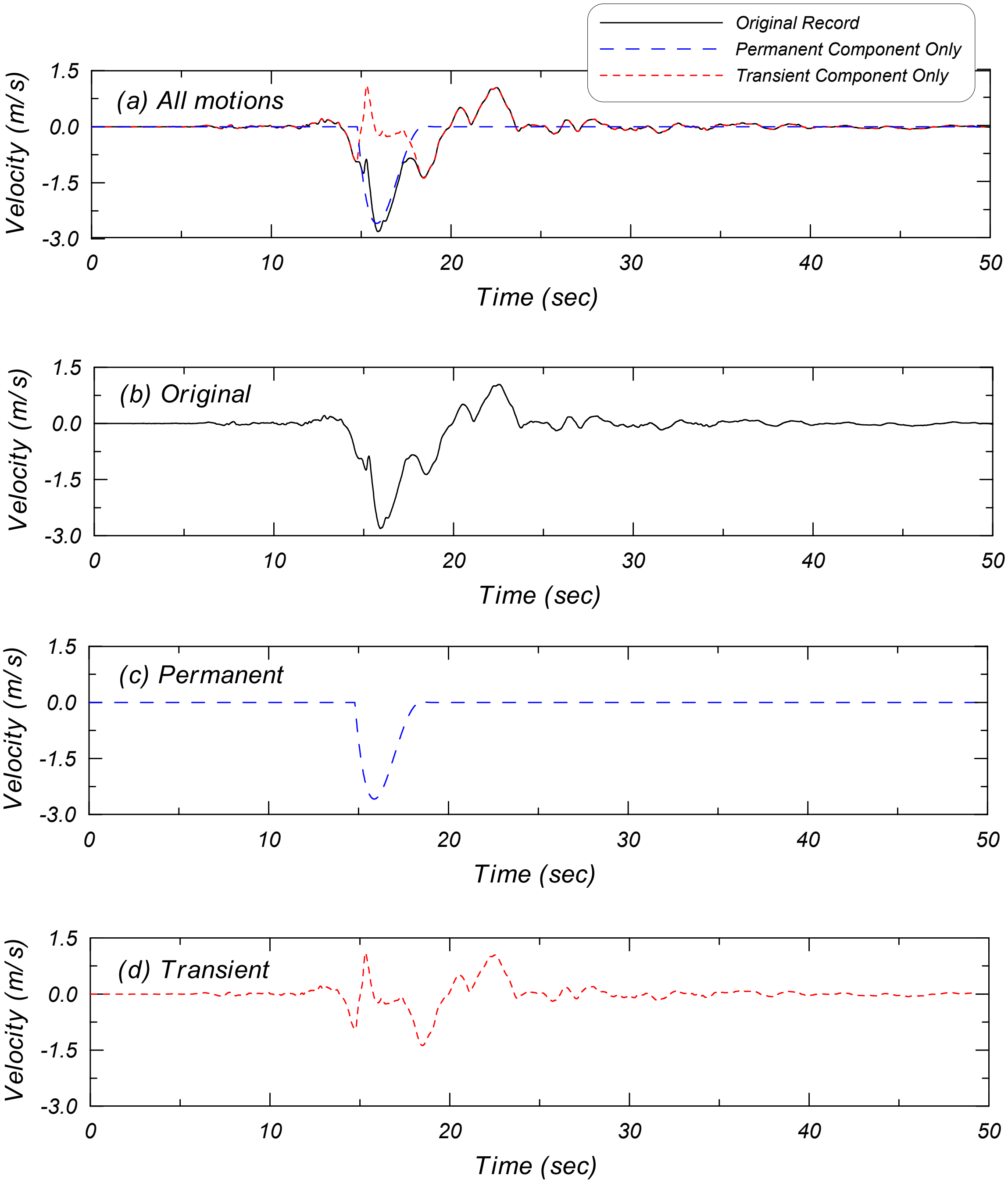

Figure 3.28 Summary of Taiwan 068E components velocity time history: (a) overlay of original, transient, and permanent motions; (b) original motion; (c) permanent component only; and (d) transient component only.

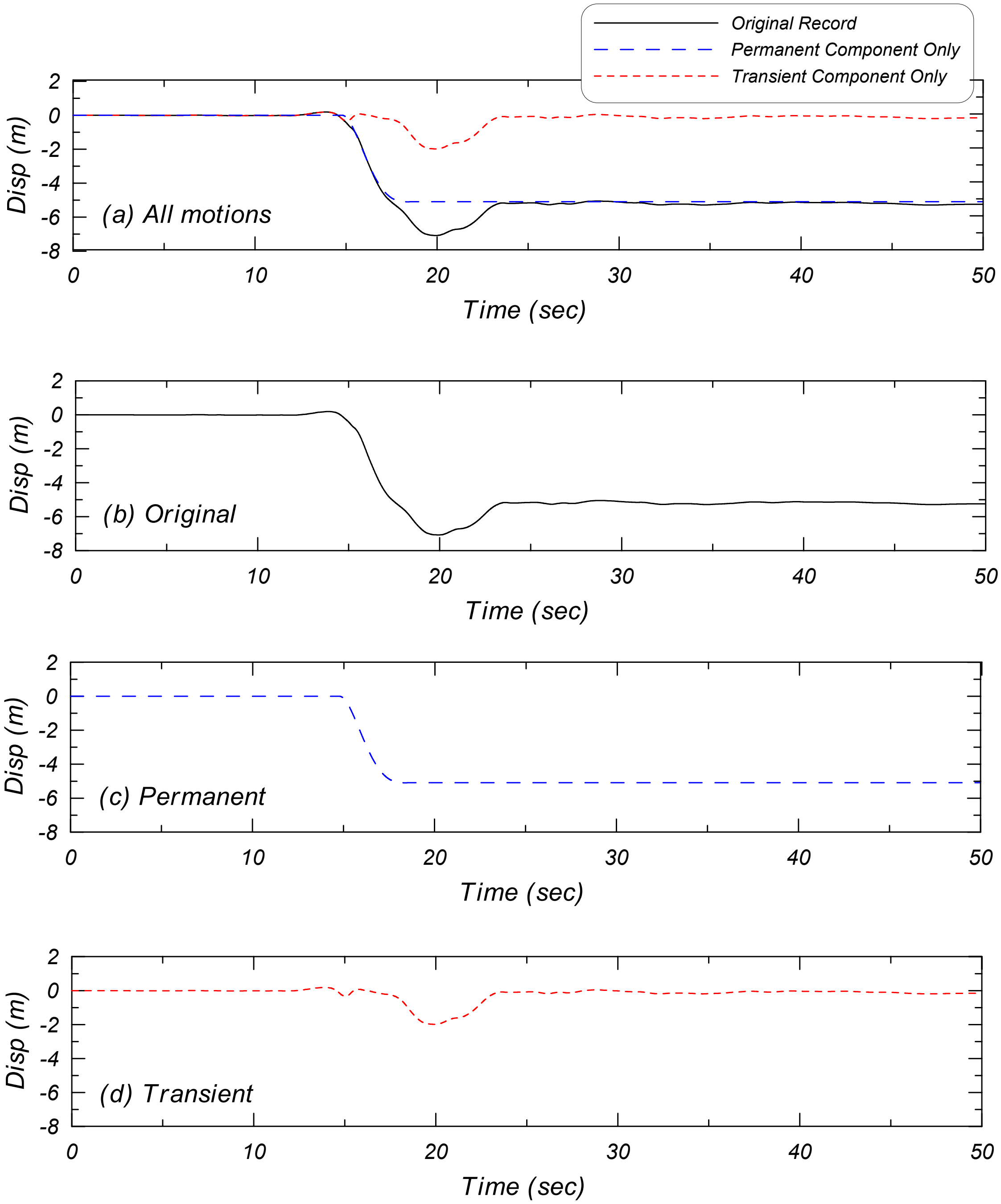

Figure 3.29 Summary of Taiwan 068E components displacement time history: (a) overlay of original, transient, and permanent motions; (b) original motion; (c) permanent component only; and (d) transient component only.

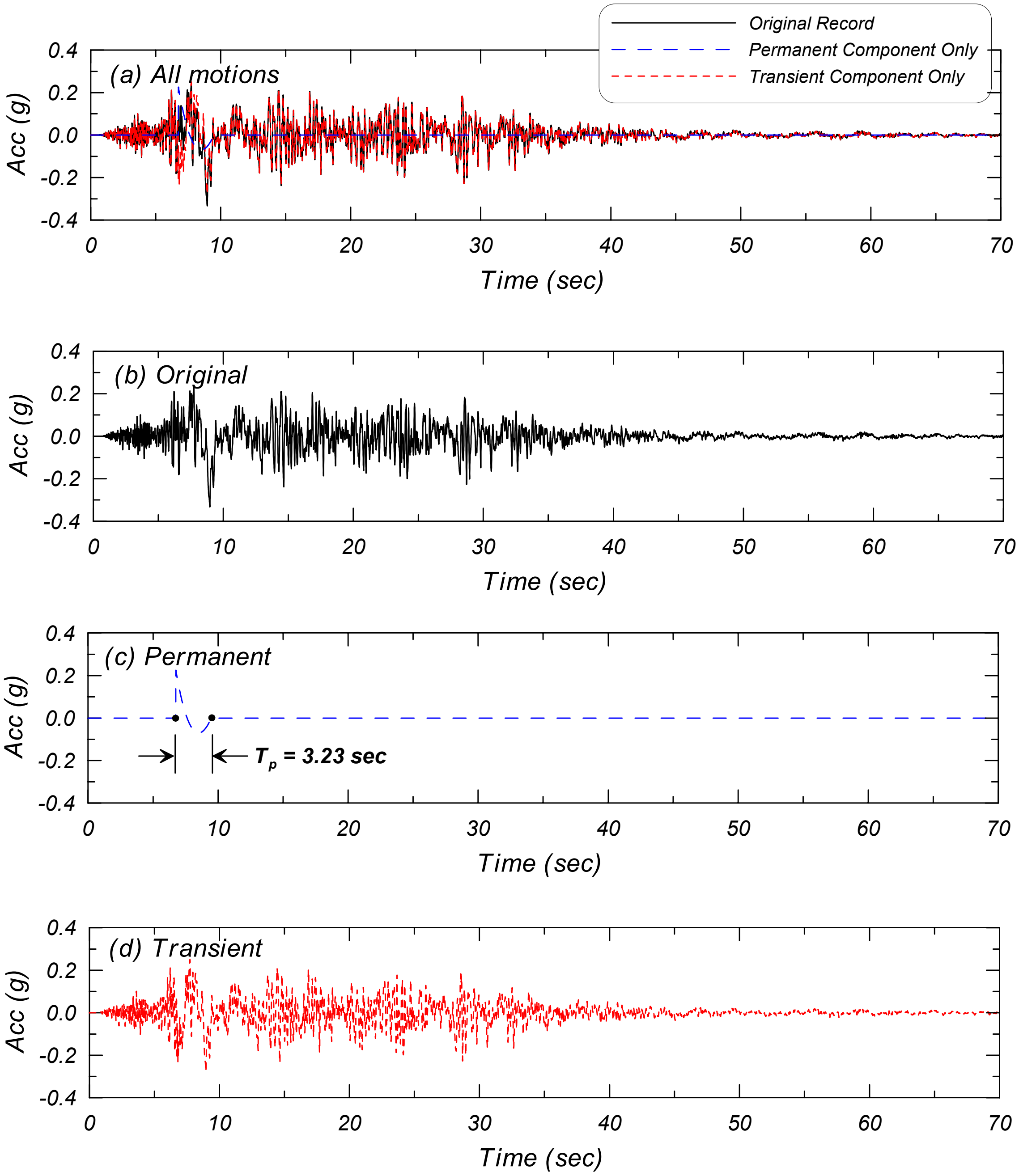

Figure 3.30 Summary of Taiwan 075E components acceleration time history: (a) overlay of original, transient, and permanent motions; (b) original motion; (c) permanent component only; and (d) transient component only.

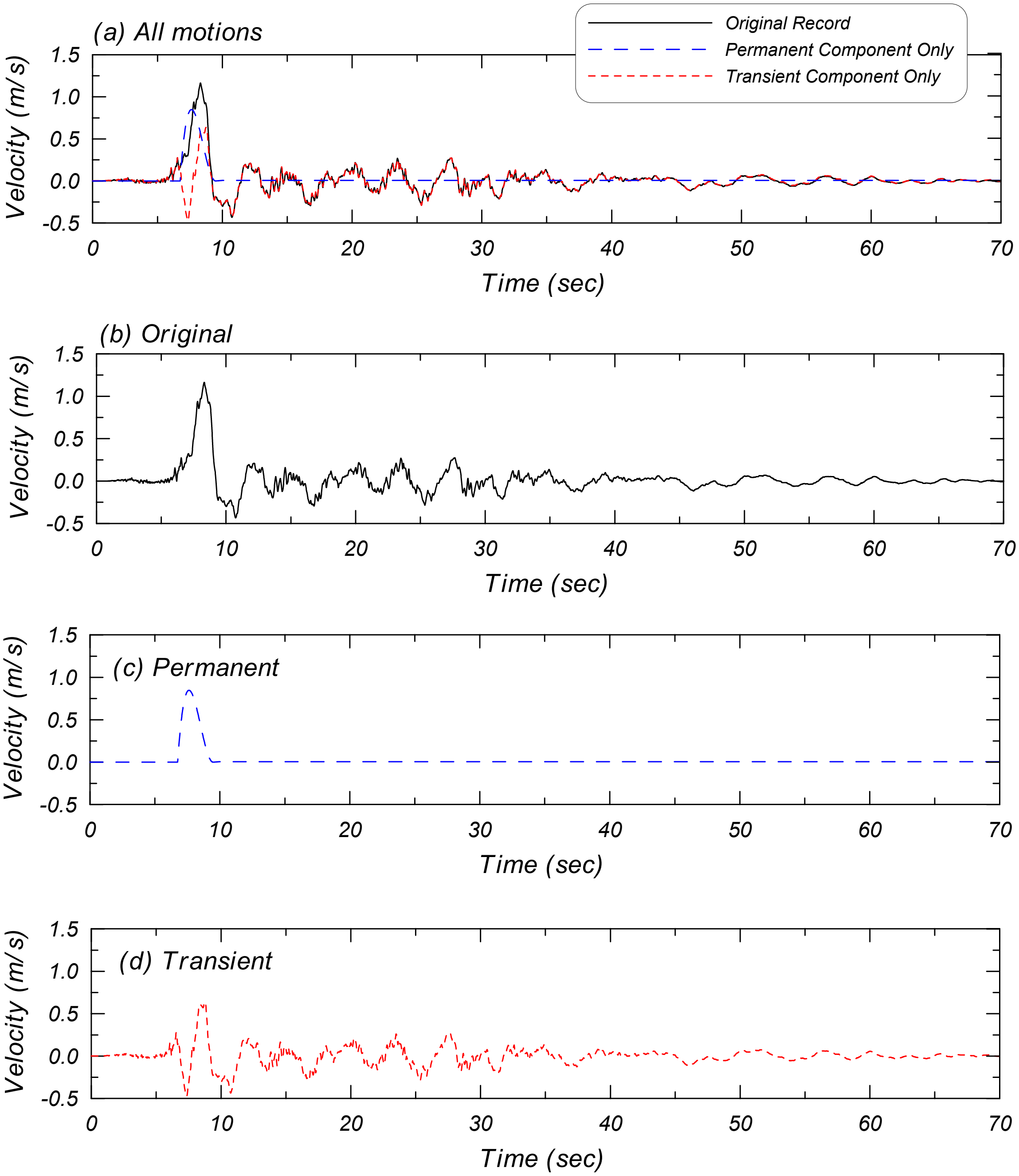

Figure 3.31 Summary of Taiwan 075E components velocity time history: (a) overlay of original, transient, and permanent motions; (b) original motion; (c) permanent component only; and (d) transient component only.

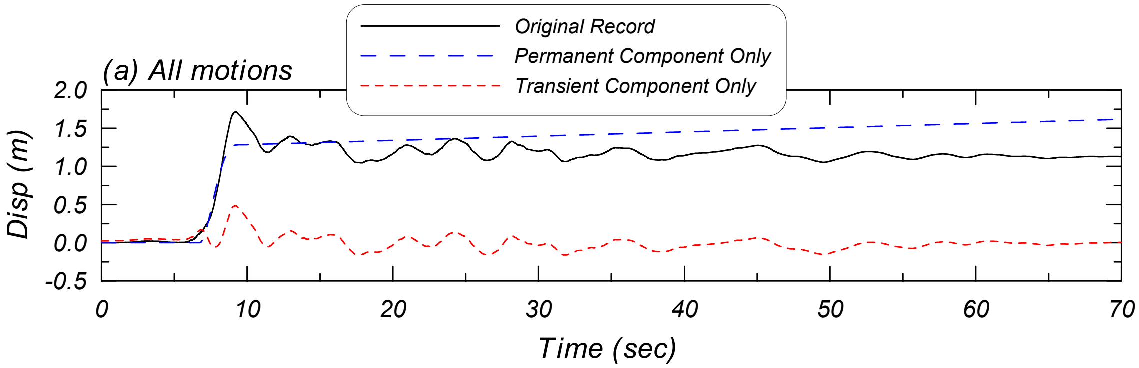

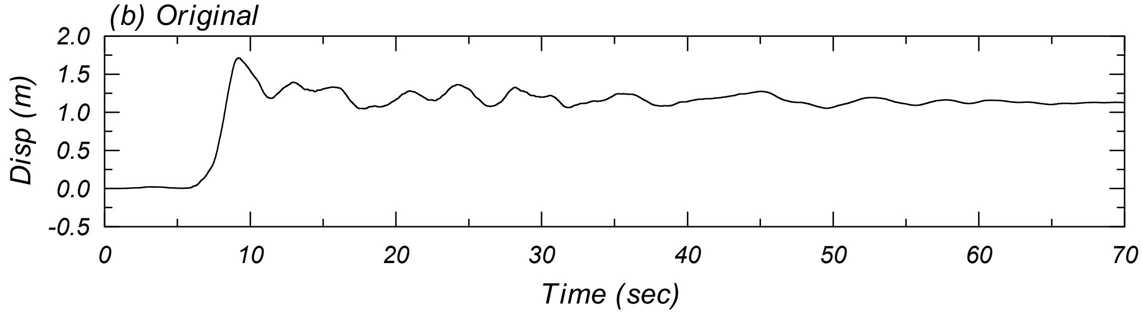

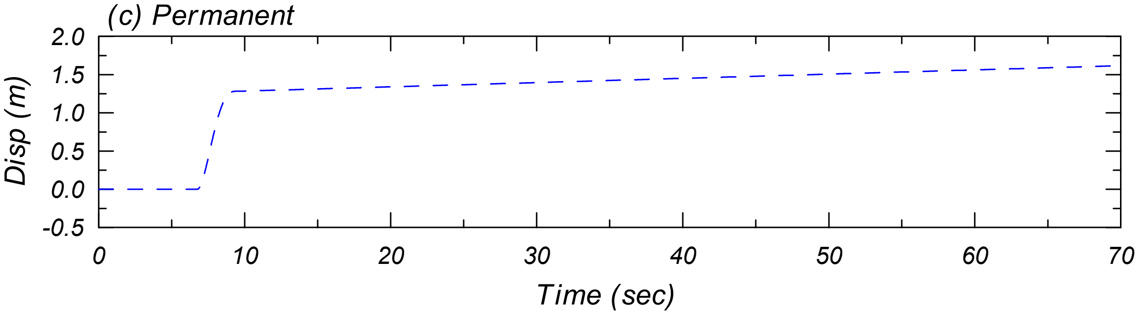

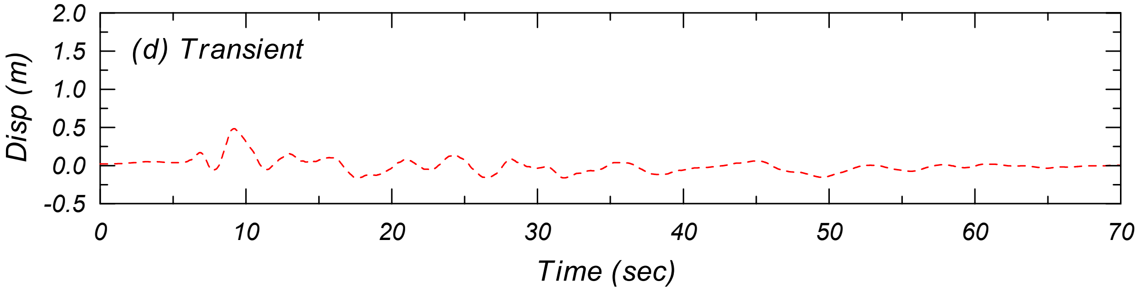

Figure 3.32 Summary of Taiwan 075E components displacement time history: (a) overlay of original, transient, and permanent motions; (b) original motion; (c) permanent component only; and (d) transient component only.

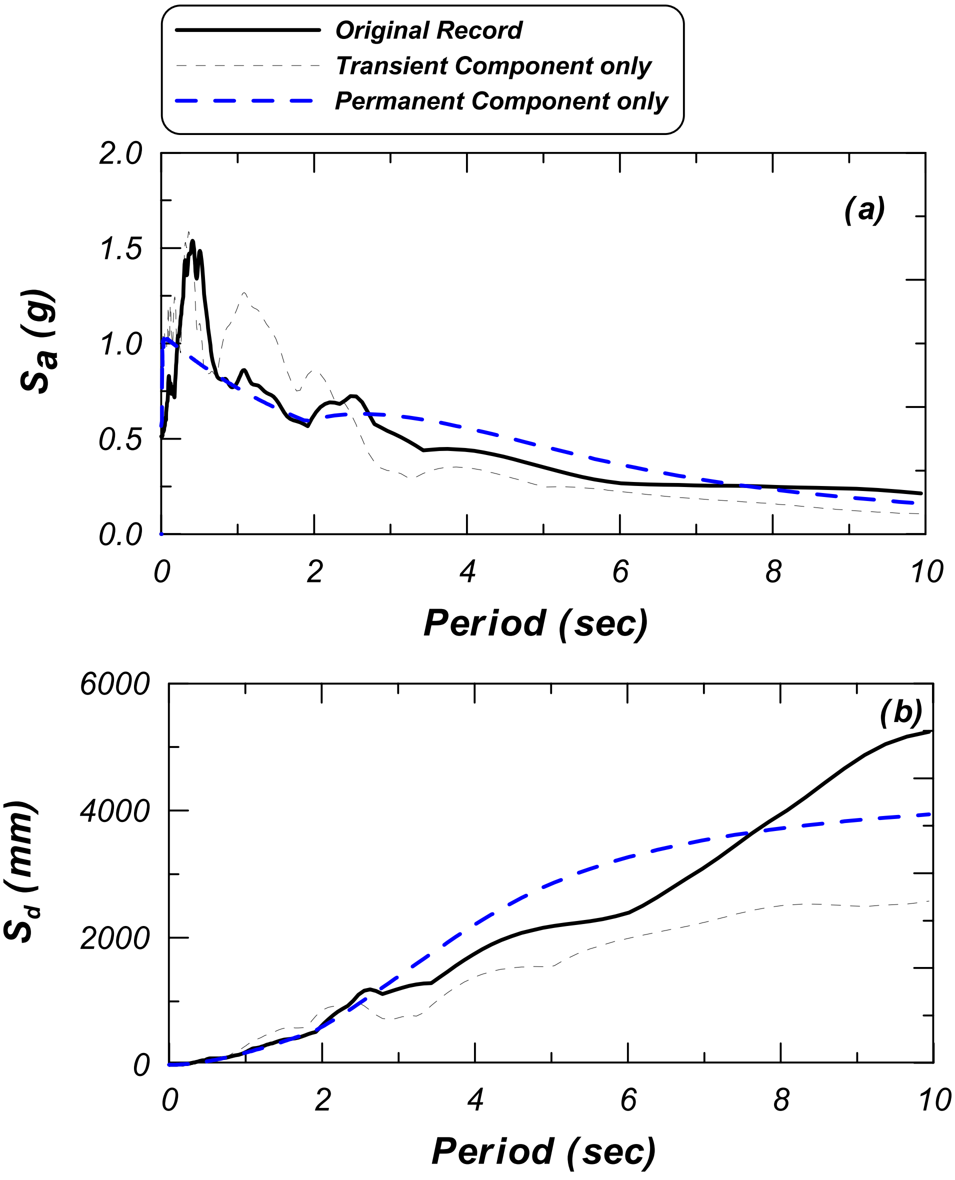

Figure 3.33 Elastic 5% damped response spectra — Taiwan 068E motions: (a) acceleration spectra and (b) displacement spectra.

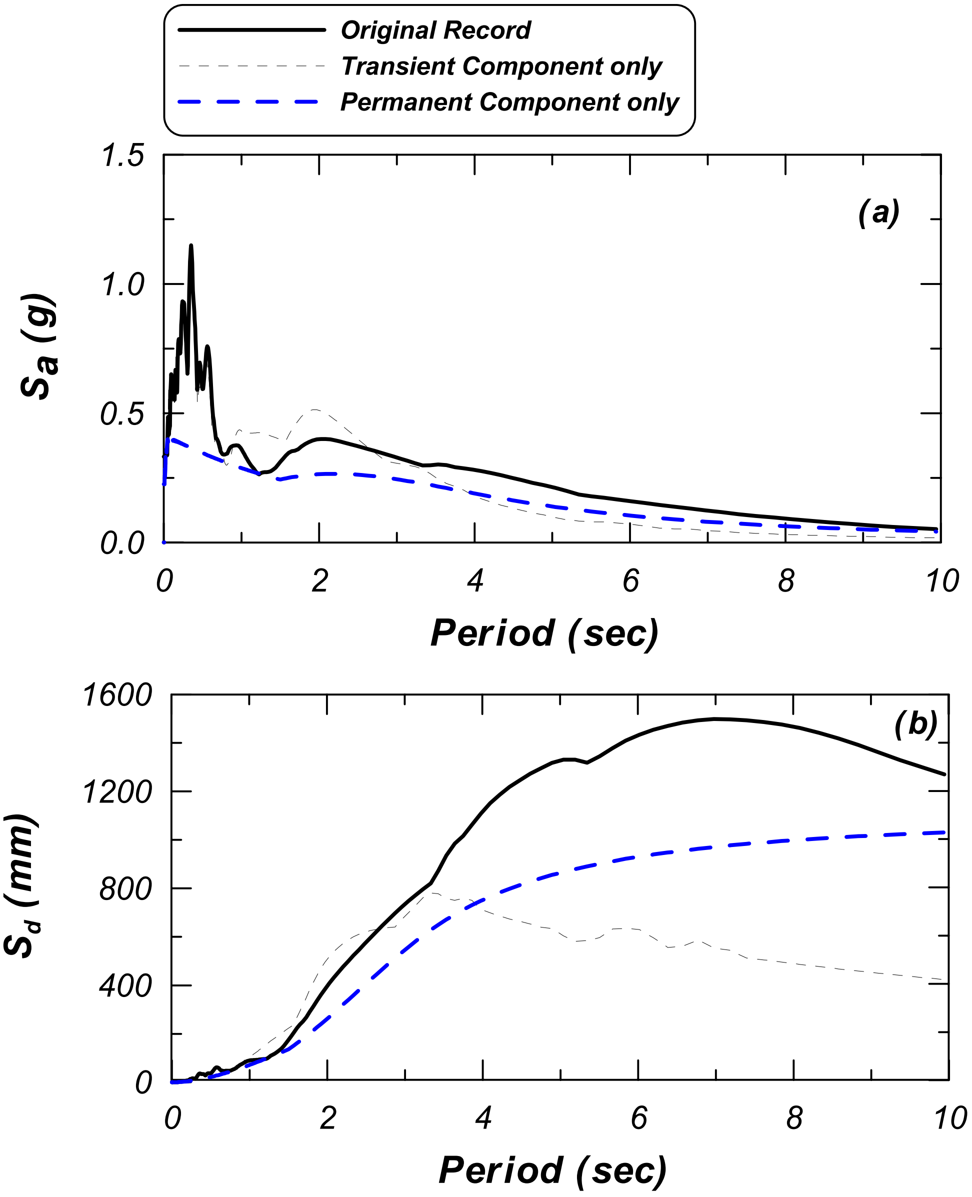

Figure 3.34 Elastic 5% damped response spectra — Taiwan 075E motions: (a) acceleration spectra and (b) displacement spectra.

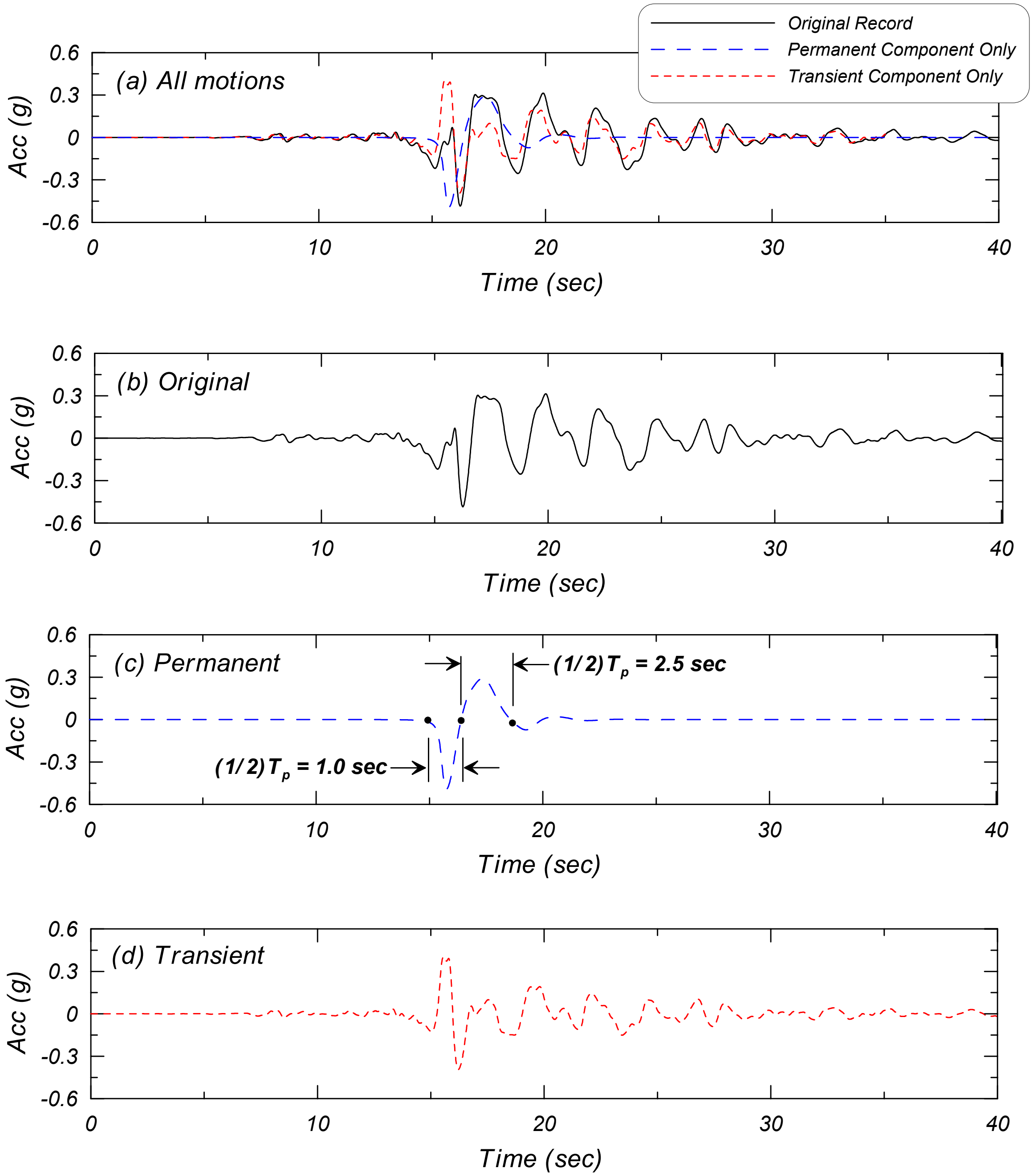

Figure 3.35 Summary of Taiwan 068E (ground surface) acceleration time history (rock outcrop scaled to a_{max} = 0.5g): (a) overlay of original, transient, and permanent motions; (b) original motion; (c) permanent component only; and (d) transient component only.

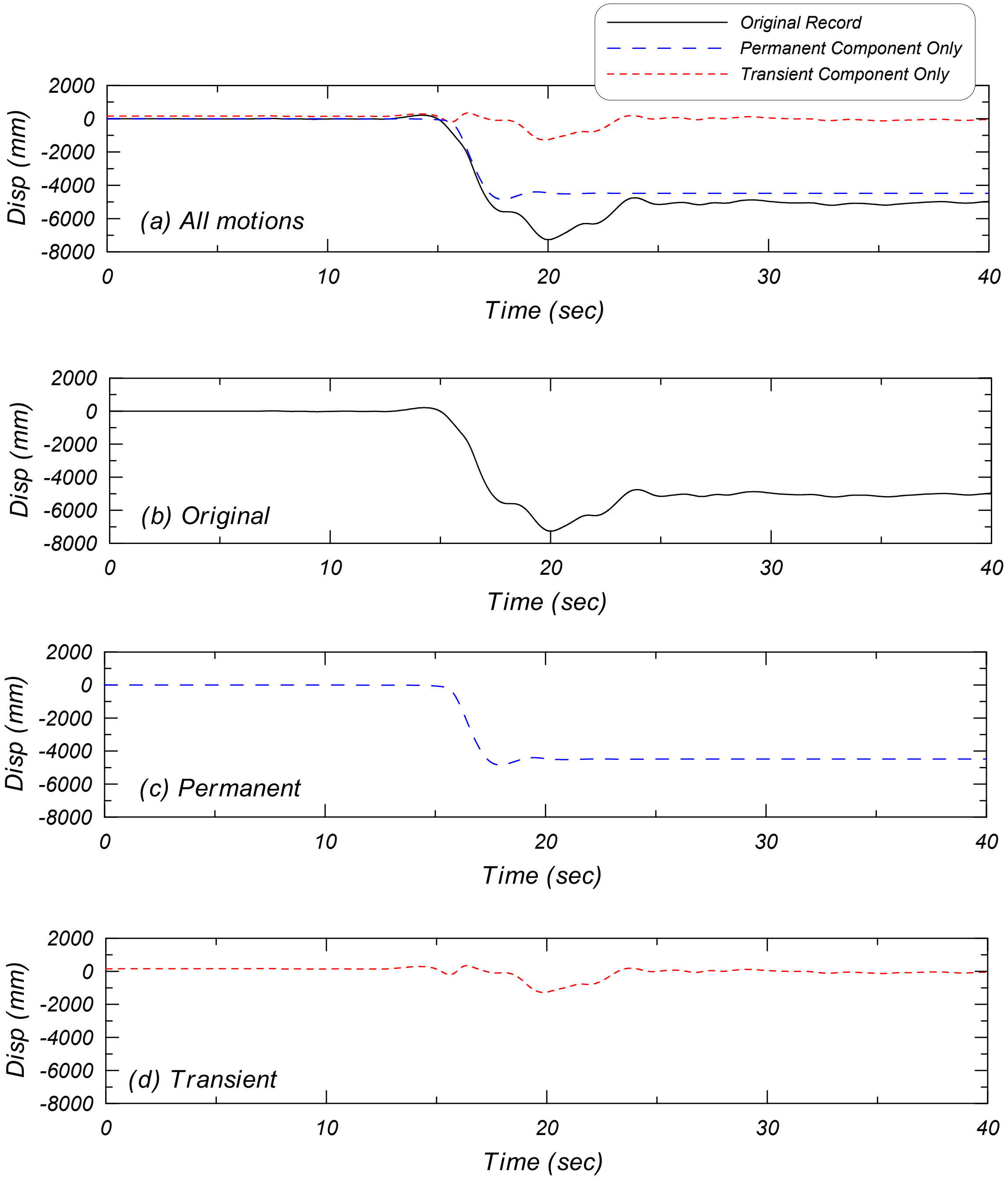

Figure 3.36 Summary of Taiwan 068E (ground surface) displacement time history (rock outcrop scaled to $a_{max} = 0.5g$): (a) overlay of original, transient, and permanent motions; (b) original motion; (c) permanent component only; and (d) transient component only.

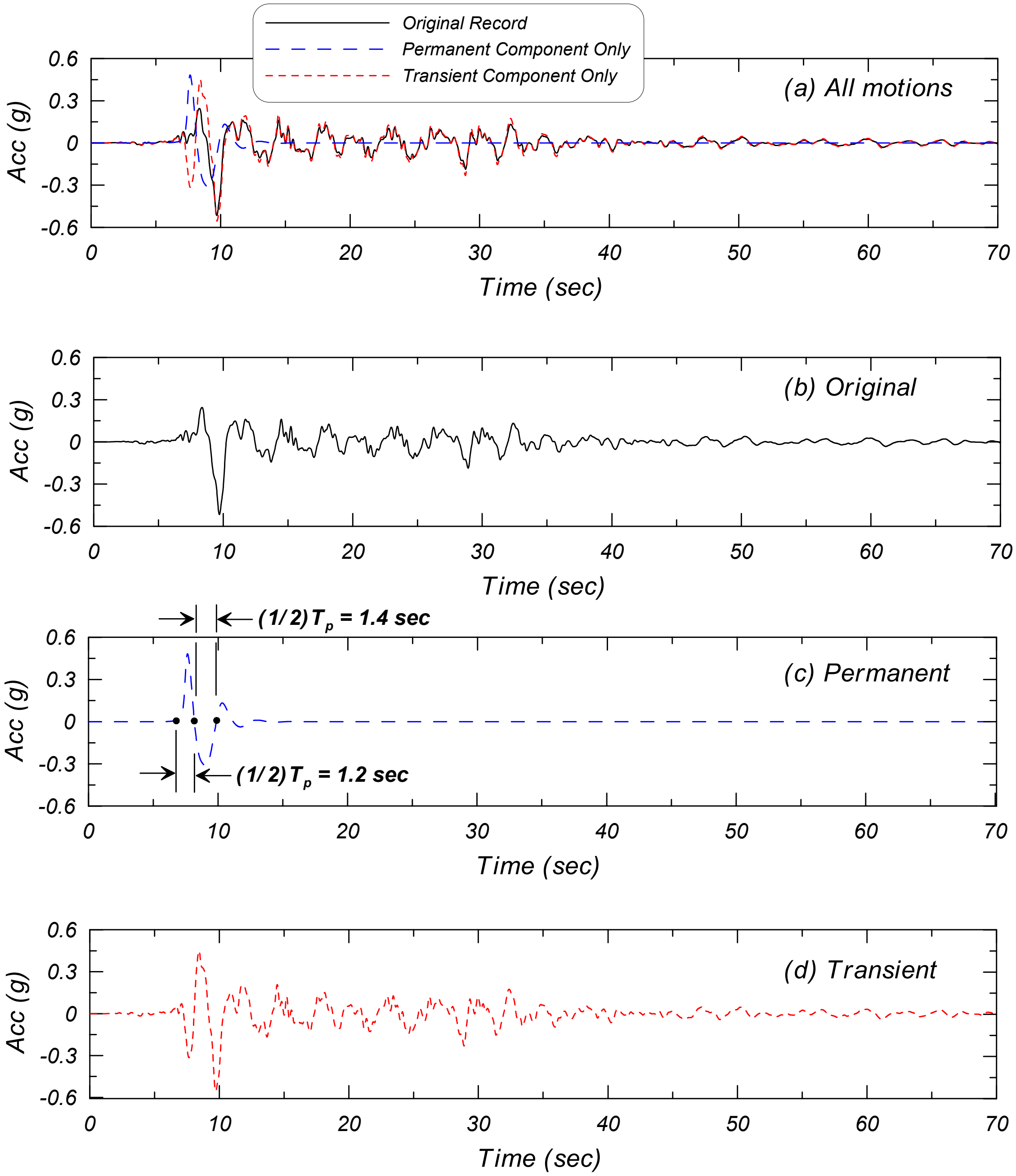

Figure 3.37 Summary of Taiwan 075E (ground surface) acceleration time history (rock outcrop scaled to a_{max} = 0.5g): (a) overlay of original, transient, and permanent motions; (b) original motion; (c) permanent component only; and (d) transient component only.

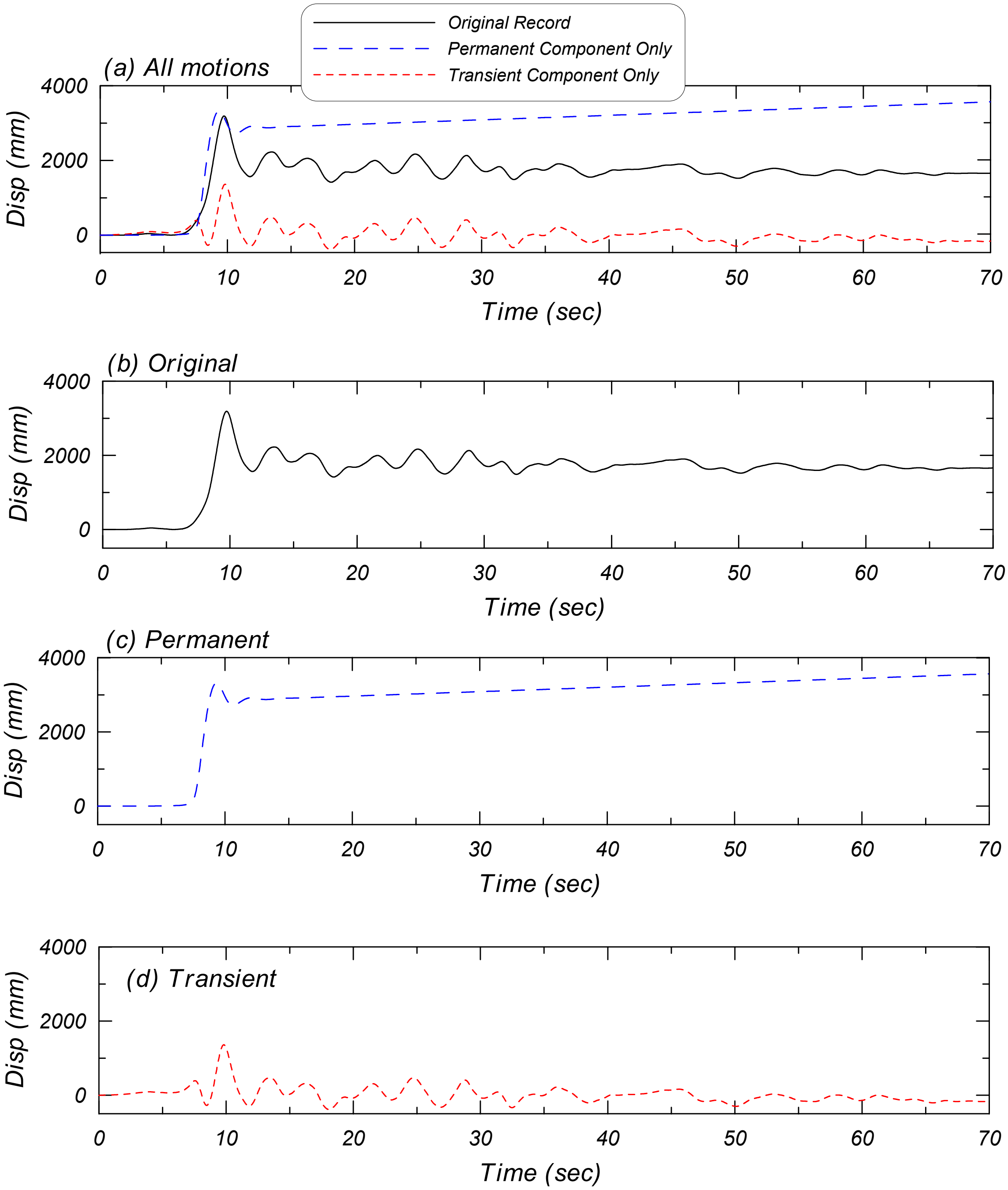

Figure 3.38 Summary of Taiwan 075E (ground surface) displacement time history (rock outcrop scaled to a_{max} = 0.5g): (a) overlay of original, transient, and permanent motions; (b) original motion; (c) permanent component only; and (d) transient component only.

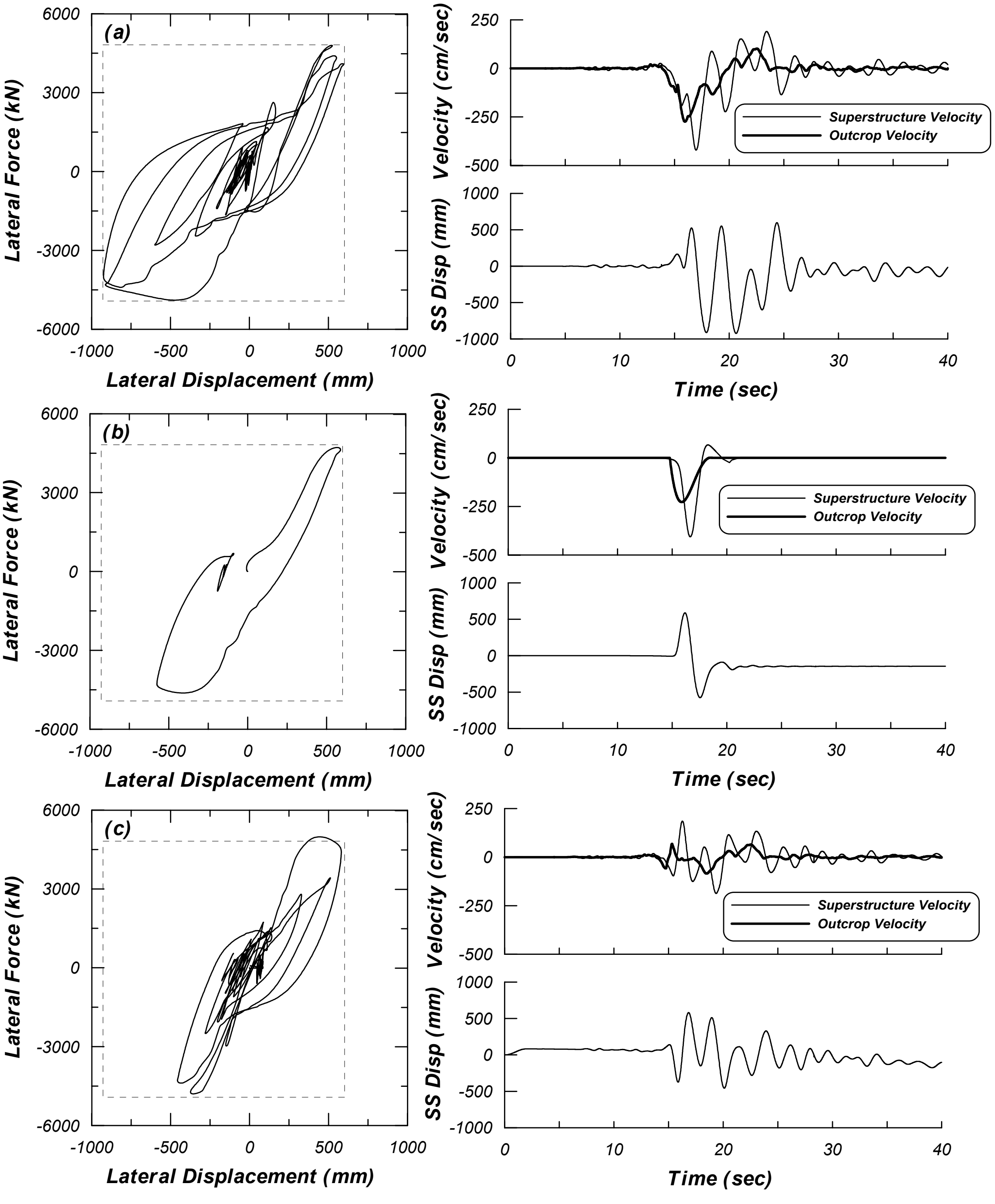

Figure 3.39 Dynamic analysis results: Taiwan 068E motions; 3.0 m diameter pile shaft with an above-ground height of 2D; lateral force-displacement response; velocity time history (of rock outcrop and superstructure); and superstructure lateral displacement time history of (a) original motion, (b) permanent component only, and (c) transient component only.

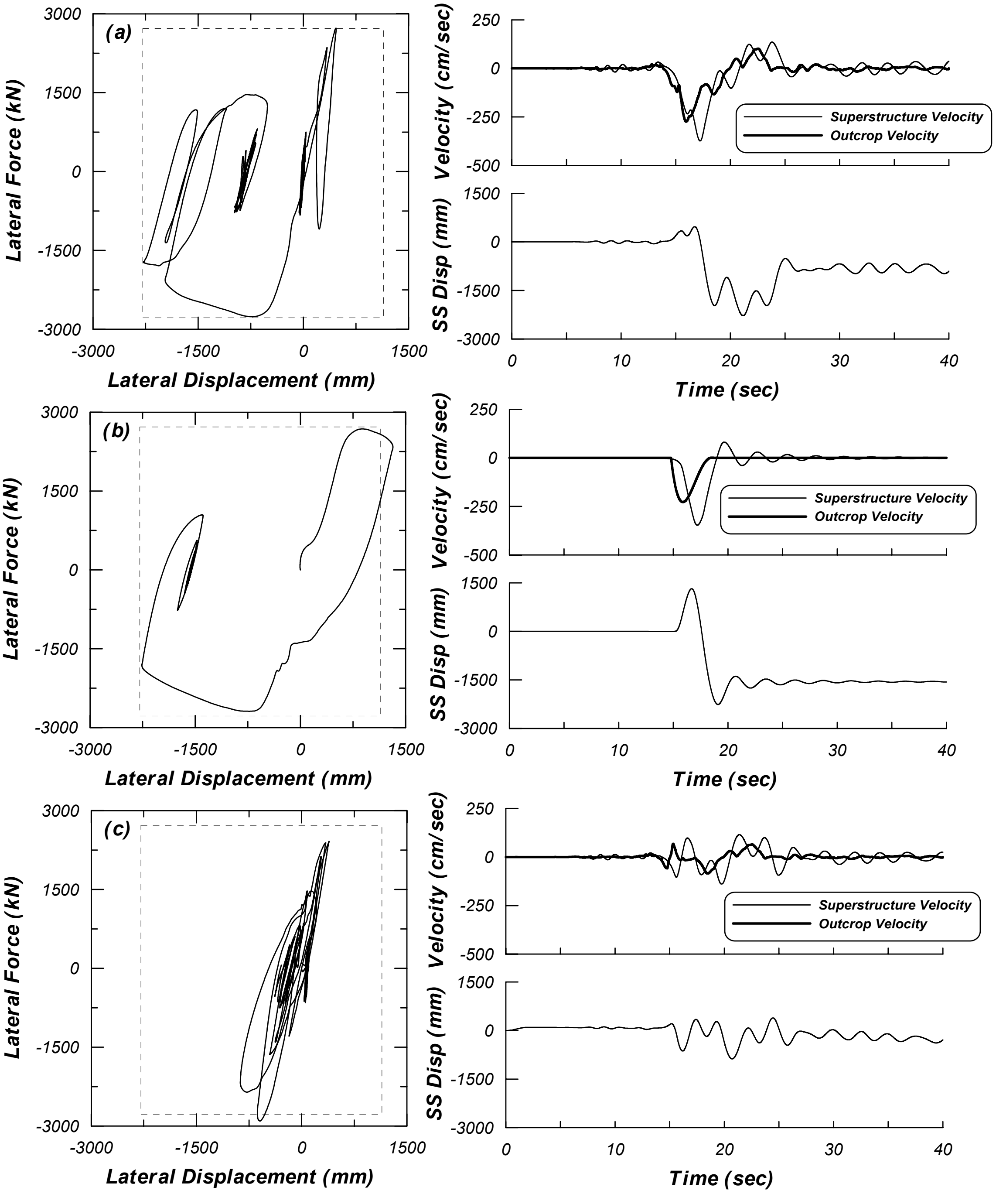

Figure 3.40 Dynamic analysis results: Taiwan 068E motions; 3.0 m diameter pile shaft with an above-ground height of 4D; lateral force-displacement response; velocity time history (of rock outcrop and superstructure); and superstructure lateral displacement time history of (a) original motion, (b) permanent component only, and (c) transient component only.

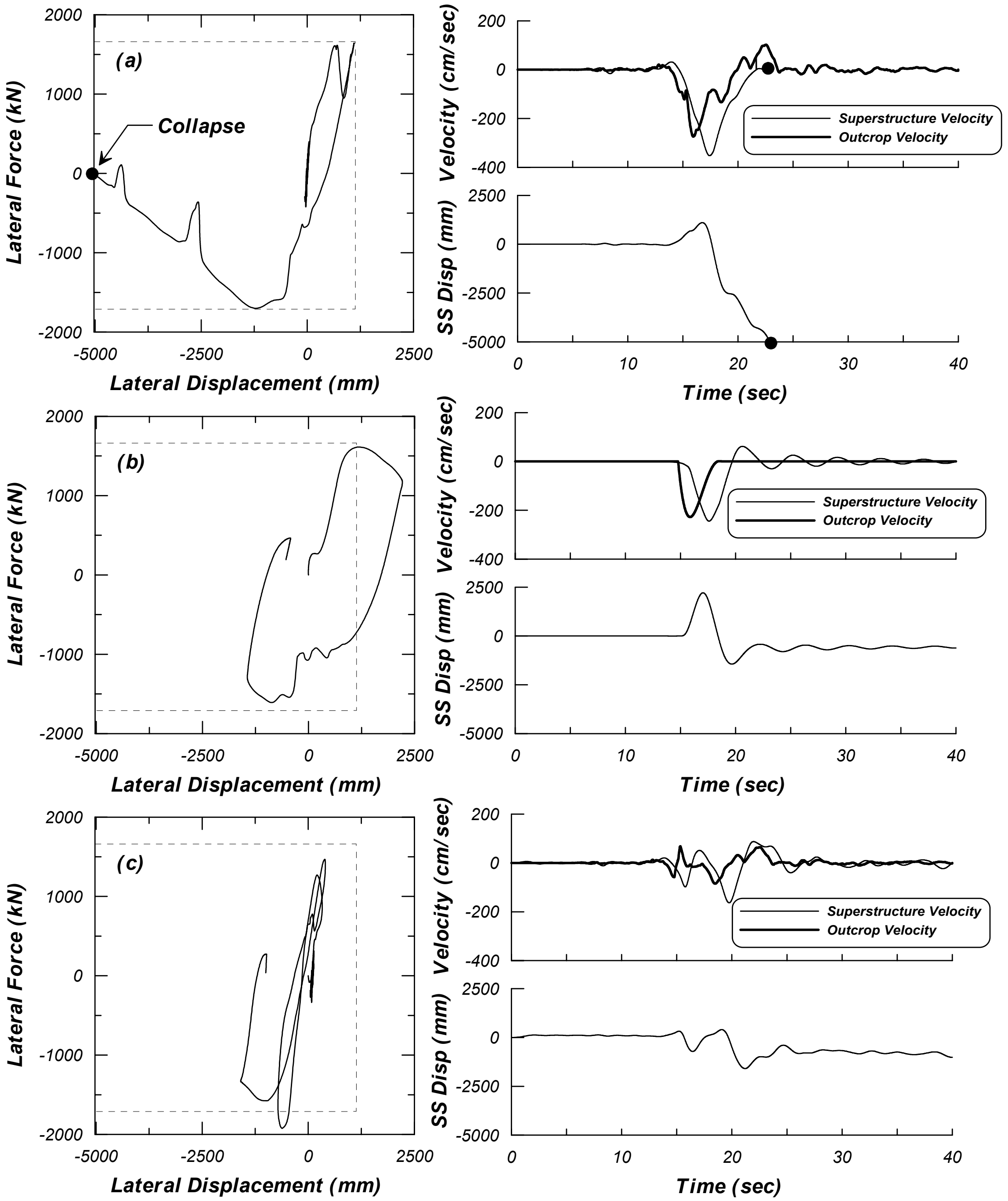

Figure 3.41 Dynamic analysis results: Taiwan 068E motions; 3.0 m diameter pile shaft with an above-ground height of 6D; lateral force-displacement response; velocity time history (of rock outcrop and superstructure); and superstructure lateral displacement time history of (a) original motion, (b) permanent component only, and (c) transient component only.

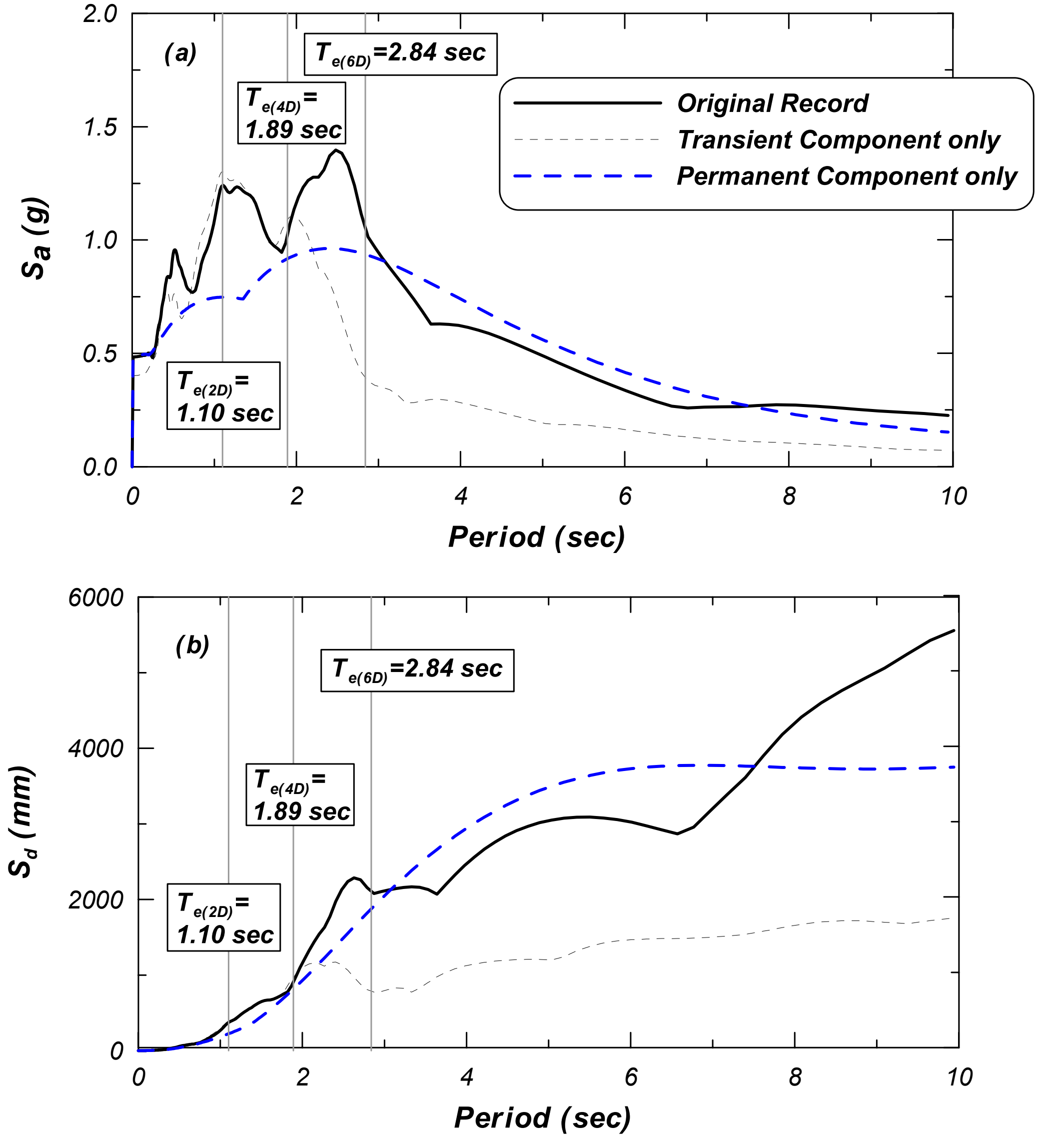

Figure 3.42 Elastic 5% damped ground surface response spectra for Taiwan 068E motions (original motion, transient, and permanent components): (a) acceleration spectra and (b) displacement spectra (outcrop motion scaled to a_{max} = 0.5g).

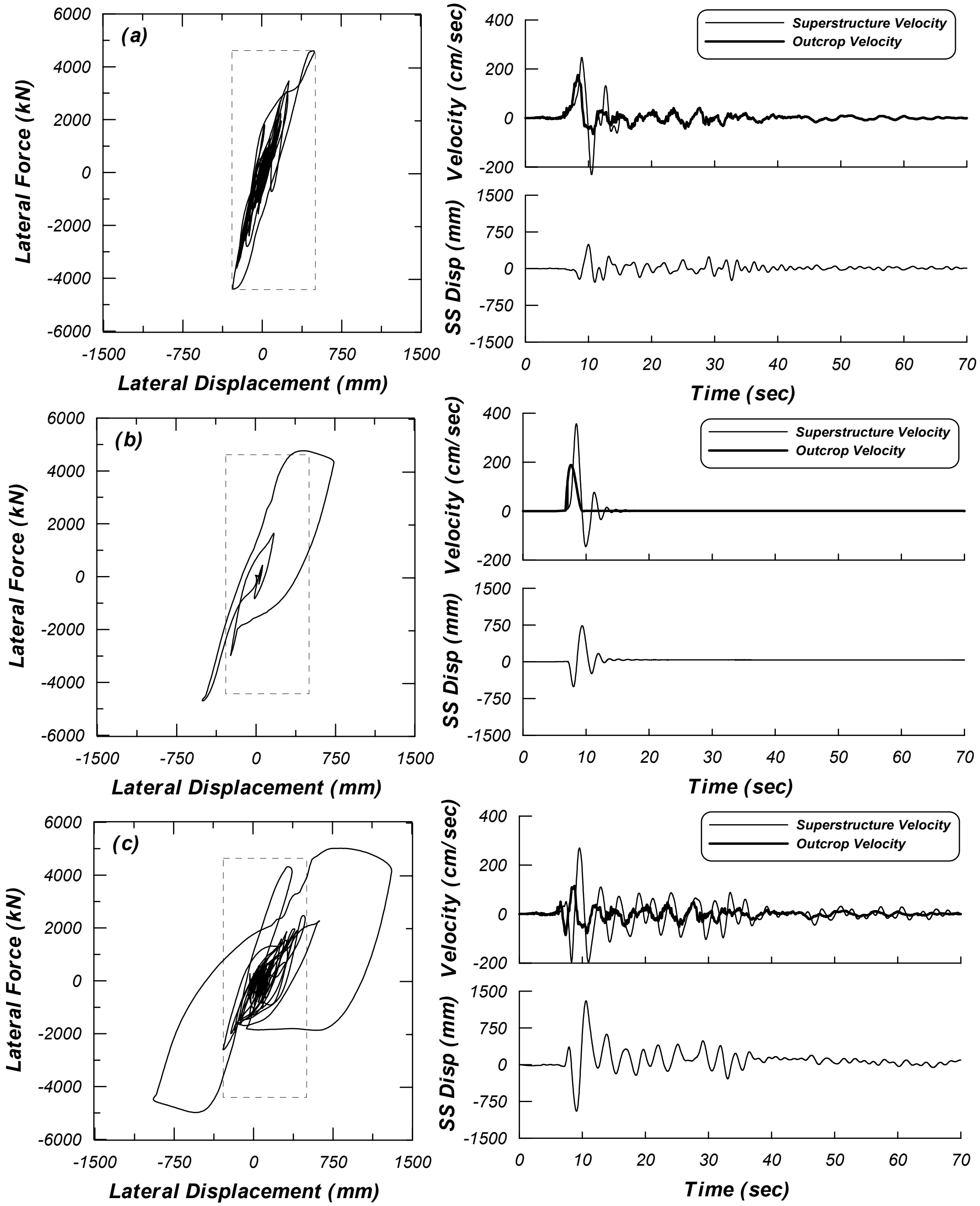

Figure 3.43 Dynamic analysis results: Taiwan 075E motions; 3.0 m diameter pile shaft with an above-ground height of 2D; lateral force-displacement response; velocity time history (of rock outcrop and superstructure); and superstructure lateral displacement time history of (a) original motion, (b) permanent component only, and (c) transient component only.

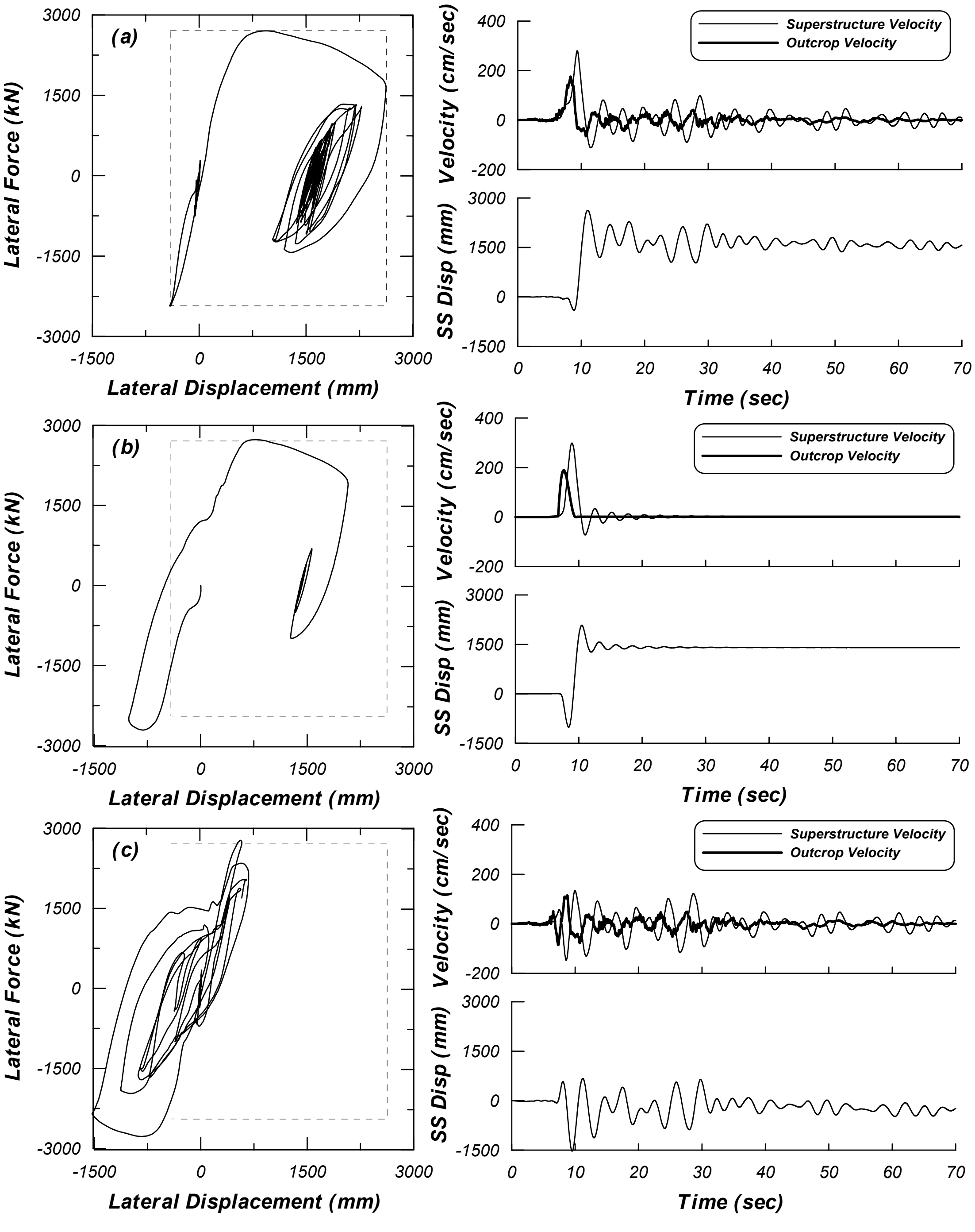

Figure 3.44 Dynamic analysis results: Taiwan 075E motions; 3.0 m diameter pile shaft with an above-ground height of 4D; lateral force-displacement response; velocity time history (of rock outcrop and superstructure); and superstructure lateral displacement time history of (a) original motion, (b) permanent component only, and (c) transient component only.

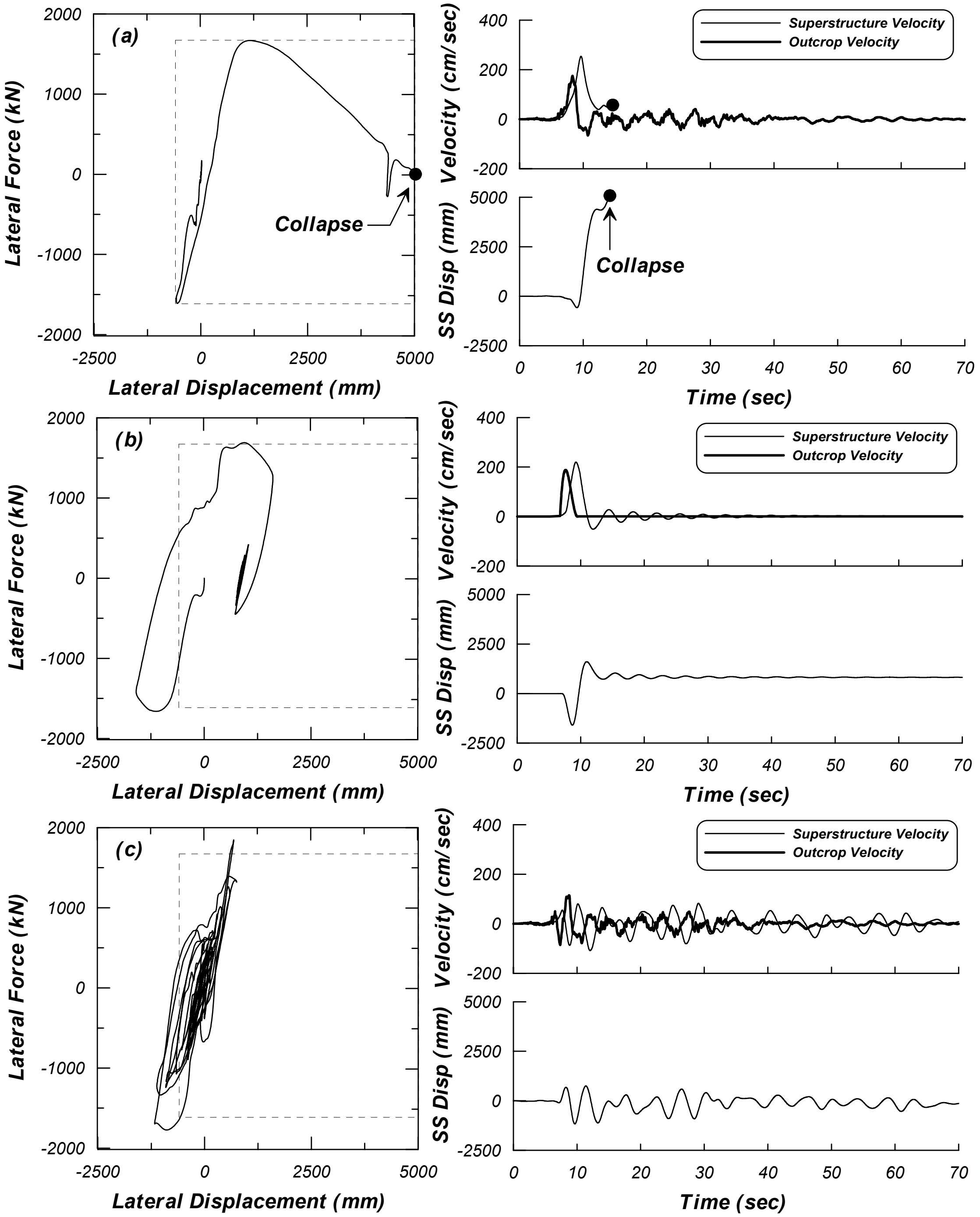

Figure 3.45 Dynamic analysis results: Taiwan 075E motions; 3.0 m diameter pile shaft with an above-ground height of 6D; lateral force-displacement response; velocity time history (of rock outcrop and superstructure); and superstructure lateral displacement time history of (a) original motion, (b) permanent component only, and (c) transient component only.

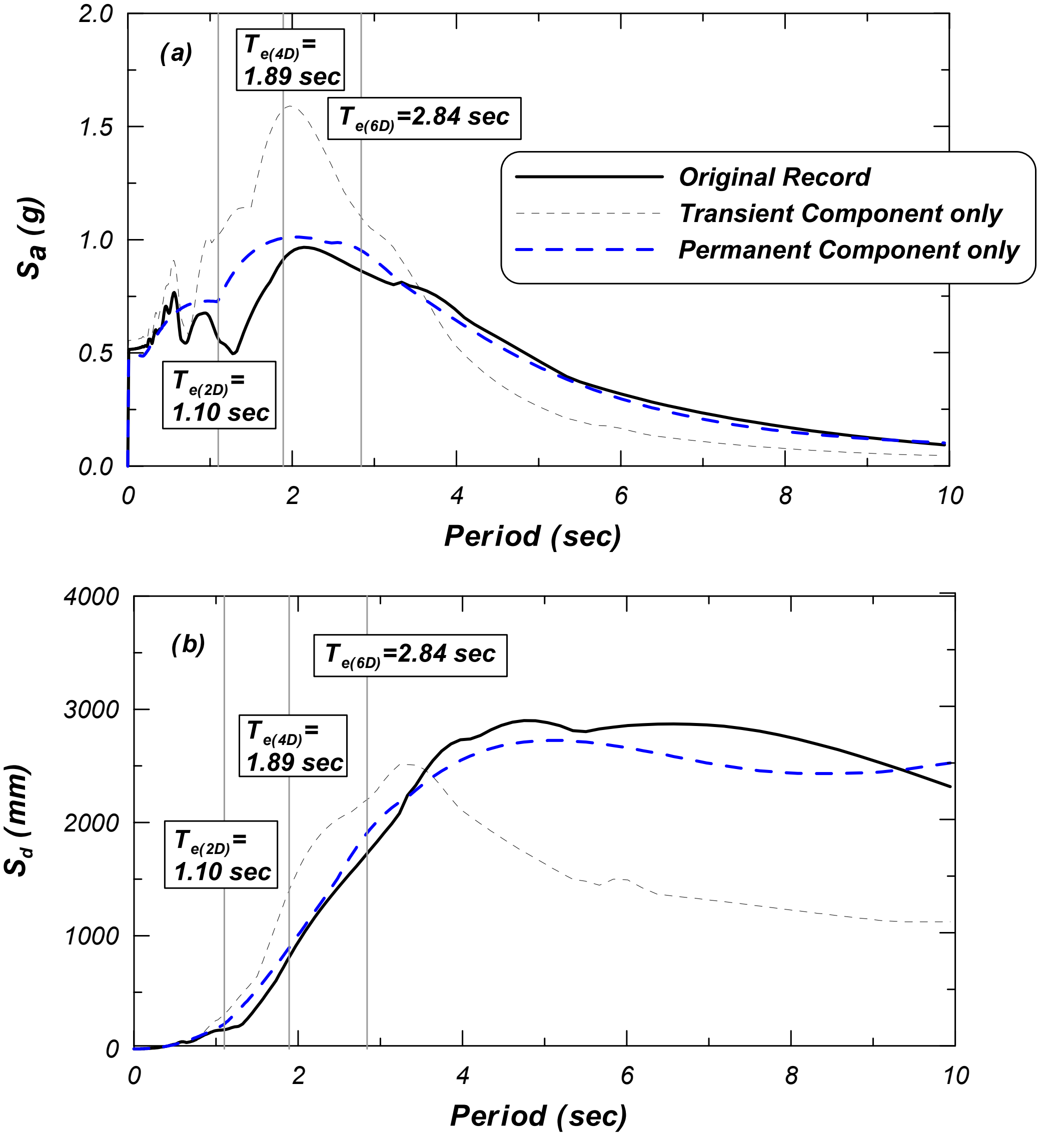

Figure 3.46 Elastic 5% damped ground surface response spectra for Taiwan 075E motions (original motion, transient, and permanent components): (a) acceleration spectra and (b) displacement spectra (outcrop motion scaled to a_{max} = 0.5g).

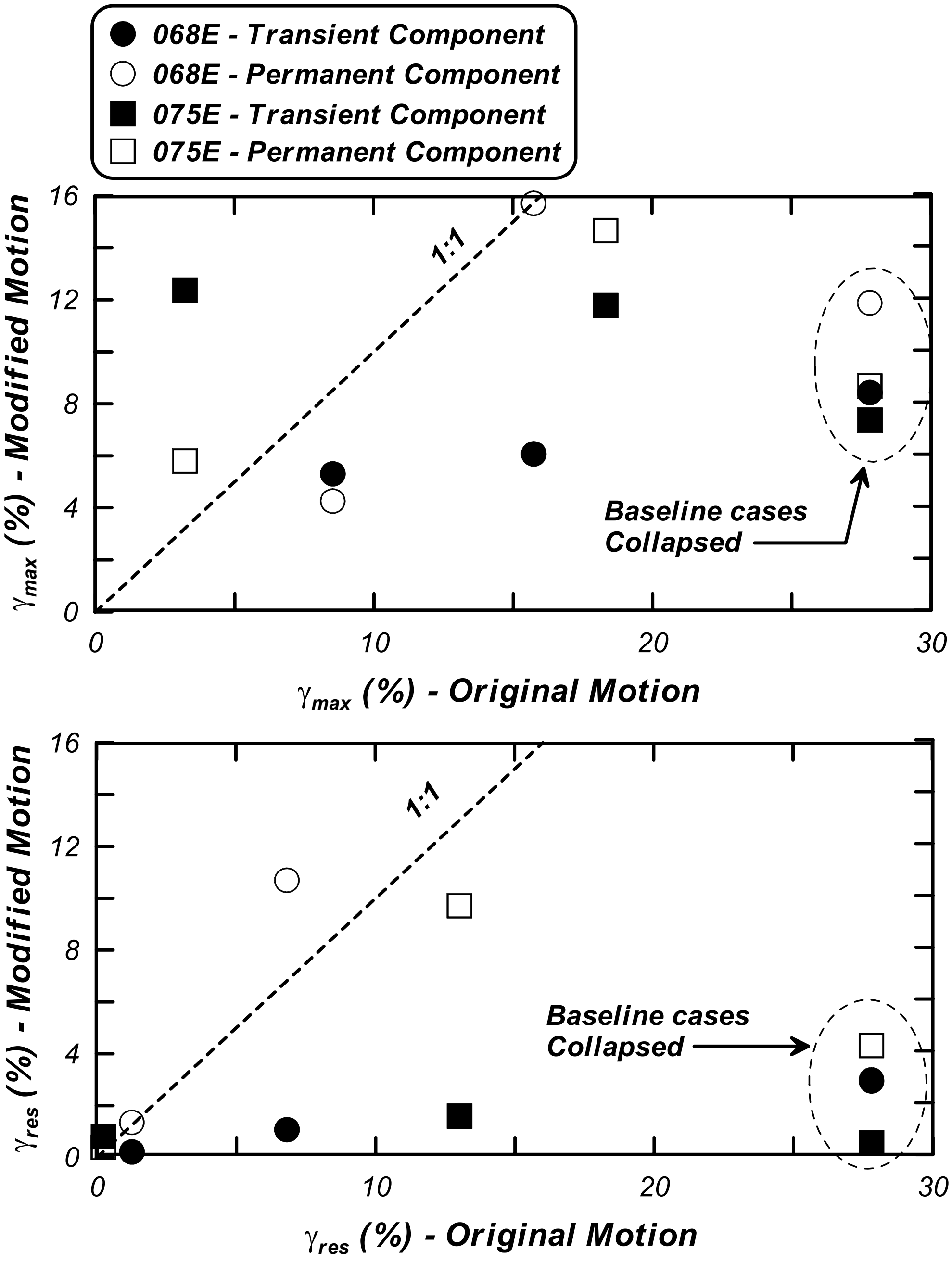

Figure 3.47 Maximum and residual drift ratios for 3.0 m diameter pile shafts with $0.05f'_cA_g$ subjected to the Taiwan 075E and 068E motions - modified motions (transient and permanent components) compared to the original motion.

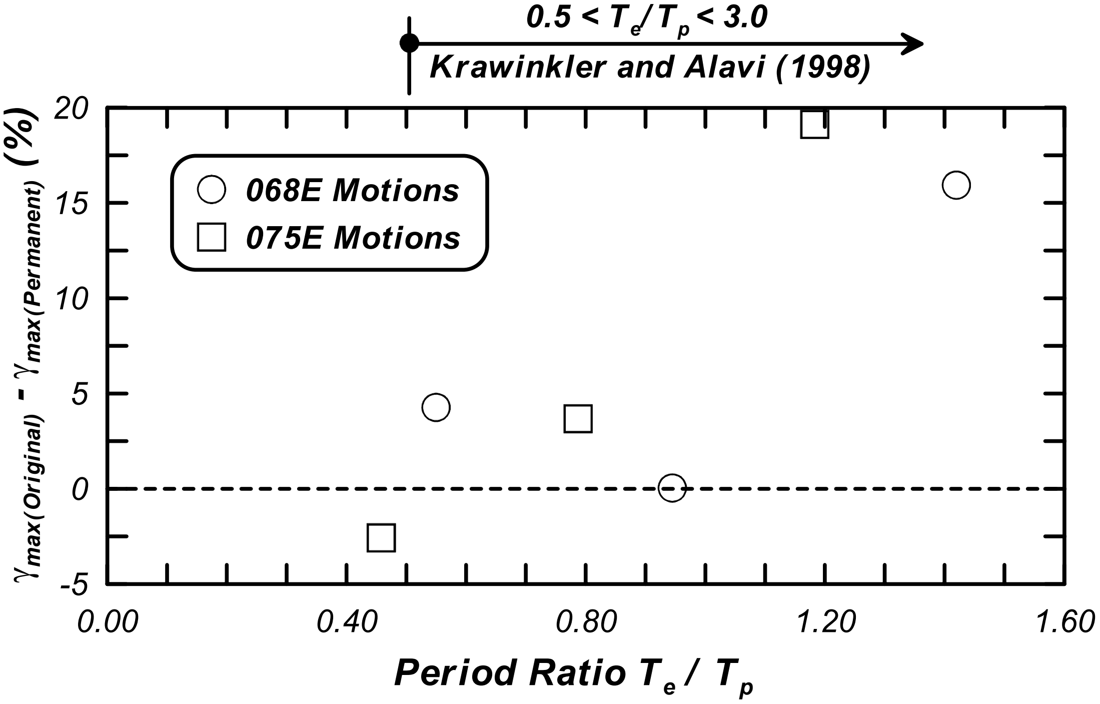

Figure 3.48 Difference in maximum drift ratios between the permanent and original motion as a function of the ratio of periods T_e/T_p.

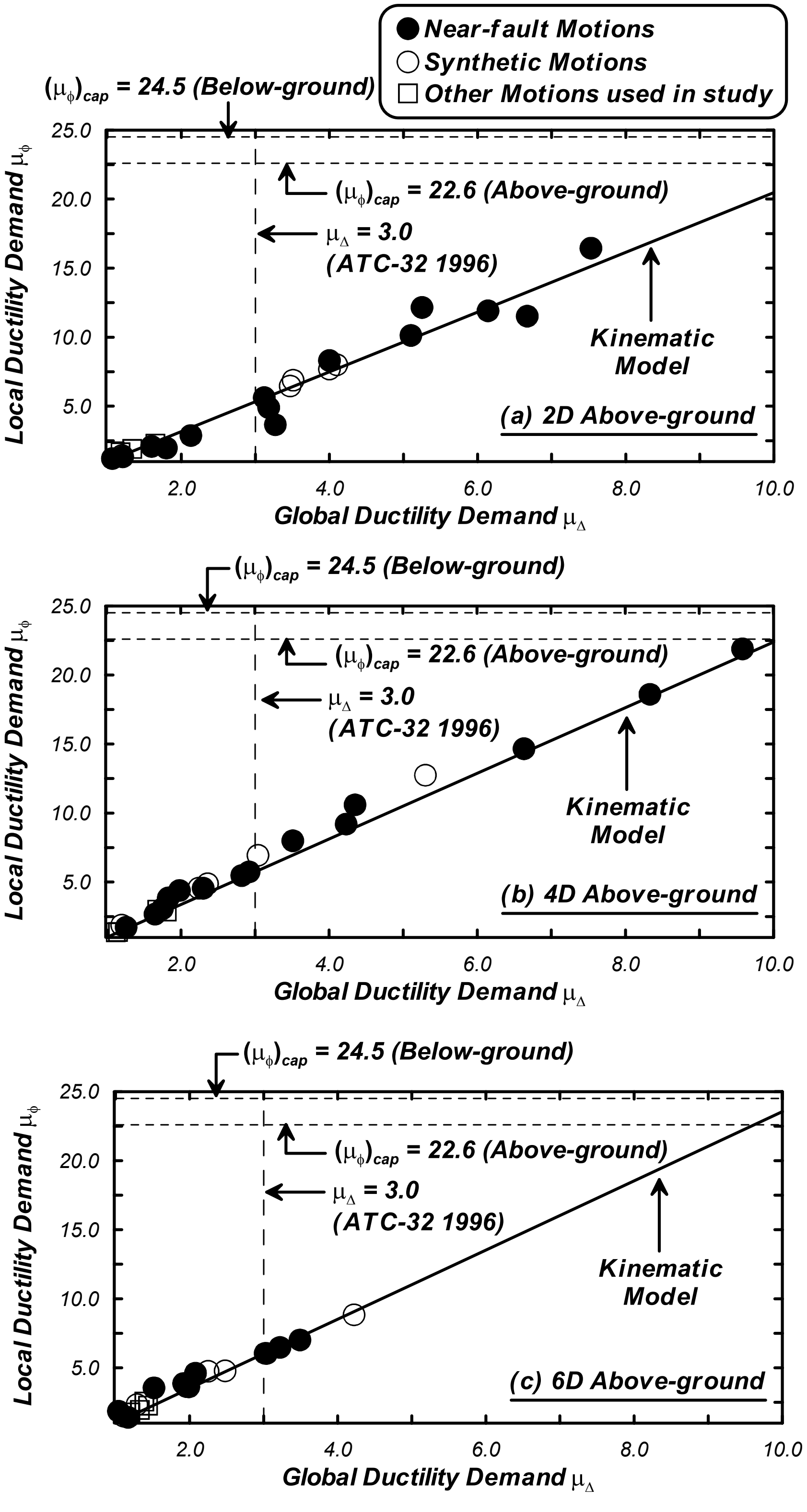

Figure 3.49 Local versus global kinematic relation for 3.0 m diameter pile shafts with $0.05f'_cA_g$ with above-ground heights of (a) 2D, (b) 4D, and (c) 6D.

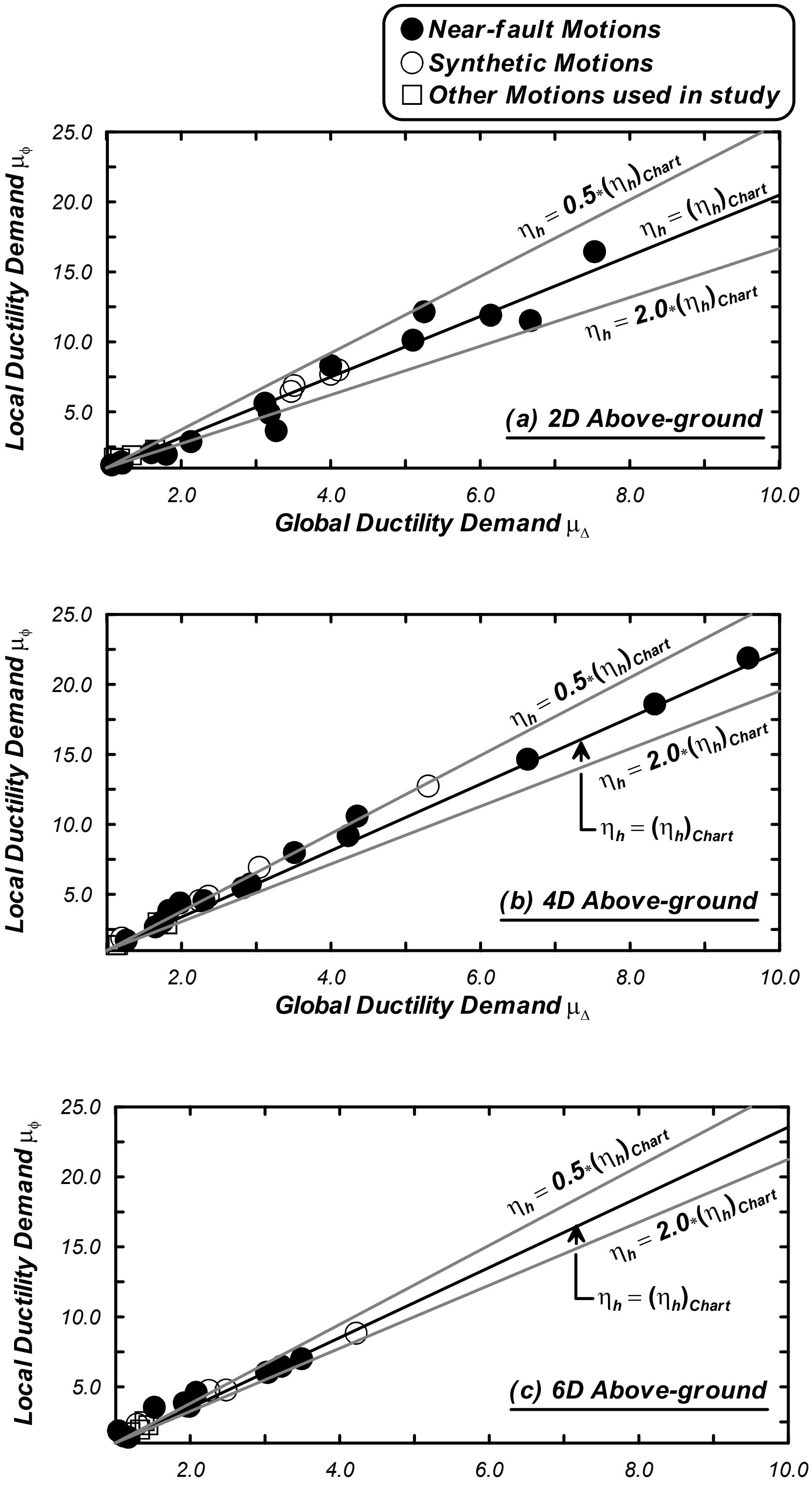

Figure 3.50 Local versus global kinematic relation for 3.0 m diameter pile shafts with $0.05f'_cA_g$ with above-ground heights of (a) 2D, (b) 4D, and (c) 6D-effect of variation of η_h on local to global ductility relation.

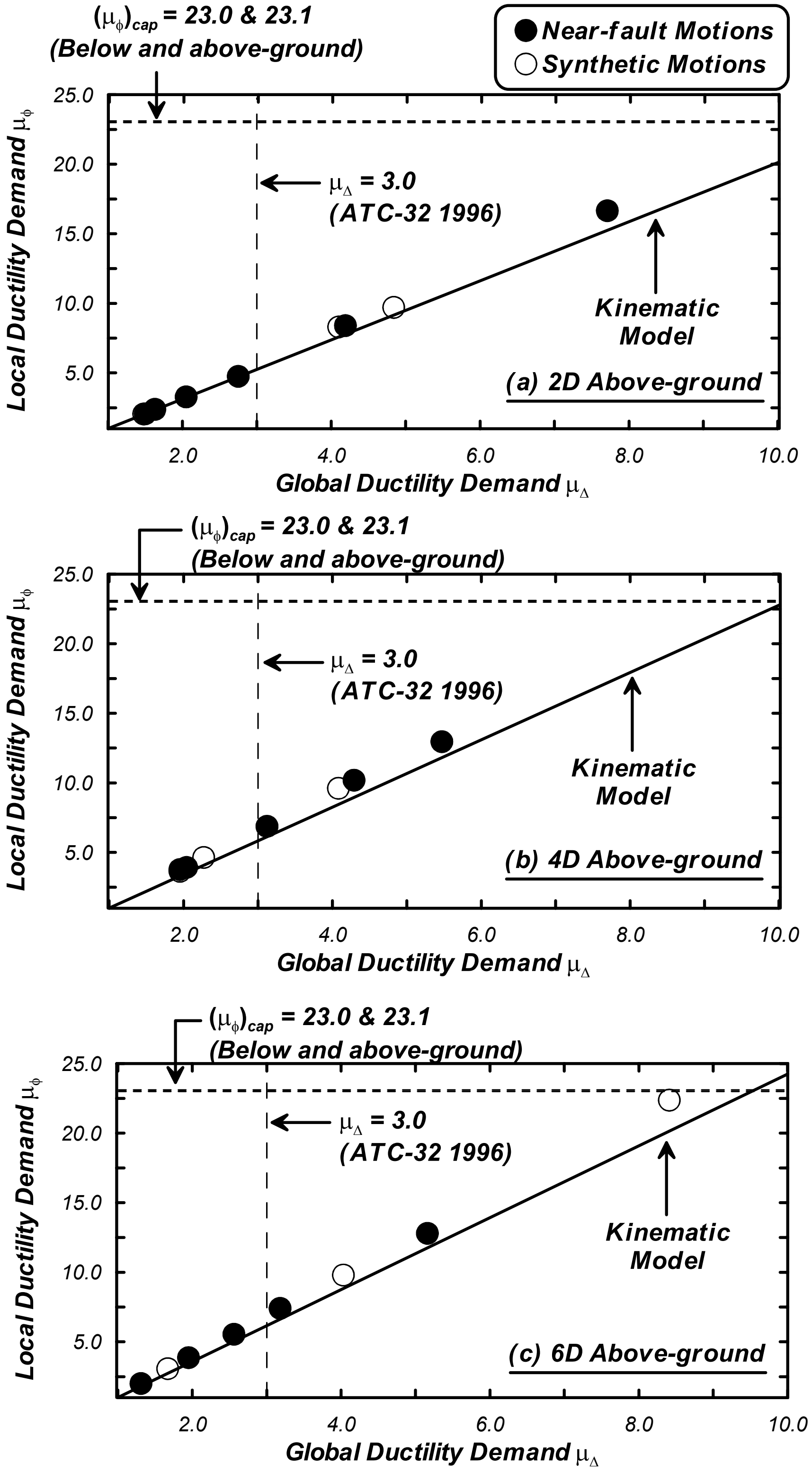

Figure 3.51 Local versus global kinematic relation for 1.5 m diameter pile shafts with $0.05f'_cA_g$ with above-ground heights of (a) 2D, (b) 4D, and (c) 6D.

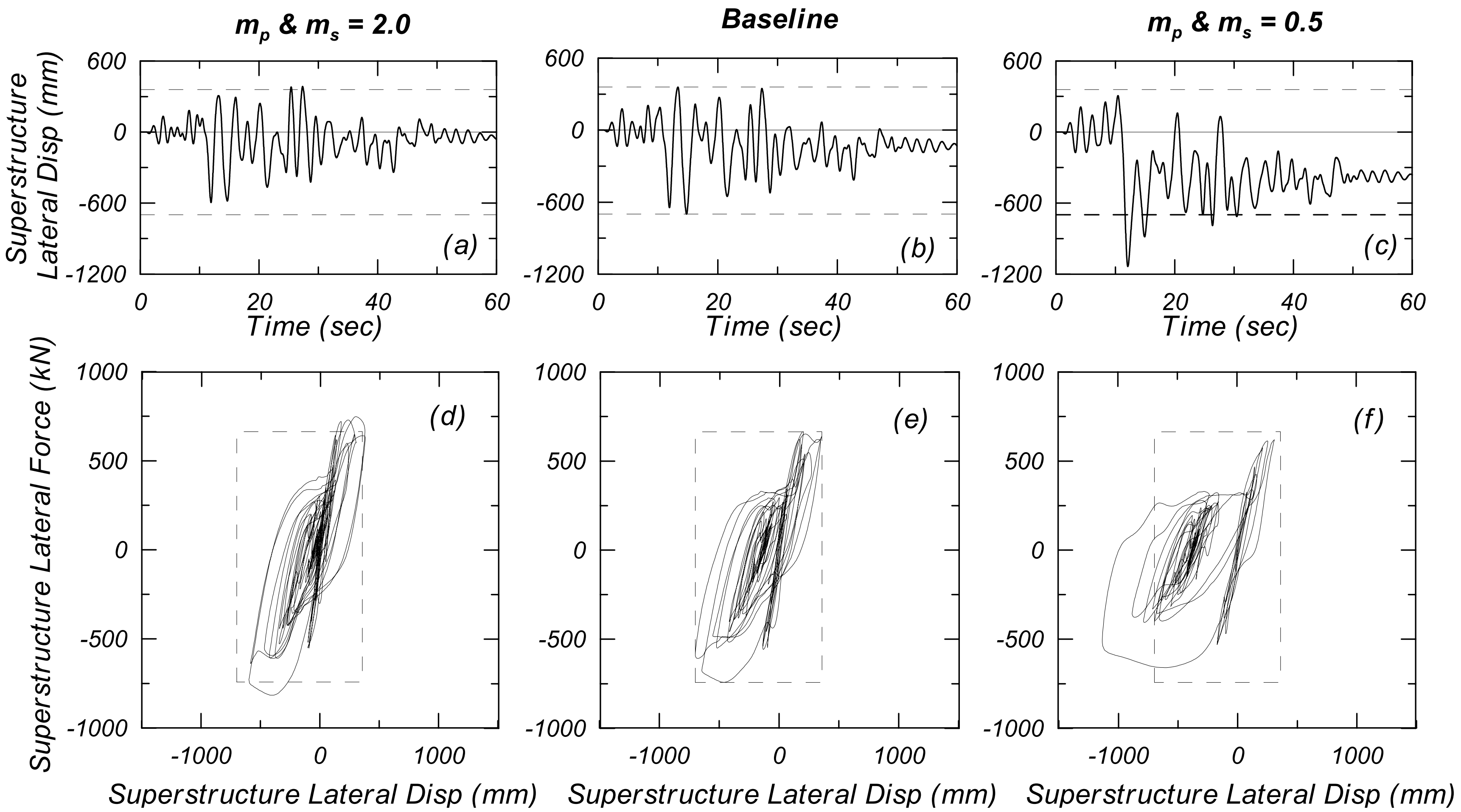

Figure 3.52 Varying the surrounding soil strength and stiffness — superstructure response for the 1.5 m diameter pile shaft, 4D above-ground structure, subjected to the Synthetic #2 outcrop motion with a_{max}=0.7g: Superstructure displacements for (a) $m_p = m_s$ = 2.0, (b) baseline, and (c) $m_p = m_s$ = 0.5; lateral force-displacement results for (d) $m_p = m_s$ = 2.0, (e) baseline, and (f) $m_p = m_s$ = 0.5. Dashed lines envelop the baseline structure's response (Curras et al. 2001).

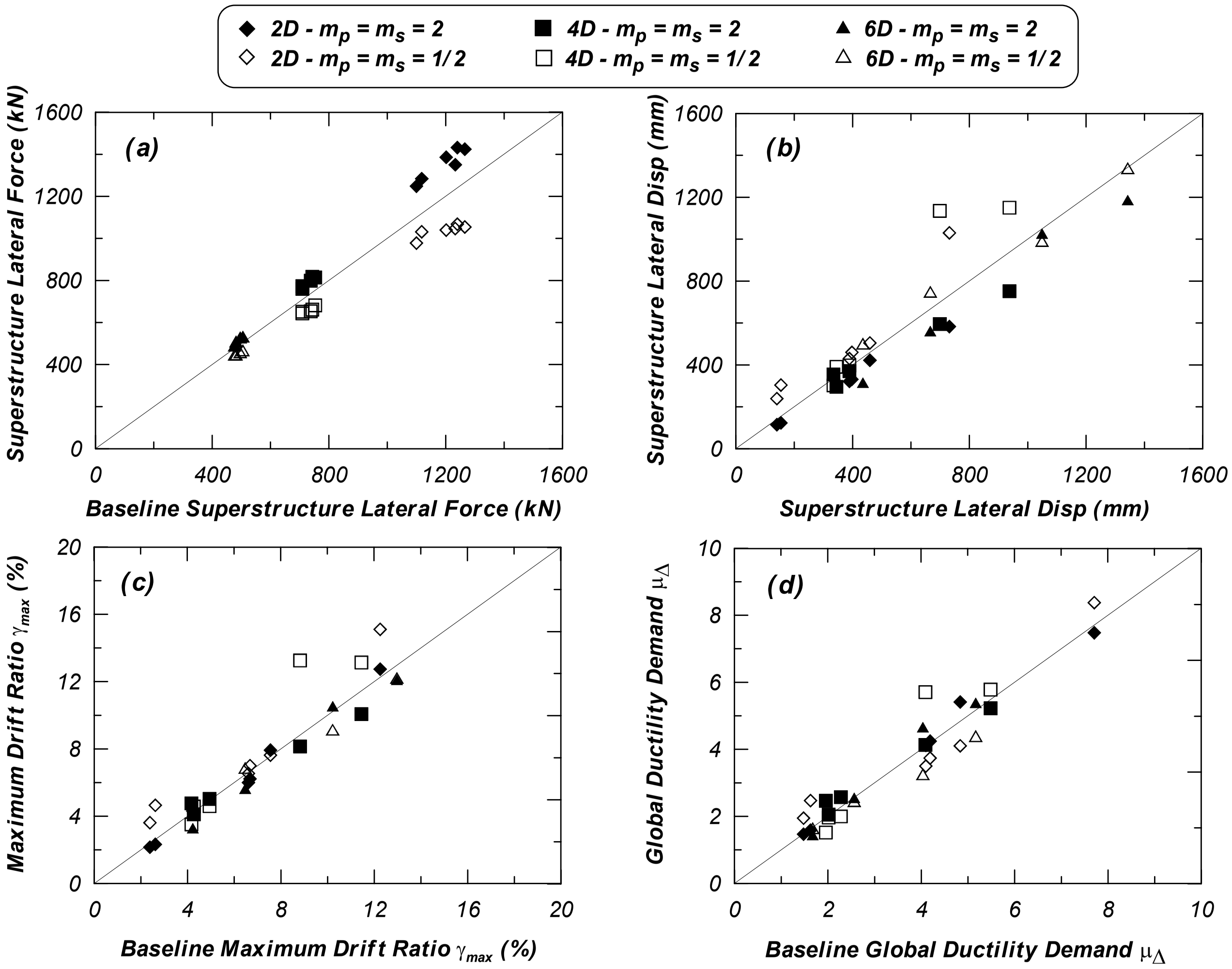

Figure 3.53 Effect of p-y parameter variations on peak responses for the 1.5 m diameter pile shaft: (a) superstructure lateral force, (b) superstructure lateral displacement, (c) superstructure drift ratio, and (d) global displacement ductility demand (Curras et al. 2001)

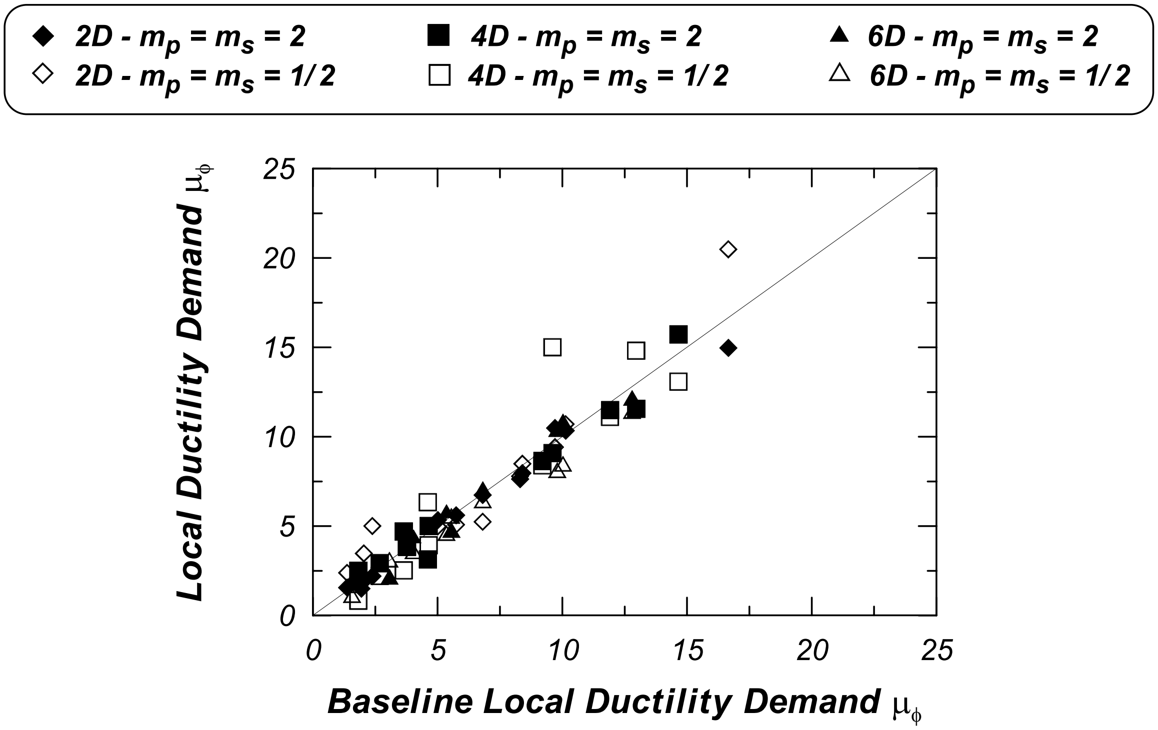

Figure 3.54 Effect of soil parameter variations on local ductility demand for the 1.5 m and 3.0 m diameter pile shafts (Curras et al. 2001).

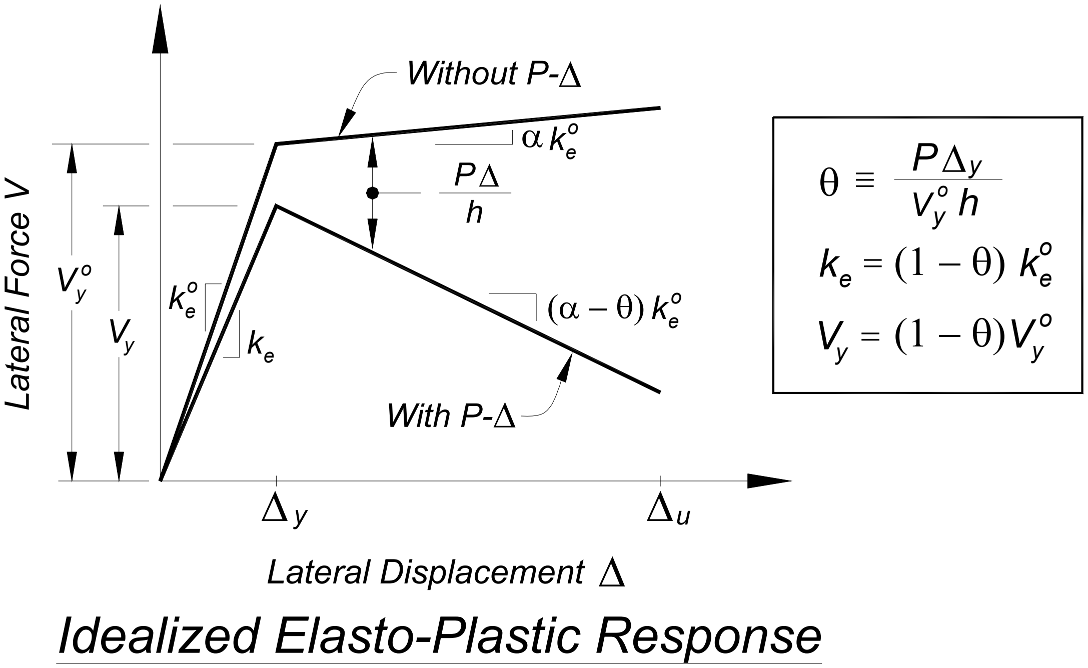

Figure 3.55 Schematic illustrating the effects of geometric nonlinearities on global response.

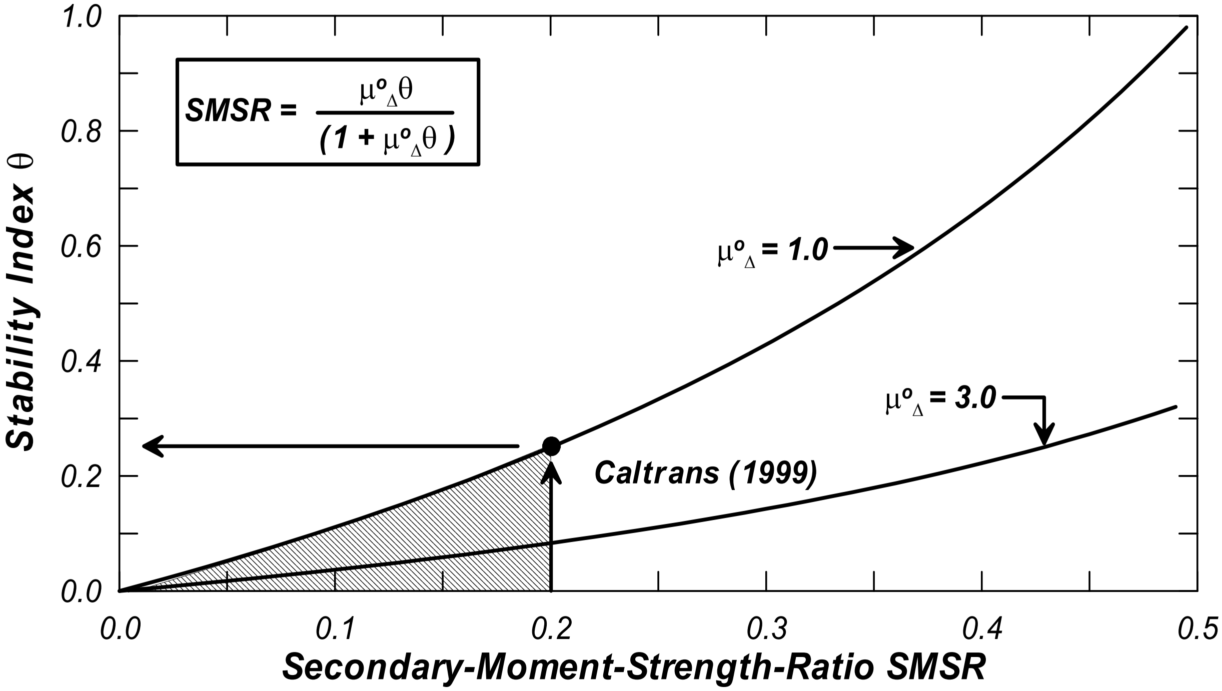

Figure 3.56 Relation between secondary-moment-strength ratio and stability index θ.

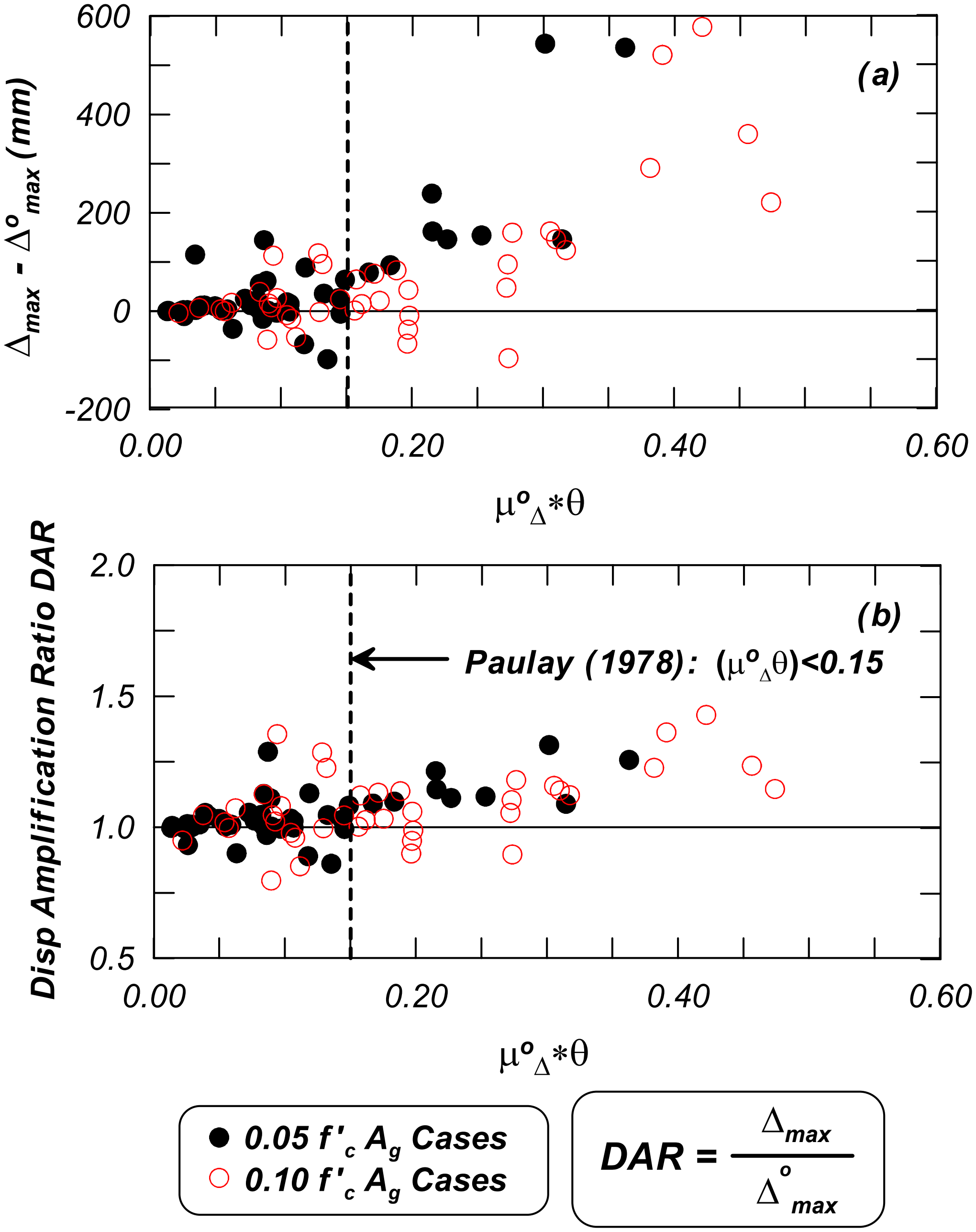

Figure 3.57 Change in displacement and ratio of maximum displacements as a function of the ductility factor μ^{o}_{Δ}* stability index θ (where μ^{o}_{Δ} does not include P-Δ effects).

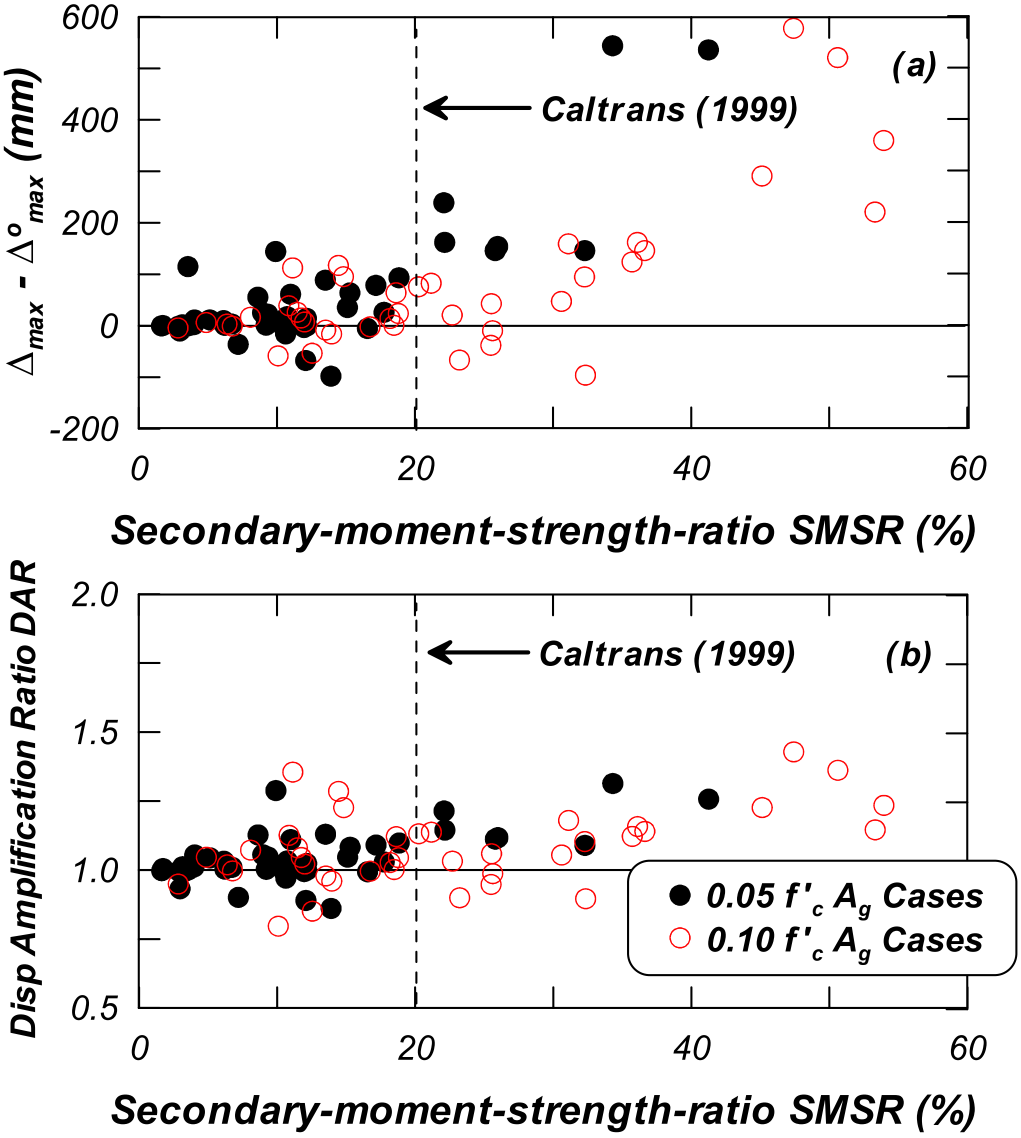

Figure 3.58 Change in maximum displacement and ratio of maximum displacements as a function of the secondary-moment-strength ratio for 3.0 m diameter pile shafts.

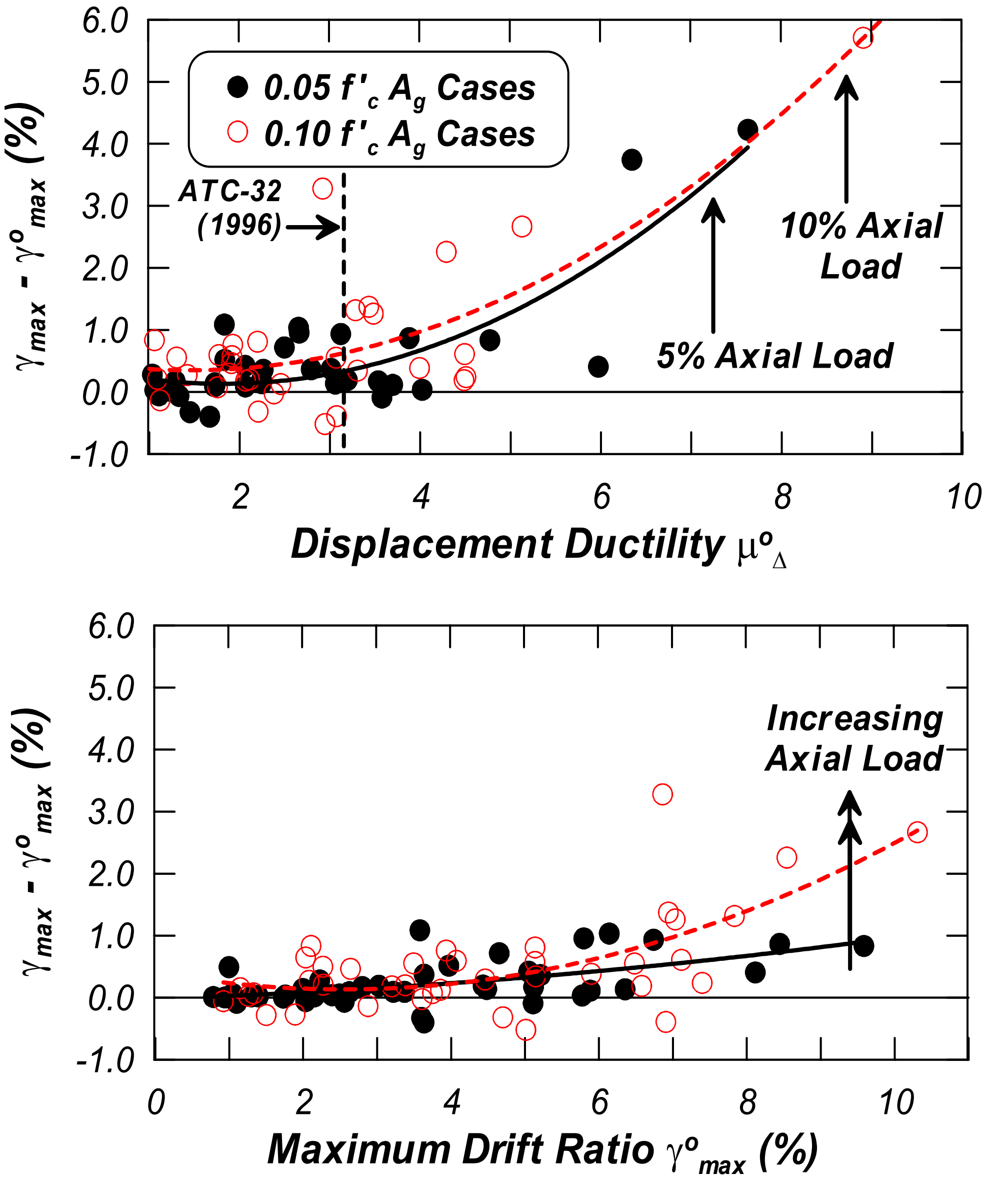

Figure 3.59 Change in maximum drift ratio γ_{max} as a function of displacement ductility μ^{o}_{Δ} and maximum drift ratio γ^{o}_{max} (where x-axis *does not* include P-Δ effects).

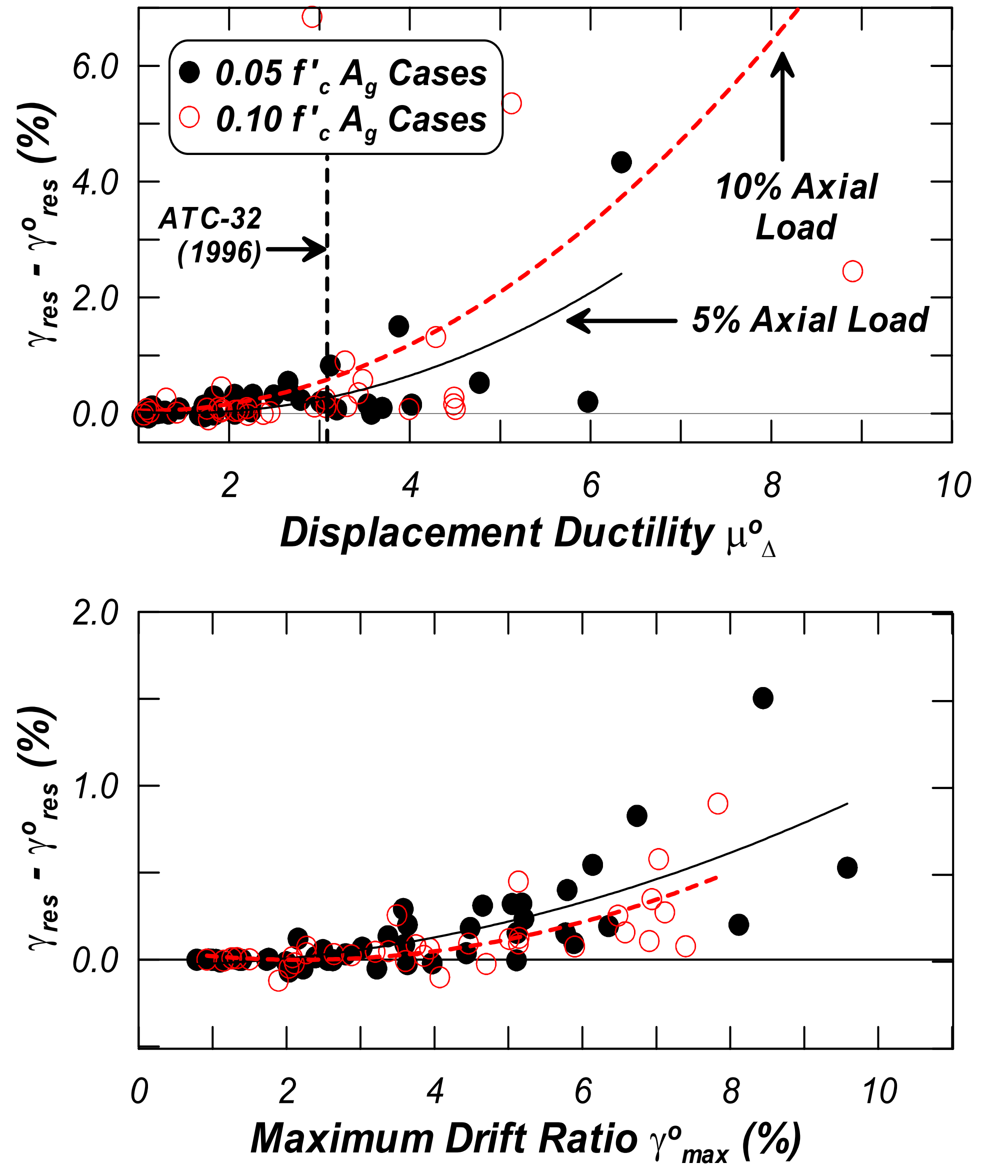

Figure 3.60 Change in residual drift ratio γ_{res} as a function of displacement ductility μ_{Δ} and maximum drift ratio γ_{max} (where x-axis *does not* include P-Δ effects).

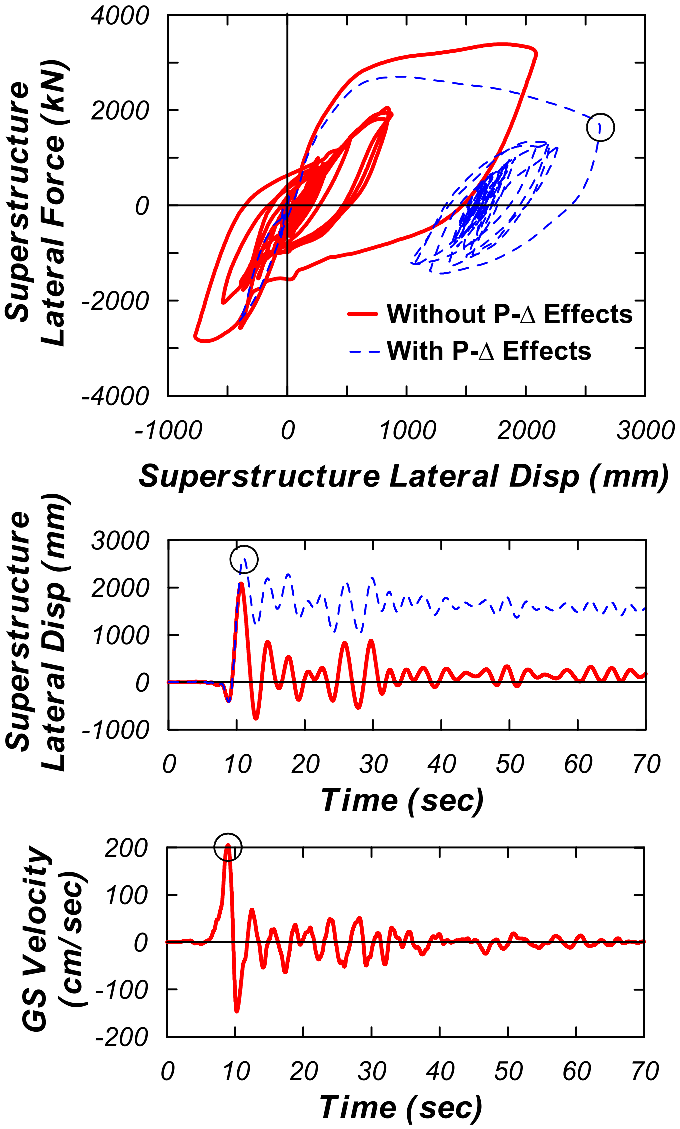

Figure 3.61 Influence of velocity pulse in near-fault ground motion (Taiwan 075E motion with $a_{max} = 0.5g$) on the lateral force-displacement response (with and without P-Δ effects) of 12.0 m tall structure with 3.0 m diameter supporting pile shaft and $0.05f'_cA_g$ axial load.

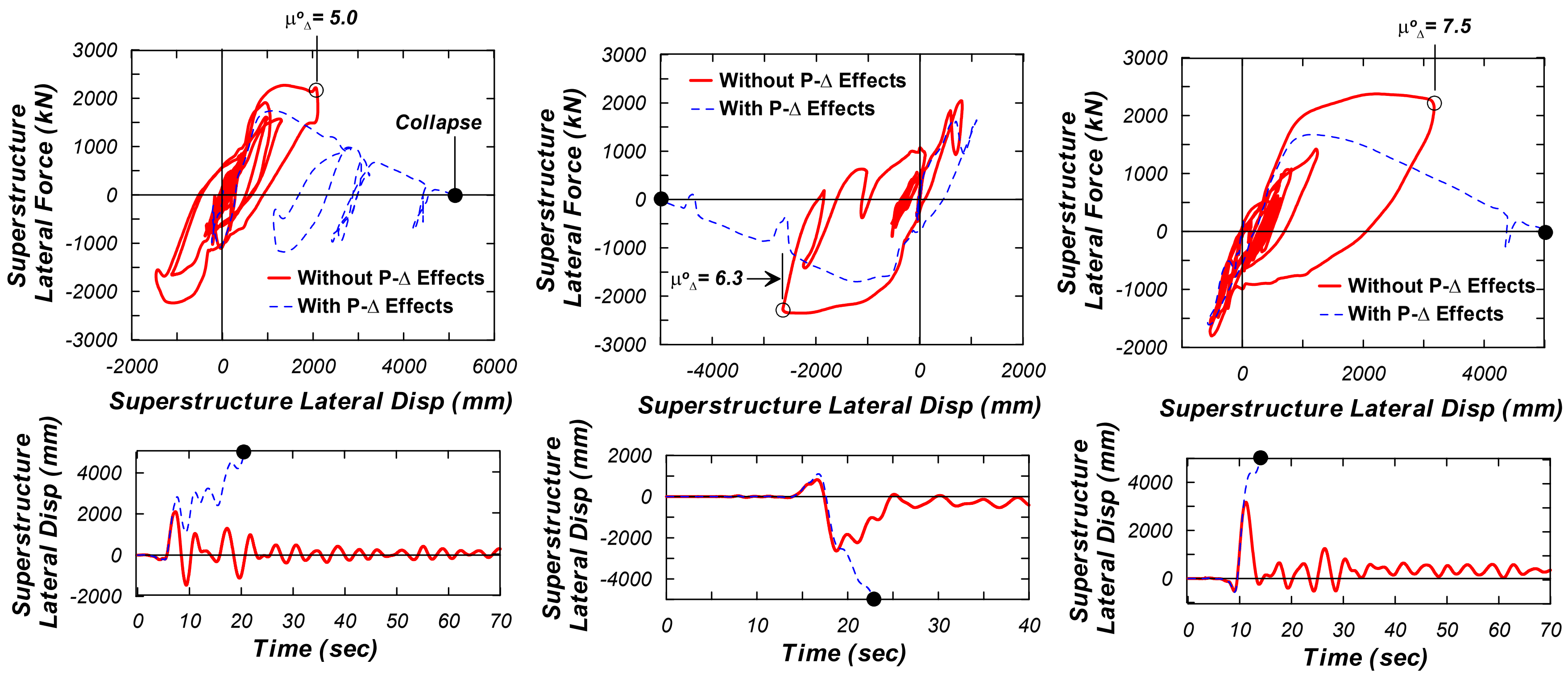

a) L_a = 18 m & Yarimca Petkim (a_{max}=0.7g)

b) L_a = 18 m & Taiwan, 068EW (a_{max}=0.5g)

c) L_a = 18 m & Taiwan, 075EW (a_{max}=0.5g)

Figure 3.62 Lateral force-displacement response at the superstructure and lateral displacement time history of structures that indicated collapse (3.0 m diameter pile shafts with $0.05f'_cA_g$ axial load).

4 Comparison of Dynamic Analyses Results with Nonlinear Static Methods

4.1 INTRODUCTION

Current simplified seismic design procedures utilize nonlinear static methods to compare system capacity with imposed demand. These methods generally couple nonlinear pushover (capacity) curves with a presumed (typically smoothed) earthquake ground surface spectrum (demand). There are several methods available in the literature to estimate displacement or force demands using the spectra for the surface ground motions. Two particularly popular methods are the substitute structure and the force-reduction approaches. Current bridge design codes generally use the force-reduction type approach (e.g., ATC-32, 1996). More recently, with the trend toward performance-based earthquake engineering, design codes for buildings have moved toward displacement-based design approaches. The basis for the estimation of inelastic displacements in these design guidelines is the substitute structure method [e.g., FEMA-273 (1997) and ATC-40 (1996)].

These spectral-based techniques generally rely on simplifying the system's response to a single-degree-of-freedom system. When utilizing force-reduction type methods, the elastic design lateral strength of a system is reduced through the use of force-reduction coefficients that relate the amount of reduction in force to the amount of tolerable or design deformation. Substitute structure based approaches rely on estimating inelastic response by replacing the nonlinear system by an equivalent linear system. The equivalent linear system will have a secant stiffness and equivalent viscous damping properties representative of the global behavior of the structure at an estimated displacement level.

Previous researchers have pointed out the limitations of such simplified methods. Nonetheless, with current computational abilities perhaps limiting the application of more rigorous analysis techniques to investigate system performance, such approaches are readily used in design. However, it has been recognized that ground motion characteristics can play an important role in the ability of such simplified methods to accurately predict inelastic demands. Of particular interest are near-fault ground motions that have strong long-period accelerations occurring early in the time history, sometimes in the form of strong, uni-directional pulses. The damaging effects near-fault motions have on structures were first observed by Bertero et al. (1978) with their analysis of the Olive View Hospital following the 1971 San Fernando earthquake. It was concluded that inelastic response could not be predicted with reasonable accuracy using methods that modify elastic response spectra. More recently, in evaluating the sensitivity of bridge structures to near-fault motions, Mahin and Hachem (1998) performed dynamic analyses of SDOF systems with details representative of bridge columns and identified trends relating the displacement demands to the fundamental period of the structure and the predominant period of the pulse. Regression analysis of their results indicated that, for intermediate- and long-period structures, current practice using the equal displacement assumption provides reasonable estimates of inelastic displacement demands. However, they noted the inaccuracy of using current spectral-based techniques for shorter-period structures. Baez and Miranda (2000), using mean values of 82 near-fault ground motions also concluded that for structures with periods less than about 1.3 seconds, inelastic displacement demands were underestimated using current spectral-based techniques. MacRae and Roeder (1999) found similar trends for short-period structures and suggested corrections to current force-reduction coefficients based on proximity to known rupture planes.

This chapter compares the inelastic displacement demands from the nonlinear dynamic finite element (FE) analyses described in Chapter 3 with displacement demands predicted using nonlinear static methods commonly used in design. The methods used for comparison are the substitute structure and the force-reduction displacement ductility period (R-μ_Δ-T) approach. An alternative method that uses the average spectral ordinates between two spectral periods of interest to the structural response is proposed and shows good promise in minimizing the error when predicting inelastic displacement demands for structures subjected to near-fault ground motions.

4.2 SUBSTITUTE STRUCTURE METHOD

The concept of the substitute structure approach relies on idealizing the behavior of an inelastic system with that of an equivalent linear system using secant stiffness and equivalent viscous damping properties representative of the global behavior of the structure at the anticipated peak displacement. Early work by Hudson (1965) and Jennings (1968) provides the general approach. Subsequent modifications by Gulkan and Sozen (1974) describe the method applied to reinforced concrete frame structures. The approach has taken several different forms in the literature. For example, Kowalsky et al. (1995) describe a displacement-based design procedure for reinforced concrete bridge columns, which is based on the substitute structure method. Recent code procedures provided by ACT-40 (1996) adopt the approach in combination with the capacity spectrum approach (Freeman 1978) to provide an alternative design procedure for retrofit of reinforced concrete buildings.

To utilize the method in the context of the structural systems studied herein, the effective damping ratio versus displacement ductility ξ_{eff} -μ_Δ relation needs to be determined for the soil-pile systems. The effective damping ratio ξ_{eff} is equivalent to the sum of the hysteretic damping of the system represented as an equivalent viscous damping term and a viscous damping component:

$$\xi_{eff} = \xi_{eq} + \xi_v \qquad \text{(Eq 4.1)}$$

where the equivalent viscous damping ratio ξ_{eq} can be determined for a range of displacement ductility μ_Δ levels as shown in Figure 4.1(a). The determination of the equivalent damping ratio ξ_{eq} for a single cycle of motion, in this case, to a target displacement ductility $\mu_\Delta = 4.0$ is shown in Figure 4.1(b) and can be determined as:

$$\xi_{eq} = \frac{A_h}{4\pi \cdot A_e} \qquad \text{(Eq 4.2)}$$

where A_h = hysteretic energy dissipated by the structure in a single cycle of motion and A_e = elastic strain energy associated with that cycle of motion, at a peak displacement. The viscous damping ratio ξ_v in Equation 4.1 was kept constant at 5%. Figure 4.2 shows the resulting damping ratio versus displacement ductility relations for the 3.0 m and 1.5 m diameter pile shafts (with an axial load = $0.05f'_cA_g$). In the design displacement ductility range for these structures (between μ_Δ = 3–5) the equivalent viscous damping ratio for these structures ranges between ξ_{eq} = 11–22%. Figure 4.2(b) compares the soil-pile-system damping (for the 3.0 m diameter pile shafts) to relations proposed by Kowalsky et al. (1995) for reinforced concrete bridge columns and Gulken and Sozen (1974) for reinforced concrete frames. In general the soil-pile damping ductility relations compare fairly well to those proposed by Gulken and Sozen (1974) and Kowalsky et al. (1995). The relation by Gulken and Sozen (1974) more closely follows the 2D-tall structures, while the Kowalsky et al. (1995) relation compares better with the 4D-tall structures. For a given displacement ductility, the 6D-tall structures have a higher effective damping ratio when compared to either the 2D- or 4D-tall structures.

The ground surface displacement spectrum (demand) and the nonlinear pushover (capacity) of the extended pile shafts considered in this study coupled with the effective damping-ratio displacement ductility ξ_{eff} -μ_Δ relation shown in Figure 4.2 for the soil-pile systems can be used to estimate the inelastic displacement demand imposed on these structures. This was done for a number of cases. However, the resulting predictions showed large variation when compared to the FE analysis, especially for ground motions with near-fault characteristics. In particular, these motions tended to have steeply increasing spectral displacement ordinates within the spectral content important to the performance of these structures (T>2–4 seconds). An example of the general difficulty in using the method when applied to near-fault motions is described below.

Figure 4.3 shows an example of the approach applied to a bridge structure supported on a 3.0 m diameter pile shaft with an above-ground height of $L_a = 2D$ and an axial load of $0.05f'_cA_g$, where the ground surface spectrum is for the Taiwan 068E motion scaled to a peak rock outcrop acceleration of $a_{max} = 0.3g$. To estimate $\Delta_{inelastic}$, the pushover analysis is used to develop the relation between superstructure displacement ($\Delta_{inelastic}$) and the structures equivalent linear period. This pushover result is then overlaid with the ground surface elastic displacement spectrum, for different values of effective damping ratio ξ_{eff}. The intersection of the pushover curve and the 5% damped displacement spectrum was used to obtain a first estimate of the displacement ductility demand, which was then used to estimate a compatible amount of damping (Figure 4.2). The displacement spectrum is determined for the new damping ratio (as shown in Figure 4.3) and the procedure is repeated until the intersection of the spectral displacement at a given damping ratio agrees with the damping-ductility relations shown in Figure 4.2.

For this case, the estimated inelastic displacement demand was $\Delta_{\text{inelastic}}$ = 450 mm which yields a displacement ductility of μ_{Δ} = 3.0, which correlates to an effective damping ratio of ξ_{eff} = 11% (from Figure 4.2). The FE analysis indicated a maximum displacement demand of $\Delta_{\text{inelastic}}$ = 320 mm or an associated displacement ductility of μ_{Δ} = 2.1, which means that the substitute structure method overestimated demands by about 40%. However, note from Figure 4.3, that the intersection of the pushover analysis and the ground surface spectrum is sensitive to small changes in effective damping because of the steep slope of the spectrum in the period range important to the structure's response. The estimated displacement demands would have been about 1050 mm for 5% damping and only 320 mm for 15% damping. As indicated by the second intersection point between the 11% damped spectrum and the pushover curve shown in Figure 4.3, an estimation of demand as high as $\Delta_{\text{inelastic}}$ = 750 mm might easily have been obtained, leading to an overprediction of demands by 230%.

This type of difficulty was generally experienced using the substitute structure approach, particularly when considering near-fault motions that have long-period spectral acceleration content resulting in rapidly changing displacement ordinates. For this reason, the substitute structure approach was not explored further.

4.3 FORCE-REDUCTION DISPLACEMENT-DUCTILITY-PERIOD (R-μ_{Δ}-T) RELATIONS

Seismic design methodologies that rely on reducing the elastic lateral force demand through force-reduction coefficients have been proposed and studied by many researchers. Miranda and Bertero (1994) provide a comprehensive review of some of these previous works. In general, force-reduction factors implemented in current codes are intended to account for damping, energy-dissipation capacity, and overstrength. However, several researchers have expressed their concern regarding the lack of physical basis for force-reduction displacement ductility relations. These and other limitations of the approach are well known [e.g., Uang (1991); Tso and Naumoski (1991); and Priestley (1993)]. Nonetheless, the current design approach for bridge structures in seismically active regions may rely on the use of force-reduction factors when simplified nonlinear static methods are applied.

In general, these force-reduction factors have been developed based on analyses of fixed-base columns. In this work, however, the approach is applied to a subset of the dynamic analyses used to study the response of extended pile shafts. In this sense, it should be clear that these relations are inherently semi-empirical by the nature of their development. It should also be noted that the "elastic period," which is used to determine the force-reduction factor (as described below), is an approximation for these systems because the soil behaves nonlinearly at much earlier stages of loading than the pile or column section.

The force-reduction factor R is defined as the ratio of the elastic lateral force demand to the lateral yield strength of the system. The elastic lateral force demand is obtained from the 5% damped elastic acceleration response spectra at the ground surface using the equivalent elastic period T_e of the system, as shown on Figure 4.4. The displacement ductility factor, as defined previously, is $\mu_\Delta \equiv \Delta_{inelastic}/\Delta_y$, where Δ_y = elasto-plastic (EP) yield displacement defined in Chapter 3, and $\Delta_{inelastic}$ = maximum displacement of the superstructure determined from the FE analyses. Monotonic pushover analyses were performed to determine the parameters V^o_y, $\Delta_{y,}$ and T_e and define the idealized EP response for the different structures; these are also shown in Chapter 3.

The relation between the force-reduction factor R and the displacement-ductility factor μ_Δ for bridge structures supported on 3.0 m diameter pile shafts is plotted in Figure 4.5. Note that the data in Figure 4.5 includes a range of periods (T_e = 1.12 to 2.84 s) and lateral strengths considered in this study, which are a result of different above-ground pile extension heights. Figure 4.5(a) shows the data for all motions listed in Table 5.1, whereas Figure 4.5(b) shows the data for only the near-fault motions used in this study. As expected, the displacement ductility demand generally increases with increasing force-reduction factor. For comparison purposes, two well-known R-μ_Δ relations proposed by Veletsos and Newmark (1960) are shown in Figure 4.5. The equal displacement observation, conceptually described in Figure 4.6, implies that $R = \mu_\Delta$ and is generally assumed to be applicable for long-period structures. The equal energy observation, which implies $R = \sqrt{(2\mu_\Delta-1)}$, is generally assumed to be applicable for medium-short-period structures. It should be noted that the data shown in Figure 4.5 include P-Δ effects in the analysis. The original proposition of Veletsos and Newmark (1960) was derived based on the observed response of elastic and elastic-plastic systems where P-Δ effects were not incorporated into the analysis. However, for these systems, the influence of P-Δ effects on the equal displacement observation was studied in Hutchinson (2001). Results indicated that the scatter of the data around the equal displacement observation existed with or without P-Δ effects incorporated in the analysis; therefore, second-order effects are included in the analysis results shown in Figure 4.5.

For displacement ductility factors $\mu_\Delta > 3.0$, 86% of the cases shown in Figure 4.5(a) fall below the equal displacement observation, and nearly all of these results are associated with near-fault or long-duration motions. Although these structures might generally be classified as "long-period" systems, the equal energy relation has been shown to be a lower bound when estimating the inelastic response of systems, particularly when the peak deformation demand is incurred during the early cycles of loading (Ye and Otani 1999). Based on energy balance concepts, Ye and Otani (1999) suggested simplified relations for estimating maximum inelastic displacements applicable for long-period systems. The lower bound of their relation is equivalent to the equal energy relation.

The data in Figure 4.5(b) are separated into the structures having a fundamental period T_e less than the pulse period T_{LP} ($T_e/T_{LP} < 1.0$) and the structures having a fundamental period T_e greater than the pulse period T_{LP} ($T_e/T_{LP} > 1.0$). Where T_{LP} is the period of the long-period pulse in the near-fault ground motions (as described in the next section). These cases suggest that modifications to the equal energy relation could be derived to capture the mean of the data with $T_e/T_{LP} < 1.0$ (i.e., as the structure "walks" into the strong spectral ordinates of the long-period pulse). A modified form is taken as:

$$R = \alpha \cdot \sqrt{(\beta \cdot \mu_\Delta - 1)} \qquad \text{(Eq 4.3)}$$

where α and β can be found by regressing through the data with $\mu_\Delta > 1.0$ and $T_e/T_{LP} < 1.0$. In this case, α and β were determined as $\alpha = 0.70$ and $\beta = 3.10$. The parameters α and β might be defined in terms of proximity to fault and/or direction of rupture propagation (e.g., fault-normal or fault-parallel) with a larger database of motions and structures, using a similar regression approach.

4.3.1 Transition between Long- and Short-Period Systems

In the use of an R-μ_Δ-T relation, one typically needs to define a transition period between the definition of a "long-" and "short"-period structure. This period will define the transition between the applicability of the equal energy and the equal displacement relations and is important in the estimation of inelastic deformations. However, it has long been recognized that there is a large variation from one earthquake to the next in the dominant frequency content of the motion. In this sense, the transition period will generally vary from one earthquake motion to the next and should be influenced by the source mechanism, the path of the motion, and the surface geology at the site. For example, studies of the frequency content of a large database of ground motions indicate there is a large variation in the mean, predominant, and smooth spectral period between any two earthquakes (e.g., Rathje et al. 1998). Several suggestions are available in the literature for this transition period. In this case, it is instructive to review the early work of Veletsos and Newmark (1960) in the original proposal of the equal displacement and equal energy observations. The ground motions used in this study were fairly "regular" motions, two of which included recordings from the 1933 Vernon and 1940 El Centro earthquakes. In this case, the predominant periods of these motions, defined as the period associated with the peak in the elastic ground surface acceleration response spectra, were less than 0.5 seconds.

In general, the trend has been to assume the transition period between the equal displacement and equal energy observations as the predominant period T_p of the ground motion, based on the peak of the elastic acceleration response spectrum. For example, Ye and Otani (1999) suggest this can be taken between 0.4–0.6 seconds, whereas Paulay and Priestley (1992) suggest a transition period of $T = 0.7$ seconds. Alternatively, ATC-32 (1996) suggests the transition period be specific to the ground motion considered and can be taken as the characteristic period T_c of the motion. The characteristic period T_c is equivalent to the peak of the input energy spectrum, which is nearly equivalent to the transition between the constant velocity and constant acceleration regions of a Newmark-Hall tripartite plot (Newmark and Hall 1982). Vidic et al. (1994) suggest a modified form of the characteristic period T_c be used as the transition period. In this case, Vidic et al. provide a slight correction to T_c that accounts for the level of cyclic ductility that the system has attained.

The large variation in the predominant period T_p when based on the peak of the acceleration ground spectra for a particular ground motion is illustrated in Figure 4.7. In this case, the ground surface motion is shown for the baseline site subjected to the Landers, Lucerne motion at four levels of scaled peak outcrop acceleration. Based on the peak in the ground surface acceleration response spectra, the predominant period T_p for each of these motions varies with the intensity of shaking and was determined as T_p = 0.23, 0.70, 0.70, and 1.10 seconds for the motions with a_{max} = 0.3, 0.5, 0.7 and 0.9g, respectively.

The use of the Newmark-Hall tripartite approach to determine T_c is illustrated in Figure 4.8(a) for the Synthetic #2 (Bay Bridge) motion. For this motion, the transition between constant acceleration and constant velocity was determined as T_c = 1.03 seconds. It should be noted that this motion has a rather smooth acceleration spectrum, where T_c is fairly easy to estimate. Other motions used in this study showed a larger degree of variability in clearly defining the intersection between the constant acceleration and constant velocity regions of the spectra, resulting in slight variations when estimating T_c graphically. Based on the peak in the elastic acceleration response spectrum, for this same case, the predominant period was estimated as T_p = 0.90 seconds [Figure 4.8(b)].

The difficulty in using either of the above mentioned definitions (T_p or T_c) as a transition period between the equal displacement and equal energy relations is that the frequency characteristics of the structural system under consideration are not accounted for in the choice of period. Figure 4.8(b) shows an alternative selection of the transition period applied to the near-fault Turkey, Yarimca Petkim motion. In this case, the transition period is defined as the peak in the acceleration response spectrum at a period greater than the equivalent elastic period T_e of the system under consideration. For this case, the period of the strong spectral ordinates in the long-period T_{LP} is determined as T_{LP} = 3.23 seconds. This definition for the transition period would be more applicable to near-fault motions that have large long-period spectral ordinates, where the (initial) elastic period of the system under consideration is greater than the predominant period T_p of the motion.

Figure 4.9 compares the characteristic period T_c of the ground motions used in this study to both the predominant period T_p and the period of the dominant spectral ordinates in the long period T_{LP}. In this case, the characteristic period T_c has been estimated using the Newmark-Hall tripartite approach, the predominant period T_p is based on the peak in the 5% damped elastic acceleration response spectra and T_{LP} is based on the long-period peak in the 5% damped elastic acceleration response spectra. In general, the predominant period T_p of the motions are lower than the characteristic period T_c, as shown in Figure 4.9(a). This figure also shows a large scatter from the 1:1 line in comparing T_p and T_c for the near-fault motions. Figure 4.9(b) shows that, as expected, for the near-fault motions, T_{LP} is larger than the characteristic period T_c.

The validity of using T_{LP} as a transition period can be studied by using a general R-μ_Δ-T relation to predict the inelastic displacement demands in these structures. Although many R-μ_Δ-T expressions exist in the literature, the analysis results for near-fault motions were compared to a general bilinear relation which assumes equal displacement in the long-period range and a linear relation between the force-reduction factor R and displacement ductility factor μ_Δ in the short-period range:

$$(\mu_\Delta)_{Formula} = \begin{cases} (R-1)\cdot\dfrac{T_{LP}}{T_e}+1 & \textbf{\textit{for}} \quad T_e \le T_{LP} \\ R & \quad\quad\;\; T_e > T_{LP} \end{cases} \qquad \text{(Eq 4.4)}$$

where T_{LP} is the period of the long-period pulse in the near-fault ground motions (as described above).

The applicability of the R-μ_Δ-T relation to bridge structures supported on extended pile shafts is studied through a comparison of the actual displacement ductility factor μ_Δ, as obtained from the FE analyses, with the displacement ductility factor $(\mu_\Delta)_{Formula}$ calculated using Equation 4.4. The set of data in Figure 4.5 with near-fault ground motions is plotted against the period ratio T_e/T_{LP} in Figure 4.10, in terms of the ratio of displacement ductility factors C_μ where:

$$C_\mu = \frac{\mu_\Delta}{(\mu_\Delta)_{Formula}} \qquad \text{(Eq 4.5)}$$

The data in Figure 4.10 correspond to the ratio of displacement ductility factors C_μ with P-Δ effects. Results without P-Δ effects are very similar and lead to the same general observations. For $T_e/T_{LP} \le 1.0$, 70% of the displacement ductility factors were underestimated using Equation 4.4 (i.e., $C_\mu > 1.0$). The mean of these analyses with $T_e/T_{LP} \le 1.0$ is $C_\mu = 1.43$, with a coefficient of variation (COV) of 41%. When T_e/T_{LP} is less than 1.0, yielding of the structure causes its secant period to lengthen and become closer to the period of the pulse in the ground motion. Conversely, if the ratio T_e/T_{LP} is greater than 1.0, yielding of the structure causes its secant period to lengthen and move further away from the period of the pulse in the ground motion. For the data with $T_e/T_{LP} \ge 1.0$, the ratio of displacement ductility factors C_μ is closer to 1.0 except for three cases where $C_\mu > 1.5$ occurred for the Taiwan motions with peak outcrop accelerations of a_{max} = 0.3 and 0.5 g. These motions had a wide long-period band of strong spectral ordinates that descended fairly slowly in the spectra. Excluding these three data points, the mean of the data where T_e/T_{LP}>1.0 was C_μ=1.05 with a COV=23%, suggesting that the equal displacement assumption is reasonable for these long-period structures, provided the elastic period of the structure is greater than the period of the pulse in the motion.

The C_μ versus T_e/T_{LP} results in Figure 4.10 show that Equation 4.4 generally underestimates ductility demands from near-fault ground motions if the elastic period of the structure is less than the ground motion's pulse period. The scatter in the analysis results is understandable given the many complicating factors, including the facts that the ratio T_e/T_{LP} provides no information on the strength of the pulse in the ground motion and that, as described above, it is difficult to define the period of the pulse T_{LP} in practice.

4.4 MEAN SPECTRAL DISPLACEMENT APPROACH

Force-reduction and substitute structure-based approaches appear to have limited accuracy in predicting the inelastic displacement demands imposed on these types of structures by ground motions with long-period pulses. One possible reason is that they generally use a single response spectra ordinate as an input to the relation, e.g., the equivalent elastic period T_e of the structure and an elastic response spectrum are often used to estimate displacement demand (or force demand through the force-reduction factor). In the example on the left side of Figure 4.11, the three motions have identical elastic response spectral values for the given elastic structural period (T_e), but have very different spectral values at longer periods (such as might be introduced by a near-fault pulse). Inelastic deformations will degrade the structural stiffness and lengthen the effective period of the system. The secant stiffness at the peak superstructure displacement can be used to define a secant period T_{sec} that represents the longest effective period of the system. The three motions on the left side of Figure 4.11 have very different spectral values at T_{sec} despite having the same value at T_e. The example on the right side of Figure 4.11 illustrates the same concept, except that the three spectra have very different spectral values at T_e and the same spectral value at T_{sec}. From these schematic examples, it seems reasonable to expect that the structure's inelastic displacement may be better related to the spectral content between T_e and T_{sec}, and not just to the spectral value at any single value of T.

An alternative approach for the prediction of inelastic displacements is explored herein. This approach uses the mean spectral displacement between two periods that are considered most relevant for the structure. Prior to describing the approach, a review of the literature indicated that a similar approach, using two frequencies to estimate force demands imposed on a system was described by Kennedy et al. (1984). First, the method described by Kennedy et al. will be discussed and the differences between this method and the approach used in this report will be provided. Subsequently, the mean spectral displacement method will be described and applied to a subset of the data used in the dynamic analyses of extended pile shaft supported structures.

4.4.1 Previous Work

A similar approach using two frequencies to estimate force demands was used by Kennedy et al. (1984) to study the seismic response of nuclear power plants subjected to a range of ground motions. Nuclear power plants typically are constructed of concrete shear wall- or braced-frame-type lateral force-resisting systems. In this case, hysteretic models with nominal degrading stiffness and strength and pinching behavior were used to model the response of these fairly short-period structures. The frequency range under consideration was between 1.8–10 hertz. Two global displacement ductilities representative of the onset of minor and major structural damage of these systems were considered ($\mu_\Delta = 1.85$ and 4.3).

Kennedy et al. performed a series of nonlinear time history analyses of representative nuclear power plant structures, and by scaling the input ground motion, determined the force-reduction (R) factors required to attain the target displacement ductility levels. The resulting R factors were then compared to R factors predicted using an approach Kennedy et al. termed the "spectral averaging method." By using the approach, R factors could be estimated with Equation 4.6.

$$R = \mu_\Delta \cdot \left(\frac{f'_{ea}}{f} \right)^2 \cdot \left(\frac{S_a(f,\xi)}{\overline{S_a}\left(f_u - f_s, \xi'_{ea}\right)} \right) \qquad \text{(Eq 4.6)}$$

where μ_Δ = displacement ductility, f_s = secant frequency, f_u = an upper-frequency bound, $S_a(f,\beta)$= spectral acceleration at the elastic frequency f and elastic damping ratio ξ (Kennedy et al. used $\xi = 3$ and 7%), $\overline{S_a}\left(f_u - f_s, \xi'_{ea}\right)$ = average spectral acceleration between the frequency f_u and f_s and at an average effective damping ratio ξ'_{ea}, and f'_{ea}, ξ'_{ea} = average effective frequency and damping ratio, respectively, within the frequency band f_u and f_s. The effective damping ratio and the different frequencies (secant and upper frequency) were given as functions of empirically derived damping and frequency shift coefficients. Damping and frequency shift coefficients provided by Kennedy et al. were based on the number of strong nonlinear cycles anticipated to reach the target displacement ductility under the ground motions considered. Comparison of R factors predicted using the spectral averaging method to those estimated with the nonlinear time history analyses indicated fairly close correlation with a low coefficient of variation for most of the cases considered. Kennedy et al. did note that averaging the acceleration ordinates using uniform weighting between the two bounding frequencies gave better results when compared with either averaging the accelerations assuming a linear increase in weighting as frequencies decreased or with using uniformly weighted average spectral velocities.

4.4.2 Approach Suggested

An alternative approach for predicting inelastic displacements is explored. This approach uses the mean spectral displacement between two spectral periods that are considered most relevant for the structure.

This work differs from the approach described above in several ways. In general, the structural systems considered are very different: the systems used herein are generally of a long-period nature, while nuclear power plants are typically very stiff, short-period structures. The approach of Kennedy et al. (1984) also estimates demands based on forces, whereas the approach used herein provides a direct estimation of displacements. In addition, the periods (or frequencies) suggested by Kennedy et al., which bound the averaging technique, consist of a period greater than the elastic period (the secant period) and an upper-bound period that is greater than the secant period. The mean spectral displacement method suggests the use of two bounding periods also, with the first period taken as the system's elastic period. The method described herein also allows for the assessment of the approach to a wide range of displacement ductility levels. Kennedy et al. focused on two primary displacement levels indicative of the performance states of interest for nuclear power plants. Finally, Kennedy et al. proposed the use of weighted averages applied to an interval of elastic spectral acceleration ordinates that have been reduced based on anticipated (changing) damping levels. The weighting scheme utilized is tied to the number of strong nonlinear cycles anticipated; therefore, this must be known in advanced. In the context of the method used herein, where the approach is primarily targeted at reducing the variation in predictions associated with near-fault motions, it may be difficult to estimate hysteretic damping dissipated by the system without performing a nonlinear dynamic analysis.

In the mean spectral displacement method presented in this research, the inelastic displacement is calculated from the elastic response displacement spectrum using:

$$\Delta_{mean} = \frac{1}{T_2 - T_1} \int_{T_1}^{T_2} S_d^e(T) \cdot dT \qquad \text{(Eq 4.7)}$$

where $S_d^e(T)$ = elastic response displacement spectrum, and T_1 and T_2 define the period interval considered most important to the structure. Note that the damping ratio for the elastic displacement spectra was taken as 5%, and was not adjusted for the hysteretic yielding of the structure. Several possibilities for defining the "period interval" for the integral in Equation 4.7 are discussed below. Each definition of the period interval was evaluated by its effect on the ability of Equation 4.7 to predict the dynamic analysis results. As was previously suggested and will be shown below, a promising choice for defining the period interval is to assume $T_1 = T_e$ = elastic period of the structure, and $T_2 = T_{sec}$ = secant period of the structure defined using the maximum inelastic displacement of the structure. The mean spectral displacement approach is shown schematically in Figure 4.12 for the case where T_e and T_{sec} are used to define the period interval for Equation 4.7.

The relative merits of this approach were evaluated in Figure 4.13 and Figure 4.14 by comparing several different choices for the period interval. The cases shown in both of these figures are for structures supported on 3.0 m diameter pile shafts with axial loads of $0.05f_c'A_g$ and including P-Δ effects (similar results were obtained without P-Δ effects). In all cases, displacement ratios C_Δ (Equation 4.8) were used to compare the dynamic analysis results to the mean displacement estimate:

$$C_\Delta = \frac{\Delta_{inelastic}}{\Delta_{mean}} \qquad \text{(Eq 4.8)}$$

where $\Delta_{inelastic}$ is the inelastic displacement from the dynamic FE analysis, and Δ_{mean} is the mean elastic displacement demand as determined by Equation 4.7. It follows that C_Δ values less than 1.0 indicate that Equation 4.7 produced a conservative (high) estimate of inelastic displacement. Figure 4.13(a) shows a case where the two periods are both taken as T_e (i.e., as if only one period was used). In this case, a displacement ratio C_Δ=1.0 would correspond to the equal displacement assumption.

Figure 4.13(b) and (c) show cases where the two periods are both taken as T_{sec} (i.e., as if only one period was used). For Figure 4.13(b), T_{sec} was defined based on the apparent stiffness at the peak inelastic displacement from the dynamic analysis, which assumes that the correct inelastic displacement is known. While this is clearly never the case, this approach was nonetheless used as a means of conceptually evaluating the method. For Figure 4.13(c), T_{sec} was defined at the peak displacement predicted by the intersection of the nonlinear pushover response and the elastic displacement spectra, as illustrated in Figure 4.15. There is a slight loss of accuracy (increase in $S_{x/y}$, the standard error of the estimate) in going from Figure 4.13(b) to (c), which is understandable given that the approach in (b) assumes that the correct inelastic displacement is known.

Figure 4.14(a), (b), and (c) show cases where the period interval is defined by T_1=T_e and T_2=T_{sec}. Parts (a) and (b) show cases where the method is applied using a 5% damped spectra (as was done for the results shown in Figure 4.13). Part (c) of Figure 4.14 uses a 15% damped spectra to determine C_Δ. The larger value of damping of ξ = 15% is more compatible with the level of hysteretic damping anticipated for these structures between ductility levels of μ_Δ = 2–5 [as shown in Figure 4.2(b)]. For Figure 4.14(a) and (c), T_{sec} was defined at the peak inelastic displacement from the dynamic analysis, while for Figure 4.14(b), T_{sec} was defined at the peak displacement predicted by the intersection of the nonlinear static pushover response and the elastic displacement spectra (as illustrated in Figure 4.15). There is a slight loss of accuracy going from Figure 4.14(a) to (b), as was seen from Figure 4.13(b) to (c), due to the fact that Figure 4.14(a) assumes that the correct inelastic displacement is known. Regardless of how T_{sec} was defined, the use of a mean spectral displacement between T_1=T_e and T_2=T_{sec} resulted in a smaller standard error than was obtained using only a single period [i.e., using only the elastic period (T_1=T_2=T_e) or only the secant period (T_1=T_2=T_{sec})]. This can be seen by comparing either Figure 4.13(a), (b), and Figure 4.14(a) or Figure 4.13(a), (c), and Figure 4.14(b). Although the regression of the data shown in Figure 4.14(c) shows a larger mean value of C_Δ, the standard error of these data is still lower than the cases using a single period. In addition, the use of a mean spectral displacement resulted in a C_Δ that had virtually no dependence on μ_Δ. The effect of damping ξ used in the mean spectral displacement approach is illustrated in comparing Figure

4.14(a) and (c). Using the lower value of ξ = 5% in the approach tends to be conservative Figure 4.14(a), while applying the approach using a higher damping of ξ = 15% is slightly unconservative Figure 4.14(c). It is reasonable to assume that for these cases, using either ξ = 10% and/or some form of weighted average, the displacement ratio C_Δ may have been closer to 1.0.

Figure 4.16 compares the use of the force-reduction approach and the mean spectral displacement method applied to the Taiwan motions with large permanent displacement offsets, which have been separated into their permanent and transient components of motion, as described in Section 3.6. The R-μ_Δ relation shown in Figure 4.16(a) shows a large degree of scatter from either the equal displacement or equal energy observation. In this case, 65% of the analysis cases fall below the equal energy relation. As anticipated, the transient and permanent components of each motion also showed very different force-reduction displacement ductility relations when compared to the original motion, as the frequency content of the permanent and remaining transient component of motion are very different. Figure 4.16(b) shows the mean spectral displacement method applied to the same set of analyses of the Taiwan motions with large permanent offsets. In this case, the estimated C_Δ is based the period interval between $T_1 = T_e$ and $T_2 = T_{sec}$ and a 5% damped spectrum. The secant period is taken as the period at the peak displacement ductility μ_Δ calculated from the dynamic analysis. The mean of these data was C_Δ = 0.83 with an associated COV = 22%. With the exception of 2 data points, all predictions of C_Δ were conservative (i.e., $C_\Delta < 1.0$).

The results in Figure 4.13, 4.14, and 4.16 represent an initial evaluation of the conceptual merits of using a mean spectral displacement method (Equation 4.7), and as such suggest that the method has promise for reducing uncertainty in predicting inelastic displacements for these types of structures. Additional efforts need to be taken to evaluate the method over a broader range of structural periods and ground motions, and to explore refinements that might improve its accuracy. For example, some immediate refinements may be to use the secant period T_{sec} that corresponds to the inelastic displacement predicted by Equation 4.7 (along with T_e for defining the period interval), or to evaluate some simple weighting functions for integrating the area under the elastic displacement spectra. Other possible refinements include adjusting the amount of damping (through the use of weighting functions) or including empirical adjustment factors.

4.5 SUMMARY AND CONCLUSIONS

Inelastic displacements calculated from the dynamic analyses presented in Chapter 3 were compared to displacement predictions using a substitute structure and a force-reduction type approach. For the ground motions considered in this study, the substitute structure approach showed a variation in its ability to predict inelastic displacement demands when compared to the FE analysis. This was particularly true when considering ground motions with near-fault characteristics, which tended to have steeply increasing spectral displacement ordinates within the period range important to the performance of these structures (T>2-4 seconds), providing for a large variation and sensitivity in the resulting displacement estimation.

An $R-\mu_\Delta-T$ relation was used to compare the displacement demands calculated by the FE analysis. The equal displacement observation, which is generally considered applicable for long-period structures, appears to be reasonable for near-fault motions provided the elastic period of the structure is longer than the period of the pulse (if present). In the shorter-period range, however, the $R-\mu_\Delta-T$ relation in Equation 4.4 underestimated the inelastic displacements. An adjustment to the $R-\mu_\Delta-T$ relation for the effects of long-period pulses was explored, where the adjustment depended on the T_e/T_{LP} ratio (T_e = equivalent elastic period of structure, T_{LP} = period of the long-period pulse). The resulting relation still had a large coefficient of variation, which is understandable given that the T_e/T_{LP} ratio provides insufficient information regarding the pulse characteristics relative to the other components of the ground motion.

An alternative design approach for prediction of inelastic displacements was explored that uses the mean elastic spectral displacement (for 5% damping) between two periods that bracket the range of periods most important to the structure. When these two periods are taken as the elastic period (T_e) and the secant period at peak displacement demand (T_{sec}), the results showed a substantial reduction in the standard error of the estimate. This improvement in the accuracy of predicting inelastic displacements, given a site-specific displacement spectrum of a near-fault ground motion, indicates that this approach has promise and should be evaluated in greater detail.

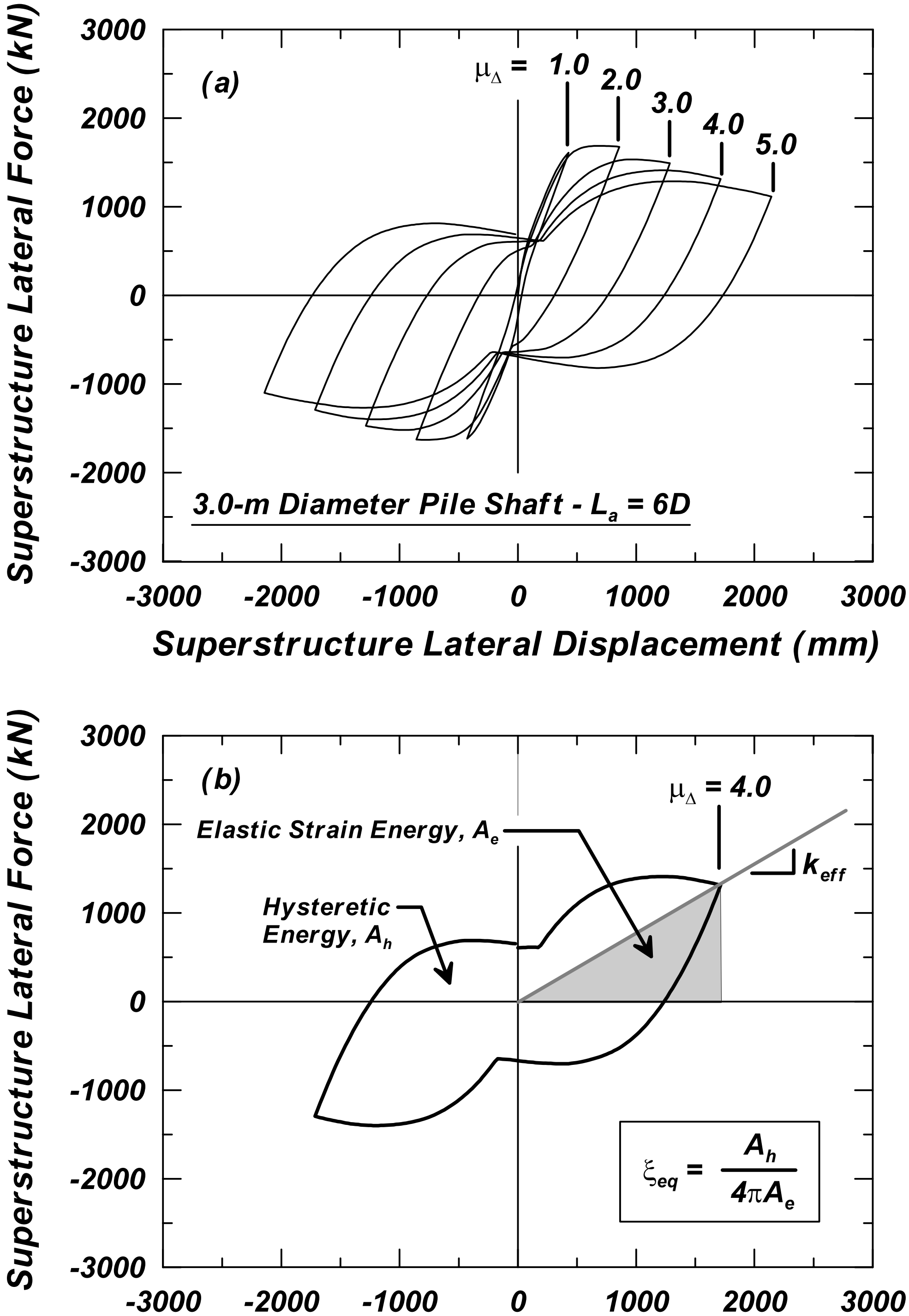

Figure 4.1 Determining the equivalent damping ratio ξ_{eq} for soil-pile systems: (a) cyclic response at target displacement ductility levels from $\mu_\Delta = 1.0$–5.0 and (b) estimation of equivalent damping ratio ξ_{eq} at a displacement ductility of $\mu_\Delta = 4.0$.

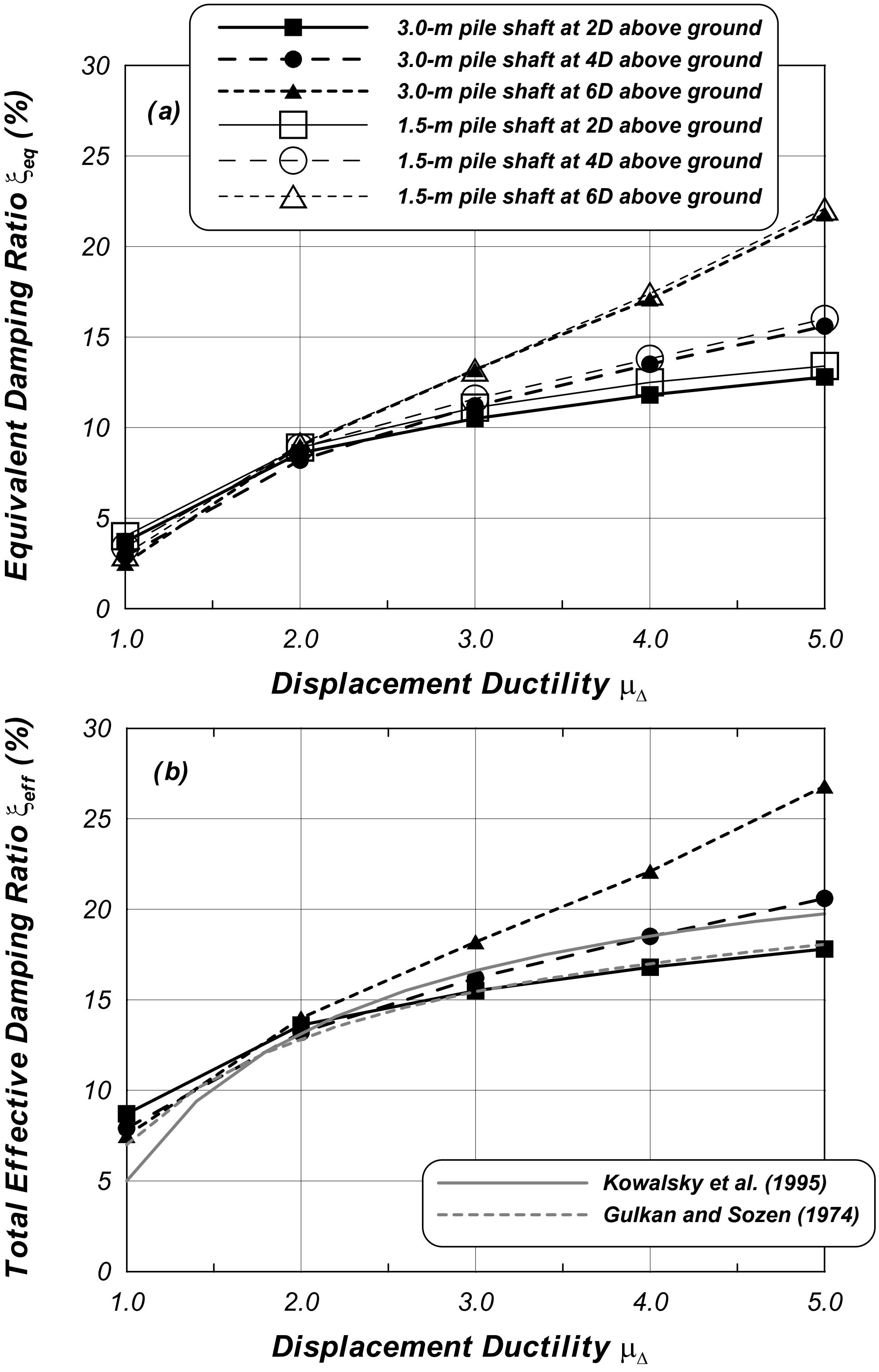

Figure 4.2 Damping ratio ξ versus displacement ductility μ_Δ: (a) equivalent damping ratio and (b) total effective damping ratio (compared to 3.0 m pile shafts only).

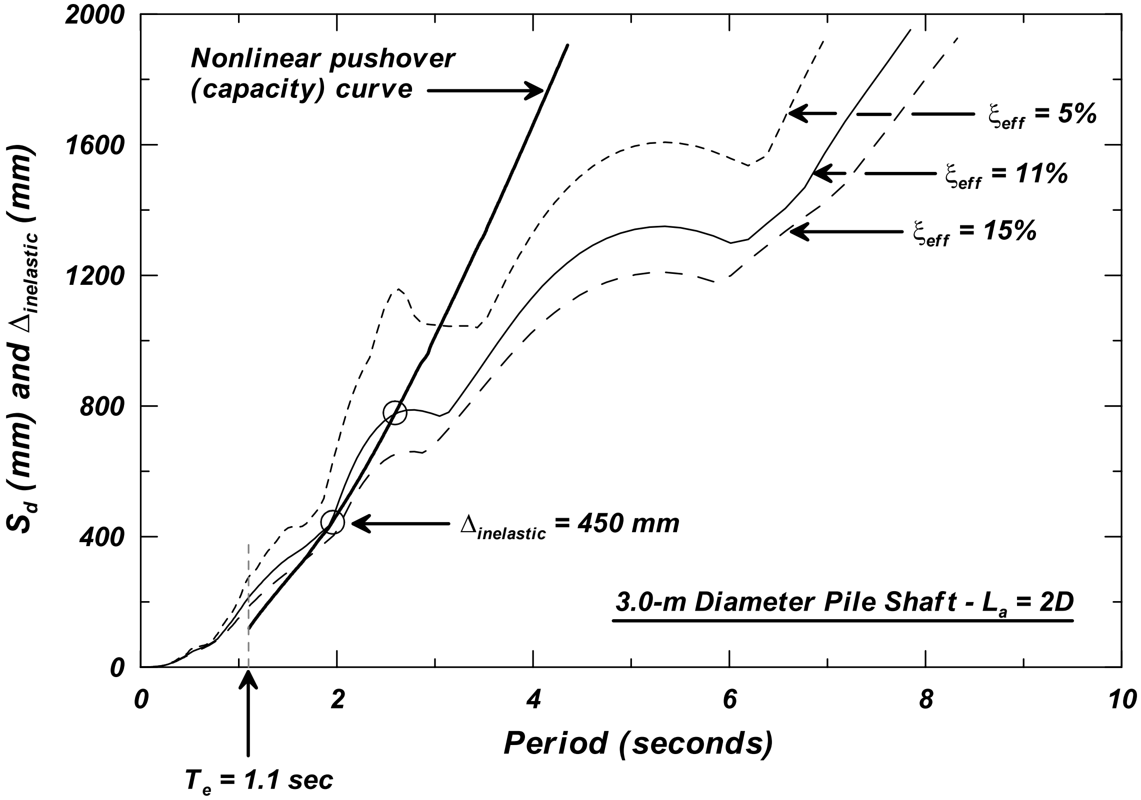

Figure 4.3 Example of estimating inelastic displacement demand using the substitute structure approach for a 3.0 m diameter pile shaft with an above-ground height of L_a = 2D supporting an axial load of $0.05f'_cA_g$ [Taiwan 068E ground surface spectra (with a scaled rock outcrop acceleration of a_{max} = 0.3g)].

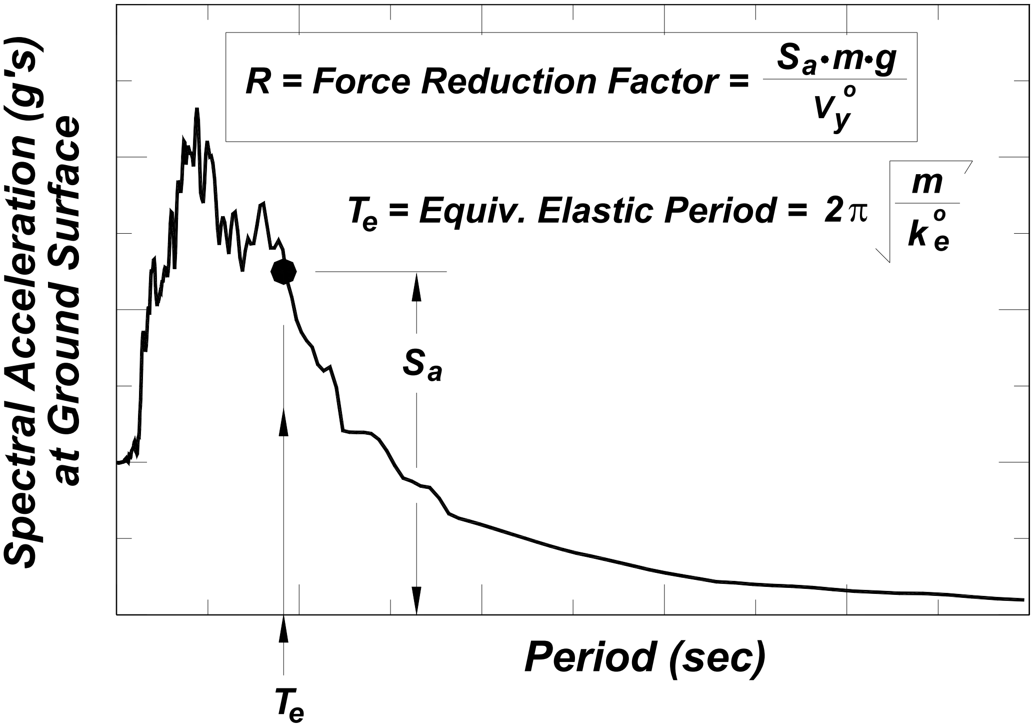

Figure 4.4 Estimating the force-reduction factor R from a ground surface acceleration spectrum based on the definitions used in this study.

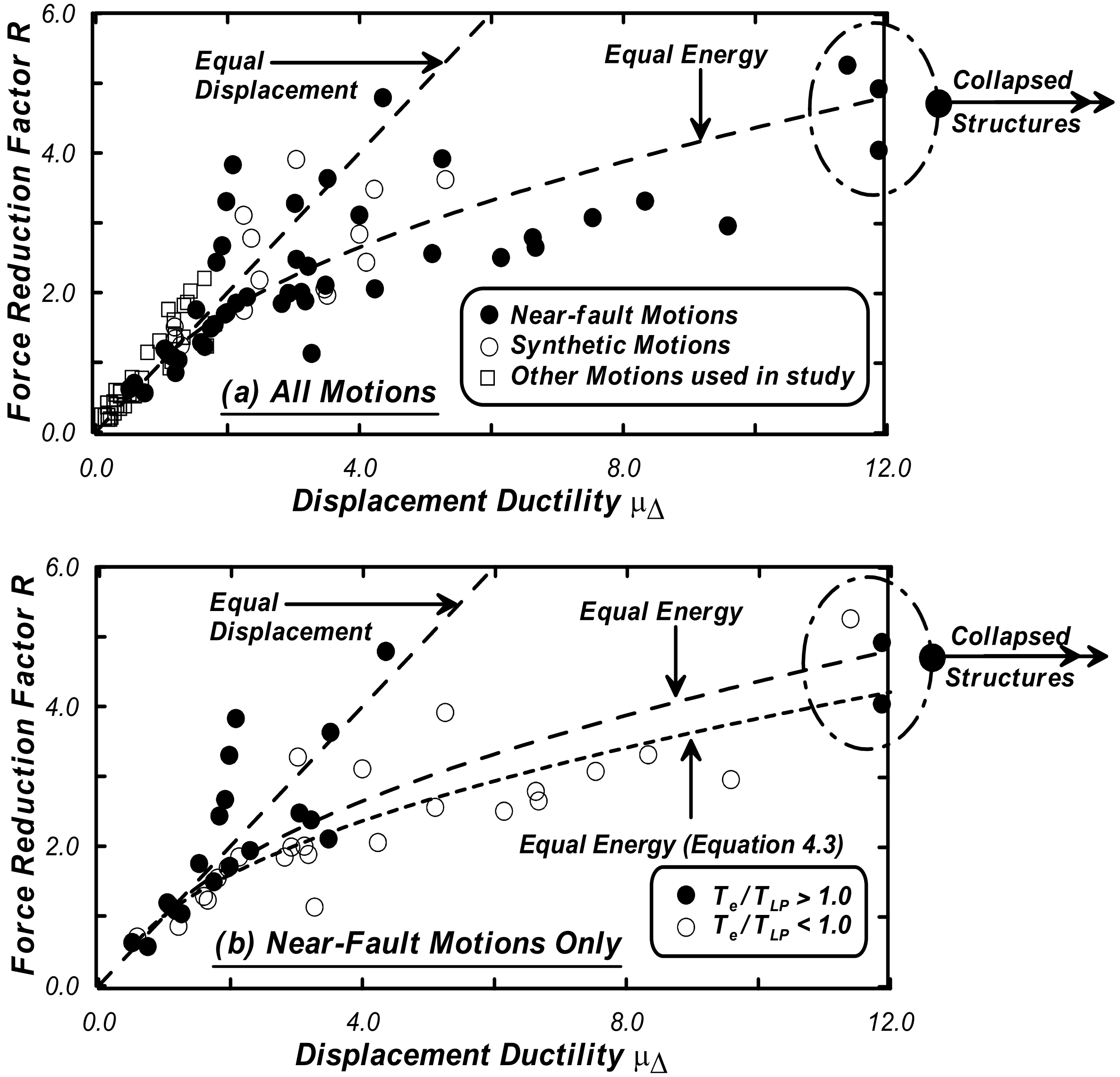

Figure 4.5 R-μ_Δ relation for structures supported on extended pile shafts — results from 3.0 m diameter pile shaft analyses with $0.05f'_cA_g$ (with P-Δ effects): (a) all motions considered in this study and (b) only near-fault motions used in this study.

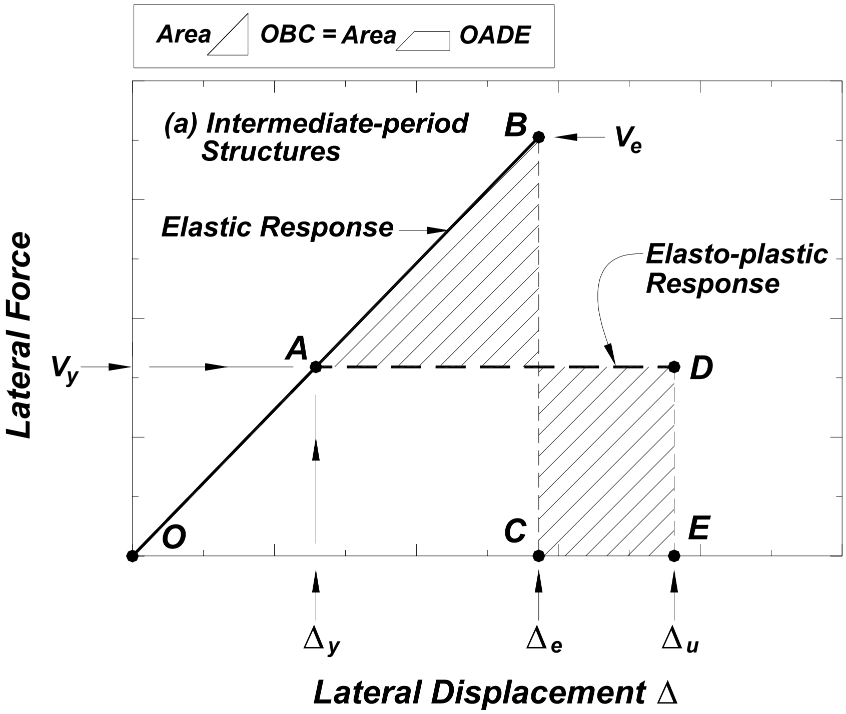

(a) Equal Velocity (Energy) Principle

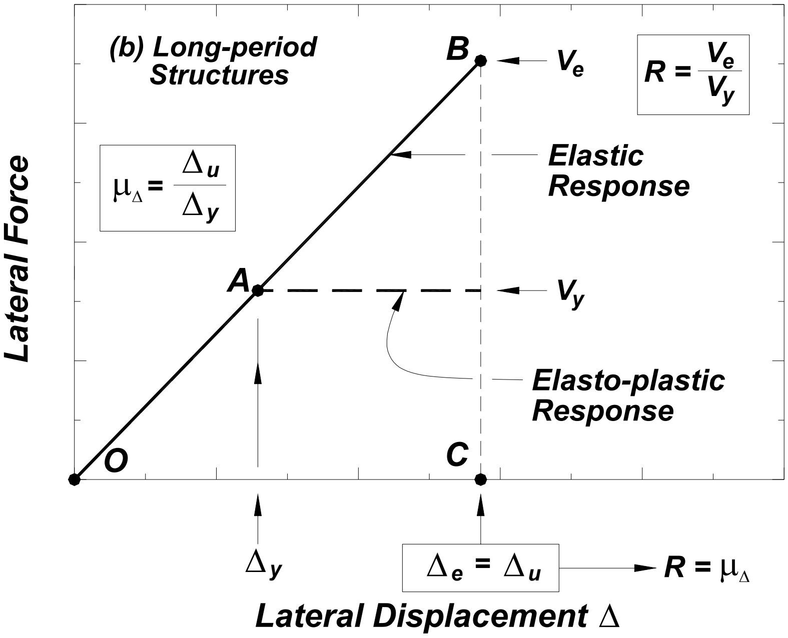

(b) Equal Displacement Principle

Figure 4.6 Select commonly used R-μ_Δ-T relations: (a) equal energy and (b) equal displacement observations.

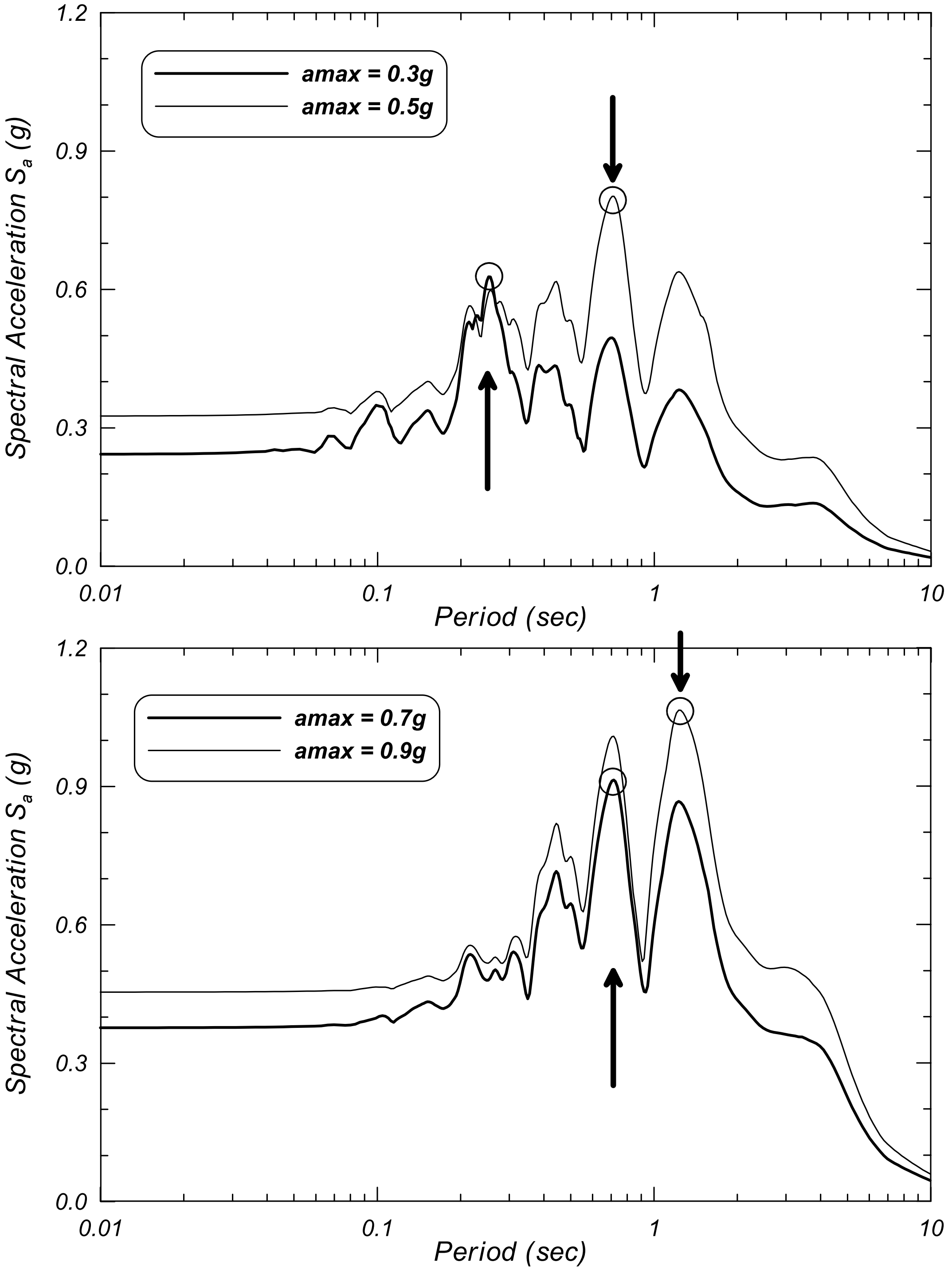

Figure 4.7 Variation in selection of predominant period T_p based on the peak in ground surface acceleration response spectra for the Landers, Lucerne motion with (a) $a_{max} = 0.3g$ and 0.5g and (b) $a_{max} = 0.7g$ and 0.9g.

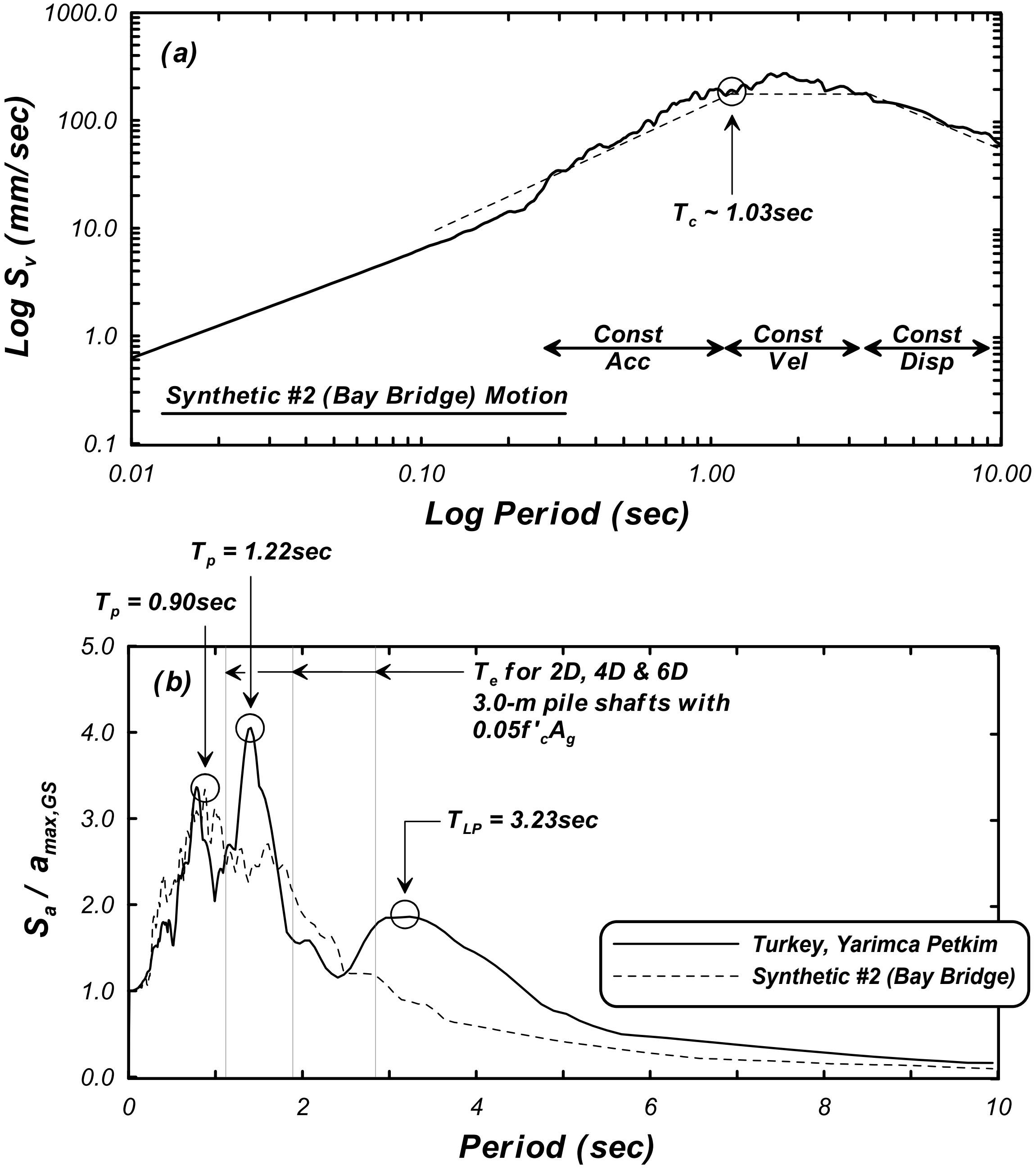

Figure 4.8 Definitions used to describe period content of ground motions: (a) characteristic period T_c based on Newmark-Hall tripartite approach — Synthetic #2 ground motion and (b) predominant periods T_p and T_{LP} based on 5% damped elastic response spectra at ground surface.

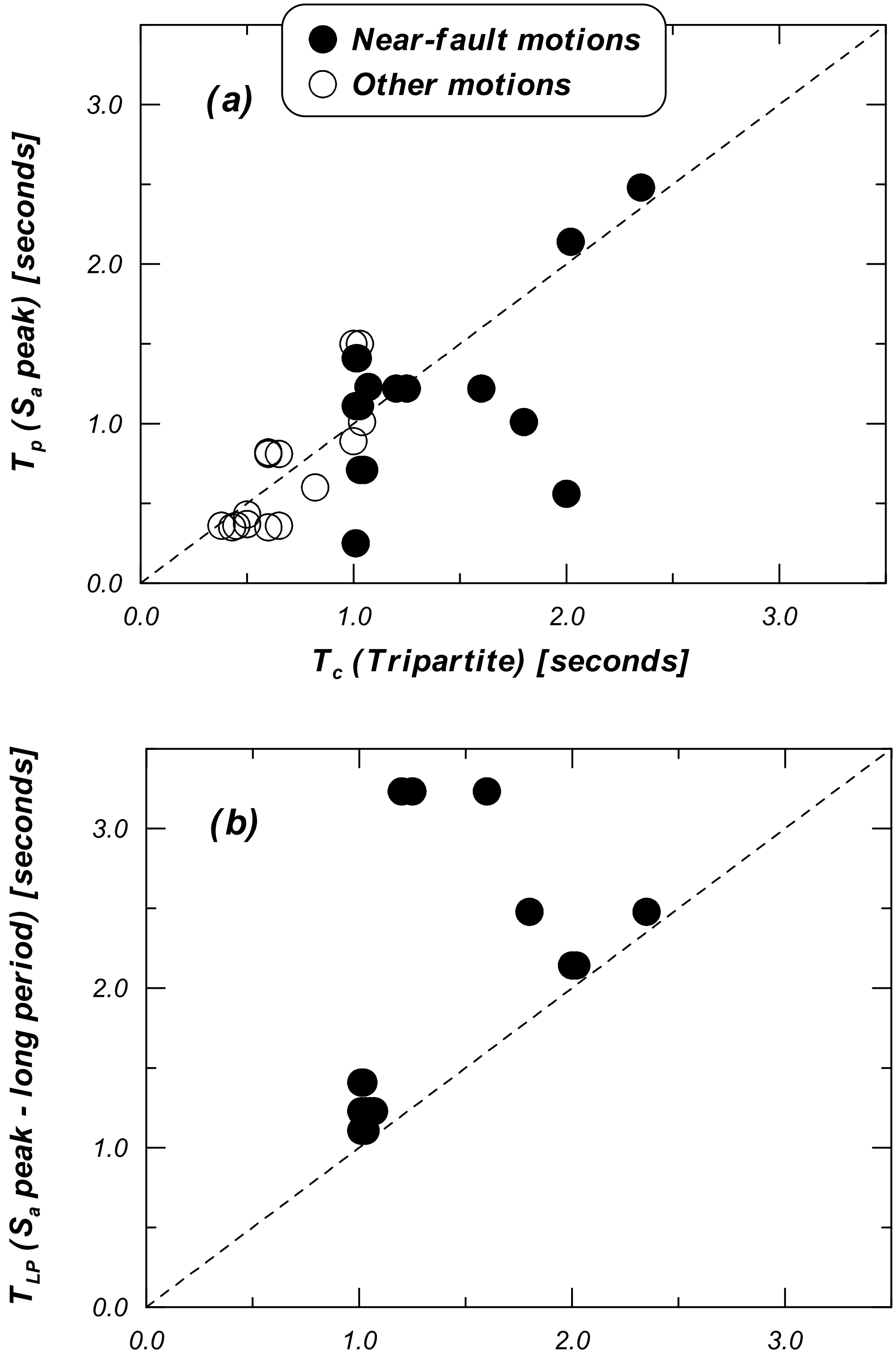

Figure 4.9 Comparison of selecting transition period using (a) the peak in the acceleration spectra and (b) the peak long-period component of the acceleration spectra.

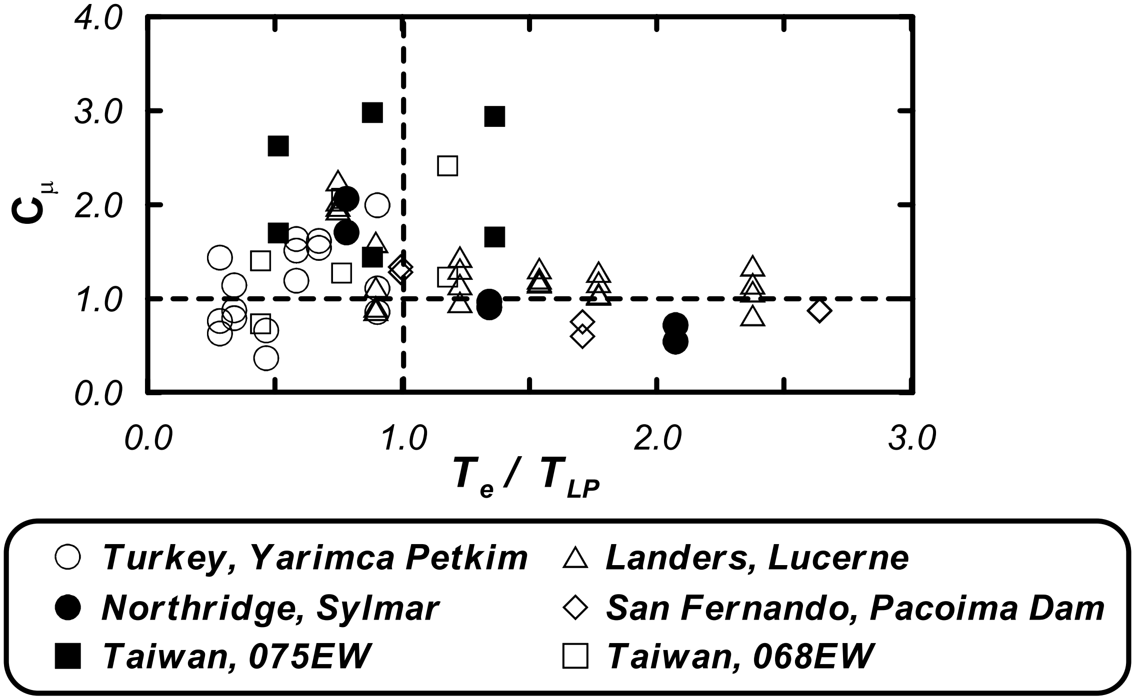

Figure 4.10 Ductility ratio C_μ versus period ratio T_e/T_{LP} for structures supported on 1.5 m and 3.0 m diameter pile shafts and subjected to the near-fault motions used in this study.

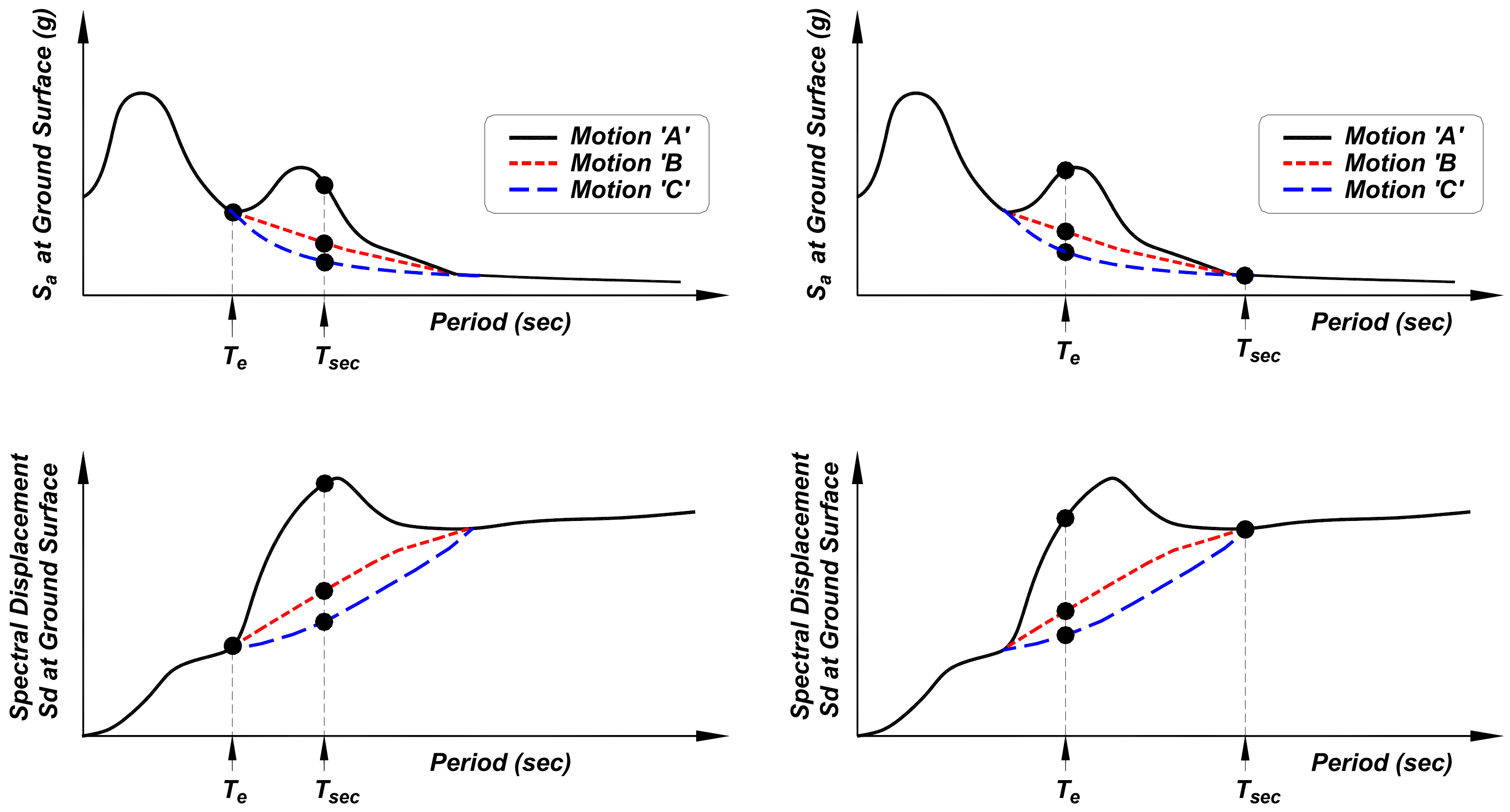

Figure 4.11 Schematic illustrating the difficulty in estimating demands from near-fault motions using a single spectral period.

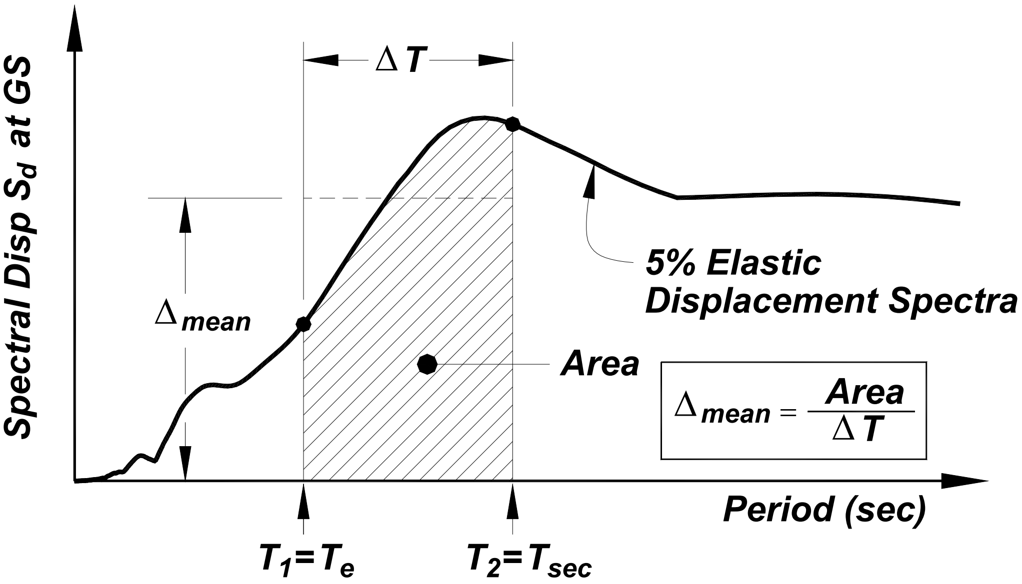

Figure 4.12 Mean spectral displacement method using the elastic displacement spectra at the ground surface and a period interval between T_1 and T_2.

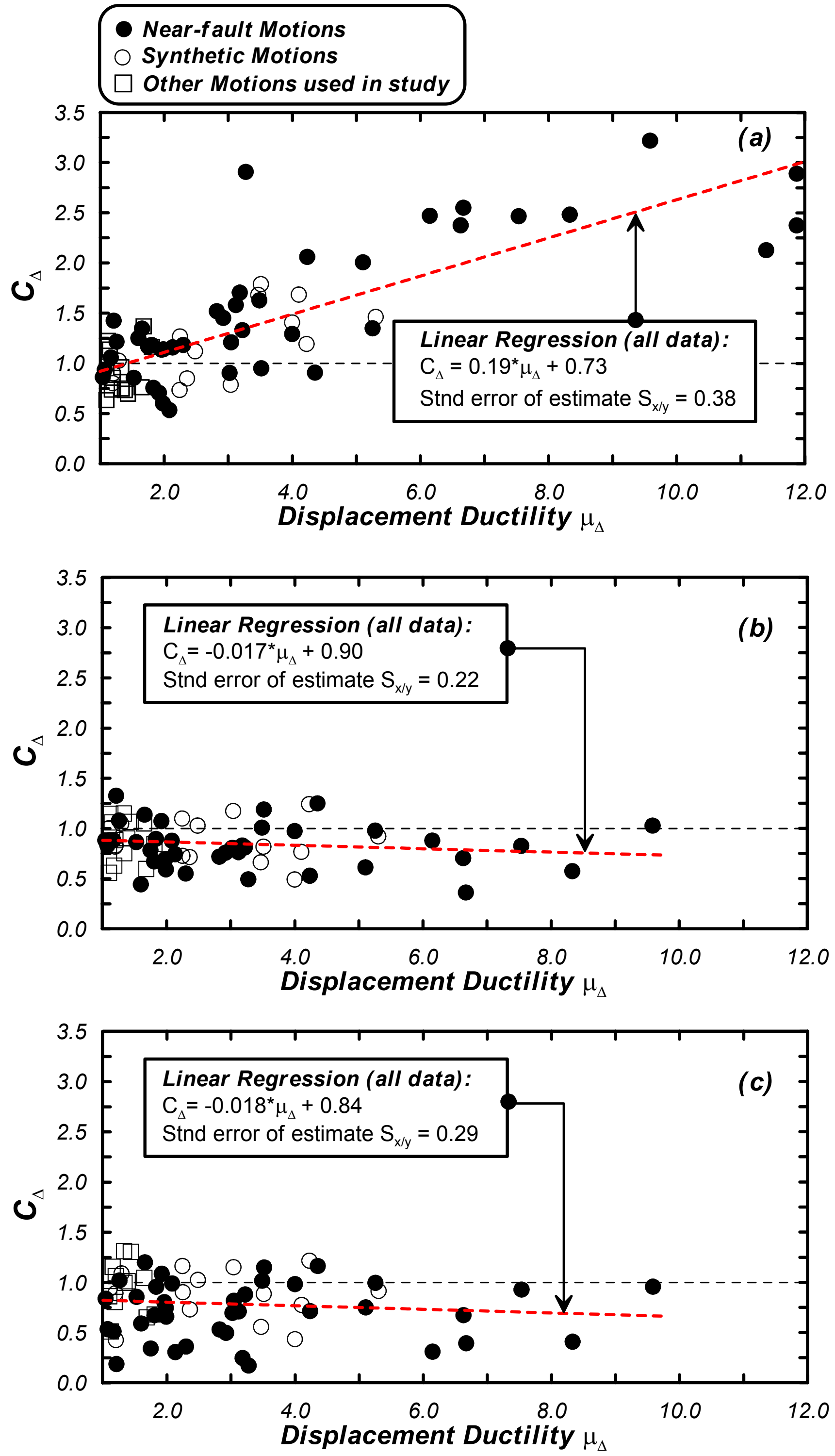

Figure 4.13 Displacement ratios C_Δ (= $\Delta_{inelastic}/\Delta_{mean}$) as a function of μ_Δ for 3.0 m diameter pile shafts with P-Δ effects: (a) C_Δ based on $T_1=T_2=T_e$, (b) C_Δ based on $T_1=T_2=T_{sec}$ at peak μ_Δ from dynamic analysis, and (c) C_Δ based on $T_1=T_2=T_{sec}$ at intersection of pushover and elastic displacement spectra.

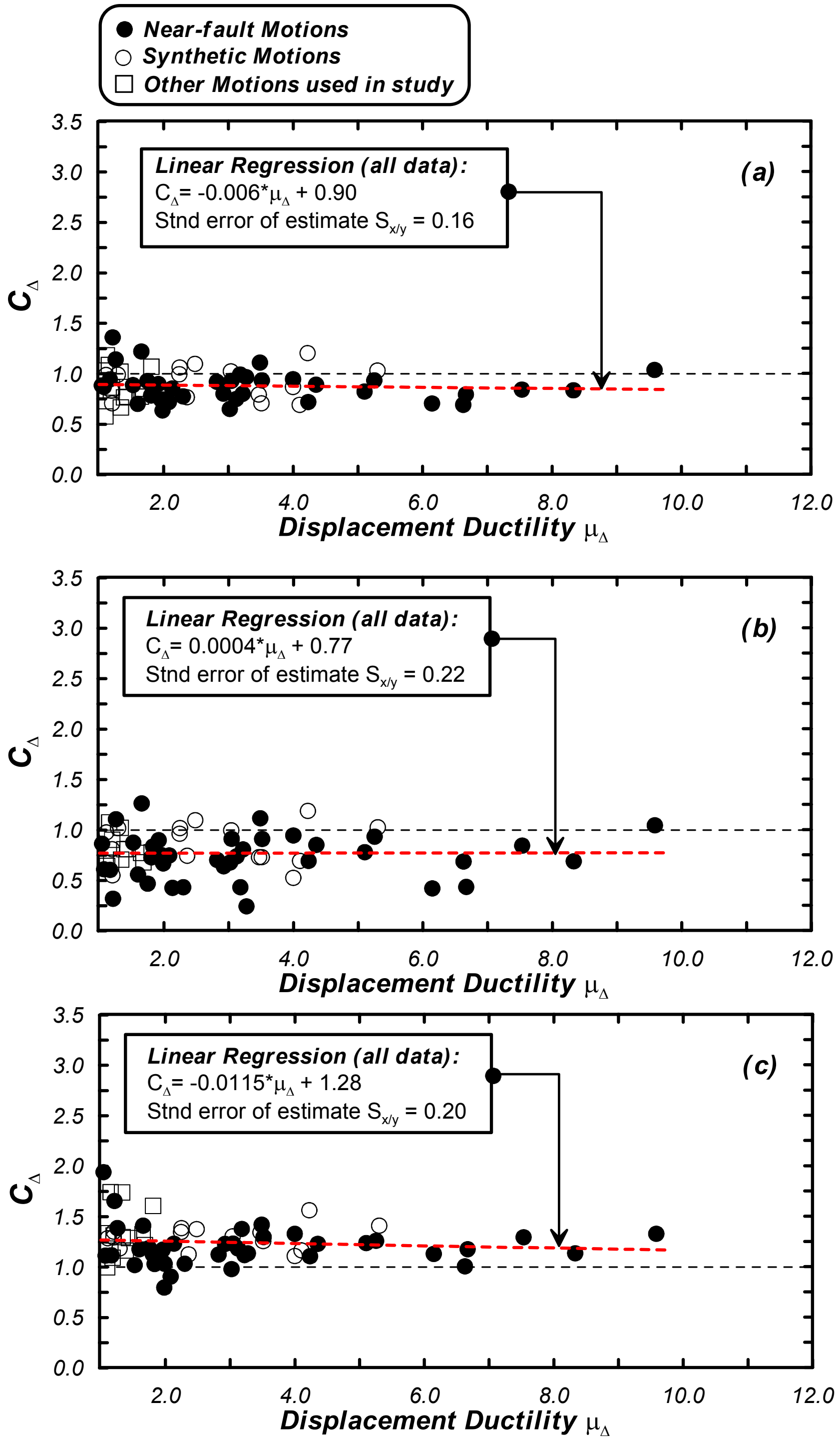

Figure 4.14 Displacement ratios C_Δ (= $\Delta_{inelastic}/\Delta_{mean}$) as a function of μ_Δ for 3.0 m diameter pile shafts with P-Δ effects: (a) C_Δ based on T_1=T_e and T_2=T_{sec} at peak μ_Δ from dynamic analysis (5% damped spectra), (b) C_Δ based on T_1=T_e and T_2=T_{sec} at intersection of pushover and elastic displacement spectra (5% damped spectra), and (c) C_Δ based on T_1=T_e and T_2=T_{sec} at peak μ_Δ from dynamic analysis (15% damped spectra).

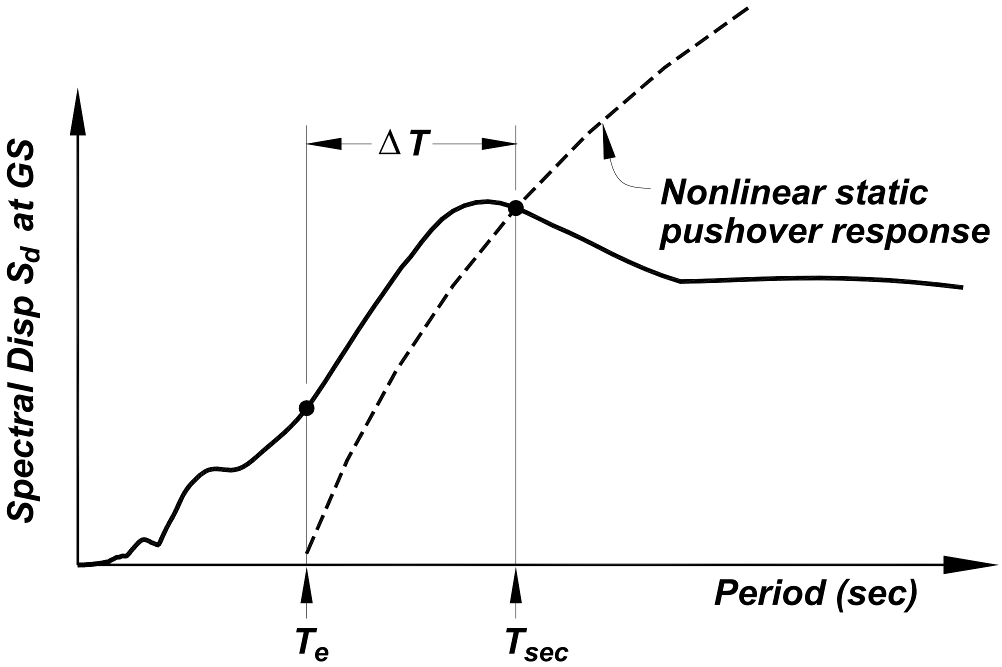

Figure 4.15 Estimating the secant period T_{sec} of a structure by the intersection of its nonlinear pushover response and the elastic displacement spectrum.

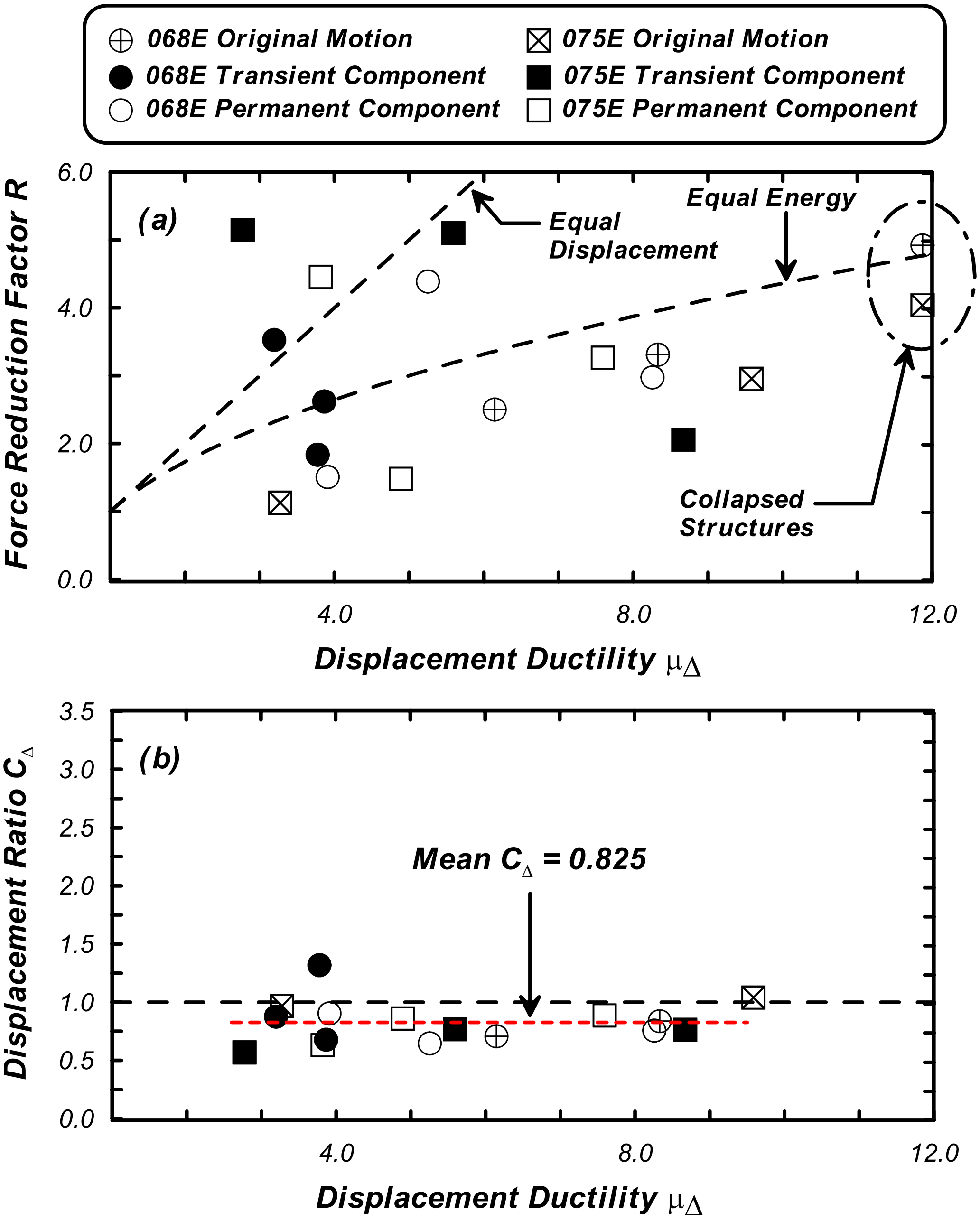

Figure 4.16 Comparison of nonlinear static methods used in this study to estimate inelastic demands applied to the Taiwan motions with large permanent offsets: (a) force-reduction approach and (b) mean spectral displacement approach (where C_Δ based on $T_1 = T_e$ and $T_2 = T_{sec}$ at peak μ_Δ from dynamic analysis).

5 Summary and Conclusions

5.1 SCOPE OF RESEARCH

Damage to pile-supported structures as observed during previous earthquakes depends on the nonlinear response characteristics of both the superstructure and substructure. However, there have been limited studies of the seismic performance of these structures where the evaluation considers the nonlinear behavior of both the geotechnical and structural elements of the system. Numerical studies are used in the work described herein to improve upon the characterization and evaluation techniques currently available in the seismic performance assessment of pile-supported bridge structures. Both static and dynamic response of bridge structures supported on extended pile shafts with detailing representative of current design practice were considered. In the dynamic analyses, particular emphasis was placed on evaluating the performance of these structures when subjected to strong, long-duration and/or long-period ground motions. Performance measures important to the overall seismic evaluation of bridge structures supported on extended pile shafts are highlighted. Finally, inelastic displacements from the dynamic analyses were compared with approaches currently used in design practice, and an alternative approach for estimating inelastic displacement demands is proposed.

5.2 SUMMARY OF APPROACH AND IMPORTANT FINDINGS

A finite element (FE) model based on a beam-on-nonlinear-Winkler (BNWF) approach was evaluated using experimental results from a series of full-scale pile tests. The FE analysis used a fiber-based beam-column element to represent the pile shaft and above-ground extension and nonlinear p-y elements to represent the lateral soil resistance. In general, reasonable agreement between global and local response quantities was seen when comparing the FE analysis with the experimental results for reversed cyclic loading. The comparisons between the FE model and the experimental results provided a degree of confidence in the FE model and substantiated the use of the model to perform a series of analyses considering a range of extended pile shaft configurations subjected to static monotonic and reversed cyclic loading. Extended pile shaft details for these analyses matched that of the experimental program (406 mm diameter). The numerical study considered a range of above-ground heights and surrounding soil strengths. Fairly good numerical agreement between the two different analytical techniques was seen in terms of soil-pile system stiffnesses K_{sp}, ultimate strengths V_u, and local curvature ductility μ_ϕ demands. The relation between global displacement ductility μ_Δ and local curvature ductility μ_ϕ was also studied for the soil-pile systems considered. The ratio of local curvature ductility and global displacement ductility (μ_ϕ/μ_Δ) was found to be relatively insensitive to the above-ground height, and more sensitive to the surrounding soil strength and pile diameter. For D = 0.406 m piles in cohesionless soils, a reasonable range of ductility ratios μ_ϕ/μ_Δ might be 3.0–3.6 for dense sands and 4.4–5.1 for loose sands. For D = 0.406 m piles in cohesive soils, a reasonable range of ductility ratios μ_ϕ/μ_Δ is 2.5–3.0 for stiff clays and 3.7–4.2 for soft clays. For piles in dense sands, μ_ϕ/μ_Δ might be 3.0–3.6 for D = 0.406 m piles and 1.7–2.4 for D = 1.5–3.0 piles. These studies show that the kinematic model provides a simple method for quantifying the relation between μ_Δ and μ_ϕ in design practice.

The performance of bridge structures supported on large-diameter (1.5 m and 3.0 m diameter) extended cast-in-drilled-hole (CIDH) pile shafts subjected to a suite of ground motions was then evaluated using a series of nonlinear dynamic analyses. Earthquake motions with a range of frequency contents, intensities, durations, velocity pulses, and permanent displacements were used as rock outcrop motions in this study. Performance measures used in evaluating the dynamic response of these structures included maximum and residual drift ratios and both local and global ductility demands. The correlation between maximum and residual drift ratios from the dynamic analyses indicates that strong near-fault motions or motions with long-durations of shaking may result in large permanent displacements in the structure, rendering it unusable or even unsafe.

The effects of near-fault ground motions with large permanent offsets were studied for a subset of the large-diameter CIDH pile-supported bridge structures by subjecting these structures to the original, permanent and transient components of motion. Removing the permanent displacement component of the motion was often unconservative in terms of the peak and residual displacement demands imposed on the system. Removing the permanent displacement component changes the frequency content of the motion, in some cases causing greater demands on the system if the shift in frequency causes the motion's predominant period to be closer to the fundamental period of the structure. Consequently, it is important that the "fling" effect from permanent ground displacements (due to surface rupture) on ground motions and their elastic response spectra be included in the design process.

A subset of motions and pile-supported bridge structures used in the overall nonlinear dynamic analyses studies were analyzed with and without P-Δ effects. Results from these analyses were compared with current design approaches used to minimize or avoid P-Δ sensitive behavior (such as excessive amplification of displacements and/or subsequent collapse). Several dynamic analyses cases subjected to long-duration or near-fault ground motions indicated collapse when P-Δ effects where included in the analysis, but all of these cases were outside of the limits of current bridge design practice for the imposed ground motions.

5.2.1 Seismic Performance Measures for Extended Pile Shafts

Although many design issues must be considered for bridge structures supported on extended pile shafts, results of the numerical studies described indicate three measures are particularly important to the overall seismic performance evaluation of this class of structures:

(a) Maximum and residual drift ratios **(γ_{max} and γ_{res})**

For extended pile shaft systems, maximum and residual drift ratios are defined as the peak and permanent slope (from vertical) of the above-ground pile extension. Maximum drift ratios γ_{max} are associated with the amount of acceptable global displacement. Residual drift ratios γ_{res}, determined after the earthquake, can be used to quantify the magnitude of permanent deformation in the bridge structure. In this sense, residual drift ratios provide an indication of the repairability of the structure after an event. Following the 1995 Hanshin earthquake, reinforced concrete columns with residual drift ratios larger than 1.75% had to be demolished. Subsequently, specifications in the Japan Road Association (1996) indicate an allowable residual drift ratio of 1% for the design of important bridge structures. The dynamic analyses of CIDH pile-supported structures described herein, indicates that if maximum drift ratios are less than about 8%, residual drift ratios will generally be less than 1% (based on the mean trend in the data) and at most 1.75%. A higher degree of confidence in keeping residual drift ratios less than

1% may be achieved by using the upper-bound relation between γ_{max} and γ_{res}, in which case maximum drift ratios would be limited to less than about 6%. However, it is recommended that the ability of the FE model to specifically capture residual displacements has not been fully explored and thus warrants calibration against experimental data.

(b) *Secondary-Moment-Strength Ratios* (*SMSR*)

The ratio of the lateral displacement times the axial load to the plastic moment capacity of the pile shaft is termed the secondary-moment-strength ratio (*SMSR*) in this study. Limiting the secondary-moment-strength ratio of the extended pile shaft system generally provides a means for minimizing the effects P-Δ moments have on these structures (such as excessive displacement amplification and/or subsequent collapse). Bridge structures supported on CIDH extended pile shafts may be susceptible to P-Δ effects due to their low strengths and large flexibilities. Bridge design guidelines suggest a reasonable criteria of providing for *SMSR* ≤ 20% (Caltrans 1999) to avoid excessive displacements and/or collapse due to dynamic P-Δ effects. The analyses cases described suggest that current design guidelines are acceptable in terms of their ability to minimize dynamic P-Δ sensitive behavior, however, the consequences of allowing *SMSR* up to 30% were not very significant.

(c) *Kinematic relation between curvature ductility* (μ_ϕ) *and displacement ductility* (μ_Δ)

This relation is important because it allows an understanding of the magnitude of local curvature demand that will be associated with a given global displacement design level. Local curvature ductility μ_ϕ can be associated with the damage to the pile below ground level (such as spalling of cover concrete, crack widths, potential for buckling or fracture of longitudinal reinforcement). Curvature ductility demands are generally limited to the dependable curvature ductility capacity of the pile shaft. As such, curvature ductility design limits are related to the collapse prevention of the bridge structure. Since detailing of extended pile shafts generally follow that of reinforced concrete columns, it is reasonable to assume a dependable curvature ductility capacity of $\mu_\phi = 13$ (ATC-32, 1996). However, it is important to note that reinforced concrete columns are generally designed as fully ductile structures (with $\mu_\Delta = 4.0$), whereas extended pile shaft systems are termed *Limited Ductility Structures* (ATC-32, 1996) and designed with lower levels of displacement ductility ($\mu_\Delta = 3.0$) with the intent of minimizing the damage below ground level. This would imply that a local curvature ductility demand less than 13 is more desirable for the below ground portions of the extended pile shafts. If the ratio between the curvature and displacement ductility (μ_ϕ/μ_Δ) is constant, limiting the displacement ductility μ_Δ to 3.0 implies that the curvature ductility demand μ_ϕ is limited to $\frac{3}{4} \cdot (13) \approx 10$.

For the smaller extended pile shaft systems considered (406 mm diameter) in Chapter 2, limiting the local demands to $\mu_\phi \leq 13$ would require (based on the calculated ductility ratios μ_ϕ/μ_Δ) that acceptable ranges of μ_Δ might be 2.5 to 4.3 for loose to dense sands, respectively, and 3.1 to 5.2 for soft to stiff clays, respectively, over the full range of above-ground heights considered. For these smaller diameter piles, limiting $\mu_\phi \leq 10$ would imply displacement ductilities of $\mu_\Delta = 1.9$ to 3.3 for the loose to dense sand conditions and $\mu_\Delta = 2.4$ to 4.0 for the soft to stiff clays, respectively. These displacement ductility levels are dependent upon the structural configuration considered in the parametric study (406 mm diameter pile shaft, $\rho_l = 2.1\%$, $\rho_s = 1.06\%$ and $P = 0.1f'_cA_g$).

For the larger diameter pile shafts studied in Chapter 3, embedded in a fairly dense sand, limiting the local demands to $\mu_\phi \leq 13$, would allow displacement ductilities ranging from $\mu_\Delta = 5.2$ to 6.1 for the 1.5 m diameter pile shafts and from $\mu_\Delta = 4.8$ to 5.5 for the 3.0 m diameter pile shafts. Limiting $\mu_\phi \leq 10$ to reduce local damage would allow displacement ductilities ranging from $\mu_\Delta = 4.0$ to 4.7 for the 1.5 m diameter pile shafts and $\mu_\Delta = 3.7$ to 4.2 for the 3.0 m diameter pile shafts. However, for pile shafts embedded in loose sand or softer clay, the local curvature ductility demand is expected to increase resulting in design displacement ductility factors smaller than that of dense sand. These results show that the kinematic model provides a simple method for relating μ_Δ and μ_ϕ for a wide range of pile and soil configurations in practice.

5.2.2 Simplified Estimation of Inelastic Displacements

Accurate estimation of inelastic displacements is important to the overall evaluation of the seismic performance of these structures. In design, inelastic displacements are often predicted using simplified nonlinear static approaches. In this study, a substitute structure approach and a force-reduction (R-μ_Δ-T) type approach were evaluated in terms of their ability to predict the inelastic displacements calculated from the dynamic FE analyses of the CIDH pile-supported bridge structures. For the ground motions considered, the substitute structure approach showed a variability in its ability to predict inelastic displacement demands and was overly sensitive in certain cases when the ground surface response spectrum had pulse-type characteristics. The $R-\mu_\Delta-T$ relation involved a linear transition at short periods to the equal displacement observation at long periods. This $R-\mu_\Delta-T$ relation appears to be reasonable for near-fault motions provided the elastic period of the structure is longer than the period of the pulse (if present). However, if the elastic period of the structure is less than the period of the pulse (in the shorter-period range), the $R-\mu_\Delta-T$ relation used in this study significantly underestimated inelastic displacements.

An alternative approach for prediction of inelastic displacements was explored that uses the mean elastic spectral displacement (for 5% damping) between two periods that bracket the range of periods most important to the structure. When these two periods are taken as the elastic period (T_e) and the secant period at the peak displacement demand (T_{sec}), the results showed a substantial reduction in the standard error of the estimate. This improvement in the accuracy of predicting inelastic displacements, given a site-specific displacement spectrum of a near-fault ground motion, indicates that this approach has promise and should be evaluated in greater detail. The alternative approach has the advantage of estimating displacements directly; therefore, it can easily be integrated into displacement-based design methodologies.

References

Abghari, A., and Chai, J. (1995). *Modeling of Soil-Pile-Superstructure Interaction for Bridge Foundations*. ASCE Geotechnical Special Publication *51*, pp. 45–59.

Abrahamson, N.A. (1998). Seismological Aspects of Near-Fault Ground Motions. *Proceedings 5th Caltrans Seismic Research Workshop*, California Department of Transportation Engineering Service Center, Sacramento, California.

Abrahamson, N.A. (2001). Personal Communication.

American Petroleum Institute (API) (1987). *API Recommended Practice for Planning, Designing, and Constructing Fixed Offshore Platforms*, API Recommended Practice 2A (RP 2A), Seventeenth Edition, Washington D.C.

American Petroleum Institute (API) (1993). *API Recommended Practice for Planning, Designing, and Constructing Fixed Offshore Platforms*, API Recommended Practice 2A (RP 2A), Twentieth Edition, Washington D.C.

Applied Technology Council (ATC) (1978). *Tentative Provisions for the Development of Seismic Regulations for Buildings: ATC-3-06.*

Applied Technology Council (ATC) (1996). *Improved Seismic Design Criteria for California Bridges: Provisional Recommendations ATC-32*. June.

Applied Technology Council (ATC) (1996). *Seismic Evaluation and Retrofit of Concrete Buildings ATC-40.* Volume 1 and 2. November.

Arias, A. (1970). A Measure of Earthquake Intensity. In R.J. Hansen, ed. *Seismic Design for Nuclear Power Plants*, MIT Press, Cambridge, Massachusetts. pp. 438–83.

Badoni, D., and Makris, N. (1997). *Analysis of the Nonlinear Response of Structures Supported on Pile Foundations*. Earthquake Engineering Research Center Report No. UCB/EERC-97-07. University of California, Berkeley.

Baez, J.I., and Miranda, E. (2000). Amplification Factors to Estimate Inelastic Displacement Demands for the Design of Structures in the Near Field. *Proceedings 12th World Conference on Earthquake Engineering*, Auckland, New Zealand.

Benioff, H. (1955). Mechanism and Strain Characteristics of the White Wolf Fault as Indicated by the After-Shock Sequence, Earthquakes in Kern County, California during 1955. (G.B. Oakeshott, ed.). *California Division of Mines Bull.* 171: 199–202.

Bertero, V.V., Mahin, S.A., and Herrera, R.A. (1978). "Aseismic Design Implications of Near-Fault San Fernando Earthquake Records." *Earthquake Engineering and Structural Dynamics* 6: 31-42.

Bolt, B.A. (1981). State-of-the-Art for Assessing Earthquake Hazards in the United States: Interpretation of Strong Ground Motion Records. Miscellaneous Paper S-73-1, Report 17, U.S. Army Engineer Waterways Experiment Station, Springfield, VA. 215 pp.

Boore, D.M. (1973). The Effect of Simple Topography on Seismic Waves: Implications for the Accelerations Recorded at Pacoima Dam, San Fernando Valley, California. *Bull. Seism. Soc. Am*. Vol. 63, 1603–09.

Boulanger, R.W., Curras, C. J., Kutter, B.L., Wilson, D.W., and Abghari, A. (1999). Seismic Soil-Pile-Structure Interaction Experiments and Analyses. *J. Geotechnical and Geoenvironmental Engineering,* ASCE*,* 125(9): 750–59.

Broms, B.B. (1964a). Lateral Resistance of Piles in Cohesionless Soils. *J. Soil Mechanics and Foundation Division,* ASCE, 90(SM3): 123–56.

Broms, B.B. (1964b). Lateral Resistance of Piles in Cohesive Soils. *J. Soil Mechanics and Foundation Division,* ASCE, 90(SM2): 27–63.

BSSC (1994). *NEHRP Provisions*, 1994 Edition, Building Seismic Safety Council, Washington, D.C.

Budhu, M., and Davies, T.G. (1987). Nonlinear Analysis of Laterally Loaded Piles in Cohesionless Soils. *Canadian Geotech. J.*, 24: 289–96.

Caltrans (1999). Caltrans Seismic Design Criteria — Version 1.1. California Department of Transportation, Division of Structures. Sacramento, California. July.

Chai, Y. H., and Hutchinson, T.C. (1999). Flexural *Strength and Ductility of Reinforced Concrete Bridge Piles.* Report UCD-STR-99-2, University of California, Davis.

Chai, Y. H. (2002). Flexural Strength and Ductility of Extended Pile-Shafts — I: Analytical Model. *J. Structural Engineering*, ASCE, 128(5): 586–94.

Chapman, H.E. (1995). Earthquake Resistant Bridges and Associated Highway Structures: Current New Zealand Practice. *Proceedings of the National Seismic Conference on Bridges and Highways — Progress in Research and Practice*. San Diego, California, December 10–13. Federal Highway Administration and California Department of Transportation.

Curras, C.J. (2000). Seismic *Soil-Pile-Structure Interaction for Bridge and Viaduct Structures*. Ph.D. Dissertation. University of California, Davis.

Curras, C.J., Hutchinson, T.C., Boulanger, R.W., Chai, Y.H., and I.M. Idriss. (2001). Lateral Loading and Seismic Response of CIDH Pile Supported Bridge Structures. *Foundations and Ground Improvement,* T.L. Brandon ed., Geotechnical Special Publication No.113. ASCE, 260–75.

EPRI (1993). *Guidelines for Determining Design Basis Ground Motions*, Volume 3. TR-102293, Electric Power Research Institute, Palo Alto, California.

Fang, H.-Y. (1991). *Foundation Engineering Handbook*. Chapman & Hall. 2nd Edition.

Federal Emergency Management Agency (1997). *NERHP Guidelines for the Seismic Rehabilitation of Buildings*. FEMA Publication 273. Washington, D.C.

Filippou, F.C. (1999). *FEDEAS: Finite Elements for Design, Evaluation, and Analysis of Structures.* On-line manual: Dept. of Civil and Environmental Engineering, Univ. of California, Berkeley, CA.
http://www.ce.berkeley.edu/~filippou/Research/fedeas.html

Filippou, F.C., Popov, E.P, and Bertero V.V. (1983). *Effects of Bond Deterioration on Hysteretic Behavior of Reinforced Concrete Joints.* EERC Report 83/19. Earthquake Engineering Research Center, University of California, Berkeley.

Gulkan, P. and Sozen, M.A. (1974). Inelastic Responses of Reinforced Concrete Structures to Earthquake Motions. *ACI J.* Title No. 71-41, 604–10.

Hetenyi, M. (1946). *Beams on Elastic Foundations: Theory with Applications in the Fields of Civil and Mechanical Engineering*. University of Michigan Press, Ann Arbor, Michigan, 255 pp.

Hilber, H.M., Hughes, T.J.R., and Taylor, R.L. (1977). Improved Numerical Dissipation for Time Integration Algorithms in Structural Dynamics. *Earthquake Engineering and Structural Dynamics* 5: 283–92.

Hudson, D.E. (1965). Equivalent Viscous Friction for Hysteretic Systems with Earthquake-like Excitations. *Proceedings 3rd World Conference on Earthquake Engineering*, Vol. II, pp. 185–202.

Hutchinson, T.C. (2001). *Characterization and Evaluation of the Seismic Performance of Pile-Supported Bridge Structures*. Ph.D. Dissertation, University of California, Davis.

Idriss, I.M., and Sun, J. (1991). *User Manual for SHAKE91.* Center for Geotechnical Modeling, Dept. of Civil and Envir. Engineering, University of California, Davis, California.

Japan Road Association (JRA) (1996). *Design Specifications of Highway Bridges. Part V: Seismic Design*. Tokyo, Japan.

Jennings P.C. (1968). Equivalent Viscous Damping for Yielding Structures. *J. Engineering Mechanics Division,* ASCE, 94(1): 103–16.

Kennedy, R.P., Short, S.A., Merz, K.L., Tokarz, F.J., Idriss, I.M., Power, M.S., and Sadigh, K. (1984). *Engineering Characterization of Ground Motion — Task I: Effects of Characteristics of Free-Field Motion on Structural Response,* Vol. 1, NUREG/CR-3805, U.S. Nuclear Regulatory Commission, Structural Mechanics Associates, Inc. and Woodward-Clyde Consultants. May.

Kent, D.C., and Park, R. (1971). Flexural Members with Confined Concrete. *J. Struc. Div*., ASCE 97(ST7): 1964–90.

Kowalsky, M.J., Priestley, M.J.N., and MacRae, G.A. (1995). Displacement-based Design of RC Bridge Columns in Seismic Regions. *Earthquake Engineering and Structural Dynamics*, 24: 1623–43.

Krawinkler, H., and Alavi, B. (1998). Development of Improved Design Procedures for Near-Fault Ground Motions. SMIP98 Seminar on Utilization of Strong-Motion Data, Oakland, CA., 21–42.

Liao, S.C., and Whitman, R.V. (1986). Overburden Correction Factors for SPT in Sand. *J. Geotech. Engrg.,* ASCE, 112(3):373–77.

Macrae, G.A. (1994). P-Δ Effects on Single-Degree-of-Freedom Structures in Earthquakes. *Earthquake Spectra* 10(3): 539–68.

MacRae, G.A., and Kawashima, K. (1997). Post-earthquake Residual Displacements of Bilinear Oscillators. *Earthquake Engineering and Structural Dynamics* 26: 701–16.

MacRae, G.A., Priestley, M.J.N., and Tao, J. (1993). *P-Delta Design in Seismic Regions*. SSRP-93/05. University of California, San Diego.

MacRae, G.A., and Roeder, C.W. (1999). *Near-Field Ground Motion Effects on Short Structures.* Final Report to PG&E/PEER, University of California, Berkeley.

Mahin, S. (1976). Effects of Duration and Aftershocks on Inelastic Design Earthquakes. *Proceedings, World Conference on Earthquake Engineering*, Rome.

Mahin, S., and Boroschek, R. (1991). Influence of *Geometric Nonlinearities on the Seismic Response and Design of Bridge Structures.* Report to California Department of Transportation, Division of Structures.

Mahin, S.A. and Hachem, M. (1998). Response of Simple Bridge Structures to Near-Fault Ground Motions. *Proceedings 5th Caltrans Seismic Research Workshop*, California Department of Transportation Engineering Service Center, Sacramento, California.

Makris, N. and Chang, S.P. (2000). Response of Damped Oscillators to Cycloidal Pulses. *J. Engineering Mechanics,* ASCE, 126(2): 123–31.

Mander, J.B., Priestley, M.J.N., and Park, R. (1988). Theoretical Stress-Strain Model for Confined Concrete. *J. Struct. Div.,* ASCE, 114(8): 1804–26.

Matlock, H. (1970). Correlation's for Design of Laterally Loaded Piles in Soft Clay. *Proceedings, 2nd Annual Offshore Technology Conference*, Houston, Texas, OTC 1204.

Matlock, H., Foo, S. H., and Bryant, L. L. (1978). Simulation of Lateral Pile Behavior. *Proc., Earthquake Engrg. and Soil Dyn*., ASCE, New York, 600–19.

Menegotto, M., and Pinto, P.E. (1973). Method of Analysis for Cyclically Loaded Reinforced Concrete Plane Frames Including Changes in Geometry and Nonelastic Behavior of Elements under Combined Normal Force and Bending. *IABSE Symposium on Resistance and Ultimate Deformability of Structures Acted on by Well-Defined Repeated Loads*, Final Report, Lisbon.

Miranda, E., and Bertero V.V. (1994). Evaluation of Strength Reduction Factors for Earthquake-Resistant Design. *Earthquake Spectra* 10(2): 357–79.

Neuenhofer, A. and Filippou, F.C. (1998). Geometrically Nonlinear Flexibility-Based Frame Finite Element. *J. Structural Engineering,* ASCE, 124(6): 704–11.

Newmark, N.M., and Hall, W.J. (1982). *Earthquake Spectra and Design*. Earthquake Engineering Research Institute, Berkeley, California.

Newmark, N.M., and Rosenblueth, E. (1971). Fundamentals of Earthquake Engineering. Prentice-Hall.

Nogami, T., Otani, J., Konagai, K., and Chen, H.-I. (1992). Nonlinear Soil-Pile Interaction Model for Dynamic Lateral Motion. *J. Geotech. Engrg*., ASCE, 118(1): 89–106.

Novak, M., and Sheta, M. (1980). Approximate Approach to Contact Problems of Piles. *Proc., ASCE Nat. Convention, Dyn. Response of Pile Found: Analytical Aspect*s, ASCE, New York, 55–79.

Page, R.A., Boore, D.M., Joyner, W.B., and Coulter, H.W. (1972). Ground Motion Values for Use in the Seismic Design of the Trans-Alaska Pipeline System. U.S.G.S. Circular 672, 23 pp.

Paulay, T. (1978). A Consideration of P-Delta Effects in Ductile Reinforced Concrete Frames. *Bull. New Zealand National Society for Earthquake Engineering* 111(3): 151–60.

Paulay, T., and Priestley, M.J.N. (1992). *Seismic Design of Reinforced Concrete and Masonry Buildings*. John Wiley and Sons, Inc. New York, NY. 744 pp.

Poulos, H.G., and Davis, E.H. (1980). *Pile Foundation Analysis and Design.* John Wiley & Sons.

Prakash, S., and Sharma, H.D. (1990). *Pile Foundations in Engineering Practice.* A Wiley-Interscience Publication.

Priestley, M.J.N. (1993). Myths and Fallacies in Earthquake Engineering — Conflicts between Design and Reality. *Bull. New Zealand National Society for Earthquake Engineering* 26(3): 329–41.

Priestley, M.J.N., Seible, F. and Calvi, G.M. (1996). *Seismic Design and Retrofit of Bridges*. John Wiley and Sons, Inc. New York, NY. 686 pp.

Randolph, M.F. (1981). The Response of Flexible Piles to Lateral Loading. *Geotechnique* 31: 247–59.

Randolph, M.F. (1991). Analysis of the Dynamics Of Pile Driving. Chapter 6 in *Advanced Geotechnical Analyses,* Banerjee P.K. and Butterfield, R., editors, Elsevier Applied Science.

Rathje, E.M., Abrahamson, N.A., and Bray, J.D. (1998). Simplified Frequency Content Estimates of Earthquake Ground Motions. *J. Geotechnical and Geoenvironmental Engineering,* ASCE, 124(2): 150–59.

Reese, L.C., Cox, W.R., and Koop, F.D. (1975). Field Testing and Analysis of Laterally Loaded Piles in Stiff Clay. *Proceedings, 7th Offshore Technology Conference*, Vol. II, 671–90.

Reese, L. C., Wang, S.T., Isenhower, W.M., Arréllaga, J. A., and Hendrix, J. (2000). LPILE Plus Version 4.0 — A Program for the Analysis of Piles and Drilled Shafts under Lateral Loads; Ensoft, Inc. Austin, Texas.

Schnabel, P.B., Lysmer, J., and Seed, H.B. (1972). *SHAKE: A Computer Program for Earthquake Response Analysis of Horizontally Layered Sites*. UCB/EERC-72/12, EERC, University of California, Berkeley, 102 pp.

Scott, B.D., Park, R., and Priestley, M.J.N. (1982). Stress-strain behavior of concrete confined by overlapping hoops at low and high strain rates. *ACI J.* 79: 13–27.

Singh, J.P. (1985). Earthquake ground motions: Implications for Designing Structures and Reconciling Structural Damage. *Earthquake Spectra*, Earthquake Engineering Research Institute, Oakland, CA, 1(2): 239–70.

Somerville, P.G., Smith, N.F., Graves, R.W. and Abrahamson, N.A. (1997). Modifications of Empirical Strong Ground Motion Attenuation Relations to Include the Amplitude and Duration Effects of Rupture Directivity. *Seismological Research Letters* 68: 180–203.

Spacone, E., Filippou, F.C., and Taucer, F. (1996). Fiber Beam-Column Model for Nonlinear Analysis of R/C Frames. *International J. Earthquake Engineering and Structural Dynamics* 25(7): 711–42.

Sun, C., Berg G., and Hanson, R. (1973). Gravity Effects on Single-Degree Inelastic Systems. *J. the Engineering Mechanics Division,* ASCE, Vol. 99(EM1).

Taylor, R.L. (1998). FEAP — A Finite Element Analysis Program. Department of Civil and Environmental Engineering, University of California, Berkeley.

Tomlinson, M.J. (1994). *Pile Design and Construction Practice*. E & FN Spon an Imprint of Chapman & Hall. 4th Edition.

Trifunac, M.D., and Brady, A.G. (1975). A Study on the Duration of Strong Earthquake Ground Motion. *Bull. Seismological Society of America* 65(3): 581–626.

Tso, W.K., and Naumoski, N. (1991). Period-Dependent Seismic Force-Reduction Factors for Short-Period Structures. *Can. J. Civ. Engr.* 18: 568–74.

Uang, C.-M. (1991). Establishing R (or R_w) and C_d Factors for Building Seismic Provisions. *J. Structural Engineering,* ASCE, 117(1): 19–28.

Veletsos, A.S., and Newmark, N.M. (1960). Effect of Inelastic Behavior on the Response of Simple Systems to Earthquake Motions. *Proceedings 2nd World Conference on Earthquake Engineering*, Vol.2: pp. 895–912.

Vidic, T., Fajfar, P. and Fischinger, M. (1994). Consistent Inelastic Design Spectra: Strength and Displacement. *Earthquake Engineering and Structural Dynamics* 23: 507–21.

Wang, S., Kutter, B.L., Chacko, J.M., Wilson, D.W., Boulanger, R.W., and Abghari, A. (1998). Nonlinear Seismic Soil-Pile-Structure Interaction. *Earthquake Spectra*, Earthquake Engineering Research Institute, Oakland, CA, 14(2): 377–96.

Wilson, D.W. (1998). *Soil-Pile-Superstructure Interaction in Soft Clay and Liquefiable Sand*. Report No. UCD/CGMDR-97-05, Center for Geotechnical Modeling, Dept. of Civ and Envir. Engrg., University of California, Davis.

Yan, L.I., and Byrne, P.M. (1992). Lateral pile Response to Monotonic Pile Head Loading. *Canadian Geotech. J.* (29): 937-956.

Ye, L., and Otani, S. (1999). Maximum Seismic Displacement of Inelastic Systems Based on Energy Concept. *Earthquake Engineering and Structural Dynamics* 28: 1483–99.

Appendix A Supplemental Data for Dynamic Analyses in Chapter 3

This appendix shows the characteristics of the ground motions used in the overall dynamic analyses study described in Chapter 3. The site response analyses of each of these motions subjected to the scaling intensities listed in Table 3.1 are also shown.

A.1 ROCK OUTCROP MOTIONS

The characteristics of the motions listed in Table 3.1 and used as input into the site response analyses are shown in Figures A.1–9. The elastic 5% damped acceleration response spectra, normalized Arias intensity, and acceleration, velocity, and displacement time histories are shown for each motion.

A.2 SITE RESPONSE RESULTS

The site response analyses of the baseline Gilroy 2 site using the ground motions and scaled intensities listed in Table 3.1 are shown in Figures A.10–19.

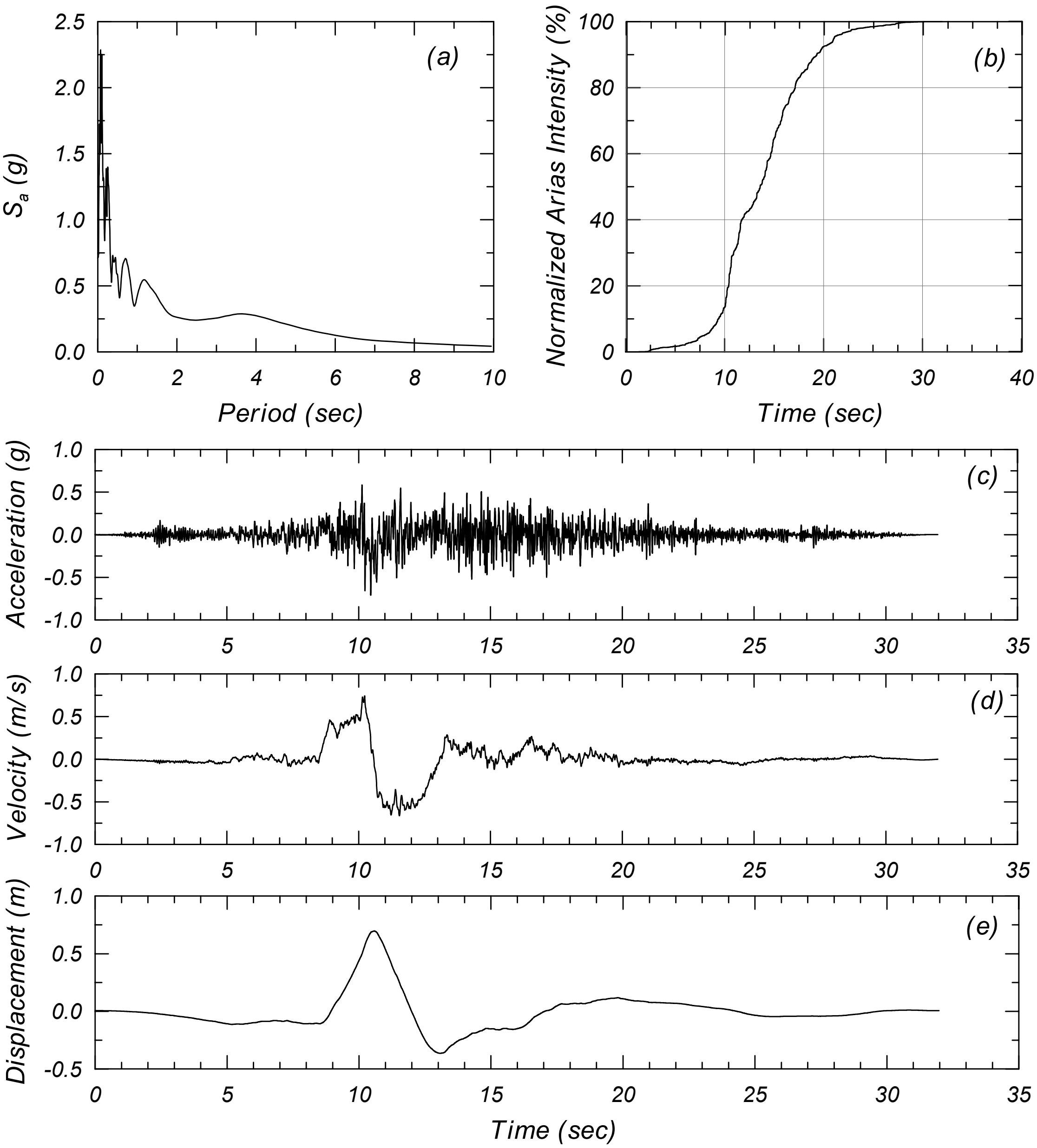

Figure A.1 Summary of Landers, Lucerne ground motion (motion used as rock outcrop): (a) elastic 5% damped response spectra, (b) normalized Arias intensity, (c) acceleration time history, (d) velocity time history, and (e) displacement time history.

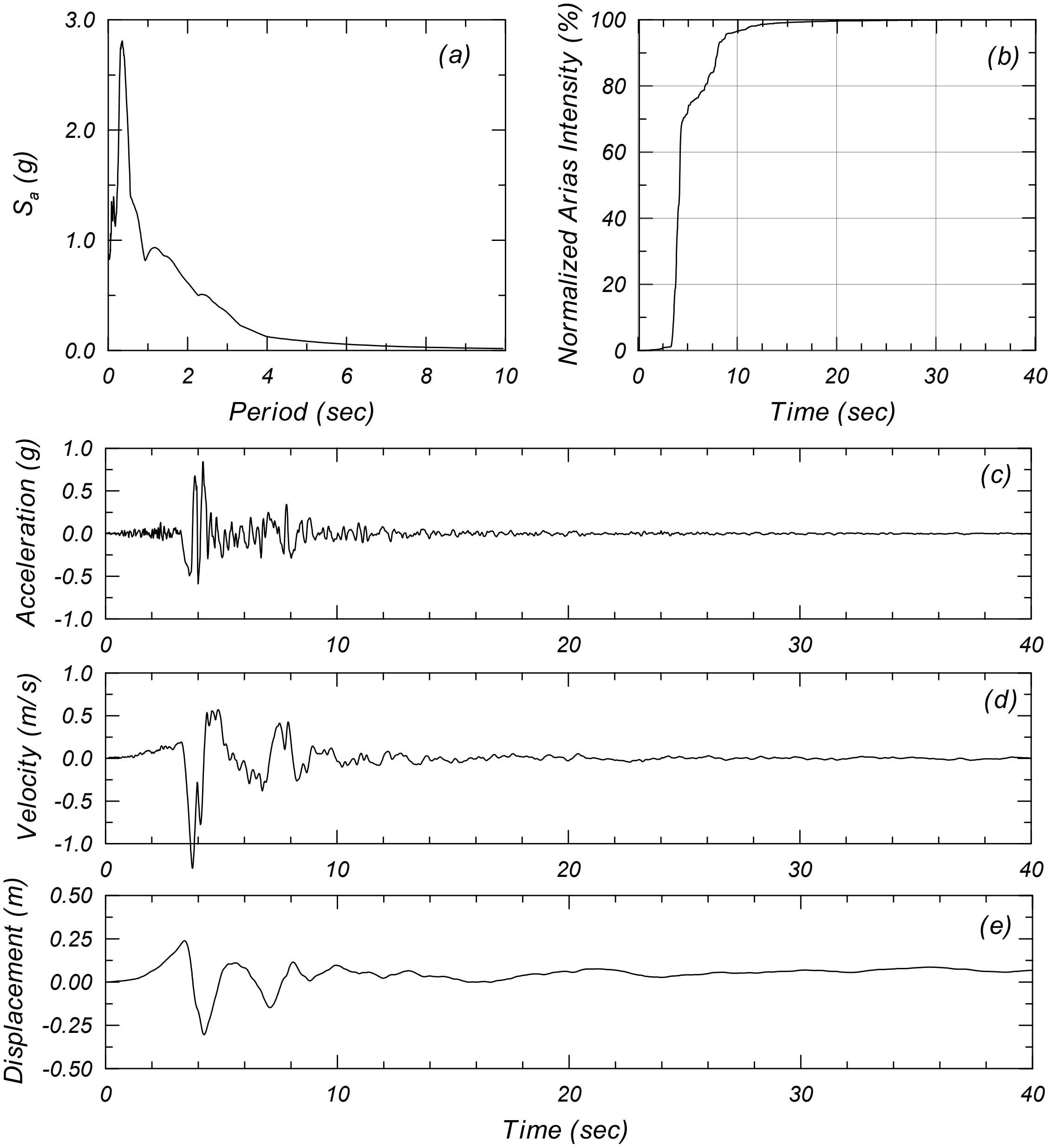

Figure A.2 Summary of Northridge, Sylmar ground motion (motion used as rock outcrop): (a) elastic 5% damped response spectra, (b) normalized Arias intensity, (c) acceleration time history, (d) velocity time history, and (e) displacement time history.

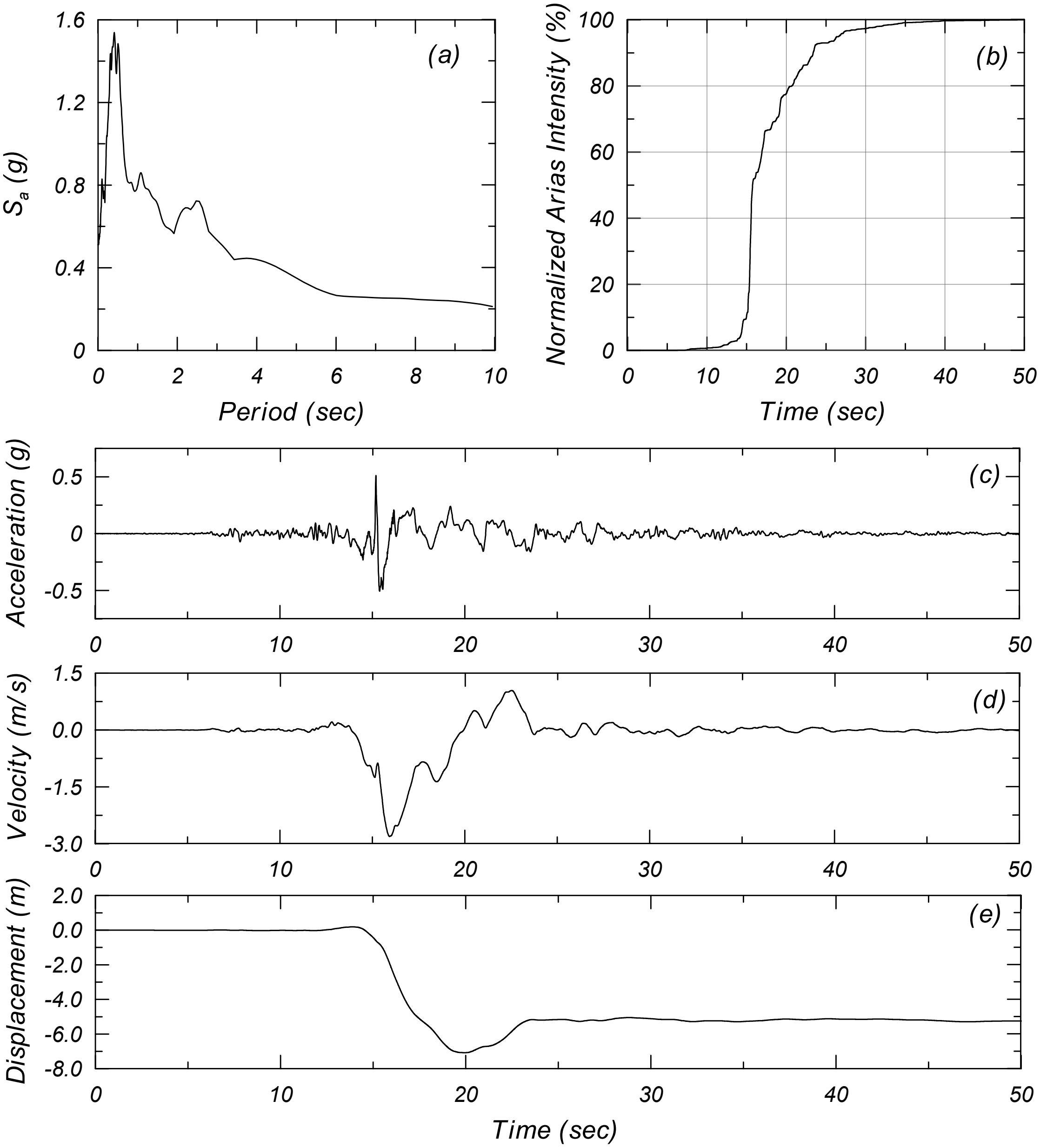

Figure A.3 Summary of Chi-Chi Taiwan, Station 068E ground motion (motion used as rock outcrop): (a) elastic 5% damped response spectra, (b) normalized Arias intensity, (c) acceleration time history, (d) velocity time history, and (e) displacement time history.

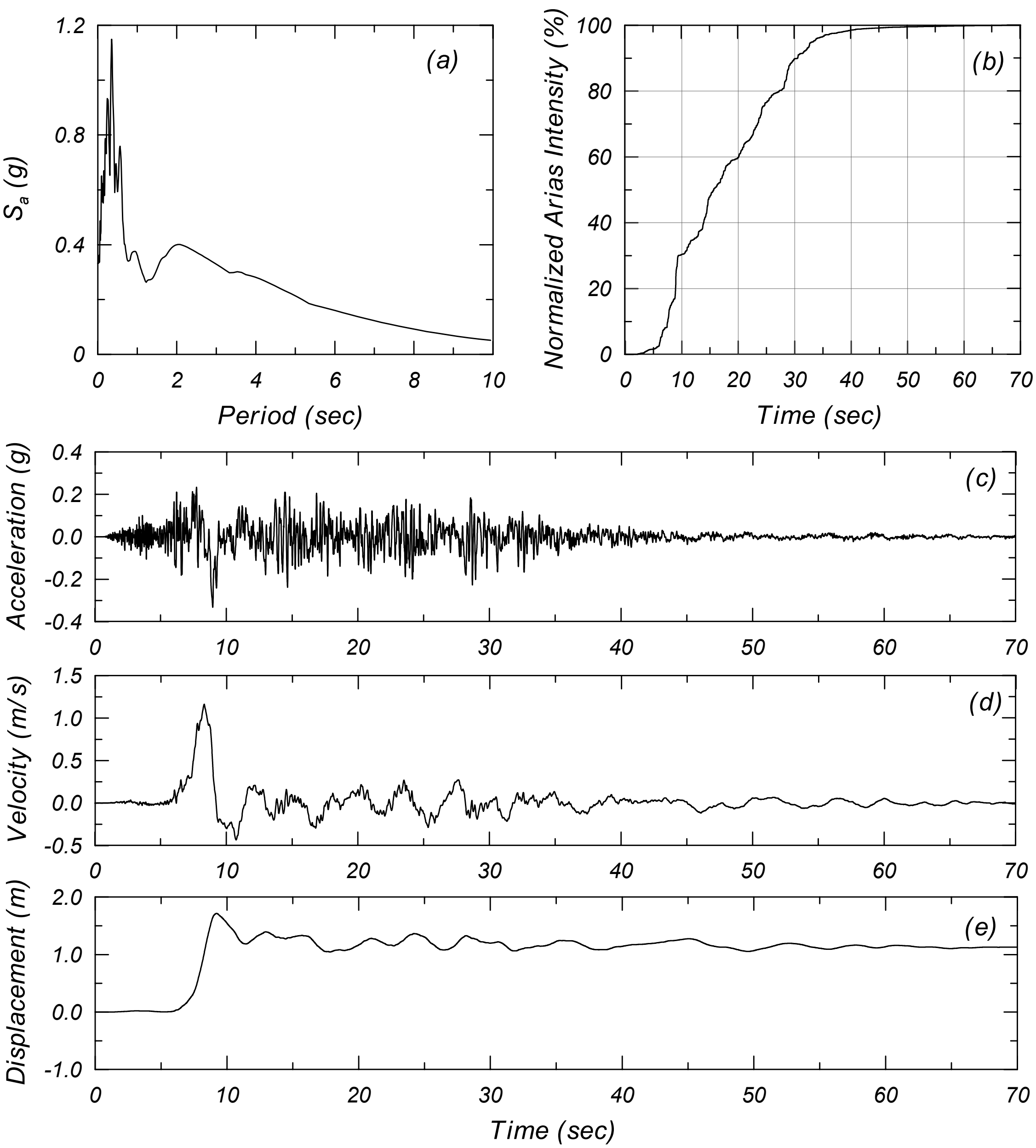

Figure A.4 Summary of Chi-Chi Taiwan, Station 075E ground motion (motion used as rock outcrop): (a) elastic 5% damped response spectra, (b) normalized Arias intensity, (c) acceleration time history, (d) velocity time history, and (e) displacement time history.

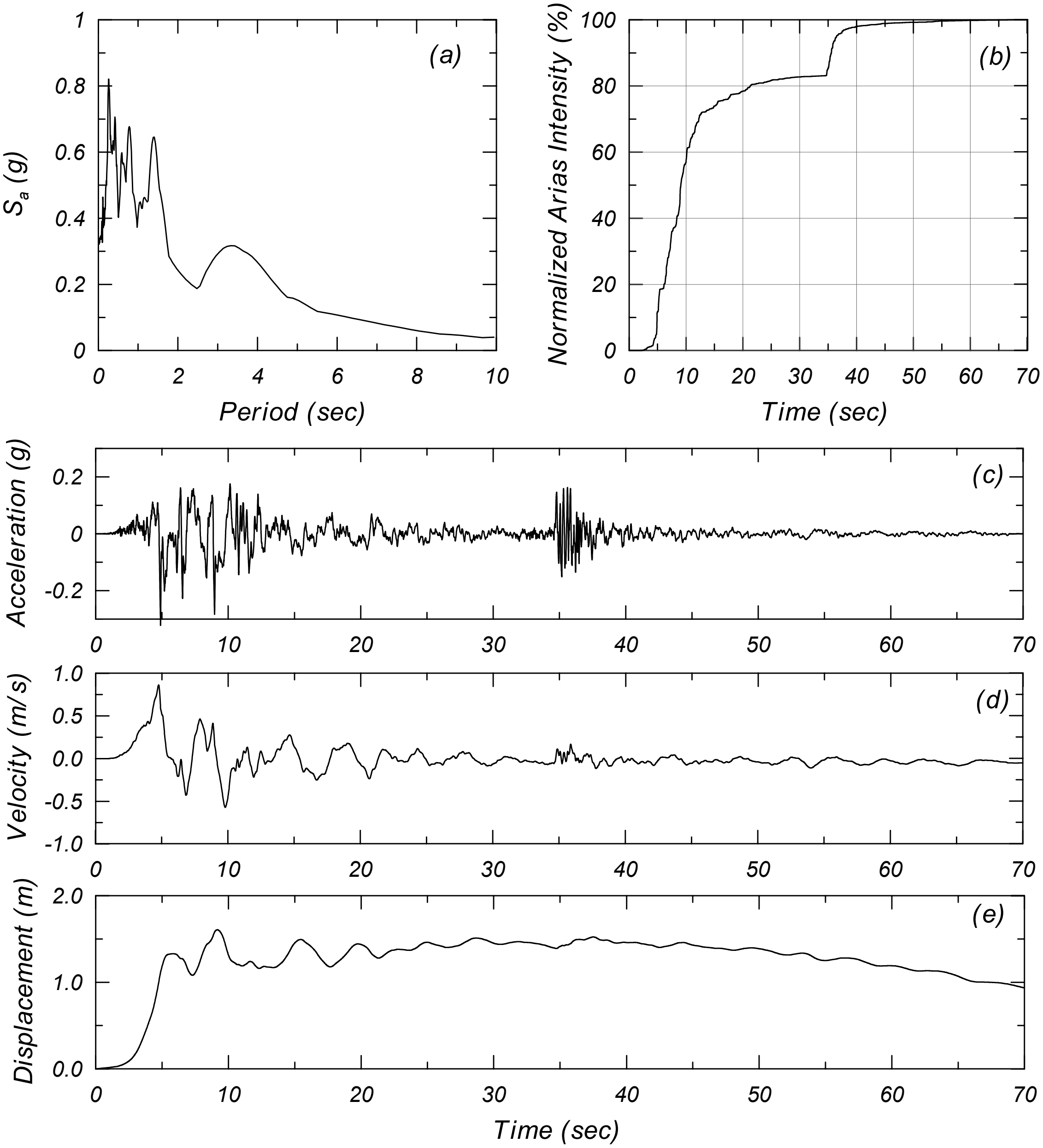

Figure A.5 Summary of Turkey, Yarimca Petkim ground motion (motion used as rock outcrop): (a) elastic 5% damped response spectra, (b) normalized Arias intensity, (c) acceleration time history, (d) velocity time history, and (e) displacement time history.

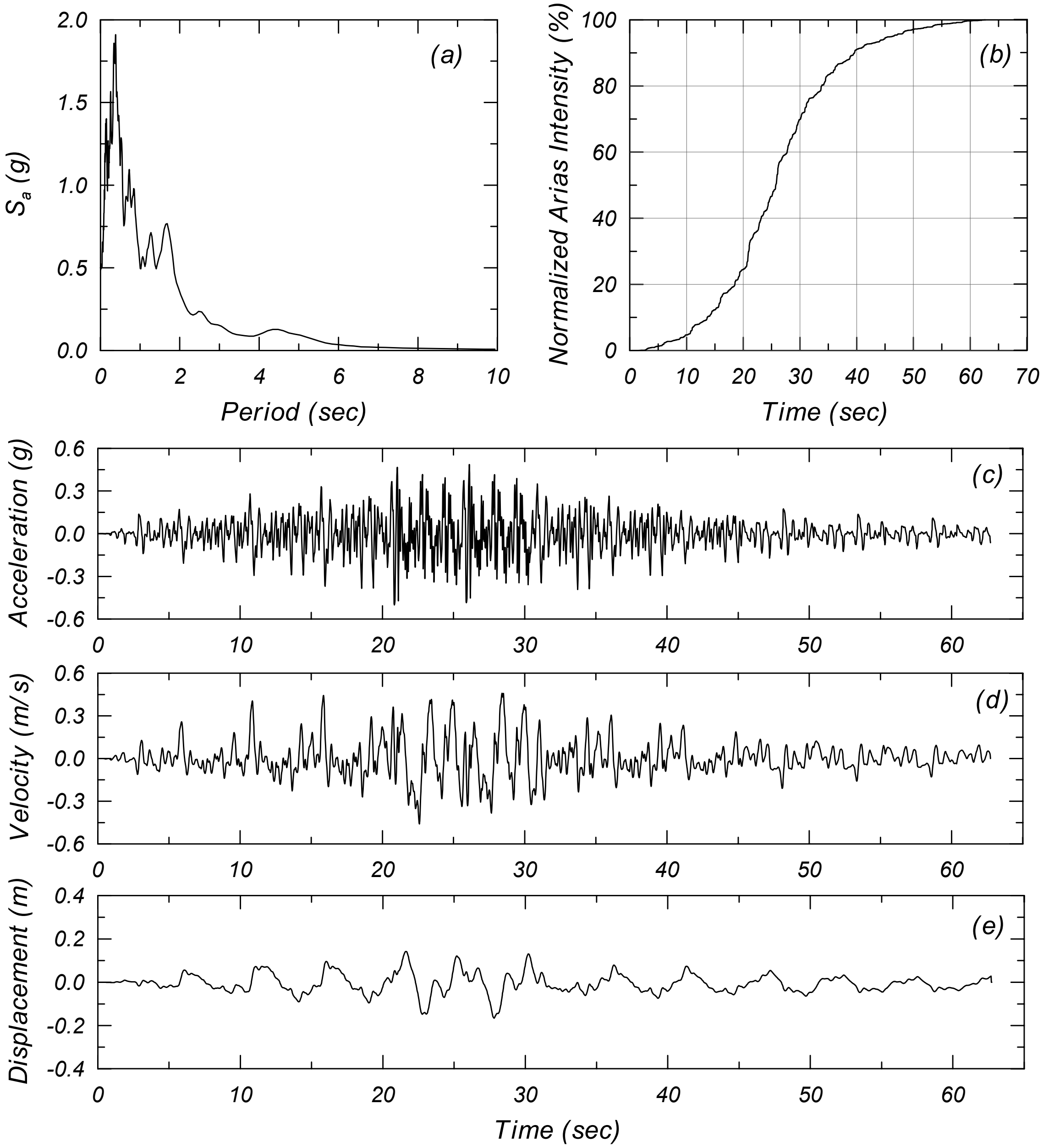

Figure A.6 Summary of Synthetic #1 (Seed and Idriss) ground motion (motion used as rock outcrop): (a) elastic 5% damped response spectra, (b) normalized Arias intensity, (c) acceleration time history, (d) velocity time history, and (e) displacement time history.

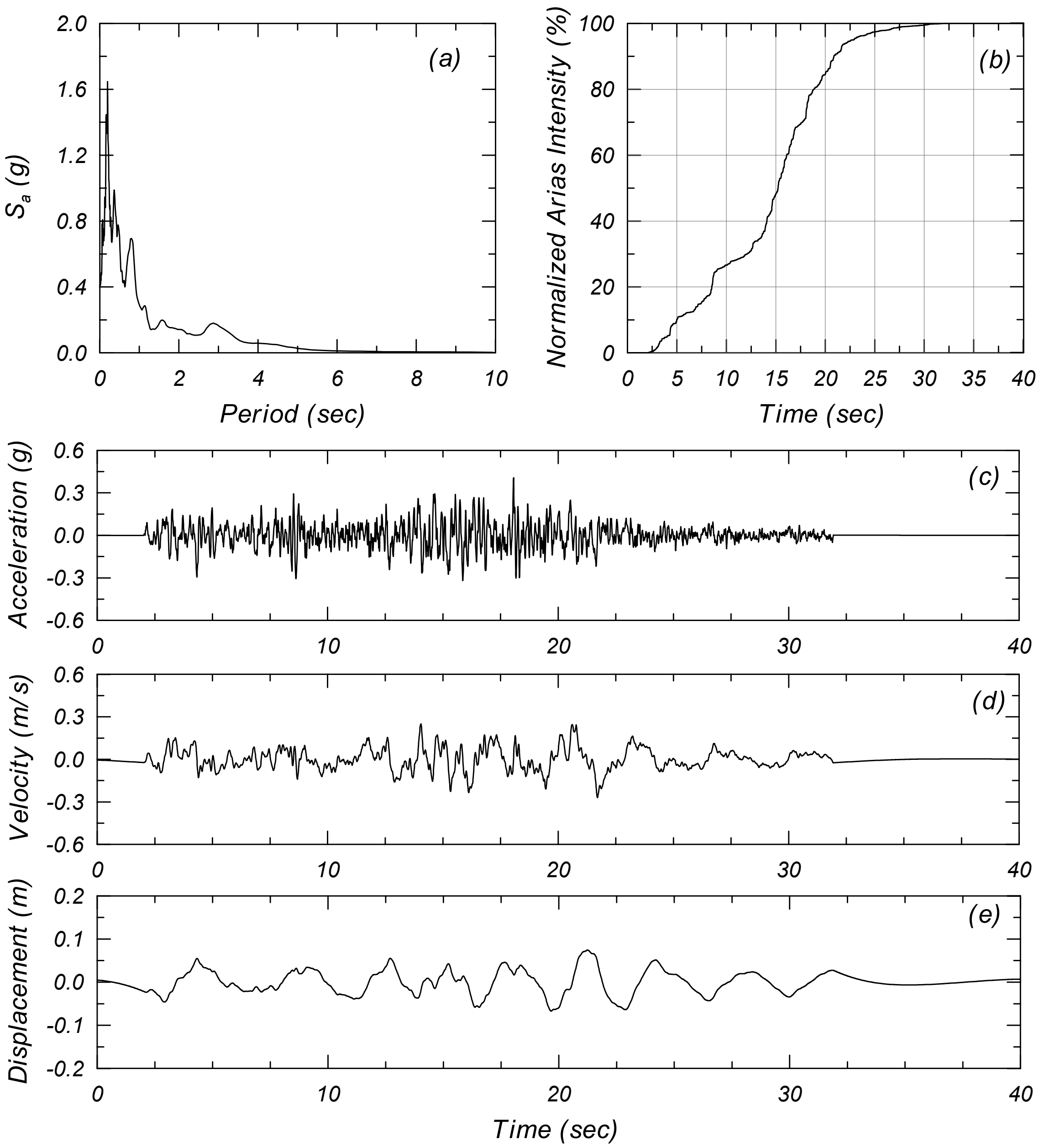

Figure A.7 Summary of Chile, Valparaiso ground motion (motion used as rock outcrop): (a) elastic 5% damped response spectra, (b) normalized Arias intensity, (c) acceleration time history, (d) velocity time history, and (e) displacement time history.

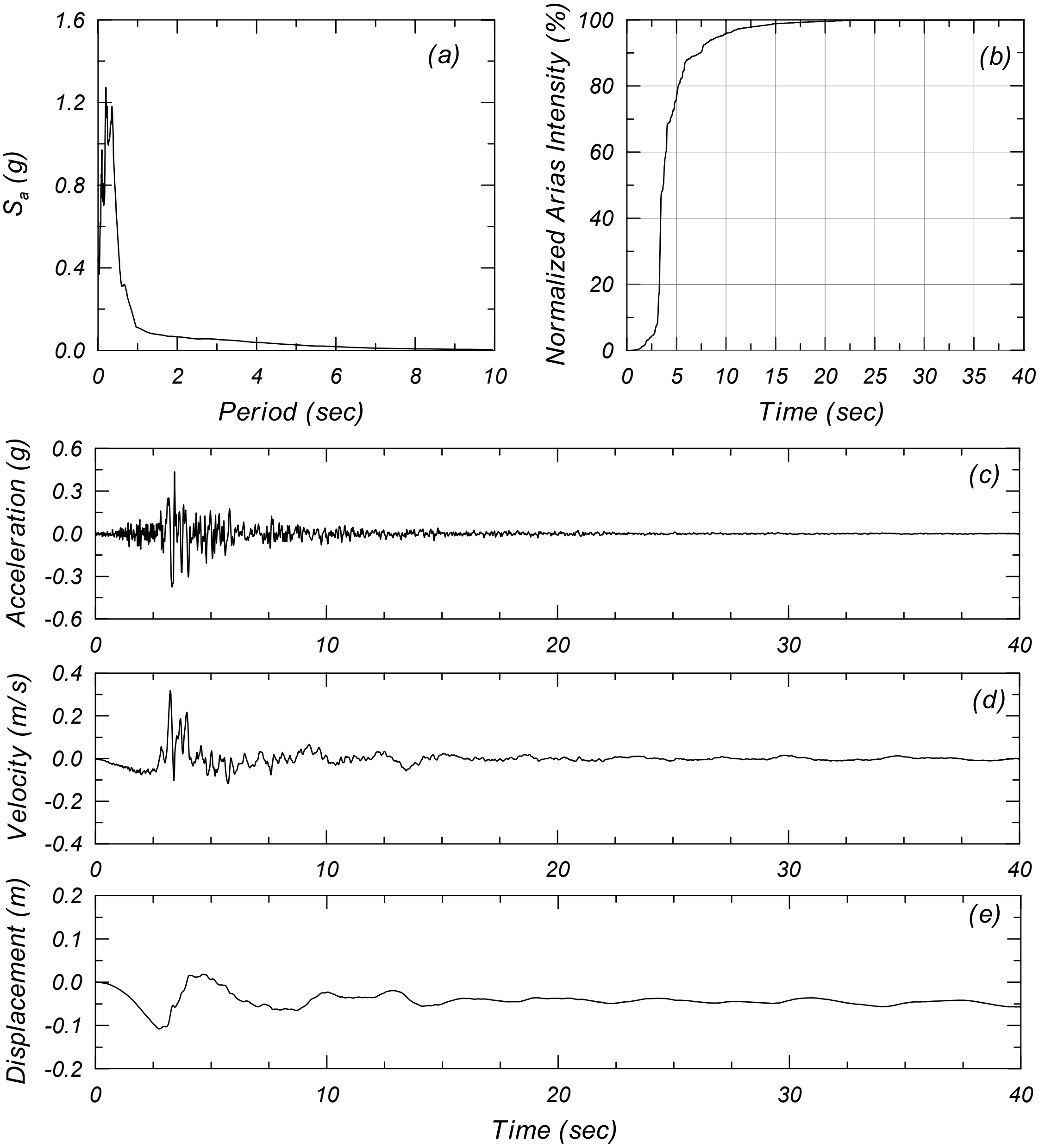

Figure A.8 Summary of Loma Prieta, Gilroy 1 ground motion (motion used as rock outcrop): (a) elastic 5% damped response spectra, (b) normalized Arias intensity, (c) acceleration time history, (d) velocity time history, and (e) displacement time history.

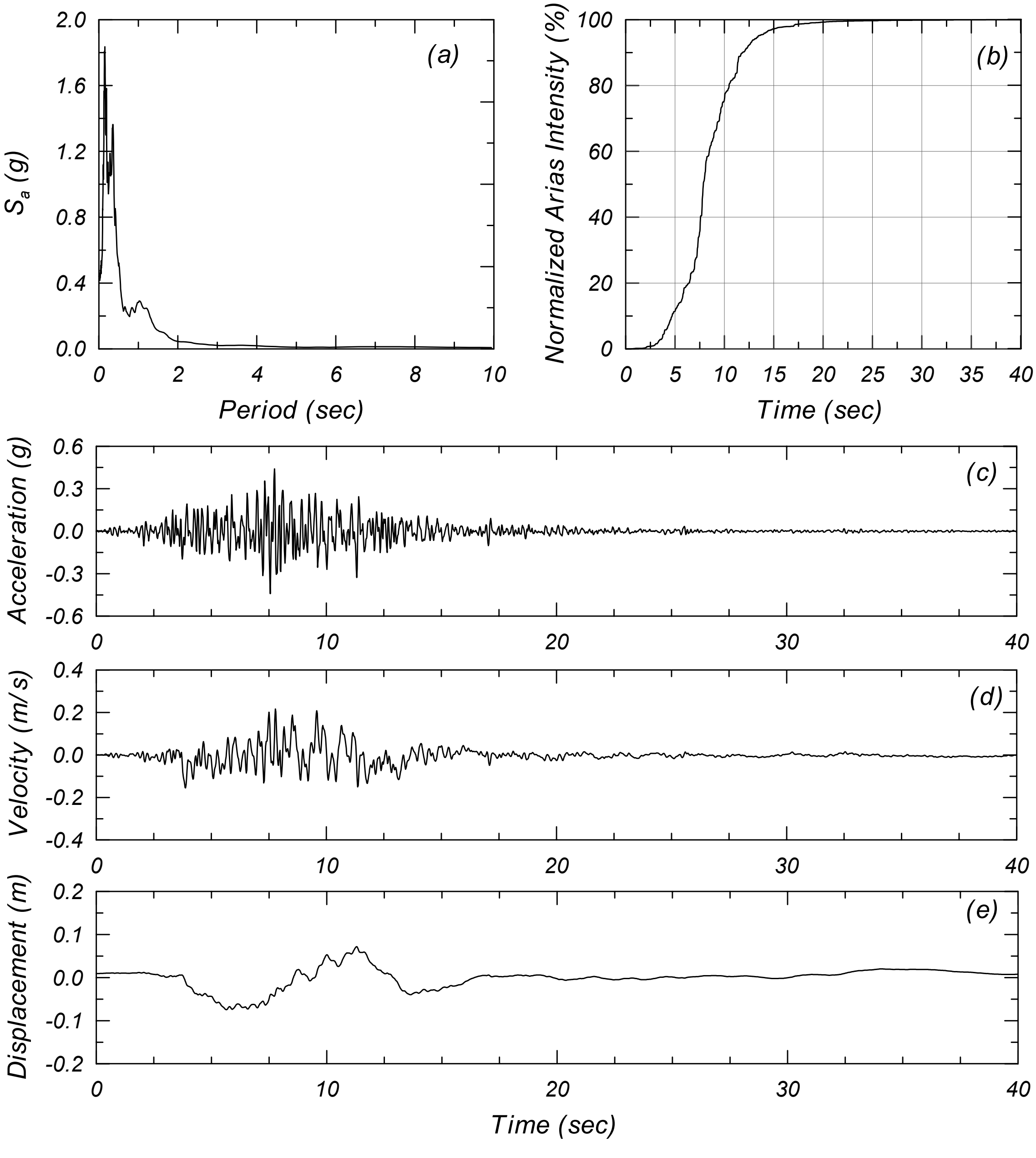

Figure A.9 Summary of Loma Prieta, Santa Cruz ground motion (motion used as rock outcrop): (a) elastic 5% damped response spectra, (b) normalized Arias intensity, (c) acceleration time history, (d) velocity time history, and (e) displacement time history.

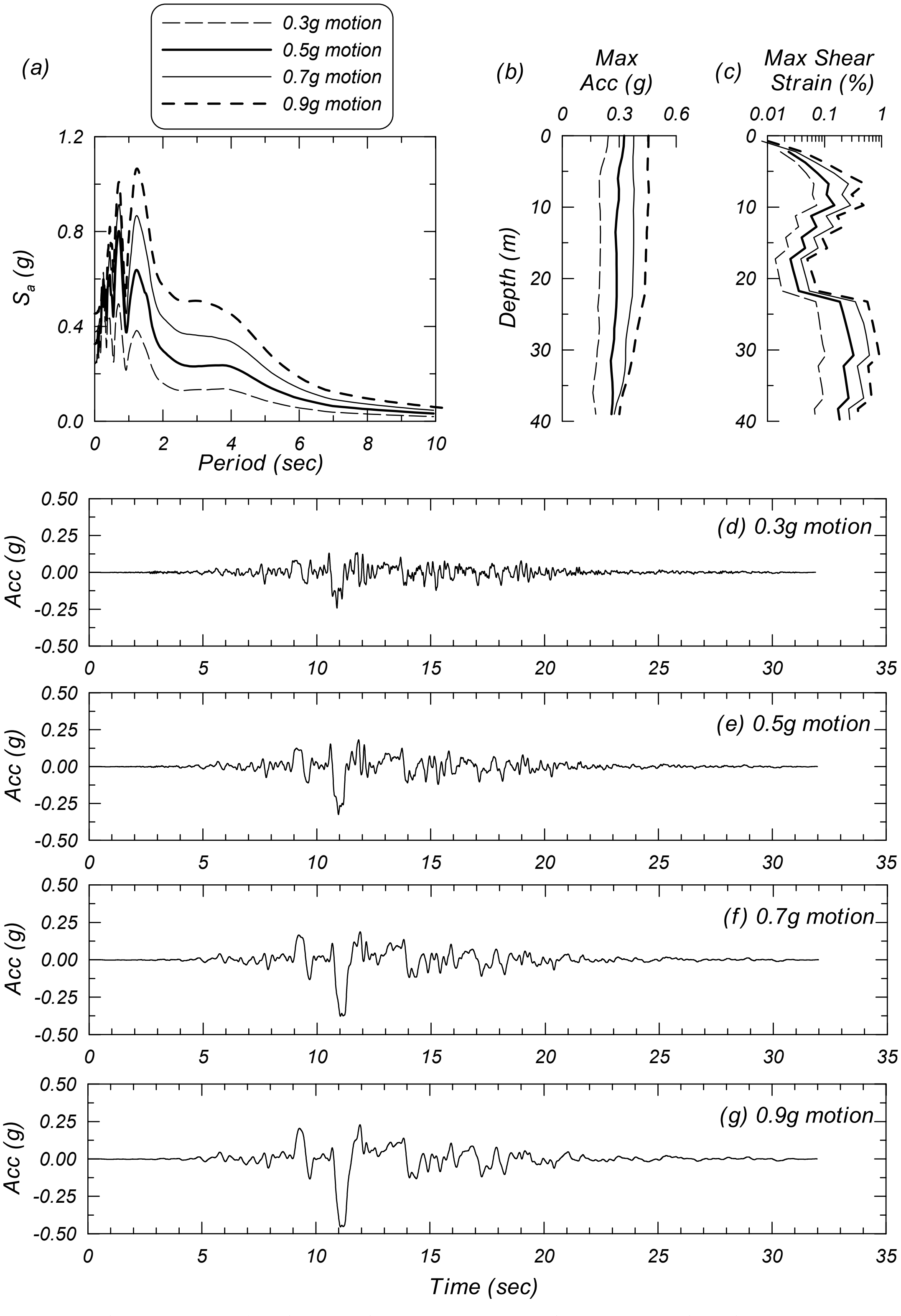

Figure A.10 Site response for the Landers, Lucerne motion: (a) acceleration response spectra (5% damping) at the ground surface, (b) maximum acceleration vs. depth, (c) maximum shear strain vs. depth, (d) surface acceleration history for 0.3g outcrop motion, (e) surface acceleration history for 0.5g outcrop motion, (f) surface acceleration history for 0.7g outcrop motion, and (g) surface acceleration history for 0.9g outcrop motion.

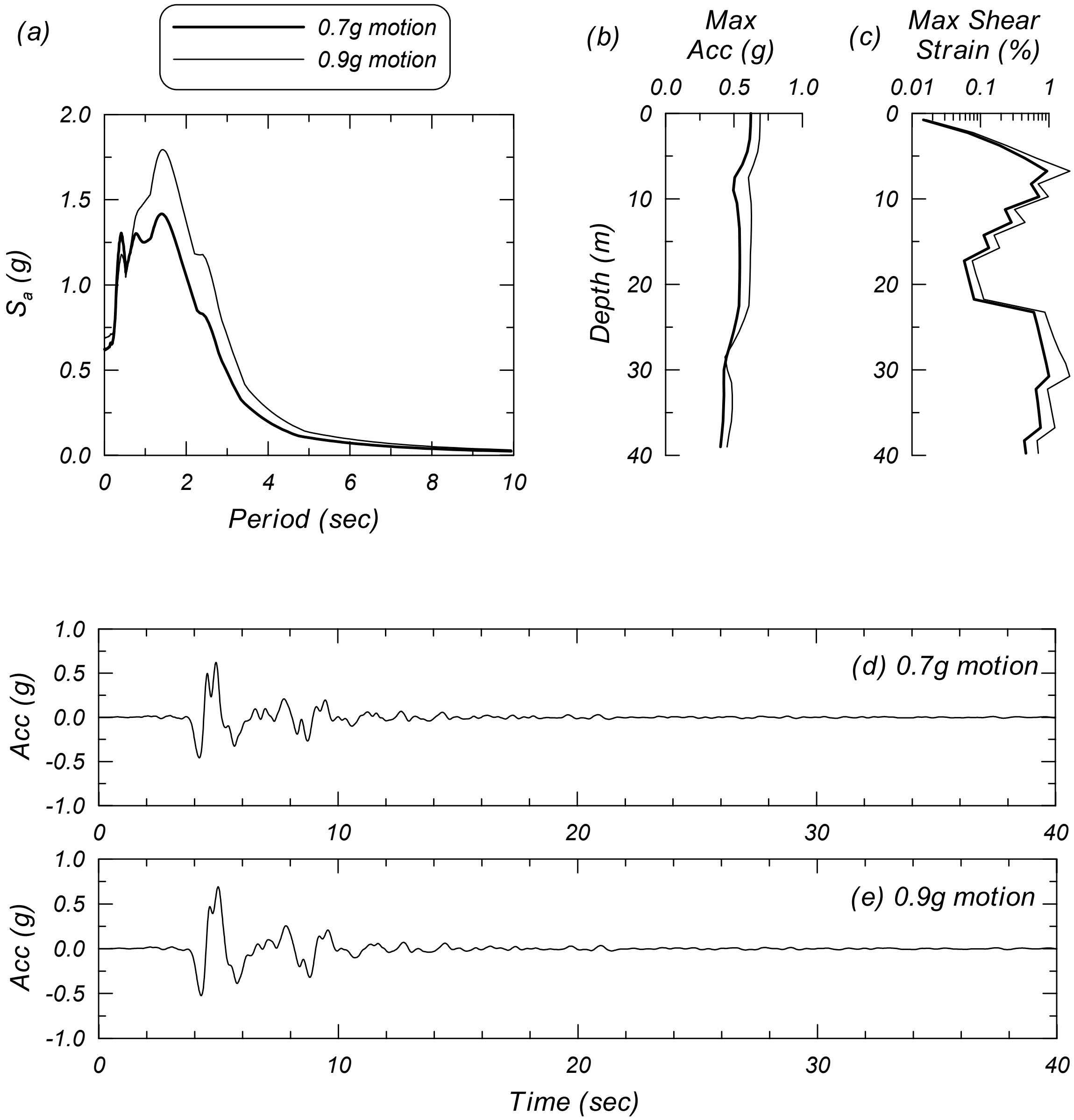

Figure A.11 Site response for the Northridge, Sylmar motion: (a) acceleration response spectra (5% damping) at the ground surface, (b) maximum acceleration vs. depth, (c) maximum shear strain vs. depth, (d) surface acceleration history for 0.7g outcrop motion, and (e) surface acceleration history for 0.9g outcrop motion.

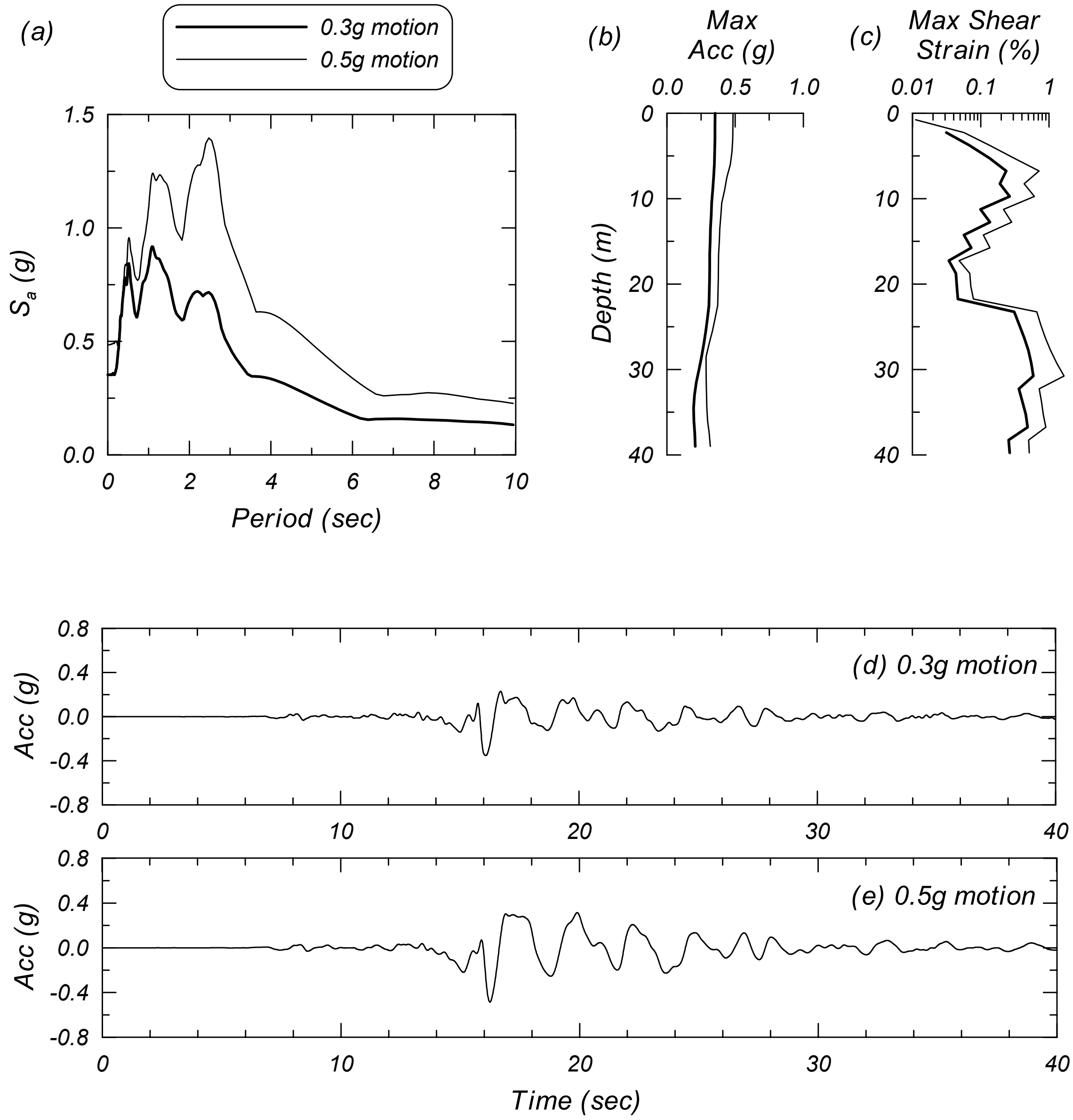

Figure A.12 Site response for the Chi-Chi Taiwan, Station 068E motion: (a) acceleration response spectra (5% damping) at the ground surface, (b) maximum acceleration vs. depth, (c) maximum shear strain vs. depth, (d) surface acceleration history for 0.3g outcrop motion, and (e) surface acceleration history for 0.5g outcrop motion.

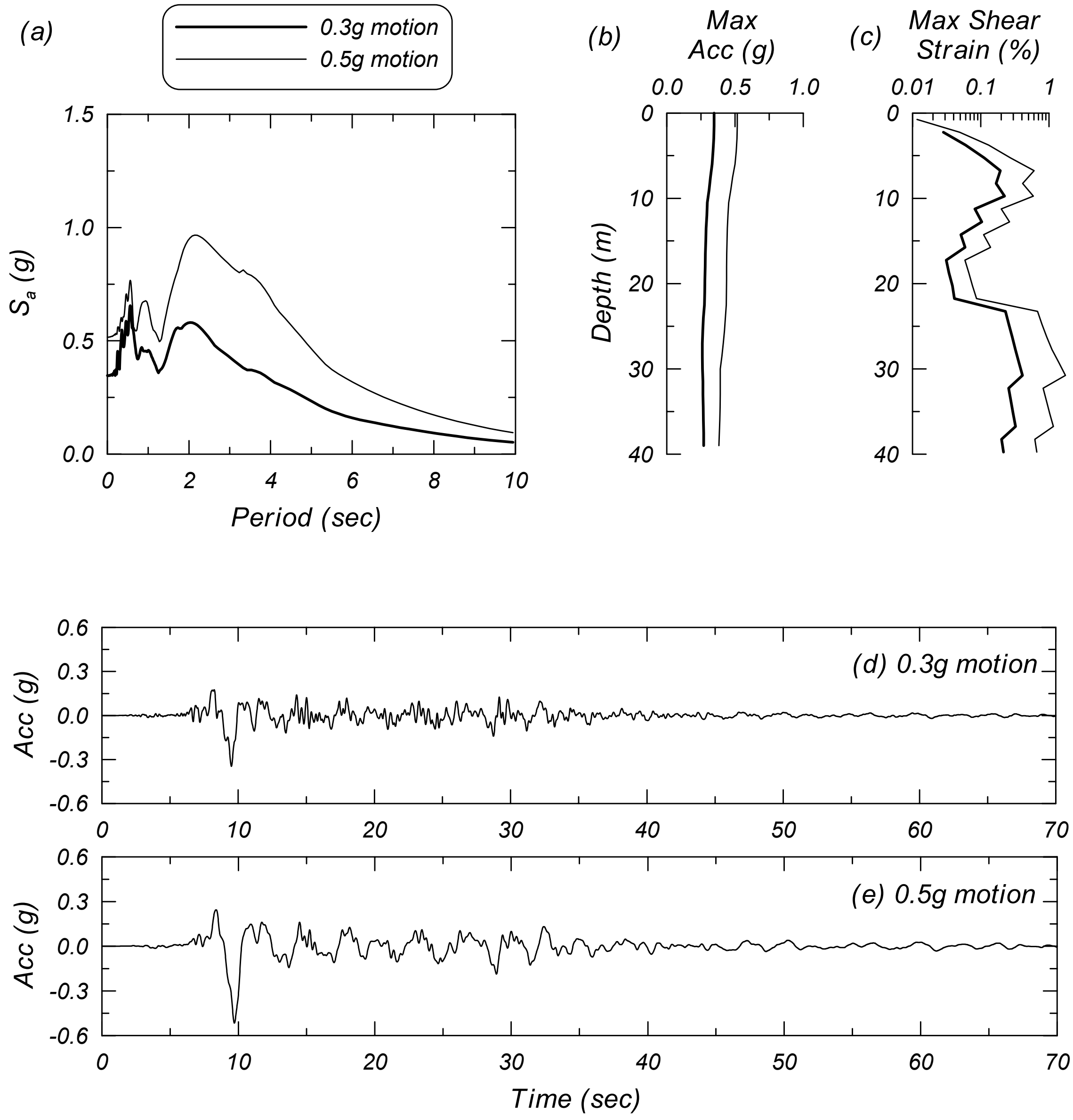

Figure A.13 Site response for the Chi-Chi Taiwan, Station 075E motion: (a) acceleration response spectra (5% damping) at the ground surface, (b) maximum acceleration vs. depth, (c) maximum shear strain vs. depth, (d) surface acceleration history for 0.3g outcrop motion, and (e) surface acceleration history for 0.5g outcrop motion.

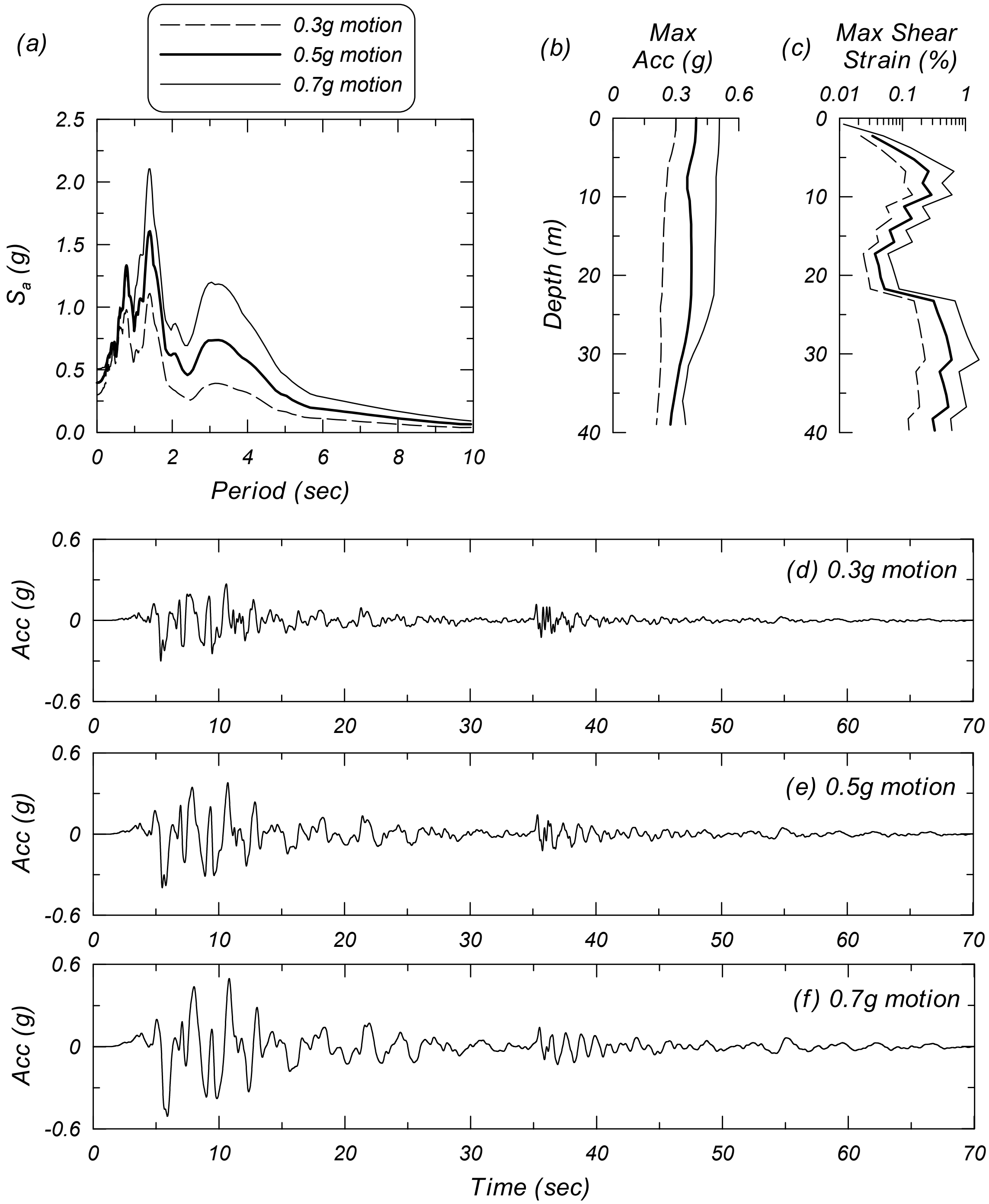

Figure A.14 Site response for the Turkey, Yarimca Petkim motion: (a) acceleration response spectra (5% damping) at the ground surface, (b) maximum acceleration vs. depth, (c) maximum shear strain vs. depth, (d) surface acceleration history for 0.3g outcrop motion, (e) surface acceleration history for 0.5g outcrop motion, and (f) surface acceleration history for 0.7g outcrop motion.

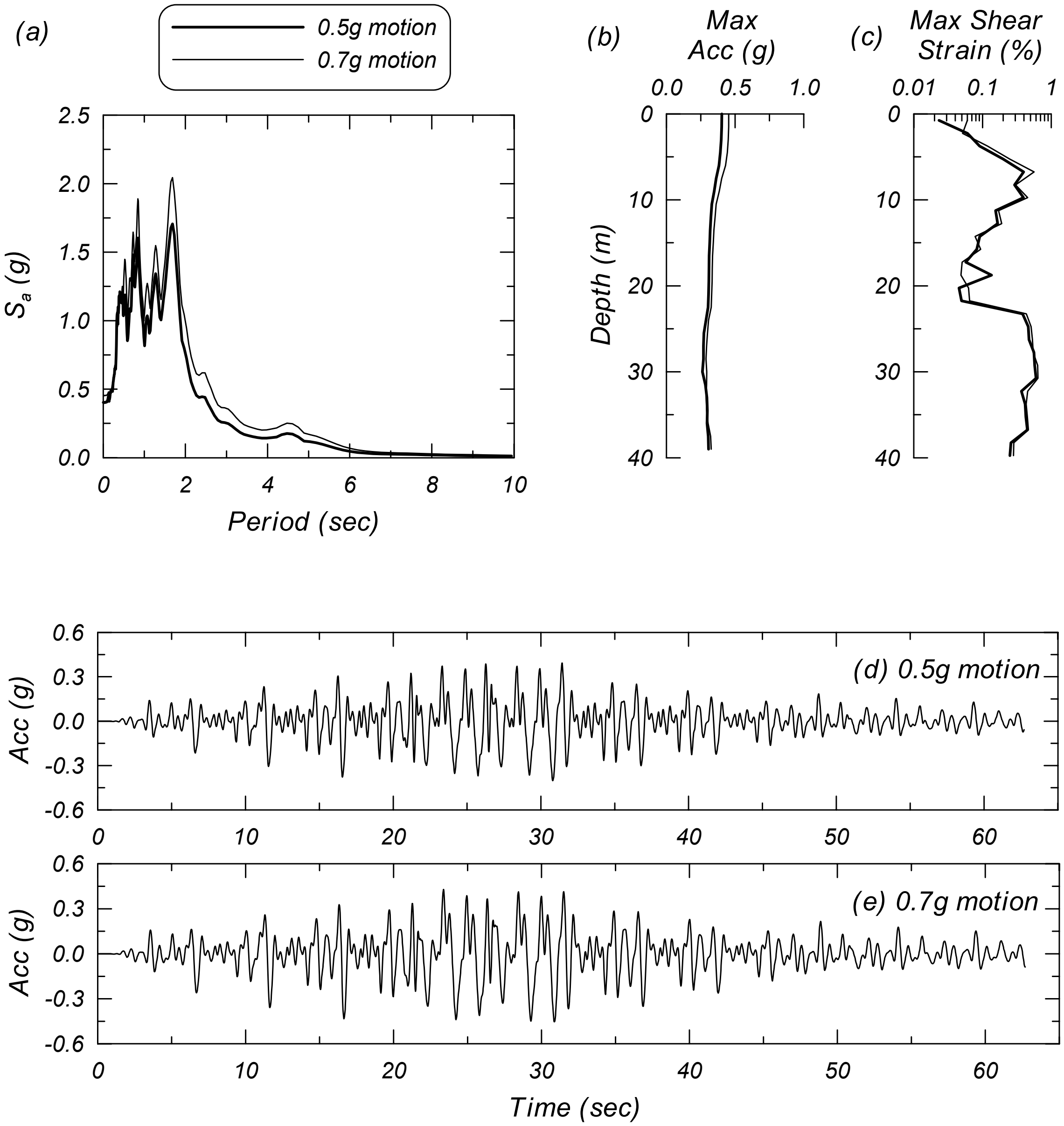

Figure A.15 Site response for the Synthetic #1 (Seed and Idriss) motion: (a) acceleration response spectra (5% damping) at the ground surface, (b) maximum acceleration vs. depth, (c) maximum shear strain vs. depth, (d) surface acceleration history for 0.5g outcrop motion, and (e) surface acceleration history for 0.7g outcrop motion.

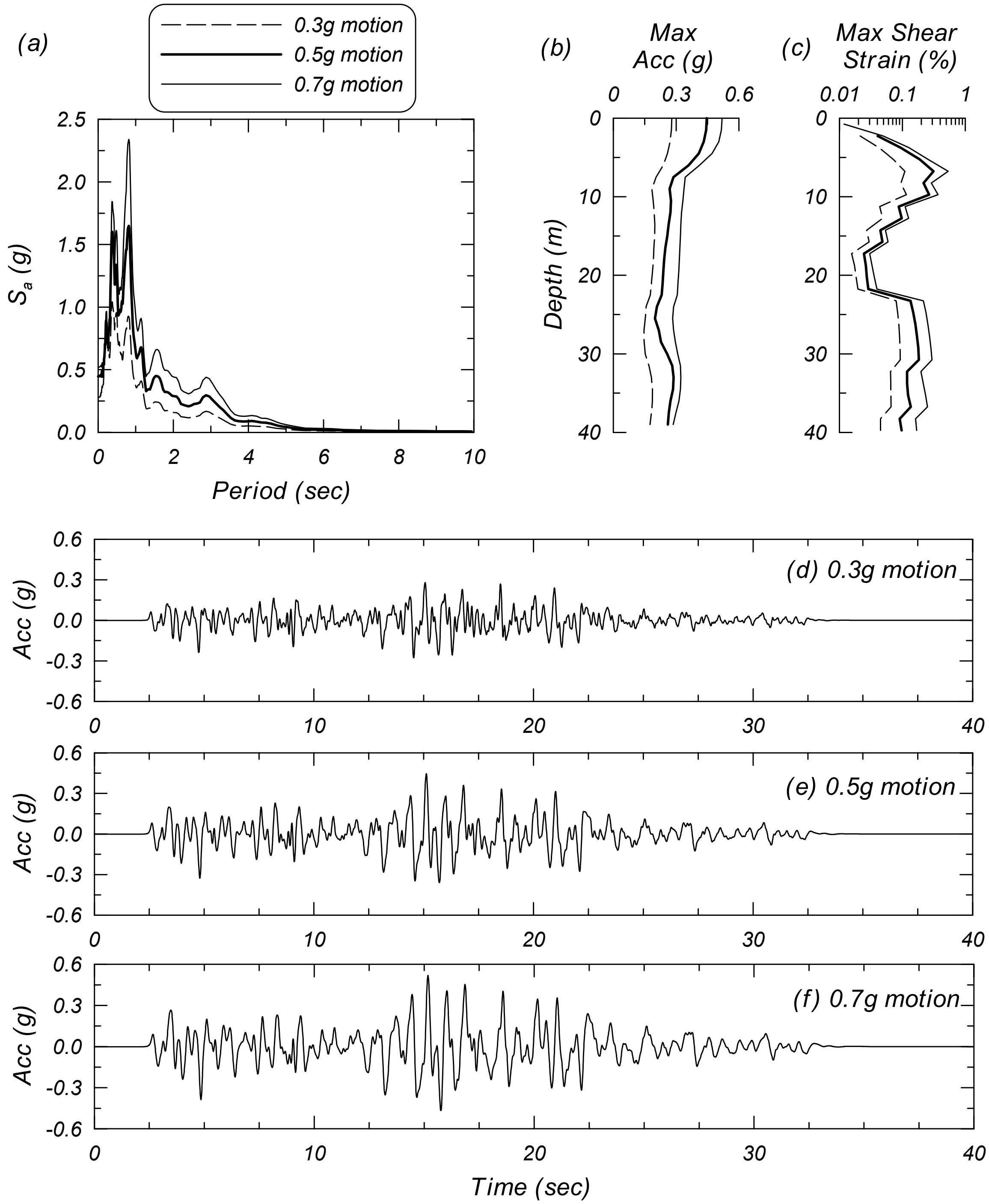

Figure A.16 Site response for the Chile, Valparaiso motion: (a) acceleration response spectra (5% damping) at the ground surface, (b) maximum acceleration vs. depth, (c) maximum shear strain vs. depth, (d) surface acceleration history for 0.3g outcrop motion, (e) surface acceleration history for 0.5g outcrop motion, and (f) surface acceleration history for 0.7g outcrop motion.

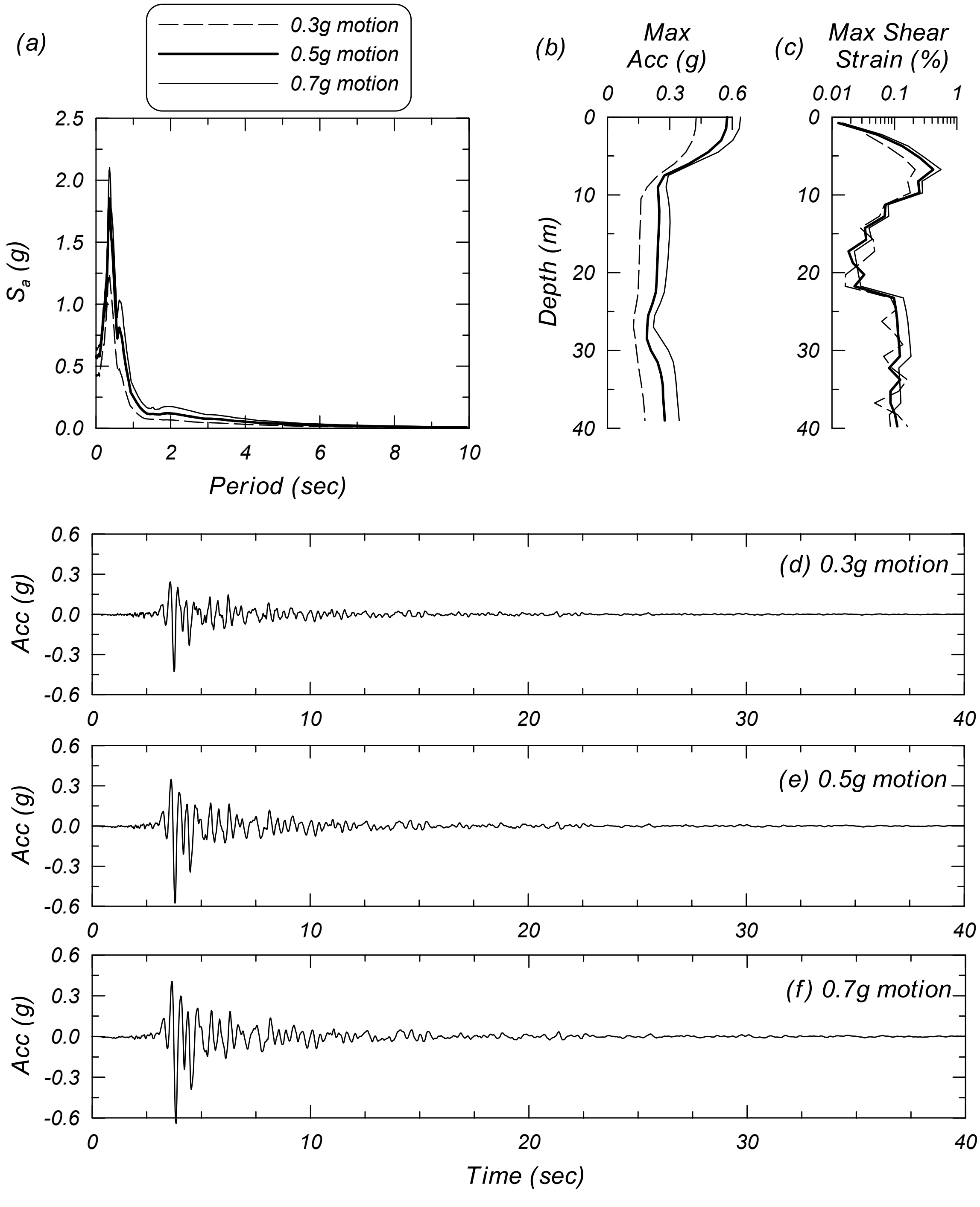

Figure A.17 Site response for the Loma Prieta, Gilroy 1 motion: (a) acceleration response spectra (5% damping) at the ground surface, (b) maximum acceleration vs. depth, (c) maximum shear strain vs. depth, (d) surface acceleration history for 0.5g outcrop motion, and (f) surface acceleration history for 0.7g outcrop motion.

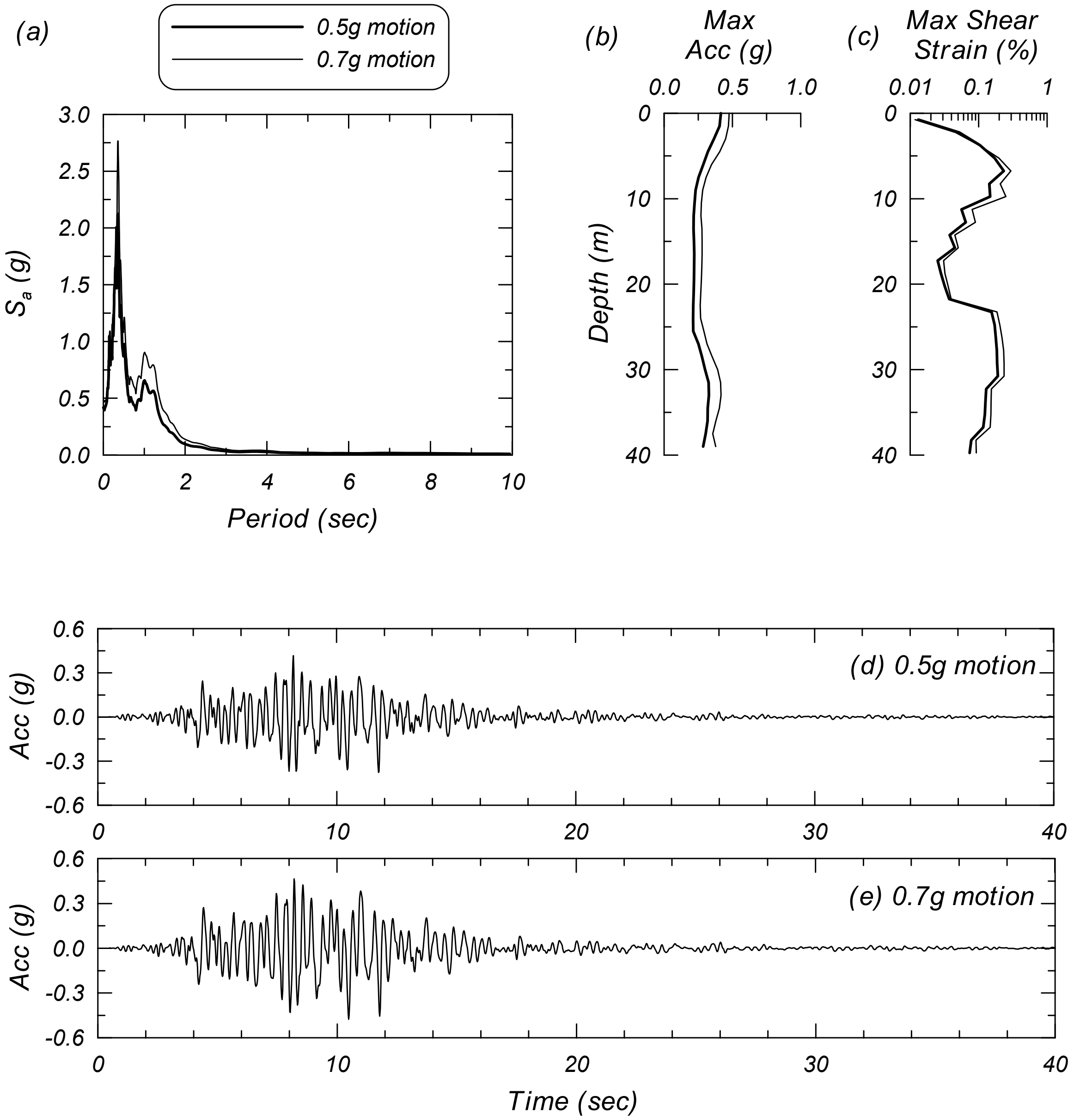

Figure A.18 Site response for the Loma Prieta, Santa Cruz motion: (a) acceleration response spectra (5% damping) at the ground surface, (b) maximum acceleration vs. depth, (c) maximum shear strain vs. depth, (d) surface acceleration history for 0.5g outcrop motion, and (f) surface acceleration history for 0.7g outcrop motion.

PEER REPORTS

PEER reports are available from the National Information Service for Earthquake Engineering (NISEE). To order PEER reports, please contact the Pacific Earthquake Engineering Research Center, 1301 South 46th Street, Richmond, California 94804-4698. Tel.: (510) 231-9468; Fax: (510) 231-9461.

PEER 2002/14 *Inelastic Seismic Response of Extended Pile Shaft Supported Bridge Structures.* T.C. Hutchinson, R.W. Boulanger, Y.H. Chai, and I.M. Idriss. December 2002.

PEER 2002/13 *Probabilistic Models and Fragility Estimates for Bridge Components and Systems.* Paolo Gardoni, Armen Der Kiureghian, and Khalid M. Mosalam. June 2002.

PEER 2002/12 *Effects of Fault Dip and Slip Rake on Near-Source Ground Motions: Why Chi-Chi Was a Relatively Mild M7.6 Earthquake.* Brad T. Aagaard, John F. Hall, and Thomas H. Heaton. December 2002.

PEER 2002/11 *Analytical and Experimental Study of Fiber-Reinforced Strip Isolators*. James M. Kelly and Shakhzod M. Takhirov. September 2002.

PEER 2002/10 *Centrifuge Modeling of Settlement and Lateral Spreading with Comparisons to Numerical Analyses***.** Sivapalan Gajan and Bruce L. Kutter. January 2003.

PEER 2002/09 *Documentation and Analysis of Field Case Histories of Seismic Compression during the 1994 Northridge, California, Earthquake.* Jonathan P. Stewart, Patrick M. Smith, Daniel H. Whang, and Jonathan D. Bray. October 2002.

PEER 2002/08 *Component Testing, Stability Analysis and Characterization of Buckling-Restrained Unbonded Braces™.* Cameron Black, Nicos Makris, and Ian Aiken. September 2002.

PEER 2002/07 *Seismic Performance of Pile-Wharf Connections.* Charles W. Roeder, Robert Graff, Jennifer Soderstrom, and Jun Han Yoo. December 2001.

PEER 2002/06 *The Use of Benefit-Cost Analysis for Evaluation of Performance-Based Earthquake Engineering Decisions*. Richard O. Zerbe and Anthony Falit-Baiamonte. September 2001.

PEER 2002/05 *Guidelines, Specifications, and Seismic Performance Characterization of Nonstructural Building Components and Equipment*. André Filiatrault, Constantin Christopoulos, and Christopher Stearns. September 2001.

PEER 2002/03 *Investigation of Sensitivity of Building Loss Estimates to Major Uncertain Variables for the Van Nuys Testbed.* Keith A. Porter, James L. Beck, and Rustem V. Shaikhutdinov. August 2002.

PEER 2002/02 *The Third U.S.-Japan Workshop on Performance-Based Earthquake Engineering Methodology for Reinforced Concrete Building Structures*. July 2002.

PEER 2002/01 *Nonstructural Loss Estimation: The UC Berkeley Case Study. Mary C. Comerio and John C. Stallmeyer.* December 2001.

PEER 2001/16 *Statistics of SDF-System Estimate of Roof Displacement for Pushover Analysis of Buildings.* Anil K. Chopra, Rakesh K. Goel, and Chatpan Chintanapakdee. December 2001.

PEER 2001/15	*Damage to Bridges during the 2001 Nisqually Earthquake.* R. Tyler Ranf, Marc O. Eberhard, and Michael P. Berry. November 2001.
PEER 2001/14	*Rocking Response of Equipment Anchored to a Base Foundation.* Nicos Makris and Cameron J. Black. September 2001.
PEER 2001/13	*Modeling Soil Liquefaction Hazards for Performance-Based Earthquake Engineering.* Steven L. Kramer and Ahmed-W. Elgamal. February 2001.
PEER 2001/12	*Development of Geotechnical Capabilities in OpenSees.* Boris Jeremic. September 2001.
PEER 2001/11	*Analytical and Experimental Study of Fiber-Reinforced Elastomeric Isolators*. James M. Kelly and Shakhzod M. Takhirov. September 2001.
PEER 2001/10	*Amplification Factors for Spectral Acceleration in Active Regions.* Jonathan P. Stewart, Andrew H. Liu, Yoojoong Choi, and Mehmet B. Baturay. December 2001.
PEER 2001/09	*Ground Motion Evaluation Procedures for Performance-Based Design.* Jonathan P. Stewart, Shyh-Jeng Chiou, Jonathan D. Bray, Robert W. Graves, Paul G. Somerville, and Norman A. Abrahamson. September 2001.
PEER 2001/08	*Experimental and Computational Evaluation of Reinforced Concrete Bridge Beam-Column Connections for Seismic Performance*. Clay J. Naito, Jack P. Moehle, and Khalid M. Mosalam. November 2001.
PEER 2001/07	*The Rocking Spectrum and the Shortcomings of Design Guidelines.* Nicos Makris and Dimitrios Konstantinidis. August 2001.
PEER 2001/06	*Development of an Electrical Substation Equipment Performance Database for Evaluation of Equipment Fragilities*. Thalia Agnanos. April 1999.
PEER 2001/05	*Stiffness Analysis of Fiber-Reinforced Elastomeric Isolators.* Hsiang-Chuan Tsai and James M. Kelly. May 2001.
PEER 2001/04	*Organizational and Societal Considerations for Performance-Based Earthquake Engineering.* Peter J. May. April 2001.
PEER 2001/03	*A Modal Pushover Analysis Procedure to Estimate Seismic Demands for Buildings: Theory and Preliminary Evaluation.* Anil K. Chopra and Rakesh K. Goel. January 2001.
PEER 2001/02	*Seismic Response Analysis of Highway Overcrossings Including Soil-Structure Interaction.* Jian Zhang and Nicos Makris. March 2001.
PEER 2001/01	*Experimental Study of Large Seismic Steel Beam-to-Column Connections.* Egor P. Popov and Shakhzod M. Takhirov. November 2000.
PEER 2000/10	*The Second U.S.-Japan Workshop on Performance-Based Earthquake Engineering Methodology for Reinforced Concrete Building Structures.* March 2000.
PEER 2000/09	*Structural Engineering Reconnaissance of the August 17, 1999 Earthquake: Kocaeli (Izmit), Turkey.* Halil Sezen, Kenneth J. Elwood, Andrew S. Whittaker, Khalid Mosalam, John J. Wallace, and John F. Stanton. December 2000.

PEER 2000/08 *Behavior of Reinforced Concrete Bridge Columns Having Varying Aspect Ratios and Varying Lengths of Confinement.* Anthony J. Calderone, Dawn E. Lehman, and Jack P. Moehle. January 2001.

PEER 2000/07 *Cover-Plate and Flange-Plate Reinforced Steel Moment-Resisting Connections.* Taejin Kim, Andrew S. Whittaker, Amir S. Gilani, Vitelmo V. Bertero, and Shakhzod M. Takhirov. September 2000.

PEER 2000/06 *Seismic Evaluation and Analysis of 230-kV Disconnect Switches.* Amir S. J. Gilani, Andrew S. Whittaker, Gregory L. Fenves, Chun-Hao Chen, Henry Ho, and Eric Fujisaki. July 2000.

PEER 2000/05 *Performance-Based Evaluation of Exterior Reinforced Concrete Building Joints for Seismic Excitation.* Chandra Clyde, Chris P. Pantelides, and Lawrence D. Reaveley. July 2000.

PEER 2000/04 *An Evaluation of Seismic Energy Demand: An Attenuation Approach.* Chung-Che Chou and Chia-Ming Uang. July 1999.

PEER 2000/03 *Framing Earthquake Retrofitting Decisions: The Case of Hillside Homes in Los Angeles.* Detlof von Winterfeldt, Nels Roselund, and Alicia Kitsuse. March 2000.

PEER 2000/02 *U.S.-Japan Workshop on the Effects of Near-Field Earthquake Shaking.* Andrew Whittaker, ed. July 2000.

PEER 2000/01 *Further Studies on Seismic Interaction in Interconnected Electrical Substation Equipment.* Armen Der Kiureghian, Kee-Jeung Hong, and Jerome L. Sackman. November 1999.

PEER 1999/14 *Seismic Evaluation and Retrofit of 230-kV Porcelain Transformer Bushings*. Amir S. Gilani, Andrew S. Whittaker, Gregory L. Fenves, and Eric Fujisaki. December 1999.

PEER 1999/13 *Building Vulnerability Studies: Modeling and Evaluation of Tilt-up and Steel Reinforced Concrete Buildings.* John W. Wallace, Jonathan P. Stewart, and Andrew S. Whittaker, editors. December 1999.

PEER 1999/12 *Rehabilitation of Nonductile RC Frame Building Using Encasement Plates and Energy-Dissipating Devices.* Mehrdad Sasani, Vitelmo V. Bertero, James C. Anderson. December 1999.

PEER 1999/11 *Performance Evaluation Database for Concrete Bridge Components and Systems under Simulated Seismic Loads.* Yael D. Hose and Frieder Seible. November 1999.

PEER 1999/10 *U.S.-Japan Workshop on Performance-Based Earthquake Engineering Methodology for Reinforced Concrete Building Structures.* December 1999.

PEER 1999/09 *Performance Improvement of Long Period Building Structures Subjected to Severe Pulse-Type Ground Motions*. James C. Anderson, Vitelmo V. Bertero, and Raul Bertero. October 1999.

PEER 1999/08 *Envelopes for Seismic Response Vectors.* Charles Menun and Armen Der Kiureghian. July 1999.

PEER 1999/07	*Documentation of Strengths and Weaknesses of Current Computer Analysis Methods for Seismic Performance of Reinforced Concrete Members.* William F. Cofer. November 1999.
PEER 1999/06	*Rocking Response and Overturning of Anchored Equipment under Seismic Excitations.* Nicos Makris and Jian Zhang. November 1999.
PEER 1999/05	*Seismic Evaluation of 550 kV Porcelain Transformer Bushings.* Amir S. Gilani, Andrew S. Whittaker, Gregory L. Fenves, and Eric Fujisaki. October 1999.
PEER 1999/04	*Adoption and Enforcement of Earthquake Risk-Reduction Measures.* Peter J. May, Raymond J. Burby, T. Jens Feeley, and Robert Wood.
PEER 1999/03	*Task 3 Characterization of Site Response General Site Categories*. Adrian Rodriguez-Marek, Jonathan D. Bray, and Norman Abrahamson. February 1999.
PEER 1999/02	*Capacity-Demand-Diagram Methods for Estimating Seismic Deformation of Inelastic Structures: SDF Systems*. Anil K. Chopra and Rakesh Goel. April 1999.
PEER 1999/01	*Interaction in Interconnected Electrical Substation Equipment Subjected to Earthquake Ground Motions.* Armen Der Kiureghian, Jerome L. Sackman, and Kee-Jeung Hong. February 1999.
PEER 1998/08	*Behavior and Failure Analysis of a Multiple-Frame Highway Bridge in the 1994 Northridge Earthquake.* Gregory L. Fenves and Michael Ellery. December 1998.
PEER 1998/07	*Empirical Evaluation of Inertial Soil-Structure Interaction Effects.* Jonathan P. Stewart, Raymond B. Seed, and Gregory L. Fenves. November 1998.
PEER 1998/06	*Effect of Damping Mechanisms on the Response of Seismic Isolated Structures.* Nicos Makris and Shih-Po Chang. November 1998.
PEER 1998/05	*Rocking Response and Overturning of Equipment under Horizontal Pulse-Type Motions.* Nicos Makris and Yiannis Roussos. October 1998.
PEER 1998/04	*Pacific Earthquake Engineering Research Invitational Workshop Proceedings, May 14–15, 1998: Defining the Links between Planning, Policy Analysis, Economics and Earthquake Engineering.* Mary Comerio and Peter Gordon. September 1998.
PEER 1998/03	*Repair/Upgrade Procedures for Welded Beam to Column Connections.* James C. Anderson and Xiaojing Duan. May 1998.
PEER 1998/02	*Seismic Evaluation of 196 kV Porcelain Transformer Bushings.* Amir S. Gilani, Juan W. Chavez, Gregory L. Fenves, and Andrew S. Whittaker. May 1998.
PEER 1998/01	*Seismic Performance of Well-Confined Concrete Bridge Columns.* Dawn E. Lehman and Jack P. Moehle. December 2000.